



THERMODYNAMIC MODELLING OF PORTLAND CEMENT CLINKER PRODUCTION

WAHAB ABDUL
MSci CHEMISTRY, QUEEN MARY UNIVERSITY OF LONDON.

A THESIS PRESENTED FOR THE DEGREE OF DOCTOR OF PHILOSOPHY
IN CHEMICAL ENGINEERING AT THE UNIVERSITY OF ABERDEEN.

DECLARATION

This thesis is submitted to the University of Aberdeen for the degree of Doctor of Philosophy. It is a record and presentation of the original research work carried out by the author under the supervision of Dr. Marcus Nigel Campbell Bannerman. This thesis has not been submitted and/or accepted in any previous application for a degree. Wherever contributions of others are involved, every effort is made to indicate this clearly, with due reference to the literature, and acknowledgement of collaborative research and discussions

A handwritten signature in black ink, appearing to read "Afawahab".

25th September 2023

Signature

Date

ABSTRACT

This thesis presents the development of a predictive thermodynamic models for the high-temperature formation of ordinary Portland cement clinkers. A thermodynamic database for the system CaO-SiO₂-Al₂O₃-MgO-Fe-O, including the melt phase, is developed utilising the CALPHAD approach. The thesis reviews cement production and the thermodynamic models suitable for its prediction before selecting to use third-generation CALPHAD functions for all end-members, the two-state model for pure liquids, and the associates model for melt phases. The fitting approach is discussed which makes use of reviewed data from literature and novel experimental data measured by collaborators, as well as newly-developed methods to allow for faster and more accurate fitting of the thermodynamic properties. This in turn provides much-needed updates to the thermodynamic properties of key clinker phases and systems which are presented over several chapters. Finally, an initial demonstration of the application of the developed database is given by using it for predictive calculations of clinker composition. This also involves the novel analysis of real industrial clinkers which were collected and analysed by collaborators within the project. Overall, the database is comparable to current best estimates while also providing estimates of many interesting factors, such as the melt fraction, substitution of Al/Fe in ferrite, and MgO in belite polymorphs. The database is also suitable for use outside the normal Portland cement formulations and a range of future applications are discussed.

Contents

Declaration	2
Abstract	5
Acknowledgements	19
1 Introduction	21
1.1 Structure, aims and objectives	23
1.2 References	24
2 The importance of thermodynamics in cement production	29
2.1 Overview of cement production	29
2.2 Major clinker phases	31
2.2.1 Alite	32
2.2.2 Belite	32
2.2.3 C ₃ A or “aluminate”	33
2.2.4 Ferrite	33
2.3 Reaction chemistry and approach to equilibrium in the kiln	34
2.4 Motivation for thermodynamic modelling of clinkerization.	35
2.5 References	36
3 Thermodynamic models for clinkerization	39
3.1 Stoichiometric phases and end-members	40
3.1.1 Solid phase models	40
3.1.2 Liquid phase model	43
3.2 Solution phase model	45
3.2.1 Solid solutions	45
3.2.2 Melt phase model	48
3.2.3 Redlich-Kister excess term	51
3.3 Magnetic model	54
3.4 Summary and justification for selected models	56
3.5 References	57

CONTENTS

4 Overview of thermodynamic fitting	63
4.1 CALPHAD approach	64
4.2 Uncertainty in literature measurements	64
4.3 Fitting methodology	65
4.3.1 Stoichiometric and end-member fitting	65
4.3.2 Solution phase fitting	67
4.4 Overall approach with application to the CaO-MgO system.	69
4.4.1 Weighting of phase diagram data.	73
4.5 Conclusions	75
4.6 References	75
5 Modelling the CaO-SiO₂ system	77
5.1 Introduction	77
5.2 Literature review of the solid phases	79
5.3 Literature review of the liquid phase.	81
5.4 Methodology	82
5.5 Results and Discussion	82
5.5.1 Calorimetric measurements	82
5.5.2 DFT Calculations	84
5.5.3 Thermodynamic modelling	85
5.6 Conclusion	91
5.7 References	91
6 Modelling CaO-Al₂O₃-SiO₂ for Portland cement clinkers	99
6.1 3rd Generation Al ₂ O ₃	99
6.2 Al ₂ O ₃ -SiO ₂	101
6.2.1 Modelling mullite	101
6.2.2 Phase diagram	103
6.3 CaO-Al ₂ O ₃	104
6.3.1 Phase diagram	104
6.3.2 Literature review of the solid phases	104
6.3.3 Melt model	106
6.4 CaO-Al ₂ O ₃ -SiO ₂	107
6.4.1 Extrapolation of the binary systems	108
6.4.2 Modelling the ternary system	109
6.5 Conclusion	111
6.6 References	112
7 Modelling ferrite: CaO-Al₂O₃-Fe-O	117
7.1 Fe-O model	119
7.2 CaO-Fe ₂ O ₃	119

7.2.1	Literature review of the solid phases	119
7.2.2	Phase diagram	121
7.3	Fe ₂ O ₃ -SiO ₂	123
7.4	Modelling of the ferrite solid solution	126
7.5	Conclusion	128
7.6	References	129
8	Modelling minor elements: CaO-MgO-SiO₂	133
8.1	MgO-SiO ₂	133
8.1.1	Literature review of the solid phases	133
8.1.2	Phase diagram	135
8.2	CaO-MgO-SiO ₂	136
8.2.1	Phases within the ternary system	137
8.2.2	Phase diagram	137
8.3	Conclusion	142
8.4	References	143
9	Clinker analysis and calculations	149
9.1	Heat of Clinkerization	150
9.2	Equilibrium and Scheil cooling	151
9.3	Comparison against clinkers	154
9.3.1	Clinker prediction	155
9.3.2	Minor element substitution	159
9.4	Conclusions	165
9.5	References	166
10	Conclusion	169
10.1	Future work	170
10.2	Impact	170
10.3	References	171
A	Appendix: Supplementary material	173
A.1	References	181
B	Appendix: TDB file	185
C	Appendix: Clinker analysis	219
D	Appendix: Submitted journal articles	225

List of Figures

2.1	CaO-Al ₂ O ₃ -SiO ₂ phase diagram	30
2.2	Diagram of cement product process	30
3.1	The volumetric heat capacity at low temperatures (less than 298 K), the Dulong-Petit law is indicated using a horizontal dashed line and is approached in the limit of high temperature.	42
3.2	Diagram of a L^0 binary interaction	52
3.3	Diagram of a L^1 binary interaction	52
3.4	Diagram of a L^2 binary interaction	53
3.5	Diagram comparing the effects of AFM factors	56
4.1	Flow diagram of the automatic approach.	70
4.2	Sequential CaO-MgO phase diagrams, optimised using the developed automatic approach.	72
4.3	Optimised phase diagram of the CaO-MgO from the present work, compared against the phase diagram of Hillert and Wang.	73
4.4	Graph of the number of parameters added with changing the weight factor of the phase diagram data, also plotted is the resultant AiCc score.	74
5.1	Error plot for the heat capacity used to fit the C ₂ S solid	83
5.2	Heat content measurements for the rankinite compound.	84
5.3	γ - and α' -Ca ₂ SiO ₄ heat content measurements.	85
5.4	Graph of the enthalpy of formation at 298 K of the stable phases at room temperature in the CaO-SiO ₂ system	87
5.5	CaO-SiO ₂ phase diagram calculated in this assessment.	88
5.6	Activity of SiO ₂ calculated from the model compared with experimental data.	89
5.7	Activity of CaO calculated from the model compared with the experimental data.	89
5.8	Abundance of C ₂ S and CS species in the melt compared against the spectroscopic data.	90

LIST OF FIGURES

6.1	CaO-Al ₂ O ₃ -SiO ₂ phase diagram.	100
6.2	Optimised Al ₂ O ₃ -SiO ₂ phase diagram.	102
6.3	Assessed diagram of the CaO-Al ₂ O ₃ system from Hallstedl	105
6.4	Optimised CaO-Al ₂ O ₃ phase diagram.	107
6.5	Optimised CaO-Al ₂ O ₃ with C ₁₂ A ₇	108
6.6	Extrapolated CaO-SiO ₂ -Al ₂ O ₃ liquidus projection.	109
6.7	Optimised CaO-Al ₂ O ₃ -SiO ₂ ternary liquidus projection.	110
7.1	Ca-O phase diagram.	118
7.2	Fe-O phase diagram.	118
7.3	Phase diagram from the assessment from Hidayat et al., alongside the phase diagram of Selleby and Sundman.	122
7.4	Optimised phase diagram of the CaO-Fe ₂ O ₃ section.	122
7.5	Computed phase diagram of the Fe ₂ O ₃ -SiO ₂ pseudo section (in air) from Hidayat et al.	124
7.6	Optimised Fe ₂ O ₃ -SiO ₂ phase diagram.	124
7.7	Optimised phase diagram of the “true” Fe ₂ O ₃ -SiO ₂ pseudo section.	125
7.8	Phase diagram of the “true” pseudo section of the Fe ₂ O ₃ -SiO ₂ as calculated by Selleby.	125
7.9	Pseudo section of the ternary system CaO-Al ₂ O ₃ -Fe ₂ O ₃	127
7.10	Optimised C ₂ A-C ₂ F pseudo section carried out in the present work.	128
8.1	Ternary liquidus projection of the CaO-MgO-SiO ₂ system assessed by Huang et al.	134
8.2	Optimised MgO-SiO ₂ phase diagram.	134
8.3	Orthosilicate section computed by the previous assessments.	138
8.4	Optimised C ₂ S-M ₂ S orthosilicate section.	140
8.5	Diopside-enstatite subsection as calculated by the work of In Ho Jung et al.	141
8.6	Optimised metasilicate section.	141
8.7	Optimised liquidus projection of the CaO-MgO-SiO ₂ ternary carried out in the present work.	142
9.1	Graph of the scheil cooling computed for the composition: CaO 69 wt %, Fe ₂ O ₃ 3.6 wt %, Al ₂ O ₃ 5.4 wt %, SiO ₂ 22 wt %.	152
9.2	Violin plot of the distribution of the oxide composition between the clinkers in the current work and the clinkers in the work by Shim et al.	155
9.3	Violin plots of the error % between the experimental values and the calculated values using the Bogue equation(top) and the modified Bogue equation (bottom).	156
9.4	Violin plots of the error % between the experimental values and the calculated values using the approach of Hanein et al.	157

9.5	Violin plots of the error % between the experimental values and the calculated values using the currently developed thermodynamic database. . .	158
9.6	Weight % of the calculated clinker phases within selected clinkers compared against the XRD values.	159
9.7	Oxide composition of the belite phase present in the clinkers within the clinker data-set.	160
9.8	Co-substitutions of oxides within the belite phase.	160
9.9	Violin plots of the ratios MgO/CaO in the belite phase, calculated from the present work compared against the EDX values.	161
9.10	Cross-plot of MgO/CaO ratio in the belite phase in individual clinkers, with the calculated ratio compared against the EDX values.	162
9.11	Ratios of Al ₂ O ₃ /Fe ₂ O ₃ and Al ₂ O ₃ /CaO within the ferrite phase.	163
9.12	Ratio of the Al ₂ O ₃ /CaO in the ferrite phase.	164
9.13	Ratio of the Al ₂ O ₃ /CaO in the ferrite phase, for individual clinkers.	164
C.1	Composition of the alite phase within the clinkers inside the clinker data-set determined by EDX.	222
C.2	Composition of the belite phase within the clinkers inside the clinker data-set determined by EDX.	222
C.3	Composition of the aluminate phase within the clinkers inside the clinker data-set determined by EDX.	223
C.4	Composition of the ferrite phase within the clinkers inside the clinker data-set determined by EDX.	223

List of Tables

1.1	Cement oxide notation.	23
2.1	Table of typical Portland cement clinker composition, weight %.	31
2.2	Table showing the composition of the four main phases found within the Portland cement clinkers in weight %.	32
4.1	Parameters for the solid MgO and CaO Gibbs energy expressions.	71
4.2	Parameters for the liquid MgO and CaO Gibbs energy expressions.	71
4.3	Resultant model for the CaO-MgO system.	73
5.1	Table showing the structures of the compounds and their respective polymorphs within the CaO-SiO ₂ system.	80
5.2	Table showing the transition temperatures and enthalpies of the polymorphs the CaO-SiO ₂ system.	81
5.3	Heat content measurements for rankinite (C ₃ S ₂) compound.	83
5.4	Ca ₂ SiO ₄ heat contents measurements in the temperature range 972.86–1471.05 K.	84
5.5	Calculated ground state energies at 0 K in eV per formula unit.	85
5.6	Calculated heat of formation at 0 K in kJ/mol relative to the oxides CaO and α -SiO ₂ (low quartz) and calculated heat of transitions for the different Ca ₂ SiO ₄ and CaSiO ₃ modifications.	86
5.7	H ₂₉₈ and S ₂₉₈ of the compounds in the CaO-SiO ₂ system as calculated by the present work compared to values from Haas et al.	86
5.8	Table showing the functions for the melt phase for the CaO-SiO ₂ system, optimised in the present work.	87
5.9	Summary of transitions and invariant reactions in the C-S system from the calculated phase diagram compared to experimental data.	88
6.1	Parameters for the solid Al ₂ O ₃ functions, found in the present work. . . .	101
6.2	Table showing the functions and parameters optimised in the work for the melt phase in the Al ₂ O ₃ -SiO ₂ system.	103
6.3	Summary of invariant points in the Al ₂ O ₃ -SiO ₂ phase diagram.	103

LIST OF TABLES

6.4	Table showing the functions optimised in the present work for the melt phase in the CaO-Al ₂ O ₃ system.	106
6.5	Summary of the invariant points in the CaO-Al ₂ O ₃ phase diagram.	107
6.6	Table of the invariant points within the CaO-Al ₂ O ₃ -SiO ₂ system.	111
6.7	Table comparing the values of the weight % of the phases present in the equilibrium at a typical “white” OPC composition.	111
6.8	Table comparing the values of the wt % of the components within the liquid phase present in the equilibrium with C ₂ S and C ₃ S.	112
7.1	Table of the parameters and thermodynamic functions for the liquid and pure iron phases in the Fe-O system.	120
7.2	Table showing the functions optimised in the present work for the melt phase in the CaO-Fe ₂ O ₃ section.	123
7.3	Table of the parameters for the ferrite solid solution calculated in the present work.	127
7.4	Enthalpy of formation (from oxides) calculated in the present work and compared against the experimental measurements for ferrite solid solution compounds.	127
8.1	Table showing the functions optimised in the present work for the melt phase in the MgO-SiO ₂	136
8.2	The ternary solid solutions and compounds found within CaO-MgO-SiO ₂ . .	137
8.3	Parameters for the olivine solid solution in the CaO-MgO-SiO ₂	139
8.4	Description of the alpha and alpha prime solid solutions in the CaO-MgO-SiO ₂ system.	139
8.5	Invariant points in the CaO rich corner of the CaO-MgO-SiO ₂ ternary. .	142
9.1	Enthalpy of formation of 1 kg of Portland cement clinker, as presented by Taylor. The products are assumed to be: C ₃ S, 0.673 kg; C ₂ S, 0.133 kg; C ₃ A, 0.118 kg; C ₆ A ₂ F, 0.064 kg; CaO (free), 0.010 kg.	150
9.2	Heat of formation for selected clinker phases contributing to the formation of 1 kg of Portland cement.	150
9.3	Table of the fractional amounts of phases calculated for the composition: CaO 69 wt %, Fe ₂ O ₃ 3.6 wt %, Al ₂ O ₃ 5.4 wt %, SiO ₂ 22 wt %.	152
9.4	Table of the mass fractions of the components of the ferrite phase calculated for the composition: CaO 69 wt %, Fe ₂ O ₃ 3.6 wt %, Al ₂ O ₃ 5.4 wt %, SiO ₂ 22 wt % at 1327°C.	153
9.5	Comparison of the weight % of the phases found in the clinker for the raw input: CaO 66.7, Al ₂ O ₃ 5.68, SiO ₂ 21.84, Fe ₂ O ₃ 4.65 and MgO 1.06. . .	154
9.6	Comparison of the average clinker oxide compositions measured in the present work and the work of Shim et al.	154

9.7	Comparison of the average clinker phase composition measured from XRD, values are in wt %.	155
9.8	Summary of the average error in wt % (alongside the standard deviation) for the calculations conducted on the present clinker data set, and the data set of Shim et al.	158
A.1	Coefficients for the 3rd generation model for the stoichiometric solids in the binary systems according to Equation A.0.1.	174
A.2	Coefficients for the 3rd generation model for the stoichiometric solids in the ternary systems according to Equation A.0.1.	175
A.3	Experimental data used to fit the sillimanite (Al_2SiO_5) phase.	176
A.4	Experimental data used to fit the solid compounds within the $\text{CaO}-\text{Al}_2\text{O}_3$ system.	177
A.5	Experimental data used to fit the solid compounds in the $\text{MgO}-\text{SiO}_2$ system.	179
A.6	Experimental data that was used to fit the compounds in the $\text{CaO}-\text{Fe}_2\text{O}_3$ system.	180
C.1	Table of oxide compositions of the clinkers measured via XRF. All masses are in weight %.	220
C.2	Table of the clinker phase composition, measured via XRD. All values are in weight %.	221

ACKNOWLEDGEMENTS

I would like to express my sincere gratitude to my supervisor Marcus Bannerman, who has constantly supported me throughout this project and taught me how to become the best programmer I can be, a skill set that I will use for life. I would also like to thank my secondary supervisor Alexander Pisch from whom I have learned so much and without whom this work could not have been completed. Together, they guided me thoroughly through the field of cement and thermodynamics. I would like to thank Nanocem for funding Core Project 17 of which this PhD thesis was a part. I am also grateful to Christiane Rößler, Theodore Hanein, and Chancel Mawalala for their experiments and results, which were vital for the modelling work. Furthermore, I would also like to express my appreciation for my research group colleagues Ryan and Craig, who alongside Marcus provided interesting python and research discussions. Finally, I would like to thank and acknowledge my parents (Qadus and Surayya).

To my wife Rabia, you never understood my research, but you provided me with unlimited motivational support and for that I am grateful.

CHAPTER
ONE

INTRODUCTION

Cement is one of the most produced materials in the world and is second only to drinking water [1] with an estimated 4.1 billion metric tons of cement being produced in 2018 and 2.3 billion metric tons being produced by China alone. This massive scale of production makes the process a large contributor to CO₂ emissions, being a source of an estimated 8% of humanity’s CO₂ emissions [2]. There is therefore an important need to optimise the cement industry to become more “environmentally friendly” to produce less CO₂ whilst also remaining economically feasible: i.e., not requiring expensive process modifications or drastically affecting the economics of cement production. The economics is key, as arguably cement is the hallmark of civilisation and is needed for everything from housing and transport infrastructure, to coastal defence.

Currently, a lot of “green” research is focused on the use of supplementary cementitious “waste” material from another process (e.g., fly ash from coal power plants) which can partially replace the cement itself, to make an environmentally friendly concrete [3]. There has also been a great deal of research into the hydration and setting of cement formulation [4, 5]. This research focuses on the hydration products of the cement clinker and looks to improve the properties of the final cement product for specific applications [6–8]; However, thanks to these research developments much of the supplementary material has now been made rare/valuable [9] by the enormous over-demand of cement producers looking to reduce their environmental burden (as well as the phasing out of coal power plants globally). There is still a research gap to optimise clinker formulations (with clinker production being the first stage of cement production) by altering the cement chemistry to form a final cement product that releases less CO₂ during production without affecting its performance. A detailed review by Ludwig and Zhang [10] on the research into clinker chemistry demonstrated the potential of alternative clinker chemistries to produce “green” cement. This includes the stabilisation of high-temperature highly-active polymorphs of alite [11] and belite [12] and the development of a more reactive belite [13]; However, the main issue impeding the research in clinker chemistry and production is the lack of a thermodynamic workflow that allows for the rapid design of alternative chemistries. This makes predictive modelling of the production of clinker phases and its optimisation a la-

brious and manual process and results in a “trial and error” process for clinker research. This is unlike the methods of the metallurgy industry for example, which have used a largely thermodynamic approach known as CALPHAD [14], to optimise and design new materials for a variety of applications [15–17] and with great success.

This is not to say that there is no thermodynamic research in the literature on cementitious phases and materials. Haas et al. [18] gathered, reviewed and evaluated a large amount of the data surrounding the alite and belite phases in a similar approach to the CALPHAD method. Additionally, this work was extended to a stoichiometric thermodynamic assessment developed for calcium sulfoaluminate cement production by Hanein et al. [19] by simply gathering the thermodynamic information in the literature and has allowed for the development of a new sulphur-based cement process; however, it is known that the compilation of Haas et al. contains typographical errors [19] and the experimental data is largely out of date [20], with new data for belite [21], CaO [22] and SiO₂ [23] existing in the literature. Furthermore, minor elements and their corresponding solid solutions, which play a major role in OPC cement, are generally not included in these thermodynamic models, except where the species have metallurgical applications, and this is the issue with the existing commercial databases. For example, the polymorphs of alite [24, 25] which are important in the clinker production process [26], are largely ignored in existing thermodynamic models containing alite [27–29].

The effectiveness of the CALPHAD approach was demonstrated by De Noirlfontaine et al. [30] who carried out a thorough review of the existing thermodynamic assessments for the CaO-Al₂O₃-SiO₂ system, which was developed for non-cement applications [31–33], but they saw success for Portland cement research in their preliminary calculations. In addition, the application of a thermodynamic database was studied by Barry and Glasser [34] who were able to perform calculations of a virtual clinkering process using the oxide database by MTDATA [35]. Additionally, Tazuddin et al. [36, 37] used the Thermo-calc [38] and Factsage [39] databases to also predict clinker compositions with an additional focus on the role of minor elements within the cement clinker. They, too, used synthetic clinkers and the results of their work were compared. These are just a few examples in the literature of how the availability of an extensive thermodynamic database could be a powerful tool in green clinker research. The development of a thermodynamic database, with a focus on Portland cement clinkers, will also allow for improvements in the production process by allowing for a carbon-accounting clinker production process [40] and the design of advanced thermal models for kiln pyro processing [41].

Overall, this shows that existing thermodynamic work and oxide databases have proven successful in cement applications; however, there are still crucial gaps to be completed and updates are required. Further research in this field demands the development of a thermodynamic database designed for Portland cement that contains:

- New experimental data that addresses gaps in the literature.
- A model for the solid, liquid, solid solutions and melt phases.

- The inclusion of minor elements substitutions within the clinker phases.

It is therefore proposed in this work, that a CaO-Al₂O₃-SiO₂-MgO-Fe-O thermodynamic database, will be developed using the CALPHAD approach. In this database, the clinker and other relevant phases will be re-fit using new and existing experimental data. The CALPHAD approach and its models will be used to review the thermodynamic data and produce phase diagrams of the relevant systems, thus including the melt phase. Finally, a new clinker data set that includes 27 industrial clinkers will be presented. This will look to add to the existing clinker literature [42–44] by giving details of the analysis of the clinker compositions and minor element substitution. The data-set will also provide a set of experimental values that will be compared against the results of the calculations of the developed thermodynamic work.

It is important to note that within the field of cement chemistry there is a notation followed by cement researchers which assumes all species are oxidised. This cement notation will be used throughout the work and so it is outlined in Table 1.1.

Table 1.1: Table showing cement oxide notation used by cement chemists.

Formula	CaO	SiO ₂	Al ₂ O ₃	Fe ₂ O ₃	MgO	SO ₃
Notation	C	S	A	F	M	S

This notation is used to describe compounds e.g., alite which has the formula Ca₃SiO₅ is written as C₃S in cement chemistry notation. Cement chemistry notation is a useful shorthand and it is important to remember that many clinker phases have significant substitution of minor elements into their structure, thus any chemical formula is to some degree incorrect (hence the prevalent use of mineralogical names). In this thesis, full chemical formulas will often be used to describe phases other than the main clinker phases but cement notation and chemical formulas are both used interchangably and with the understanding that there are typically other impurities present. Full chemical formula must be used when dealing with iron as it appears in several oxidation states here, i.e. FeO and Fe₂O₃.

1.1 Structure, aims and objectives

This PhD project is funded by Nanocem, which has now become Innovandi, and is a consortium of Europe's largest cement manufacturers and academic institutions, as part of Nanocem Core Project 17. This is a collaborative project between the University of Aberdeen, Grenoble INP, Bauhaus-Universität Weimar and the University of Sheffield. This thesis will focus on the modelling work conducted by the University of Aberdeen but contains experimental results from collaborators and where this is the case this will be explicitly stated.

The thesis is outlined as follows:

- Chapter 2: Brief introduction to cement thermodynamics
- Chapter 3: Introduction and overview of the models used in the present work.
- Chapter 4: Introduction to the fitting approach including a review of optimisation under uncertainty methodologies and the development of an accurate and robust fitting methodology.
- Chapters 5-8: Thermodynamic modelling of binary and ternary systems crucial for Portland cement.
- Chapter 9: Presentation and analysis of the new clinker data set and applications of the thermodynamic database, with calculations that are useful for Portland cement clinkers.
- Chapter 10: Concluding remarks, including the impact of the work and the future work.

1.2 References

- [1] J. Watts. ‘Concrete: the most destructive material on Earth’. In: *The Guardian* (25th Feb. 2019). URL: <https://www.theguardian.com/cities/2019/feb/25/concrete-the-most-destructive-material-on-earth>.
- [2] Johanna Lehne and Felix Preston. *Chatham House Report Making Concrete Change Innovation in Low-carbon Cement and Concrete*. The Royal Institute of International Affairs, 2018, pp. 1–122. ISBN: 9781784132729.
- [3] Bambang Suhendro. ‘Toward Green Concrete for Better Sustainable Environment’. In: *Procedia Engineering* 95 (2014), pp. 305–320. DOI: [10.1016/j.proeng.2014.12.190](https://doi.org/10.1016/j.proeng.2014.12.190).
- [4] Joseph Mwiti Marangu, Joseph Karanja Thiong’o and Jackson Muthengia Wachira. ‘Review of Carbonation Resistance in Hydrated Cement Based Materials’. In: *Journal of Chemistry* 8489671 (2019). DOI: [10.1155/2019/8489671](https://doi.org/10.1155/2019/8489671).
- [5] Luca Lavagna and Roberto Nisticò. ‘An Insight into the Chemistry of Cement: A Review’. In: *Applied Sciences* 13.203 (2023). DOI: [10.3390/app13010203](https://doi.org/10.3390/app13010203).
- [6] Hao Wang, Liang Wang, Xin Qian, Ke Cao, Ying Xu, Yi Fang and Liyun Cui. ‘Hydration, Compressive Strength and Durability of Eco-friendly Cement Mortars Containing Recycled Brick Powder and Metakaolin’. In: *Journal of Civil Engineering* 26.9 (2022), pp. 4023–4037. DOI: [10.1007/s12205-022-0035-3](https://doi.org/10.1007/s12205-022-0035-3).

- [7] K Baltakys, T Dambrauskas, D Rubinaite, R Siauciunas and A Grineviciene. ‘Formation and hydration of eco-friendly cement using industrial wastes as raw materials’. In: *Scientific Reports* 11.14742 (2021). DOI: 10.1038/s41598-021-94148-x.
- [8] Abathar Al-Hamrani, Murat Kucukvar, Wael Alnahhal, Elsadig Mahdi and Nuri C. Onat. ‘Green Concrete for a Circular Economy: A Review on Sustainability, Durability, and Structural Properties’. In: *Materials* 14.2 (2021). DOI: 10.3390/ma14020351.
- [9] Chandana Kulasuriya, Vanissorn Vimonsatit and W.P.S. Dias. ‘Performance based energy, ecological and financial costs of a sustainable alternative cement’. In: *Journal of Cleaner Production* 287.125035 (2021). DOI: 10.1016/j.jclepro.2020.125035.
- [10] Ludwig Horst-Michael and Zhang Wensheng. ‘Research review of cement clinker chemistry’. In: *Cement and Concrete Research* 78 (2015), pp. 24–37. DOI: 10.1016/j.cemconres.2015.05.018.
- [11] Wensheng Zhang, Xuehong Ren and Shixi Ouyang. ‘Development on ion substitution effect on the crystal structure and properties of tricalcium silicate’. In: *Journal of The Chinese Ceramic Society* 39.10 (2011), pp. 1666–1672.
- [12] T. Link, F. Bellmann, H.M. Ludwig and M. Ben Haha. ‘Reactivity and phase composition of Ca_2SiO_4 binders made by annealing of α -dicalcium silicate hydrate’. In: *Cement and Concrete Research* 67 (2015), pp. 131–137. DOI: 10.1016/j.cemconres.2014.08.009.
- [13] Hideki Ishida, Satoru Yamazaki, Kaori Sasaki, Yoshihiko Okada and Takeshi Mitsuda. ‘ α -Dicalcium Silicate Hydrate: Preparation, Decomposed Phase, and Its Hydration’. In: *Journal of the American Ceramic Society* 76.7 (1993), pp. 1707–1712. DOI: 10.1111/j.1151-2916.1993.tb06638.x.
- [14] Larry Kaufman and John Ågren. ‘CALPHAD, first and second generation - Birth of the materials genome’. In: *Scripta Materialia* 70.1 (2014), pp. 3–6. DOI: 10.1016/j.scriptamat.2012.12.003.
- [15] ‘Applications of CALPHAD modelling and databases in advanced lightweight metallic materials’. In: *Calphad* 62 (2018), pp. 1–17. DOI: 10.1016/j.calphad.2018.04.009.
- [16] ‘Efficient exploration of the High Entropy Alloy composition-phase space’. In: *Acta Materialia* 152 (2018), pp. 41–57. DOI: 10.1016/j.actamat.2018.04.012.
- [17] R Ursula. ‘The Calphad method and its role in material and process development’. In: *Tecnologia em Metalurgia, Materiais e Mineracao* 13.1 (2016), pp. 3–15.

- [18] John L. Haas Jr., Glipin R. Robinson Jr. and Bruce S. Hemingway. ‘Thermodynamic tabulations for selected phases in the system CaO-Al₂O₃-SiO₂-H₂ at 1 atm between 273.15 and 1800 K’. In: *Journal of Physical and Chemical Reference Data* 10.3 (1981), pp. 575–670. DOI: 10.1063/1.555645.
- [19] Theodore Hanein, Fredrik P. Glasser and Marcus N. Bannerman. ‘Thermodynamic data for cement clinkering’. In: *Cement and Concrete Research* 132.106043 (2020). DOI: 10.1016/j.cemconres.2020.106043.
- [20] Mats Hillert, Bo Sundman, Xizhen Wang and Tom Barry. ‘A re-evaluation of the rankinite phase in the CaO-SiO₂ system’. In: *Calphad* 15.1 (1991), pp. 53–58. DOI: 10.1016/0364-5916(91)90025-f.
- [21] K. D. Grevel, F. Bellmann, J. Majzlan, E. Dachs, A. Benisek and H. M. Ludwig. ‘Thermodynamic data of belite polymorphs’. In: *Cement and Concrete Research* 152.106621 (2022). DOI: 10.1016/j.cemconres.2021.106621.
- [22] Guillaume Deffrennes, Noël Jakse, Cecilia M.S. Alvares, Ioana Nuta, Alain Pasturel, Alexandra Khvan and Alexander Pisch. ‘Thermodynamic modelling of the Ca-O system including 3rd generation description of CaO and CaO₂’. In: *Calphad* 69 (2020), p. 101764. DOI: 10.1016/j.calphad.2020.101764.
- [23] I. Bajenova, A. Khvan, A. Dinsdale and A. Kondratiev. ‘Implementation of the extended Einstein and two-state liquid models for thermodynamic description of pure SiO₂ at 1 atm’. In: *Calphad* 68.101716 (2020). DOI: 10.1016/j.calphad.2019.101716.
- [24] Andre Guinier and Micheline Regourd. ‘Structure of Portland Cement Minerals’. In: *5th International Congress on the Chemistry of Cement. Part 1*. 1968.
- [25] M Bigaré, A Guinier, C Mazières, M Regourd, N Yannaquis, W Eysbl, T.H Hahn and E Woermann. ‘Polymorphism of tricalcium silicate and its solid solutions’. In: *Journal of the American Ceramic Society* 50.11 (1967), pp. 609–619. DOI: 10.1111/j.1151-2916.1967.tb15009.x.
- [26] T Staňek and P Sulovský. ‘The influence of the alite polymorphism on the strength of the Portland cement’. In: *Cement and Concrete Research* 32.7 (2002), pp. 1169–1175. DOI: 10.1016/S0008-8846(02)00756-1.
- [27] Gunnar Eriksson, Ping Wu, Milton Blandert and Arthur D. Pelton. ‘Critical evaluation and optimization of the thermodynamic properties and phase diagrams of the MnO-SiO₂ and CaO-SiO₂ systems’. In: *Canadian Metallurgical Quarterly* 33.1 (1994), pp. 13–21. DOI: 10.1179/cmq.1994.33.1.13.
- [28] J. R. Taylor and A. T. Dinsdale. ‘Thermodynamic and phase diagram data for the CaO-SiO₂ system’. In: *Calphad* 14.1 (1990), pp. 71–88. DOI: 10.1016/0364-5916(90)90041-w.

- [29] Mats Hillert, Bo Sundman and Xizhen Wang. ‘An assessment of the CaO-SiO₂ system’. In: *Metallurgical Transactions B* 21.2 (1990), pp. 303–312. DOI: 10.1007/bf02664198.
- [30] M. N. De Noirlfontaine, S. Tusseau-Nenez, C. Girod-Labianca and V. Pontikis. ‘CALPHAD formalism for Portland clinker: Thermodynamic models and databases’. In: *Journal of Materials Science* 47.3 (2012), pp. 1471–1479. DOI: 10.1007/s10853-011-5932-7.
- [31] Huahai Mao, Mats Hillert, Malin Selleby and Bo Sundman. ‘Thermodynamic assessment of the CaO-Al₂O₃-SiO₂ system’. In: *Journal of the American Ceramic Society* 89.1 (2006), pp. 298–308.
- [32] Gunnar Eriksson and Arthur D Pelton. ‘Critical evaluation and optimization of the thermodynamic properties and phase diagrams of the CaO-Al₂O₃, Al₂O₃-SiO₂, and CaO-Al₂O₃-SiO₂ systems’. In: *Metallurgical Transactions B* 24.5 (1993), pp. 807–816. DOI: 10.1007/BF02663141.
- [33] Elena Yazhenskikh, Klaus Hack and Michael Müller. ‘Critical thermodynamic evaluation of oxide systems relevant to fuel ashes and slags. Part 3: Silica-alumina system’. In: *Calphad* 32.1 (2008), pp. 195–205. DOI: 10.1016/j.calphad.2007.05.004.
- [34] T I Barry and Fredrik Glasser. ‘Calculation of Portland cement clinkering reactions’. In: *Advances in Cement Research* 12 (2000), pp. 19–28. DOI: 10.1680/adcr.2000.12.1.19.
- [35] John Gisby, Pekka Taskinen, Jouni Pihlasalo, Zushu Li, Mark Tyrer, Jonathan Pearce, Katri Avarmaa, Peter Björklund, Hugh Davies, Mikko Korpi, Susan Martin, Lauri Pesonen and Jim Robinson. ‘MTDATA and the Prediction of Phase Equilibria in Oxide Systems: 30 Years of Industrial Collaboration’. In: *Metallurgical and Materials Transactions B* 48.1 (2017), pp. 91–98. DOI: 10.1007/s11663-016-0811-x.
- [36] Tazuddin, Hemantkumar N. Aiyer and Amit Chatterjee. ‘Phase equilibria studies of CaO-SiO₂-Al₂O₃-Fe₂O₃-MgO system using CALPHAD’. In: *Calphad* 60 (2018), pp. 116–125. DOI: 10.1016/j.calphad.2017.12.003.
- [37] A Tazuddin, Hemantkumar Aiyer and Amit Chatterjee. ‘Thermodynamic simulation in evaluating the role of minor oxides and mineralizers in Portland cement clinker phase formation’. In: *SN Applied Sciences* 2.10 (2020), pp. 17–37. DOI: 10.1007/s42452-020-03548-7.
- [38] J-O Andersson, Thomas Helander, Lars Höglund, Pingfang Shi and Bo Sundman. ‘Thermo-Calc and DICTRA, computational tools for materials science’. In: *Calphad* 26.2 (2002), pp. 273–312. DOI: 10.1016/S0364-5916(02)00037-8.

- [39] C. W. Bale, E. Bélisle, P. Chartrand, S. A. Dechterov, G. Eriksson, A. E. Gheribi, K. Hack, I. H. Jung, Y. B. Kang, J. Melançon, A. D. Pelton, S. Petersen, C. Robelin, J. Sangster, P. Spencer and M. A. Van Ende. ‘FactSage thermochemical software and databases, 2010-2016’. In: *Calphad* 54 (2016), pp. 35–53. DOI: 10.1016/j.calphad.2016.05.002.
- [40] Jun Xia Peng, Liang Huang, Yu Bo Zhao, Pan Chen, Lu Zeng and Weimin zheng. ‘Modeling of Carbon Dioxide Measurement on Cement Plants’. In: *Progress in Environmental Science and Engineering*. Vol. 610. Advanced Materials Research. Feb. 2013, pp. 2120–2128. DOI: 10.4028/AMR.610-613.2120.
- [41] H.A. Spang. ‘A dynamic model of a cement kiln’. In: *Automatica* 8.3 (1972), pp. 309–323. DOI: 10.1016/0005-1098(72)90050-7.
- [42] Sang-Hyo Shim, Tae-Hee Lee, Seong-Joon Yang, Norhazilan Bin Md. Noor and Jang-Ho-Jay Kim. ‘Calculation of Cement Composition Using a New Model Compared to the Bogue Model’. In: *Materials* 14.16 (2021). DOI: 10.3390/ma14164663.
- [43] M. Kristmann. ‘Portland cement clinker mineralogical and chemical investigations: Part II electron microprobe analysis’. In: *Cement and Concrete Research* 8.1 (1978), pp. 93–102. DOI: 10.1016/0008-8846(78)90062-5.
- [44] Paul Stutzman, Pan Feng and Jeffrey W. Bullard. ‘Phase Analysis of Portland Cement by Combined Quantitative X-Ray Powder Diffraction and Scanning Electron Microscopy’. In: *Journal of research of the National Institute of Standards and Technology* 121 (2016), pp. 47–107.

CHAPTER
TWO

THE IMPORTANCE OF THERMODYNAMICS IN CEMENT PRODUCTION

This chapter introduces the process of cement production and the major phases present within the clinker that is ground and blended to form the cement. There are many formulations of cement with wide ranges of material properties and thus wide ranges of application. The most common formulation is Ordinary Portland Cement (OPC). Figure 2.1 presents a $\text{CaO}-\text{Al}_2\text{O}_3-\text{SiO}_2$ phase diagram that shows the rough compositional regions of different ceramic materials and highlights the compositional region corresponding to Portland cements. It is clear that cements can differ significantly in composition, for example alumina cements are close to the $\text{CaO}-\text{Al}_2\text{O}_3$ binary system whereas OPC lies nearer the $\text{CaO}-\text{SiO}_2$ system. The thermodynamic models developed in this thesis cover the entire $\text{CaO}-\text{Al}_2\text{O}_3-\text{SiO}_2$ system and beyond; however, the focus of this thesis is the OPC system due to its importance. Thus, it is important to discuss OPC cement production to understand where thermodynamics may play a key role. This understanding will be used later when establishing the scheil cooling approach used in the final clinker simulations in Chapter 9.

2.1 Overview of cement production

An overview of the cement production process is given in Fig. 2.2. The main raw materials of OPC are limestone (calcium carbonate) and clay which are mined from the ground. There are other materials present such as chalk, shale, and iron ore. Sometimes these are deliberately added as part of the formulation, and sometimes they are an unintended result of the mining process cutting through many layers of a rock formation. After mining, the rocks are crushed and ground, and at this stage, supplementary material such as fly ash is also added and mixed in well. The ground-up raw material is typically fed into a large cylindrical rotary kiln that is inclined at a slight angle to cause motion through the kiln with the rotation. The horizontal rotary kiln is the most common kiln type used today. The material is fed in from one side whilst a flame from a burner is inserted in the other, with the solids and gases flowing counter-current to one another to

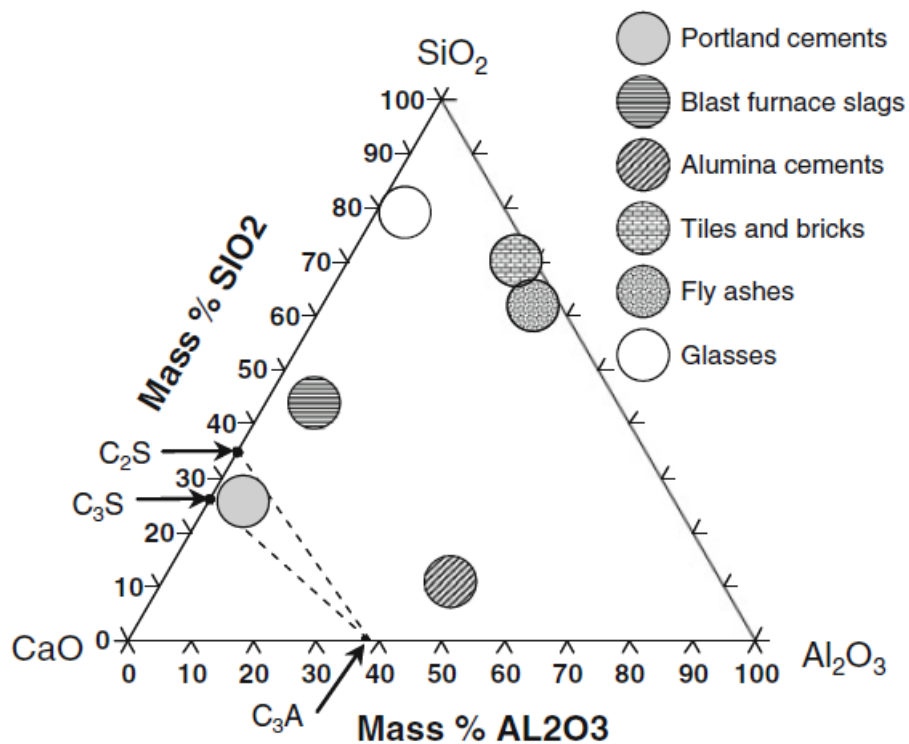


Figure 2.1: CaO-Al₂O₃-SiO₂ phase diagram showing the range of compositions region at which the different materials are made. This figure is adapted from Ref [1].

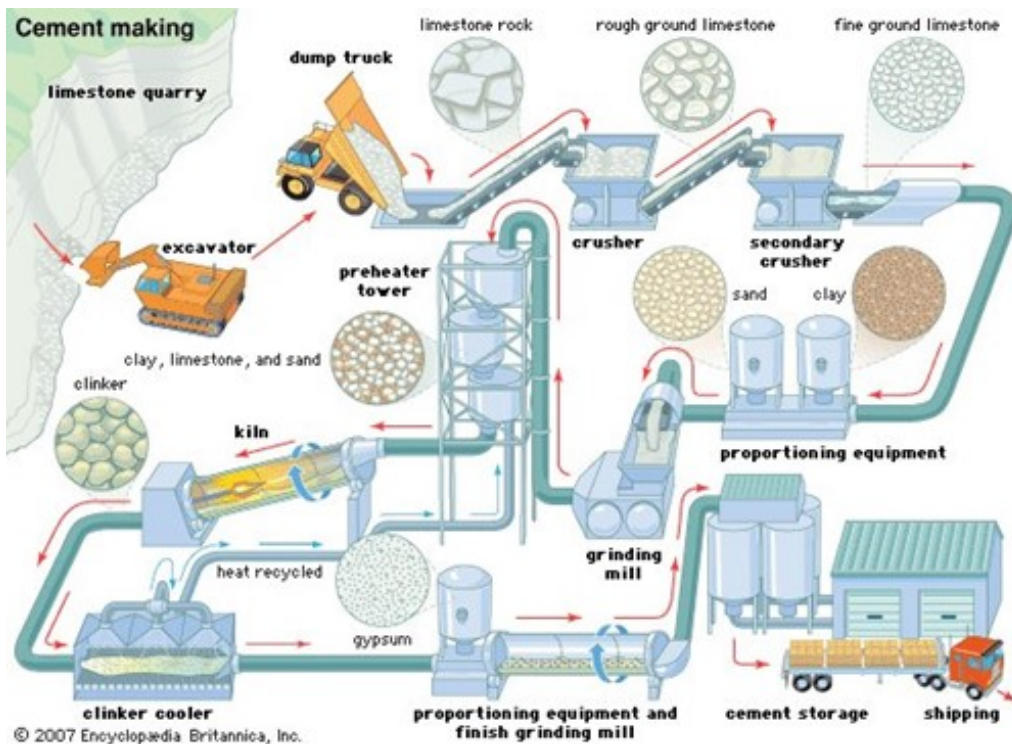


Figure 2.2: Diagram outlining the cement clinker production process from mining to clinker production and finally transportation. The figure is adapted from Ref. [2].

Table 2.1: Table of typical Portland cement clinker composition, weight %.

Phase	C ₂ S	C ₃ S	C ₃ A	C ₄ AF
Composition range, mass %	20–45	25–50	5–12	6–12

facilitate heat exchange. The kiln heats the cement material to roughly 1400–1500 °C, and during heating to this temperature many elements are vaporised off in the form of gases. In particular CO₂ originates from the decomposition of calcium carbonate (CaCO₃) may be released, although this commonly happens in modern processes at the bottom of the pre-heater tower in a fluidised bed reactor called the calciner. The liberation of CO₂ from calcium carbonate produces lime (CaO) which, at high temperatures, fuses with the other oxides aided by a partial melting of the raw material. As the material moves through the kiln it wets with the melt, rolls, and combines to form small grey balls which are known as the clinker nodules. These are then discharged from the bottom of the kiln and cooled in a clinker cooler to recover heat and to “freeze” the high temperature phases. The clinker nodules are then crushed, ground, and mixed with small amounts of gypsum as a setting time control agent to form OPC.

Ultimately, it is the high-temperature equilibrium present at the hot-end of the kiln which defines the final morphology and phase composition of OPC. This morphology is sealed into the clinker through cooling thus the melting and subsequent precipitation during cooling are critical thermodynamic processes to capture. The later chapters on thermodynamic modelling (i.e., Chapters 5, 6, 7, and 8) spend considerable time modelling the melt phase due to its importance even though it is the solid phases which are the final product.

2.2 Major clinker phases

As may be inferred from the general location of Portland cement in the C-A-S diagram of Fig. 2.1, it is primarily composed of calcium silicate phases C₂S and C₃S, also known as belite and alite respectively. These phases form up to 75% of the weight of the clinker and are important for the cement’s development of binding and strength properties. Within the clinker, C₃A (aluminate) and C₄AF (ferrite) are also present, with their amounts varying based on the process but forming roughly 10% of the clinker weight each, the remainder of the clinker consists of gypsum and other minor compounds (see Table 2.1).

The four main clinker phases, C₃S, C₂S, C₃A, and C₄AF, are critical in giving the clinker the desired strength and workability properties. Although they are typically given by their stoichiometric formulas, they are in-fact solid solutions with many substitutions and dissolved species. An average composition of these clinker phases is given in Table 2.2 to highlight how varied these substitutions can be. In addition to being made up of several components, the clinker phases may also have several polymorphs, which is the same chemical compound existing with a different structural unit. In this section, the

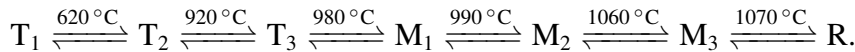
structures and polymorphs of the main phases will be discussed here to provide essential background for the later discussion.

Table 2.2: Table showing the composition of the four main phases found within the Portland cement clinkers in weight %. Values from the table are taken from Ref [3]; however, updated values from this project are presented and compared in Chapter 9.

	CaO	SiO ₂	Al ₂ O ₃	Fe ₂ O ₃	MgO	SO ₃	Na ₂ O	K ₂ O	TiO ₂	MnO	P ₂ O ₅
elite	71.6	25.2	1.0	0.7	1.1	0	0.1	0.1	0	0	0.2
belite	63.5	31.5	2.1	0.9	0.5	0.1	0.1	0.9	0.2	0	0.2
ferrite	47.5	3.6	21.9	21.4	3.0	0	0.1	0.2	1.6	0.2	0
C ₃ A	56.6	3.7	31.3	5.1	1.4	0	1	0.7	0.2	0	0

2.2.1 Alite

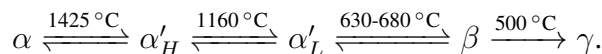
Alite is known as C₃S in cement chemistry notation and is responsible during the early strength development (i.e., first few days) due to its high reactivity with water [3]. It is given the stoichiometric formula Ca₃SiO₅, although it typically contains 3-4% of minor oxides, which substitute for the major oxides CaO and SiO₂. Alite is known to exist as seven different polymorphs split into three distinct structures [4]: triclinic (1, 2, 3), monoclinic (1, 2) and rhombohedral. The stability of the transition temperatures between the different structures are as follows,



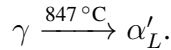
In alite, the room temperature polymorph is T₁, but the final clinker product mostly contains the monoclinic polymorph which is produced from the cooling of the rhombohedral phase formed at high temperatures and stabilised with the insertion of Mg²⁺ [5]. The polymorph affects the sites of the calcium, silica and oxygen ions, which in turn affects the substitution of these coordination sites.

2.2.2 Belite

Belite is known as C₂S and reacts much slower with water than the alite phase. This means that is mostly responsible for long-term strength development with little to no effect of upon strength during initial setting. It is given the stoichiometric formula Ca₂SiO₄; however, it has been known to typically contain 4-6% of other oxides, with similar substituents as the alite phase. Belite exists in 5 possible polymorphs [4]: α , α'_H , α'_L (where H=high and L=low), β and γ . The α , α'_H , α'_L and β polymorphs are structurally very similar and can reversible transition from one form to another,



Furthermore, whilst γ polymorph is structurally different, having the olivine structure, it is known to directly transform into the α'_L , without transforming into β first,



γ -C₂S is the polymorph that is stable at room temperature, whilst the β polymorph is meta-stable. The α and α' polymorphs cannot be stabilised at room temperature without the addition of minor elements that substitute for CaO or SiO₂. Similarly, whilst the β polymorph is typically meta-stable and not found at room temperatures, it is the most found to form within the clinker with some existence of the α and α' polymorphs. Suggesting high levels of substitutions that help stabilise, these unstable and reactive polymorphs.

2.2.3 C₃A or “aluminate”

C₃A is a major clinker phase, that is sometimes known as “aluminate” by cement chemists. This name is not used in the present work, as it is deemed confusing because “aluminate” also refers to any compound containing Al_xO_y ions. It is therefore, instead referred to by its cement chemistry notation name: C₃A, which has the stoichiometric formula Ca₃Al₂O₆. While pure C₃A has not been found to exhibit polymorphism and exists only as a cubic structure, substitution of the calcium ions can lead to the formation of orthorhombic and monoclinic structures of C₃A. It is, for this reason, the final clinker tends to have either cubic C₃A or orthorhombic C₃A or both in combination [3].

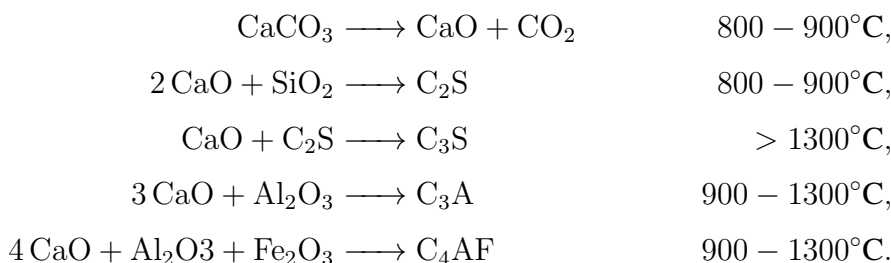
2.2.4 Ferrite

Typically, ferrite is given the cement chemistry notation C₄AF; however, this is misleading as it suggests that ferrite exists as a stoichiometric compound. It is to be noted that even though all the other clinker phases are not truly stoichiometric, as indicated by Table 2.2, and exist in reality as solid solutions, the levels of substitution are not very broad and they are often modelled as stoichiometric compounds when performing mass balances or simple thermodynamic calculations. This is not the case for ferrite which exists over a broad range of substitution with the general formula, Ca₂(Al_xFe_{1-x})₂O₅ with limits of 0 < x < 0.7. The formula suggests a substitution of the Al and Fe ions, which isn't reflected in the cement chemistry notation and makes ferrite somewhat unique in the so-called “major” clinker phases. At x = 0.5, C₄AF occurs and is therefore just a single composition of this wider solid solution. The end-members of this solid solution are Ca₂Fe₂O₅ (known as C₂F) at x = 0 and Ca₂Al₂O₅ (known as C₂A) at x = 1. C₂F is a stable compound found within the CaO-Fe₂O₃ binary section. However, the C₂A end-member is only stable at high pressures.

Within the clinker, Al and Fe ions are regularly substituted for minor elements and whilst the calcium ions have been found to exist at a fixed composition. The typical composition of the ferrite phase [3] is found to have the formula, Ca₂AlFe_{0.6}Mg_{0.2}Si_{0.15}T_{0.05}O₅ which is close to the calcium-alumina ratio for C₄AF but with significant amounts of Fe being replaced by Mg, Si, and Ti ions.

2.3 Reaction chemistry and approach to equilibrium in the kiln

The critical temperature for OPC clinker production is its peak temperature at roughly ≈ 1450 °C. At this temperature alite is sufficiently stable over belite to rapidly form. The raw material formulation typically includes sufficient iron to cause a partial melt to occur. The temperature at which some melt is observed is associated with the melting of species containing iron and alumina compounds (i.e., the mixing of iron oxide in the system drastically reduces the melt temperature) [6, 7]. This melt is why the alumina and iron content is important despite OPC being primarily a calcium silicate cement. There are some additional beneficial effects around workability too, but these are not discussed here to focus on the high-temperature chemistry and formation of these clinker phases. The melt phase acts as a flux/solvent for the raw materials such as lime and clay solids to dissolve, react, and subsequently precipitate out again as clinker phases. Too much melt would cause mechanical issues with the kiln operation, and too little would limit the rate of reaction. It is clear from this dynamic with the melt that there isn't a single set of reactions but more of a soup of melting/dissolving and precipitating phases depending on their stability at that local composition and temperature; However, it is common to simplify this as a set of chemical reactions which ignore the role of the melt. For example, Lee's cement chemistry [6] gives the following reaction set,



From the chemical reactions, one can see that C_3S is formed from the reaction of the C_2S phase with CaO . This is more a statement of the stability of C_3S over C_2S at high temperatures. This does highlight that C_3S is meta-stable at room temperature and the clinker must be rapidly cooled upon production to prevent the dissociation of C_3S back into C_2S and CaO . Using this idea of the reactions and their temperatures, Robert Bogue [8] developed the famous Bogue equations as a tool for predicting the composition of the clinker for a given raw meal. The Bogue equation is a set of simultaneous equations and is as follows:

$$\begin{aligned}\text{C}_4\text{AF} &= 3.043 \cdot F \\ \text{C}_3\text{A} &= 2.650 \cdot A - 1.692 \cdot F \\ \text{C}_2\text{S} &= -3.071 \cdot C + 8.6024 \cdot S + 1.0785 \cdot F + 5.0683 \cdot A \\ \text{C}_3\text{S} &= 4.0710 \cdot C - 7.6024 \cdot S - 1.4297 \cdot F - 6.7187 \cdot A\end{aligned}$$

The Bogue equation is a mass balance developed on the assumptions [8],

1. The amount of F determines the amount of C_4AF and is therefore fixed.
2. The amount of C_3A is determined by the total alumina content minus the alumina in C_4AF .
3. The amount of the C_2S and C_3S is solved by two simultaneous equations derived from the remaining C and S.

Despite being a simple set of equations, the Bogue equations are widely used in industry to get a rough estimate of the final clinker composition; however, it is not entirely accurate, with comparisons with XRD, showing that the Bogue equation tends over-predict the amount of C_2S and under-predict the amount of C_3S [9–11]. To address this and other drawbacks, Taylor [9] produced modifications to the calculations to try and account for minor elements including various alkalis, MgO and SO_3 . Ultimately though, the role of the melt phase cannot be ignored if the effects of solid solutions or sequential precipitation are to be captured.

2.4 Motivation for thermodynamic modelling of clinkerization.

It can be seen that the high-temperature chemistry of OPC production is quite complex, with many factors affecting the production of the clinker phases in their desired amount. These factors add many degrees of freedom when trying to optimise the clinker formulation, chemistry, and temperature. Whilst predictive calculations like the Bogue equations [8] and its many modifications [9, 10, 12] are popular due to their simplicity and rough accuracy, they do not take into account many important factors such as the melt phase and temperature, or even mass balance constraints such as non-negative species amounts. It is therefore necessary to use calculations which account for the melt phase to predict the clinker composition, similar to the work of Barry and Glasser [13]. To carry out such extensive calculations, a thermodynamic database which contains models for solid, liquid, and melt interactions within OPC clinkers must be developed.

If only the main oxides of the clinker phases are taken into account, the simplest system required for modelling is $CaO-Al_2O_3-SiO_2-Fe-O$, with $Fe-O$ used to account for the oxidation states of iron. However, as shown in Table 2.2, assuming the clinker phases to be pure is far from reality. Therefore, it is important to account for the major substitutions that can occur, such as MgO into belite. Furthermore, MgO is the minor oxide that is present in significant quantities in the raw material. This necessitates the modelling of MgO and its interactions within the major oxide system and makes the final thermodynamic database to be modelled, the $CaO-Al_2O_3-SiO_2-Fe-O-MgO$ system.

2.5 References

- [1] M. N. De Noirlfontaine, S. Tusseau-Nenez, C. Girod-Labianca and V. Pontikis. ‘CALPHAD formalism for Portland clinker: Thermodynamic models and databases’. In: *Journal of Materials Science* 47.3 (2012), pp. 1471–1479. DOI: 10.1007/s10853-011-5932-7.
- [2] *cement | Definition, Composition, Manufacture, History, & Facts | Britannica*. URL: www.britannica.com/technology/cement-building-material (visited on 16/01/2022).
- [3] H.F.W. Taylor. *Cement chemistry*. 2nd edition. Thomas Telford Publishing, 1997. DOI: 10.1680/cc.25929.
- [4] Andre Guinier and Micheline Regourd. ‘Structure of Portland Cement Minerals’. In: *5th International Congress on the Chemistry of Cement. Part 1*. 1968.
- [5] I. Maki and K. Kato. ‘Phase identification of alite in portland cement clinker’. In: *Cement and Concrete Research* 12.1 (1982), pp. 93–100. DOI: 10.1016/0008-8846(82)90103-X.
- [6] Peter del Strother. *Lea’s Chemistry of Cement and Concrete (Fifth Edition)*. Ed. by Peter C. Hewlett and Martin Liska. Butterworth-Heinemann, 2019. ISBN: 978-0-08-100773-0. DOI: 10.1016/B978-0-08-100773-0.00002-2.
- [7] Samira Telschow, Flemming Frandsen, Kirsten Theisen and Kim Dam-Johansen. ‘Cement Formation-A Success Story in a Black Box: High Temperature Phase Formation of Portland Cement Clinker’. In: *Industrial & Engineering Chemistry Research* 51.34 (2012). DOI: 10.1021/ie300674j.
- [8] R. H. Bogue. ‘Calculation of the Compounds in Portland Cement’. In: *Industrial and Engineering Chemistry - Analytical Edition* 1.4 (1929), pp. 192–197. DOI: 10.1021/ac50068a006.
- [9] H. F. W. Taylor. ‘Modification of the Bogue calculation’. In: *Advances in Cement Research* 2.6 (1989), pp. 73–77. DOI: 10.1680/adcr.1989.2.6.73.
- [10] Sang-Hyo Shim, Tae-Hee Lee, Seong-Joon Yang, Norhazilan Bin Md. Noor and Jang-Ho-Jay Kim. ‘Calculation of Cement Composition Using a New Model Compared to the Bogue Model’. In: *Materials* 14.16 (2021). DOI: 10.3390/ma14164663.
- [11] L. P. Aldridge. ‘Accuracy and precision of phase analysis in portland cement by Bogue, microscopic and X-ray diffraction methods’. In: *Cement and Concrete Research* 12.3 (1982), pp. 381–398. DOI: 10.1016/0008-8846(82)90087-4.
- [12] Tazuddin, Hemantkumar N. Aiyer and Amit Chatterjee. ‘Phase equilibria studies of CaO-SiO₂-Al₂O₃-Fe₂O₃-MgO system using CALPHAD’. In: *Calphad* 60 (2018), pp. 116–125. DOI: 10.1016/j.calphad.2017.12.003.

- [13] T I Barry and Fredrik Glasser. ‘Calculation of Portland cement clinkering reactions’. In: *Advances in Cement Research* 12 (2000), pp. 19–28. DOI: 10.1680/adcr.2000.12.1.19.

CHAPTER
THREE

THERMODYNAMIC MODELS FOR CLINKERIZATION

An overview of the thermodynamic models used in this thesis is given in this chapter. These models are taken from the work developed by the CALPHAD community, which is discussed in more detail in section 4.1. There is a variety of models that have been used to describe the various phases; however, at the time of writing, the latest models found within the literature are used for all phase types. In addition, comparisons are also made against previous models where updates have been made.

The primary goal in the thermodynamic modelling in this work is to predict the stable clinker phases and their interactions with the melt to better understand the cement production process. The stability of any phase is tied to its free energy, in particular the Gibbs free energy, G (when temperature and pressure are the explicit variables). All other thermodynamic properties can be derived from the Gibbs free energy, thus thermodynamic modelling is also concerned with modelling the heat capacity C_p , entropy S , enthalpy H , and others. Over the years various models have been developed to better represent the experimental data collected on these properties, and in more modern times also includes DFT calculations. While it may seem attractive to take existing models from the literature for individual phases and to assemble them for subsequent calculations, as has been done in the past (e.g., Ref. [1]), the models are often slightly incompatible with each other due to differences in reference states. From experience, it appears that many models also contain errors or simply the data sets have not been updated to take advantage of the wealth of new experimental data. It is for these reasons that the majority of phases of interest, aside from some key reference states (i.e., the simple oxides such as CaO, SiO₂, etc), are refit from the ground up to develop the thermodynamic database.

The models in this chapter are organised into the following categories:

- Stoichiometric phases/end-members - these are phases with a fixed composition e.g. pure solids, pure liquids, and compositional limits of solutions. The distinction between stoichiometric phases and end-members is not always clear, as a stoichiometric phase in one range of compositions may be an end-member in higher-order systems with more components.

- Solution phases - solid or liquid phases without a fixed composition. In the case of solids these are known as solid-solutions and in the case of liquids, these are known here as melt phases. These phases are comprised of end-members that may substitute for one another. This section primarily focusses on the details of modelling of the excess Gibbs free energy of these solution phases resulting from the interactions of their end-members.
- Magnetic model - These terms are used for phases which exhibit peaks in their heat capacity due to magnetism, such as iron.

In this chapter, many thermodynamic models for the different phases are reviewed and discussed and a summary and justification for the selected models in the present work is given.

3.1 Stoichiometric phases and end-members

In this section, the models used for end-members and stoichiometric solids as well as models for their corresponding pure liquids is detailed. An example of this includes the polymorphs of SiO_2 along with its corresponding pure oxide melt, as well as phases like C_3A where the substitutions are not modelled. This section will include some details on historical models for the Gibbs free energy of stoichiometric phases and will end with details on the latest in CALPHAD modelling via the third generation and the two-state models for the solid and liquids respectively.

3.1.1 Solid phase models

When modelling solid phases outside of geological processes, it is often assumed that the pressure contributions to the free energy are ignored. This can formally be stated as either the pressure is constant, or the solid has a negligible volume change. The simplest useful model for the thermodynamic properties of a solid phase is a first order perturbation about some temperature T_0 ,

$$G(T) \approx G_0 - S_0(T - T_0) = H_0 - S_0 T, \quad (3.1.1)$$

where H_0 and S_0 are constant enthalpy and entropy values determined at the reference temperature T_0 . Such simple models are useful in a narrow region around a particular temperature. To fit wider temperature intervals these terms must be expanded further. The second derivative of the free energy is the heat capacity,

$$\left(\frac{\partial G}{\partial T}\right)_p = -S \quad \left(\frac{\partial^2 G}{\partial T^2}\right)_p = -\frac{C_p}{T} \quad (3.1.2)$$

Experimentalist have long modelled heat capacity temperature dependence (and thus the dependence of Gibbs free energy too) using polynomial expansions. For example, Maier and Kelly [2] proposed a three-parameter model,

$$C_p(T) \approx C_1 + C_2 T + C_3 T^{-2}. \quad (3.1.3)$$

where C_n represents a fitting constant that is entirely determined by a regression against experimental data. A natural extension for higher accuracy in a polynomial series is to include more terms (i.e., Ref. [3]). One expression that has proven popular in modelling the heat capacity is as follows,

$$C_p(T) \approx C_1 + C_2 T + C_3 T^{-2} + C_4 T^2 + C_5 T^{-0.5}. \quad (3.1.4)$$

Modern datasets such as NIST-JANAF [4], Haas et al. [5], and SGTE [6] now use various forms of Eqn. (3.1.4), either with fewer terms or more terms, to model the thermodynamic properties of the solids of interest. The only disconnect from the Gibb's free energy and these heat capacity polynomials is the two integration constants lost in the derivatives of Eqs.(3.1.2) which can also be treated as fit constants and determined through regression to experimental data.

A massive disadvantage to these models built on polynomial expansions is that it has little physical justification for the constants and the form of the equation. In particular, extrapolation and even interpolation can be very dangerous due to unphysical behaviour. In short, the polynomials are chosen as they fit the data the best not because they are the best description of the underlying physics.

The so-called first-generation models which did not include heat capacity, i.e., Eqn. (3.1.1), have given way to the second-generation models, such as Eqns. (3.1.3) and (3.1.4), due to their improved performance; however, now a new third-generation set of models, based on simple but physical models for the underlying physics is now used. These models are built upon the Einstein or Debye models which assume a lattice with discrete and finite excitation modes. These terms allow a much better fitting of low-temperature heat capacity data, whilst also obeying the 3rd law of thermodynamics. A graph of the low-temperature volumetric heat capacity using Einstein terms can be seen in Figure 3.1. Practically, the use of Debye terms proves difficult when trying to calculate the entropy and enthalpy and therefore the Gibbs free energy, this is due to non-analytic terms when integrating the heat capacity, thus the Einstein model is preferred [7].

Third Generation Model

The latest development in the modelling of the stoichiometric solid phase is the 3rd generation CALPHAD function [8]. This equation was developed using combinations of Einstein terms with a small polynomial correction to allow fitting from absolute zero up to the melting point of the solid with a single function. Including zero kelvin in the

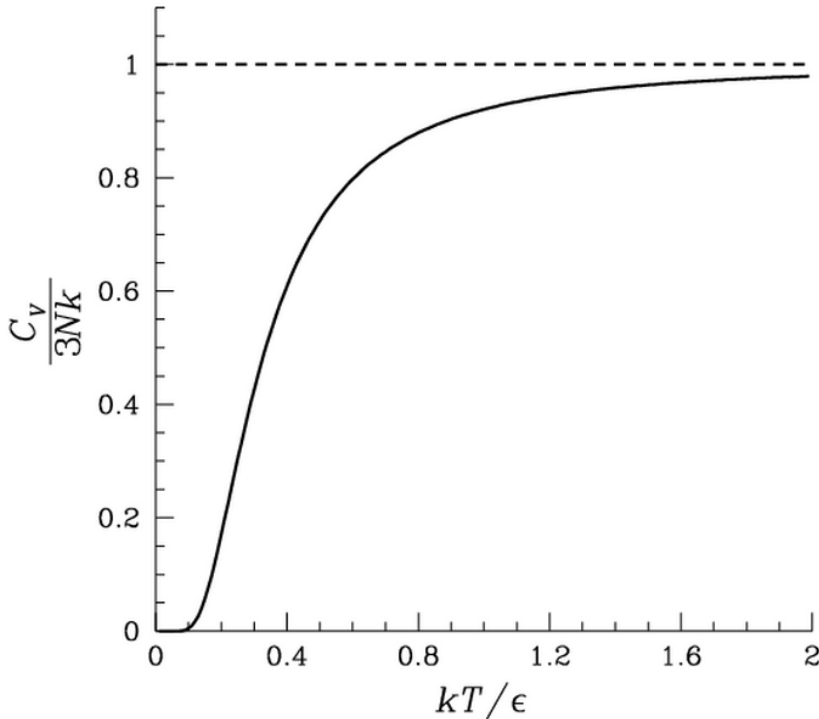


Figure 3.1: The volumetric heat capacity at low temperatures (less than 298 K), the Dulong-Petit law is indicated using a horizontal dashed line and is approached in the limit of high temperature.

fit is vital, as it is the primary method of connecting to the third law of thermodynamics and thus establishing the entropy which cannot be directly measured. Using only one expression for all temperatures also ensures thermodynamic consistency, as piece-wise expressions based on polynomial expansions have discontinuities in their derivatives at the crossover points which may lead to unphysical discontinuities in their thermodynamic properties. The 3rd generation CALPHAD function has the following general form,

$$G_{\alpha,solid}(T) = H_{0,\alpha} + \sum_{j=1}^{N_{P,\alpha}} \frac{C_{j,\alpha}}{j!} T^{D_{j,\alpha}} + 3R \sum_{i=1}^{N_{E,\alpha}} C_{i,\alpha} \left[\frac{\theta_{E,i,\alpha}}{2} + T \ln(1 - e^{-\theta_{E,i,\alpha}/T}) \right] \quad (3.1.5)$$

where $G_{\alpha,solid}$ is the Gibbs free energy of the solid compound α , $H_{0,\alpha}$ is a constant setting the absolute enthalpy of the compound, R is the gas constant and T is the temperature. There are $N_{E,\alpha}$ Einstein terms with Einstein temperatures $\theta_{E,i,\alpha}$ and prefactors $C_{i,\alpha}$. These terms have somewhat loose constraints; for example, there should be as many Einstein terms as there are atoms in a unit cell as the Einstein model approximates the lattice vibration contribution to the heat capacity and each atom has a unique energetic environment. A more strict constraint is that the sum of the Einstein prefactors, $\sum_i C_{i,\alpha}$, should also add up to the number of atoms in the formula so that the Dulong-Petit law is approximated (i.e., $\lim_{T \rightarrow \infty} C_v \approx 3N R$); however, there is still some flexibility as neither the Einstein nor the Dulong-Petit models are exact. For example, in the assessments of CaO [9] and SiO₂ [10] a triple-Einstein function was used. To add further flexibility in

fitting real data, $N_{P,\alpha}$ polynomial correction terms are also added with exponents $D_{j,\alpha}$ and prefactors $C_{j,\alpha}$. These terms are attributed to the anharmonic corrections at high temperatures, i.e., the correction of C_v to C_p at high temperatures; however, they also account for the approximations in the Einstein/Debye model. Typically, two terms with exponents $D_{j,\alpha} = \{2, 4\}$ are used; however, it was found that oxides typically exhibit an increase in heat capacity just before melting [9] and due to this it is better to use a pair of $D_{j,\alpha} = \{2, 13\}$ terms or the triplet $D_{j,\alpha} = \{2, 7, 8\}$ for the work presented here.

In fitting this function, typically low-temperature heat capacity data (> 298 K) is used to fit the Einstein terms (ideally low temperature C_v would be used, which can be gathered from DFT). This low temperature data will fit the Einstein temperatures $\theta_{E,i}$ and prefactors C_i , which in turn fits the S_{298} of the solid. High-temperature data relative enthalpy or heat capacity data is used to fit the additional polynomial terms and absolute enthalpy i.e., formation data is used to fit the enthalpy constant H_0 . Additional enthalpy data such as reaction data and transition energies can also be used to fit the enthalpy constant. While the data can be fit simultaneously, it has been found to fit the data individually in the first instance to provide a starting point for the minimiser before a simultaneous fit is carried out. More details on the fitting of solids and the 3rd generation function can be found in Chapter 4.

3.1.2 Liquid phase model

This section describes the model used for the pure liquid species. This is needed for each of the oxide end-members used in the melt phase e.g. CaO, SiO₂, Al₂O₃ etc. The challenge in general melt modelling is that a reasonable extrapolation for the pure liquids is required at temperatures well below the pure melting points. For example, pure CaO melts at 3222 K; however, the lowest melting point in the C-S system is at 1737 K (see Chap. 5). A method is needed to provide this reasonable extrapolation. In general, the liquid phase can be described using the same models as the solid phases, including third-generation functions; however, the experimental data for the liquid phase is limited to high temperatures thus little information is available to fit near absolute zero leaving the einstein/debye terms relatively unconstrained.

This issue can be sidestepped somewhat with the two-state model [11], which adds a model for the frozen amorphous state of the liquid. This amorphous state can then be modelled entirely using experimental data on glasses or, if there is a lack of data, it can be assumed to be close to the crystalline solid phase and utilise the same third-generation functions. The two-state model then attempts to model the liquid-glass transition using an ideal mixture of “solid-like” molecules (the amorphous glass) and “liquid-like” molecules (fully molten phase) which are in equilibrium. The liquid-like molecules are assumed to only have a small correction from the glass phase, given by the following expression

$$\Delta G_\alpha = G_{\alpha,ll} - G_{\alpha,st} = A + T * B + C * T (\ln(T) - 1), \quad (3.1.6)$$

where A , B , and C are fitting constants which are related to corrections to the enthalpy, entropy, and heat capacity respectively, and the subscripts ll and sl denote liquid-like and solid-like compounds. There are some psychical constraints on the fitting parameters, for example,

- $A > 0$, this is to ensure there is a positive enthalpy of melting.
- B is a negative value leading to a positive entropy of melting.
- and C is the difference in heat capacity between the solid-like and liquid-like atoms.

With this difference defined, the Gibbs free energy of the melt phase is given by the following classical ideal-mixing expression,

$$G_{\alpha,\text{liquid}} = x_{\alpha,\text{sl}} G_{\alpha,\text{sl}} + x_{\alpha,\text{sl}} \ln x_{\alpha,\text{sl}} + x_{\alpha,\text{ll}} G_{\alpha,\text{ll}} + x_{\alpha,\text{ll}} \ln x_{\alpha,\text{ll}} + \Delta G_{\alpha}, \quad (3.1.7)$$

where $x_{\alpha,\text{ll}} = (1 - x_{\alpha,\text{sl}})$ is the fraction of “liquid-like” molecules in the melt and $G_{\alpha,\text{ll}}$ is their corresponding free energy. Solving for equilibrium (i.e., minimum Gibbs energy) between the “solid-like” molecules and “liquid-like” molecules in the melt gives the following expression for the fraction of “liquid-like” molecules,

$$x_{\alpha,\text{ll}} = \frac{e^{-\Delta G_{\alpha}/(RT)}}{1 + e^{-\Delta G_{\alpha}/(RT)}}. \quad (3.1.8)$$

Substituting Eq. (3.1.8) into Eq. (3.1.7), the overall free energy of the melt is determined,

$$G_{\alpha,\text{liquid}} = G_{\alpha,\text{sl}} - RT \ln (1 + e^{-\Delta G_{\alpha}/(RT)}). \quad (3.1.9)$$

When modelling the two-state model, the first step is to model the amorphous phase using Eq. 3.1.5. Where available the heat capacity of the amorphous phase is fit with the Einstein terms a linear correction term only against the low-temperature glass/amorphous data. If this data is not available then the amorphous phase is assigned the same Gibbs free energy expression as the crystalline solid phase, removing the non-linear terms. Then the parameters of A , B and C can be fit to get the Gibbs free energy of the liquid phase, in the first instance it is recommended to set the value of B to $-R$ or $-0.75R$. A , B , and C should be optimised to the high-temperature liquid data [7].

It is to be noted, that this two-state model is used to model a liquid-solid glass transition as a way to extrapolate the liquid model; however, in theory any smooth transition between two-states can be expressed in this way where desirable. For example, Chen and Sundman [7] used a similar two-state model to describe the two states of magnetism seen within the solid Fe phase. This is not relevant to the current thermodynamic database as similar results are also achieved by using a simple magnetic model discussed later in Sec. 3.3.

3.2 Solution phase model

In the previous section, the models for the pure liquids and solids were detailed, in this section the models of solid and liquid solution phases are discussed. First, the main models for solid solutions phases are described. Variations of these models for melt solution phases are then introduced before the modelling of the excess Gibbs free energy is described, which is used for the modelling of non-ideal solutions.

3.2.1 Solid solutions

Solid solutions are identified as solids which have other solids dissolved or substituted within them, more simply they are defined as solids without a fixed composition and instead exist over a composition range. Their name as solid solutions implies that they can be modelled as the mixing of solids in the same manner as liquids are modelled [12]. This is most popularly achieved in the literature by the compound energy formalism (CEF) [13], which makes use of ideal mixing of the species on the different sublattices. Other models for the modelling of solid solutions also exist such as the modified quasi-chemical model [14], which takes into account the bond formation of the species.

Review of compound energy formalism and the modified quasi-chemical model

Further modelling is required when accurately modelling solid solutions i.e solids that are composition dependant. The most common model to fit solid solutions is the compound energy formalism [13]. In this model, multiple species can exist on the same sublattice and the model takes into the ideal and non-ideal mixing of the species within the sublattices that make up the solid. In the model, the sublattices can be “physically” determined i.e represent the crystallographic sublattices; however, they can be simplified further to avoid the use of multiple sublattices where complex representation is not necessarily required. For example, the mullite solid solution present in the Al_2O_3 - SiO_2 system has been represented by Mao et al [15] by using the sublattices $(\text{Al})_1(\text{Al})_1(\text{Al}, \text{Si})_1(\text{O}, \text{Va})_5$, however, it has also been found sufficient to simplify this sublattice model to $(1.5 \text{ Al}_2\text{O}_3, \text{Al}_2\text{SiO}_5)$. In the model, the compositional limits of the sublattice model are known as the end-members of the solution phase, e.g., in $(\text{Al}_3\text{O}_{4.5}, \text{Al}_2\text{SiO}_5)$ the end-members are $\text{Al}_3\text{O}_{4.5}$ and Al_2SiO_5 . The Gibbs free energy of the end-members can be determined using the Gibbs free energy of the solid phase (refer to Eqn. (3.1.5)). The energy is then determined by the summation of the product of the site fraction and end-member free energies,

$${}^{ref}G^\alpha = \sum_i y_i^{em}G_i, \quad (3.2.1)$$

where, y_i is the site fraction of species i and ${}^{em}G_i$ is the gibbs free energy of endmember i . Bragg-William ideal mixing [16] is used to define the configurational entropy,

$$-S^\alpha = R \sum_i y_i \ln(y_i) \quad (3.2.2)$$

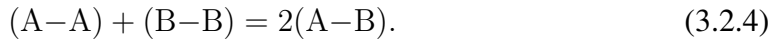
Summing the above equations across all sublattices plus non-ideal mixing gives the Gibbs free energy of the solution phase ϕ as,

$$G^\phi = \sum ({}^{ref}G^\alpha) - T \sum S^\alpha + {}^{excess}G^\phi. \quad (3.2.3)$$

The final term is the excess Gibbs free energy of the solution phase is given by the Redlich-Kister polynomial which is discussed in further detail in Section 3.2.3. The CEF is very useful as it covers a range of models that have a similar form, for example, the associate model [13] is a model for the melt phase, and the Gibbs free energy of this model is treated the same as the case for a single sublattice (see section 3.2.2). Similarly, the two-ionic sublattice is an ionic melt model which makes use of the CEF.

A different class of model used for the modelling of solution phases is the quasi-chemical model, which is a model which accounts for the non-random distribution of atoms (non-regular solution). The model is known as quasi-chemical as it contains a mass action equation similar to chemical reactions, with the quasi-chemical model being developed by Guggenheim and Fowler [17], but in the present literature a modified form of their model is used and was developed by Pelton and Blander [14, 18], this is known as the modified quasi-chemical model (MQM).

The modified quasi-chemical model is based on the idea that the interactions between particles can be approximated by a pairwise potential energy function. This means that the energy of the system can be written as a sum of the energy of each pair of particles, with each term in the sum being a function of the distance between the particles. The energy of the system can then be minimised by finding the configuration of the particles that minimises the pairwise potential energy. For example, in a binary solution (A,B), where A and B are atoms that can mix on a lattice. A pair exchange reaction is as follows,



Z_i and n_i is the coordination numbers and moles of species i , respectively. The following expression is obtained,

$$Z_A n_A = 2n_{AA} + n_{AB} \quad (3.2.5)$$

$$Z_B n_B = 2n_{BB} + n_{AB}. \quad (3.2.6)$$

From here, the “co-ordination-equivalent” fractions which after simplification are as fol-

lows,

$$Y_A = X_{AA} + X_{AB}/2 \quad (3.2.7)$$

$$Y_B = X_{BB} + X_{AB}/2, \quad (3.2.8)$$

where X_{AA} and X_{BB} is defined as the pair fractions for the pair ij

$$X_{ij} = n_{ij}/n_{AA} + n_{BB} + n_{AB}. \quad (3.2.9)$$

The Gibbs energy of the binary solution phase is then defined as,

$$G = (n_A g_A + n_B g_B) - T * \Delta S^{config} + (n_{AB}/2) \Delta g_{AB}, \quad (3.2.10)$$

where g_A and g_B are the Gibbs free energies of the pure components A and B, respectively. T is the temperature and ΔS^{config} is the configurational entropy of mixing which arises from the random distribution of the bond pairs,

$$\Delta S^{config} = -R(\sum n_i \ln(X_i)) - R[\sum (n_{ii} \ln(X_{ii}/Y_i^2) + n_{AB} \ln(X_{AB}/2Y_A Y_B))] \quad (3.2.11)$$

Finally, Δg_{AB} is the Gibbs energy change for the formation of AB pairs,

$$\Delta g_{AB} = (\omega_{AB}^\circ - \eta_{AB}^\circ T) + \sum_{(i+j \geq 1)} ((\omega_{AB}^{ij} - \eta_{AB}^{ij} T)) Y_A^i Y_B^j, \quad (3.2.12)$$

where ω_{AB}° , η_{AB}° , (ω_{AB}^{ij}) and η_{AB}^{ij} , are adjustable parameters and are used to fit experimental data in real systems i.e non-ideal systems. This term is equivalent to the Redlich-Kister polynomials in the compound energy formalism used to model the excess Gibbs free energy, this is discussed in later sections.

While the modified quasichemical model has not been used in the present work, it has proven useful in the literature to model solution phases including oxide systems of interest for cementitious applications [19, 20]. Pelton and Blander in collaboration with various authors produced an insightful series on the modified quasichemical model [18, 21–24], its derivations, applications and the specific cases e.g binary, multi-component, two-sublattice solutions etc, of which further reading is encouraged.

The compound energy formalism and the quasichemical models are important to understand as they are used to model solid solution phases, which are common in many systems. Furthermore, they have also been developed further to also be able to model liquid solution phases (known as melt phases in the present work). In the next section, the melt phase models are detailed and described.

3.2.2 Melt phase model

In the literature, many melt phase models exist, with some being more popular than others. The most common ones today include the two-sub lattice model [25], the modified quasi chemical model [22] and the associates model [26], although many more exist, they have fallen out of use, since the creation of the CALPHAD approach, in addition, the main commercial databases make use one of the three models listed above, e.g.

- The MTDATA/NPL databases make use of the associates model [27].
- The Thermocalc databases make use of the two-sublattice model [28].
- The FACTSAGE databases make use of the MQM [29].

The choice of model is up to the modeller's preference, as they have all been found to model melt phase to a good degree and all advantages and disadvantages of the models have to be taken into account for the specific use case, e.g. in the CaO-Al₂O₃-SiO₂ system (which is an important ternary system for Portland cement), all of the listed models have been used to successfully model this melt phase of this ternary system [30]. Even once the model is chosen for the melt phase it is important to make a choice of the species and sub-lattices present within the melt. For the same system, any differences in the species will drastically change the final phase diagram parameters even if the same model is used. This often results in using the modeller's experience to first select the appropriate model and then choose the appropriate species and excess parameters, this may result in a trial and error exercise, to see what results in the best fit of the experimental data. The model is fit against phase diagram data, activity data and mixing data. However, the melt phase can be fit against only the experimental phase diagram data, as it is well constrained containing information on the compositions and temperatures of the phase in equilibrium.

Melt: Associates Model

An associate model is used to approximate the melt as a mixture of neutral species, called the “associates”. This model is popular in systems where the melt phase exhibits short-range order [26] which is the case in the metal-oxygen system. The associates may be fictive species but typically have some experimental evidence for their existence such as spectroscopic data. For example, in the CaO-SiO₂ system the possible associates are justified by the idea of “Q” species typically seen in Si-O-M systems. In Si-O-M systems two types of bonds occur:

- bridging oxygens (an oxygen atom linking two Si atoms)
- non-bridging oxygens (an oxygen atom linking Si and a metal atom)

As a result of this, the idea of “Qⁿ” species has arisen to explain some observed spectroscopic phenomena, where *n* is the number of bridging oxygens, using this the “Q” species that are seen in these systems are as follows:

- $Q^4 = \text{SiO}_2$
- $Q^3 = \text{Si}_2\text{O}_5^{2-}$
- $Q^2 = \text{SiO}_3^{2-}$
- $Q^1 = \text{Si}_2\text{O}_7^{6-}$
- $Q^0 = \text{SiO}_4^{2-}$

In the CaO-SiO₂ system, these species are combined with the metal atom (Ca) to form neutral species resulting in all of the possible associates:

- $Q^4 = \text{SiO}_2$
- $Q^3 = \text{CaSi}_2\text{O}_5 = \text{CS}_2$
- $Q^2 = \text{CaSiO}_3 = \text{CS}$
- $Q^1 = \text{Ca}_3\text{Si}_2\text{O}_7 = \text{C}_3\text{S}_2$
- $Q^0 = \text{Ca}_2\text{SiO}_4 = \text{C}_2\text{S}$

Additionally, the chosen associates are also typically normalised in some way, e.g it is generally accepted to have a constant metal amount in all associate species in the model; however, there is no strict rule regarding normalisation but there are trends in the literature to use either 1 or 2 metallic atoms per species, this is mainly to overcome issues in modelling and extrapolations to higher order systems e.g. unwanted miscibility gaps and associate instability. In choosing the associates, not all of the possible associates have to be selected, and it is up to the modeller to choose the amount and normalisation of the associates to sufficiently model the experimental data. In previous studies of CaO-SiO₂ system, authors have normalised associates to have 2 non-oxygen atoms per mole of species [31], whereas in the current CaO-SiO₂ assessment the following non-normalised associates were chosen: C₁S₀, C₂S₁, , C₁S₁ and C₀S₁, out of the possible 6 associates.

The Gibbs free energy of the associates can be made from the addition of oxide end members with a correction for the enthalpy and entropy,

$$G_{ab,\text{associate}} = (x G_{a,\text{liq.}} + y G_{b,\text{liq.}}) + \Delta H_{ab} - T \Delta S_{ab}, \quad (3.2.13)$$

where x and y are the molar amounts of end members a and b respectively. $G_{a,\text{liq.}}$ and $G_{b,\text{liq.}}$ are the Gibbs free energy of the pure end members a and b respectively, which in the case of the CaO-SiO₂ system are CaO and SiO₂. ΔH_{ab} and ΔS_{ab} are constants that correct for the enthalpy and entropy for the associate respectively. For the pure end members, the Gibbs free energy of the end member associates is just the Gibbs free energy of the end member liquid multiplied by the molar amount of the associate, with no correction for the enthalpy and entropy. In the first instance it is useful to fit the enthalpy correction to the

heat of fusion and the entropy to the entropy of fusion of the corresponding compound, if this is not available, then the entropy of fusion is set to 0 and the enthalpy correction is fit to the phase diagram point. Once the associates are chosen, the total Gibbs free energy of the melt phase is then given by the following expression,

$$G_{melt} = \sum_{\alpha} x_{\alpha} G_{\alpha} + RT \sum_{\alpha} x_{\alpha} \ln(x_{\alpha}) + {}^{excess}G, \quad (3.2.14)$$

where x_{α} is the mole fraction of the associate α . The final term is the gibbs energy of the excess free energy of mixing, usually modelled using Redlich-Kister corrections, which is discussed in detail in Sec. 3.2.3.

The use of the associates model is advantageous due to its simplicity, it is essentially a form of the CEF model with only one sublattice (see 3.2.1), and it can be implemented in all of the most common thermodynamic packages such as Thermocalc [28], FACTSAGE [29], PANDAT [32] and ESPEI [33]; however, the big criticism of the associates model is that it produces sharp minima [34] in the Gibbs free energy in the regions of the associate species, which may cause problems with melt stability. Furthermore, the choice of associates is not always straightforward; a model that works in a binary melt may cause huge errors in the ternary melt, which then requires refitting of the binary melt phase. This is to say, it is difficult to predict the effects and any possible issues of the chosen associates in higher-order melt interactions. However, it is to be noted that the issue of extrapolating to higher order systems is not just a problem specific to the associates model and is a major problem with all melt models, which is why great emphasis is put on the choice of the model in the CALPHAD approach.

Melt: Two-Sublattice Model

The two-sublattice model is a popular model for the modelling of phase diagrams. It was developed in 1985 by Hillert et al [25], part of its popularity is due to the accurate recalculation of the phase diagram data and its extensive development and application. The model accounts for the species on different sublattices in the melt phase, the different sublattices allow the accounting of the compositional variation in the melt phase, based on expressions of configurations entropy. It is called such due to the use of two sublattices, with one sublattice containing anions and the other containing cations. It is, for this reason, also sometimes known as the “ionic two-sublattice model”.

$$G_m = \sum \sum y_i y_j \Delta^{\circ} G_{i-v_j j v_i} + P \sum y_i (\Delta^{\circ} G_i + RT \ln y_i) + Q \sum y_j (\Delta^{\circ} G_j + RT \ln y_j), \quad (3.2.15)$$

where the y_i and y_j are the site fractions of component i and j respectively. P and Q refer to the stoichiometric numbers of the sublattices given by,

$$P = \sum (-v_j y_j) \quad (3.2.16)$$

$$Q = \sum (v_i y_i), \quad (3.2.17)$$

where v_i and v_j refer to the valence of components i and j respectively. Combining P and Q maintains electroneutrality in Eq. (3.2.15). In Eq. (3.2.15) the first term refers to the reference energy of the sublattices and the 2nd and 3rd term refers to the ideal mixing of the species on sublattice 1 and 2 respectively. Additionally, excess Gibbs free energy parameters can be added to further model the phase diagram data like the Redlich-Kister term.

Depending on the species used in the sublattices the associates and two-sublattice may be made equivalent. For example, the model for the CaO-SiO₂ binary melt has been represented by Hillert et al by the two sublattices [35],



This model is very similar to using the associates “CaO”, “C₂S”, “CS” and “SiO₂”. The difference in the models is the mixing entropy between the one sublattice (associates) and the two-sublattice models. Overall, while the two-sub lattice model is seen as more “physical” as it accounts for different ions on the sublattices and the configurational entropy of the melt phase, the model is still a simplified view of the species within the melt phase and due to this, the same issues may arise when extrapolating to higher order systems.

3.2.3 Redlich-Kister excess term

The excess properties of the phase (e.g excess Gibbs free energy of mixing) can be described by a Redlich-Kister polynomial [36]. This polynomial is often chosen as it returns 0 at the limits of $x = 0$ and $x = 1$. This makes it favourable to use in the mixing of components, where mixing behaviour may deviate from ideal mixing[37]. For a binary interaction between species α and β , the Gibbs free energy of the interaction is given by the third term in Eq. (3.2.14):

$${}^{excess}G^{\alpha\beta} = \sum_{\alpha,\beta \neq \alpha} x_\alpha x_\beta \sum_k (x_\alpha - x_\beta)^k L_{\alpha,\beta}^k, \quad (3.2.18)$$

where $L_{\alpha,\beta}^k$ is the Redlich-Kister polynomial and is expressed as,

$$L_{\alpha,\beta}^k = A + B * T, \quad (3.2.19)$$

where A and B are fitting constants that relate to the enthalpy and entropy of mixing respectively, this form is similar to Eq. (3.1.4) and similarly, a $c * T * \ln(T)$ term can be added, however, this is not typical and not advised. k refers to the order of the interaction

e.g 0,1,2 and determines the position of the peaks in the interaction energies, from this one can decide what terms to use (see Fig. 3.2, 3.3 and 3.4). Furthermore, it is common to use

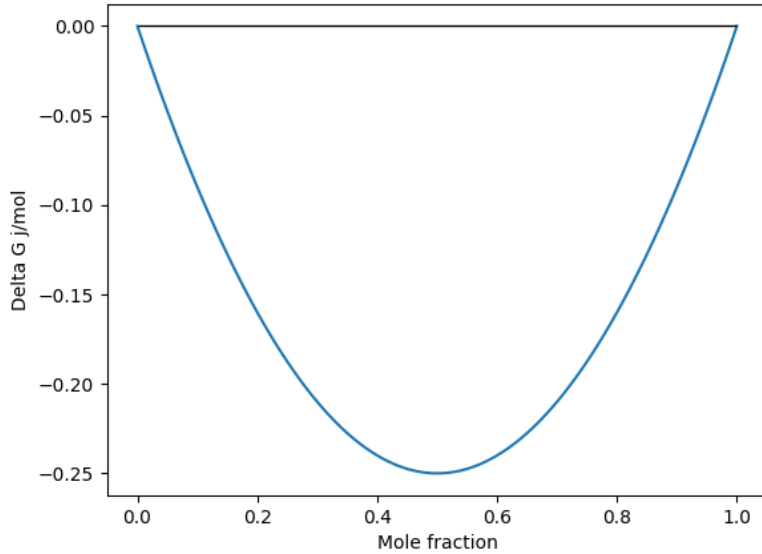


Figure 3.2: Graph of a L^0 interaction between two species from $x = 0$ and $x = 1$.

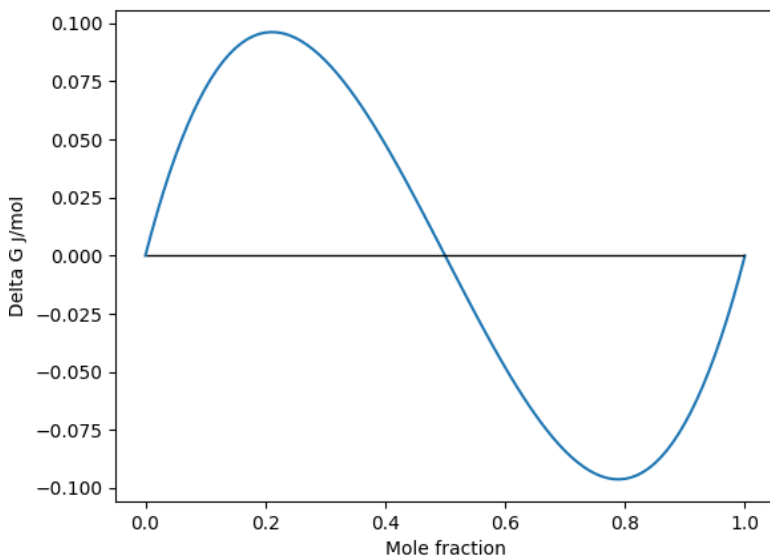


Figure 3.3: Graph of a L^1 interaction between two species from $x = 0$ and $x = 1$.

combinations of these terms to model specific features of the phase diagram. Additionally, whilst theoretically, there is no maximum order for the L terms, in practical fitting, it has been advised to use a maximum of order two, however, occasionally third order term is used to overcome certain features of the phase diagram.

Extrapolating these binary interactions to higher-order systems is simple and the Gibbs free energy of the ternary melt is given by the same of the binary melt interactions. This

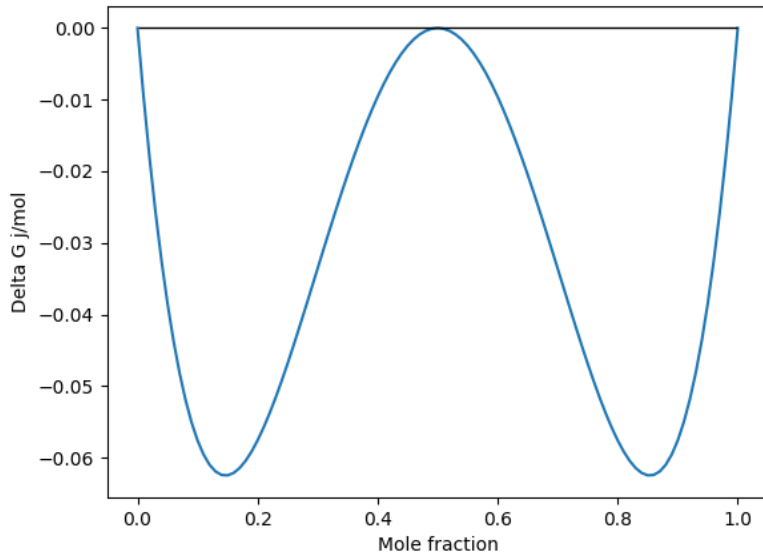


Figure 3.4: Graph of a L^2 interaction between two species from $x = 0$ and $x = 1$.

gives the general formulation of the Gibbs free energy of a binary interaction in a solution phase ϕ with c components as follows,

$$excess G^{binary,\phi} = \sum_{\alpha=1}^{c-1} \sum_{\beta>1}^c x_\alpha x_\beta \sum_{k=0}^c (x_\alpha - x_\beta)^k L_{\alpha,\beta}^k. \quad (3.2.20)$$

Eq. (3.2.20) is what is known as a symmetric geometric model or Muggianu extrapolation [38] which is by far the most commonly used model in higher-order extrapolations [39], however an asymmetric geometric model can also be used to extrapolate to higher order systems using the Kohler-Toop model, where one the mixing of one component is treated differently and two components are treated identical [39] (as this model is not used in the project, due to only being relevant in specific use cases the details of the expressions for this model will not be discussed here). Finally, although rarely used, a ternary interaction term can also be added to the Gibbs free energy of a solution phase (e.g Eq. (3.2.14)) to model interactions between three species α , β and γ , this is given by the equation,

$$excess G^{ternary,\phi} = \sum_{\alpha=1}^{c-2} \sum_{\beta>\alpha}^{c-1} \sum_{\gamma>\beta}^c x_\alpha x_\beta x_\gamma [(x_\alpha + \delta_{\alpha,\beta,\gamma}) L_{\alpha,\beta,\gamma}^1 + (x_\beta + \delta_{\alpha,\beta,\gamma}) L_{\alpha,\beta,\gamma}^2 + (x_\gamma + \delta_{\alpha,\beta,\gamma}) L_{\alpha,\beta,\gamma}^3], \quad (3.2.21)$$

where,

$$\delta_{\alpha,\beta,\gamma} = (1 - x_\alpha - x_\beta - x_\gamma)/3. \quad (3.2.22)$$

This term is used to preserve the symmetry of the interactions when extrapolating into

higher order systems i.e when $c = 3$, $\delta_{\alpha,\beta,\gamma} = 0$ and when $c > 3$, $\delta_{\alpha,\beta,\gamma} \neq 0$, Hillert found that when $L_{i,j,k}^1$, $L_{i,j,k}^2$, and $L_{i,j,k}^3$ are the same Eq. (3.2.22) can be reduced to,

$$excess G^{ternary,\phi} = \sum_{\alpha=1}^{c-2} \sum_{\beta>\alpha}^{c-1} \sum_{\gamma>\beta}^c x_{\alpha} x_{\beta} x_{\gamma} L_{\alpha,\beta,\gamma} \quad (3.2.23)$$

where $L_{\alpha,\beta,\gamma} = L_{i,j,k}^1 = L_{i,j,k}^2 = L_{i,j,k}^3$. Although rather complicated, the ternary term is rarely used and is found to be avoided and it is better to use binary interactions to fit the experimental data in the first instance in the high-order systems or improve on the binary interactions in lower-order systems (e.g. add more binary interactions in the ternary melt or refit the binary melt interactions) [40].

These excess terms are useful in further modelling behaviour that cannot be captured by Bragg-Williams mixing in the phase diagram and activity data. These terms are used in models for the solution phases i.e solid solutions and melt phases. It is important to maintain what is known as the equal entropy criterion (EEC) proposed by Sundman et al. [41], whereby the melt must always have higher entropy than the solid above the melting temperature of the solid to avoid poor extrapolation of the solid at high temperatures resulting in the solid becoming stable again (which can occur when using the 3rd generation function). The EEC defines a temperature at which the entropy of the solid and the liquid is the same and it is suggested to prevent the Gibbs free energy of the solid from being stable above this temperature. This constraint may be violated through the use of unreasonable Redlich-Kister terms, so care must be taken in choosing and fitting interaction terms.

3.3 Magnetic model

Finally, it is important to model the magnetic properties and transitions of the solid species, if applicable (i.e. if the phase of interest has magnetic properties) as magnetism causes a sharp peak in the C_p at the Curie temperature (T_c). These features cannot be captured by only a solid phase model like Eq. (3.1.4) or Eq. (3.1.5). This was important in this work when introducing FeO, Fe₂O₃, and other iron-containing compounds. The magnetic model used in this work and most commonly used is based on the work by Inden and later modified by Hillert and Jarl and is now known as the Inden-Hillert-Jarl (IHJ) model [42]. The model is based on a Taylor expansion of the magnetic contribution of the heat capacity of the ferromagnetic (FM) and paramagnetic states (PM), which is as follows,

$$\begin{aligned} C_p^{FM} &= K^{FM} R(\tau^m + \frac{1}{3}\tau^{3m} + \frac{1}{5}\tau^{5m}), \tau < 1 \\ C_p^{PM} &= K^{PM} R(\tau^{-n} + \frac{1}{3}\tau^{-3n} + \frac{1}{5}\tau^{-5n}), \tau > 1, \end{aligned} \quad (3.3.1)$$

where $m = 3$ and $n = 5$, and τ is the ratio of the temperature and the Curie temperature ($\frac{T}{T_c}$). K^{FM} and K^{PM} are constants related to the enthalpy and entropy of transitions of the FM and PM states respectively. The maximum entropy of the ordering transition is a function of the mean magnetic model, β ,

$$S^{magn} = R \ln(\beta + 1). \quad (3.3.2)$$

Integrating Eq. (3.3.1) and combining it with Eq. (3.3.2), the Gibbs free energy of the magnetic contribution is given (the full transformation to get the Gibbs free energy is not shown in this work, however, one can look at reference [42] for a more detailed derivation of the magnetic Gibbs free energy),

$$G^{magn} = RT(\beta + 1) g(\tau) \quad (3.3.3)$$

where,

$$\begin{aligned} g(\tau) &= 1 - \frac{1}{D} \left[\frac{79\tau^{-1}}{140p} + \frac{474}{497} \left(\frac{1}{p} - 1 \right) \left(\frac{\tau^3}{6} + \frac{\tau^9}{135} + \frac{\tau^{15}}{600} \right) \right], \tau < 1 \\ g(\tau) &= -\frac{1}{D} \left[\frac{1}{10}\tau^{-5} + \frac{1}{315}\tau^{-15} + \frac{1}{1500}\tau^{-25} \right], \tau \geq 1 \\ D &= \frac{518}{1125} + \frac{11692}{15975} \left(\frac{1}{p} - 1 \right). \end{aligned} \quad (3.3.4)$$

p is the structure factor, which is the ratio of the magnetic enthalpy in the PM state and is related to the structure of the species (generally $p = 0.28$ for BCC structures and 0.4 for non-BCC structures). This description was satisfactory for the FM order, however, to describe the anti-ferromagnetic (AFM) ordering, Weiss and Tauer [43] proposed using AFM factors so that a single expression for the magnetic contribution could still be used (see Figure 3.5). The AFM factors are the relation of the Neel temperature (T_N) and the Curie temperature (T_c) (for BCC structures $-T_N = T_c$ and $-3T_N = T_c$ for non-BCC structures). This is based on some experimental observations by Weiss and Tauer, however, it is not entirely accurate and is a massive generalization. To overcome the use of AFM factors, for greater accuracy in modelling both AFM, FM and PM states using a single function, Xiong et al [44] proposed a modification to the IHJ model (the full details of the model including its derivation can be found in Ref [44]),

$$G^{magn} = RT(\beta^* + 1)g(\tau) \quad (3.3.5)$$

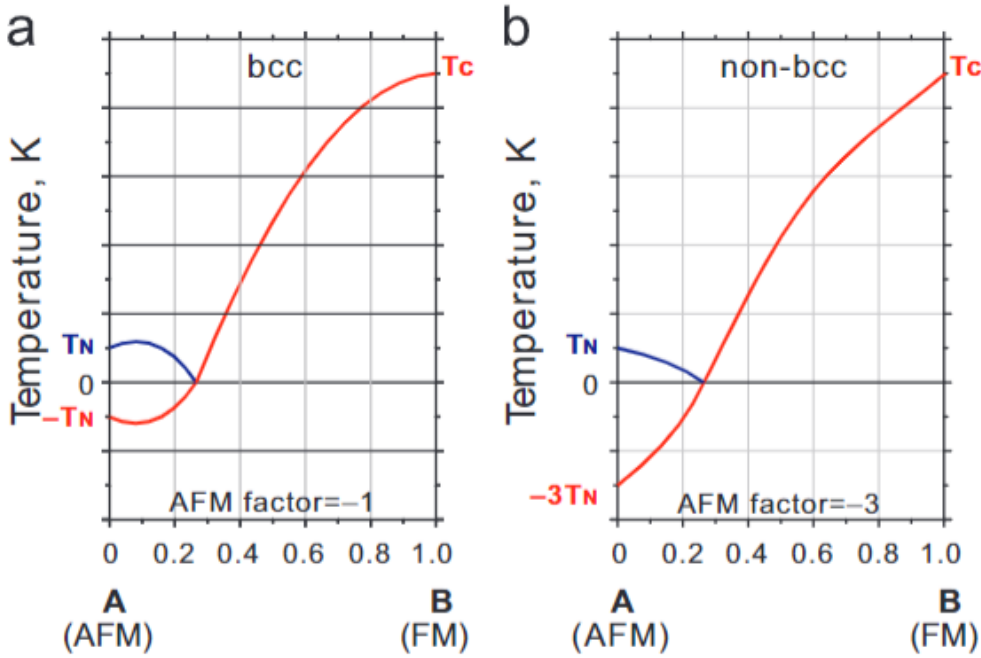


Figure 3.5: Graph showing temperature vs magnetic ordering ratio of an A-B system using the AFM factors for (a) BCC structure and (b) non-BCC structure. This diagram is adapted from Xiong et al [44].

where β^* is the effective magnetic moment (replacing the mean magnetic moment) and $g(\tau)$ is,

$$g(\tau) = 1 - \frac{1}{D} \left[\frac{0.3843876\tau^{-1}}{p} + 0.63570895 \left(\frac{1}{p} - 1 \right) \left(\frac{\tau^3}{6} + \frac{\tau^9}{135} + \frac{\tau^{15}}{600} + \frac{\tau^{21}}{1617} \right) \right], \tau \leq 1 \quad (3.3.6)$$

$$g(\tau) = -\frac{1}{D} \left[\frac{1}{21}\tau^{-7} + \frac{1}{630}\tau^{-21} + \frac{1}{2975}\tau^{-35} + \frac{1}{8232}\tau^{-49} \right], \tau > 1$$

$$D = 0.33471979 + 0.49649686 \left(\frac{1}{p} - 1 \right)$$

In this model, the structure factor p is also different, where $p = 0.37$ for BCC structures and 0.25 for non-BCC structures. The two models, although similar are not interchangeable with one another and produce very similar results, it is for this reason the IHJ was chosen along with the AFM factors in the present work to fit the magnetic contributions for the relevant species, as the magnetic parameters for the phases of interest are widely available in the literature.

3.4 Summary and justification for selected models

Various thermodynamic models were described in this chapter, with a focus on the use of new developments in thermodynamic models such as the latest 3rd generation models

for the solid and liquid phases. In the melt phase, there are a variety of models used in the literature and in this chapter the main models were discussed and reviewed.

In the present work, the 3rd generation models were chosen to model the solid and liquid phases as the model parameters are based on underlying physical models and allow for extrapolation and interpolation with a higher degree of confidence. Furthermore, these sets of functions are beneficial as they allow for an accurate thermodynamic description of the phases with a single function spanning an entire temperature range. The CEF model will be used to model the solid solutions in the present work. There is great debate about the choice of the melt phase model. In reviewing the melt phase models, the associates model was found to be a good balance between accuracy, complexity, and compatibility with modern codes and is proven to work well with oxide systems such as those contained in the present work.

With the models that are used in the present work, chosen and justified, there are now a wide range of parameters to select and optimise, with not all parameters required to fit the thermodynamic data within all phases. In general, parametrization should be conducted with a delicate balance of complexity and accuracy. How this is dealt within the OPC clinker system, in particular model selection, is discussed in the following chapter, with details of newly developed fitting methodologies.

3.5 References

- [1] Theodore Hanein, Fredrik P. Glasser and Marcus N. Bannerman. ‘Thermodynamic data for cement clinkering’. In: *Cement and Concrete Research* 132.106043 (2020). DOI: [10.1016/j.cemconres.2020.106043](https://doi.org/10.1016/j.cemconres.2020.106043).
- [2] Chas G. Maier and K. K. Kelley. ‘An equation for the representation of high-temperature heat content data’. In: *The Journal of the American Chemical Society* 54.8 (1932), pp. 3243–3246. DOI: [10.1021/ja01347a029](https://doi.org/10.1021/ja01347a029).
- [3] J. L. Haas and J. R. Fisher. ‘Simultaneous evaluation and correlation of thermodynamic data’. In: *American Journal of Science* 276.4 (1976), pp. 525–545. ISSN: 0002-9599. DOI: [10.2475/ajs.276.4.525](https://doi.org/10.2475/ajs.276.4.525).
- [4] M. W. Chase. ‘NIST-JANAF Thermochemical Tables, 4th Edition’. In: (1998). DOI: [10.18434/t42s31](https://doi.org/10.18434/t42s31).
- [5] John L. Haas Jr., Glipin R. Robinson Jr. and Bruce S. Hemingway. ‘Thermodynamic tabulations for selected phases in the system CaO-Al₂O₃-SiO₂-H₂ at 1 atm between 273.15 and 1800 K’. In: *Journal of Physical and Chemical Reference Data* 10.3 (1981), pp. 575–670. DOI: [10.1063/1.555645](https://doi.org/10.1063/1.555645).
- [6] A. T. Dinsdale. ‘SGTE data for pure elements’. In: *Calphad* 15.4 (1991), pp. 317–425. DOI: [10.1016/0364-5916\(91\)90030-n](https://doi.org/10.1016/0364-5916(91)90030-n).

- [7] Qing Chen and Bo Sundman. ‘Modeling of thermodynamic properties for Bcc, Fcc, liquid, and amorphous iron’. In: *Journal of Phase Equilibria* 22.6 (2001), pp. 631–644. DOI: 10.1361/105497101770332442.
- [8] Malcolm W Chase, Ibrahim Ansara, Alan Dinsdale, Gunnar Eriksson, Goran Grimvall, Lars Hoglund and Harumi Yokokawa. *Group 1: Heat capacity models for crystalline phases from 0 K to 6000 K*. Vol. 19. 4. 1995, pp. 437–447.
- [9] Guillaume Deffrennes, Noël Jakse, Cecilia M.S. Alvares, Ioana Nuta, Alain Pasturel, Alexandra Khvan and Alexander Pisch. ‘Thermodynamic modelling of the Ca-O system including 3rd generation description of CaO and CaO₂’. In: *Calphad* 69 (2020), p. 101764. DOI: 10.1016/j.calphad.2020.101764.
- [10] I. Bajenova, A. Khvan, A. Dinsdale and A. Kondratiev. ‘Implementation of the extended Einstein and two-state liquid models for thermodynamic description of pure SiO₂ at 1 atm’. In: *Calphad* 68.101716 (2020). DOI: 10.1016/j.calphad.2019.101716.
- [11] John Agren. ‘Thermodynamics of Supercooled Liquids and their Glass Transition’. In: *Physics and Chemistry of Liquids* 18.2 (1988), pp. 123–139. DOI: 10.1080/00319108808078586.
- [12] Bo Sundman, Qing Chen and Yong Du. ‘A Review of Calphad Modeling of Ordered Phases’. In: *Journal of Phase Equilibria and Diffusion* 39.5 (2018), pp. 678–693. DOI: 10.1007/s11669-018-0671-y.
- [13] Mats Hillert. ‘The compound energy formalism’. In: *Journal of Alloys and Compounds* 320.2 (2001), pp. 161–176. DOI: 10.1016/S0925-8388(00)01481-X.
- [14] Mats Hillert, Malin Selleby and Bo Sundman. ‘An attempt to correct the quasi-chemical model’. In: *Acta Materialia* 57 (Oct. 2009), pp. 5237–5244. DOI: 10.1016/j.actamat.2009.07.026.
- [15] Huahai Mao, Malin Selleby and Bo Sundman. ‘Phase Equilibria and Thermodynamics in the Al₂O₃-SiO₂ System-Modeling of Mullite and Liquid’. In: *Journal of the American Ceramic Society* 88.9 (2005), pp. 2544–2551. DOI: 10.1111/j.1551-2916.2005.00440.x.
- [16] T. Ikeda, H. Numakura and M. Koiwa. ‘A Bragg-Williams model for the thermodynamic activity and the thermodynamic factor in diffusion for ordered alloys with substitutional defects’. In: *Acta Materialia* 46.18 (1998), pp. 6605–6613. DOI: 10.1016/S1359-6454(98)00287-0.
- [17] R.H. Fowler and E.A. Guggenheim. *Statistical Thermodynamics: A Version of Statistical Mechanics for Students of Physics and Chemistry*. Macmillan, 1939. ISBN: 9780608304403.

- [18] Arthur D Pelton and Milton Blander. ‘Thermodynamic analysis of ordered liquid solutions by a modified quasichemical approach-application to silicate slags’. In: *Metallurgical Transactions B* 17.4 (1986), pp. 805–815.
- [19] Gunnar Eriksson, Ping Wu, Milton Blandert and Arthur D. Pelton. ‘Critical evaluation and optimization of the thermodynamic properties and phase diagrams of the MnO-SiO₂ and CaO-SiO₂ systems’. In: *Canadian Metallurgical Quarterly* 33.1 (1994), pp. 13–21. DOI: 10.1179/cmq.1994.33.1.13.
- [20] Ping Wu, Gunnar Eriksson, Arthur D Pelton and Milton Blander. ‘Prediction of the thermodynamic properties and phase diagrams of silicate systems-evaluation of the FeO-MgO-SiO₂ system’. In: *ISIJ international* 33.1 (1993), pp. 26–35.
- [21] Arthur D Pelton and Patrice Chartrand. ‘The modified quasi-chemical model: Part II. Multicomponent solutions’. In: *Metallurgical and Materials Transactions A* 32.6 (2001), pp. 1355–1360.
- [22] Arthur D Pelton, SA Degterov, Gunnar Eriksson, Christian Robelin and Yves Des-sureault. ‘The modified quasichemical model I-Binary solutions’. In: *Metallurgical and Materials Transactions B* 31.4 (2000), pp. 651–659.
- [23] Patrice Chartrand and Arthur D Pelton. ‘The modified quasi-chemical model: Part III. Two sublattices’. In: *Metallurgical and Materials Transactions A* 32.6 (2001), pp. 1397–1407. DOI: 10.1007/s11661-001-0229-0.
- [24] Arthur D Pelton, Patrice Chartrand and Gunnar Eriksson. ‘The modified quasi-chemical model: Part IV. Two-sublattice quadruplet approximation’. In: *Metallurgical and Materials Transactions A* 32.6 (2001), pp. 1409–1416.
- [25] Mats Hillert, Bo Jansson, Bo Sundman and John Ågren. ‘A two-sublattice model for molten solutions with different tendency for ionization’. In: *Metallurgical Transactions A* 16.2 (1985), pp. 261–266. DOI: 10.1007/bf02816052.
- [26] Rainer Schmid and Y.Austin Chang. ‘A thermodynamic study on an associated solution model for liquid alloys’. In: *Calphad* 9.4 (1985), pp. 363–382. DOI: 10.1016/0364-5916(85)90004-5.
- [27] John Gisby, Pekka Taskinen, Jouni Pihlasalo, Zushu Li, Mark Tyrer, Jonathan Pearce, Katri Avarmaa, Peter Björklund, Hugh Davies, Mikko Korpi, Susan Martin, Lauri Pesonen and Jim Robinson. ‘MTDATA and the Prediction of Phase Equilibria in Oxide Systems: 30 Years of Industrial Collaboration’. In: *Metallurgical and Materials Transactions B* 48.1 (2017), pp. 91–98. DOI: 10.1007/s11663-016-0811-x.
- [28] J-O Andersson, Thomas Helander, Lars Höglund, Pingfang Shi and Bo Sundman. ‘Thermo-Calc and DICTRA, computational tools for materials science’. In: *Calphad* 26.2 (2002), pp. 273–312. DOI: 10.1016/S0364-5916(02)00037-8.

- [29] C. W. Bale, E. Bélisle, P. Chartrand, S. A. Dechterov, G. Eriksson, A. E. Gheribi, K. Hack, I. H. Jung, Y. B. Kang, J. Melançon, A. D. Pelton, S. Petersen, C. Robelin, J. Sangster, P. Spencer and M. A. Van Ende. ‘FactSage thermochemical software and databases, 2010-2016’. In: *Calphad* 54 (2016), pp. 35–53. DOI: 10.1016/j.calphad.2016.05.002.
- [30] M. N. De Noirlfontaine, S. Tusseau-Nenez, C. Girod-Labianca and V. Pontikis. ‘CALPHAD formalism for Portland clinker: Thermodynamic models and databases’. In: *Journal of Materials Science* 47.3 (2012), pp. 1471–1479. DOI: 10.1007/s10853-011-5932-7.
- [31] Theodore M. Besmann and Karl E. Spear. ‘Thermochemical Modelling of Oxide Glasses’. In: *Journal of the American Ceramic Society* 85.12 (2002), pp. 2887–2894. DOI: 10.1111/j.1151-2916.2002.tb00552.x.
- [32] S. L. Chen, S. Daniel, F. Zhang, Y. A. Chang, X. Y. Yan, F. Y. Xie, R. Schmid-Fetzer and W. A. Oates. ‘The PANDAT software package and its applications’. In: *Calphad: Computer Coupling of Phase Diagrams and Thermochemistry* 26.2 (2002), pp. 175–188. DOI: 10.1016/s0364-5916(02)00034-2.
- [33] Brandon Bocklund, Richard Otis, Aleksei Egorov, Abdulmonem Obaied, Irina Roslyakova and Zi-Kui Liu. ‘ESPEI for efficient thermodynamic database development, modification, and uncertainty quantification: application to Cu-Mg’. In: *MRS Communications* 9.2 (2019), pp. 618–627. DOI: 10.1557/mrc.2019.59.
- [34] Arthur D Pelton and Youn-Bae Kang. ‘Modeling short-range ordering in solutions’. In: *International Journal of Materials Research* 98.10 (2007), pp. 907–917.
- [35] Mats Hillert, Bo Sundman and Xizhen Wang. ‘An assessment of the CaO-SiO₂ system’. In: *Metallurgical Transactions B* 21.2 (1990), pp. 303–312. DOI: 10.1007/bf02664198.
- [36] Otto Redlich and A T Kister. ‘Algebraic Representation of Thermodynamic Properties and the Classification of Solutions’. In: *Industrial & Engineering Chemistry* 40.2 (1948), pp. 345–348. DOI: 10.1021/ie50458a036.
- [37] Mats Hillert. ‘Partial Gibbs energies from Redlich-Kister polynomials’. In: *Thermochimica Acta* 129.1 (1988), pp. 71–75. DOI: 10.1016/0040-6031(88)87198-3.
- [38] Yves-Marie Muggianu, Michèle Gambino and Jean-Pierre Bros. ‘Enthalpies de formation des alliages liquides bismuth-étain-gallium à 723 K. Choix une représentation analytique des grandeurs excès intégrales et partielles de mélange’. In: *Jurnal de Chimie Physique* 72 (1975), pp. 83–88. DOI: 10.1051/jcp/1975720083.
- [39] Arthur D. Pelton. ‘A general “geometric” thermodynamic model for multicomponent solutions’. In: *Calphad* 25.2 (2001), pp. 319–328. DOI: 10.1016/S0364-5916(01)00052-9.

- [40] Andreas Janz and Rainer Schmid-Fetzer. ‘Impact of ternary parameters’. In: *Calphad* 29.1 (2005), pp. 37–39. DOI: [10.1016/j.calphad.2005.01.003](https://doi.org/10.1016/j.calphad.2005.01.003).
- [41] Bo Sundman, Ursula R. Kattner, Mats Hillert, Malin Selleby, John Ågren, Sedigheh Bigdeli, Qing Chen, Alan Dinsdale, Bengt Hallstedt, Alexandra Khvan, Huahai Mao and Richard Otis. ‘A method for handling the extrapolation of solid crystalline phases to temperatures far above their melting point’. In: *Calphad* 68 (2020), p. 101737. DOI: [10.1016/j.calphad.2020.101737](https://doi.org/10.1016/j.calphad.2020.101737).
- [42] Mats Hillert and Magnus Jarl. ‘A model for alloying in ferromagnetic metals’. In: *Calphad* 2.3 (1978), pp. 227–238. DOI: [10.1016/0364-5916\(78\)90011-1](https://doi.org/10.1016/0364-5916(78)90011-1).
- [43] R.J. Weiss and K.J. Tauer. ‘Components of the Thermodynamic Functions of Iron’. In: *Physical Review* 102.6 (1956), pp. 1490–1495. DOI: [10.1103/PhysRev.102.1490](https://doi.org/10.1103/PhysRev.102.1490).
- [44] Wei Xiong, Qing Chen, Pavel A. Korzhavyi and Malin Selleby. ‘An improved magnetic model for thermodynamic modeling’. In: *Calphad* 39 (2012), pp. 11–20. DOI: [10.1016/j.calphad.2012.07.002](https://doi.org/10.1016/j.calphad.2012.07.002).

CHAPTER
FOUR

OVERVIEW OF THERMODYNAMIC FITTING

Part of this chapter has been submitted as a journal article titled “CaO-SiO₂ Assessment: 3rd generation modelling of thermodynamic properties”.

There are a variety of phases to be dealt with when producing a multi-component database the CaO-SiO₂-Al₂O₃-Fe-O-MgO which will contain information on the solid and melts of the 4 major clinker phases: C₃S, C₂S, C₃A and C₄AF.

It is nearly impossible and undesirable to start modelling the multi-component system directly from the quint-ternary, as each component exists to form a mixture with another component or set of components. To model these individual interactions and melts, it is therefore favourable to start from the lowest complexity mixtures. This challenge scales significantly by the number of components within the database. For example, the oxide CaO can be modelled from the elemental components Ca-O, which is often how the metals industry models such systems. In the present work, this is avoided by assuming Ca only exists as CaO due to being present in oxidising conditions. Next, SiO₂ is added, which results in the CaO-SiO₂ system. With this binary system, there are now solid compounds and a binary melt phase to model. When Al₂O₃ is added, two more binary systems have to be modelled (Al₂O₃-SiO₂ and CaO-Al₂O₃), all with their own compounds and melt phases. Thus adding a single component to a 2-component system, results in the modelling of 2 additional binary systems and 1 higher-order ternary system, with these new systems all having their own parameter sets. This step-by-step approach, starting from the least complexity is known as the CALPHAD approach.

The next section will introduce the CALPHAD approach which is employed in almost all thermodynamic assessments and form the basis of the thermodynamic approach used in the present work. A key part of this approach is the evaluation and assessment of the available thermodynamic data, so the remainder of this chapter will discuss the importance of evaluating data including uncertainties as well as the approach to fitting thermodynamic data that was developed in this work.

4.1 CALPHAD approach

CALPHAD which stands for CALculation of PHAse Diagrams is a book, journal, a conference, and most importantly an approach which was developed in 1970 by Larry Kaufman [1]. It enables the development of thermodynamic databases through the calculation of phase diagrams. It relies on the idea that phase diagrams are a sum of thermodynamic properties within a given system, so to calculate a full phase diagram, one must start from the individual thermodynamic properties. The approach can be outlined as follows:

- Collect and review all available thermodynamic data including experimental and DFT measurements.
- Select appropriate models to describe the Gibbs free energy of each phase within the system (this was discussed in detail in the previous chapter).
- Optimize the adjustable parameters of the chosen model to the selected thermodynamic data.
- Recalculate the phase diagram and calculate all available thermodynamic information on the system.

In summary, this approach starts from individual phases and combines these to produce and calculate systems with multiple phases. This step-by-step approach for a given system is known as a “CALPHAD assessment” in the literature. The CALPHAD approach started from the need for database development to optimise the production of alloys within the metals industry and has proven very successful in the development of metal atomic databases for a variety of industrial applications. CALPHAD research has also helped to develop the gathering and measurement of thermodynamic data via experimental methods or from first principles i.e. DFT. Additionally, dedicated software has been developed to aid in producing CALPHAD assessments as well as to carry out phase diagrams or equilibrium calculations. This software includes Thermo-calc [2], PANDAT [3], FACTSAGE [4] and ESPEI [5].

4.2 Uncertainty in literature measurements

The CALPHAD approach starts with a thorough literature review of the experimental data which includes a variety of measurements and DFT calculations. This is often the key part of the CALPHAD approach for database development as it is carried forward to the other steps and therefore forms the basis of all the models in the successive steps. Reviewing the literature is not as simple as collecting all data but entails the most important aspect/skill of the approach which is the evaluation of the literature. This involves

assigning uncertainties to the measurements, which is easy if you assume no flaws in experimental techniques, as in this case the authors' uncertainties can be taken; however, it is more common to see a variety of results in the same measurement, and in this scenario, uncertainties have to be carefully adjusted so that all measurements are fit to the models so that the phase of interest is described as it behaves. This often results in rejecting data that are clear outliers or accepting the results of one author over the results of another.

This description of the literature review/evaluation is often a subjective exercise, and it is often the case in the CALPHAD approach to use the experience of the modeller. However, more objective approaches can be taken which use mathematical tools. These tools are used in the present work to develop state-of-the-art and robust fitting methodologies, which are explained in the next section.

4.3 Fitting methodology

This section outlines the different fitting methodologies used in this project to fit the 3rd generation CALPHAD function and the associate model including solid solutions via the CEF model. For the 3rd generation function, a non-linear least squares approach is utilised. Whilst a Bayesian approach was studied in this work, it was not fully developed, but will be discussed in this section. For the fitting of the associates model, an automated algorithm that was developed in this work, is presented and discussed.

4.3.1 Stoichiometric and end-member fitting

Faced with this diversity of data, a holistic approach is taken to optimise all model parameters simultaneously to all available experimental data. For the stoichiometric phases, a custom Python code was written, which takes as its input, experimental data in its original reported units to minimise transcription errors. This is then transformed into standardised units and constraints to carry out a non-linear least-squares regression. All experimental conditions and observations/measurements can have uncertainties attached, and these uncertainties are propagated through to the final uncertainty estimate for that measurement.

For example, consider a single experimental measurement enumerated by α for a thermodynamic property (e.g., enthalpy of reaction, heat capacity), $y_{\text{obs},\alpha}$, with estimated measurement uncertainty $\sigma_{y,\alpha}$. This is observed at experimental conditions (i.e., temperature and pressure), $\vec{x}_{\text{obs},\alpha}$, which may also have an associated uncertainty $\vec{\sigma}_{x,\alpha}$. The current predicted model value is given by $y(\vec{c}, \vec{x}_{\text{obs},\alpha})$ where \vec{c} are the coefficients being fit. The reduced error, e_α , is then given by the following expression,

$$e_\alpha(\vec{c}) = \sigma_\alpha^{-2} (y_{\text{obs},\alpha} - y(\vec{c}, \vec{x}_{\text{obs},\alpha}))^2, \quad (4.3.1)$$

where the total uncertainty σ_α , assuming no correlations between variables and Gaussian

distributed noise, is given from the standard expression for uncertainty propagation,

$$\sigma_\alpha = \sqrt{\sigma_{y,\alpha}^2 + \sum_i \sigma_{x_i,\alpha}^2 \left(\frac{\partial y}{\partial x_i} \right)^2}. \quad (4.3.2)$$

The uncertainty estimates on the observed value σ_y typically account for all sources of uncertainty in the experimental conditions, $\vec{\sigma}_x$; however, transition temperatures are set up in the fitting framework as reactions with an “observed” Gibbs free energy change of zero. It is challenging to specify the uncertainty in the free energy; however, assigning uncertainty to the transition temperature is much more natural and facilitated by this approach.

In general, the values of the uncertainties are the subject of much debate in thermodynamic modelling. Although they are absolute measures, the fitting process only considers their relative magnitude. In an attempt to reduce human bias, the estimation of the uncertainties of each dataset is optimised deterministically. In the first instance, the author’s stated uncertainties for the experimental measurement are entered. After an initial fit, the deviation between the model predictions and the experimental measurements is used to scale the uncertainty estimates. The error limits suggested by Haas et al. [6] are employed, where the uncertainties are adjusted to keep 95% of the data within 2σ (standard deviations) of the final fit and no more than a 1/3 of data outside 1σ , to prevent over and under weighting of datasets. This method is a deterministic way of estimating uncertainty where there is conflicting data; however, where there is no conflicting data, the uncertainty estimates converge to zero. This is not a problem, but simply an indication that there is only a single source for this thermodynamic information. The approach taken here to determine the uncertainties has been discussed in the literature [7]; however, there is no solid consensus on the best approach yet. The simple approach used here still requires that data which is unphysical or seriously conflicting is excluded entirely as it can move the initial fit too far from the consensus fit, thus resulting in a lack of convergence. But even with this limitation, this approach applied here is a powerful method that allows the corroboration of results from separate authors and techniques. To provide an initial estimate of the coefficients for the global optimisation, individual phases are added to the optimisation sequentially as determined by the required data dependencies before a global optimisation is carried out. The underlying minimiser used is the COIN-OR IP-Opt solver [8] and all derivatives required for the minimisation, uncertainty propagation, and thermodynamic functions are generated using a custom Computer Algebra System (CAS), with symbolic differentiation. This allows arbitrary thermodynamic functions to be fit with little work and facilitated early comparisons with Debye functions, as well as transformations into other thermodynamic calculation software.

Bayesian Approach

The Bayesian approach carried out in this work, was based on the work carried out by Noah et al. [9]. In this approach, the objective function is based on Bayes' Thereom.

$$P(\theta|D, M) = \frac{P(D|\theta, M)P(\theta|M)}{P(D|M)}, \quad (4.3.3)$$

where $P(\theta|D, M)$ is the probability density function (“Prosterior Distribution”) for a model M with parameters θ against some data D . $P(D|\theta, M)$ is the conditional probability that the model M with parameters θ fits the data D , also known as the “Likelihood”. $P(\theta|M)$ is known as the “priors”, which are previous knowledge of the parameters e.g. bounds. Finally, $P(D|M)$ is the evidence, that the model generates the data, also known as the “marginal Likelihood”. The biggest difference between this approach, against the least squares approach (which is a frequentist approach), is that the data and the model are assumed to be random variables, and the probability the data fits the model is what is determined. This allows us to get a probability distribution (prosterior) of model parameters for the given data. More details on this approach can be found in Ref [9].

The benefit of this approach is that the confidence of fitted model parameters in relation to the experimental data can be determined, which in effect allows the determination of the confidence of the data. This confidence is the uncertainty of the experimental data against the model parameters, which is deterministically calculated in the least squares approach. In summary, with this approach, the appropriate uncertainties on each experimental point can automatically be determined for a given model. This approach can also be used to test and select models for a given dataset [5, 7].

The limitation of this approach is the computational cost of using a Monte Carlo or nested sampler to minimise the likelihood. Simple examples such as those discussed by Noah et al. [9] can be completed with great success; however, there is a great cost when scaling up the modelling with a large amount of data and many more compounds such as in the present work. It is for this reason, the Bayesian approach was not developed further and instead, the gradient descent approach described above was used. This resulted in quick minimisations of the objective function for the scale of data and compounds in the present work.

4.3.2 Solution phase fitting

When faced with the task of modelling the liquid, there are an enormous number of choices that can be made. Once an appropriate sub-lattice has been chosen to represent the melt of the system and a model has been chosen for the melt, only the ideal interactions of the species on the sublattice are accounted for, this is often not enough to fit the experimental phase diagram data and excess terms have to be added, these excess models are described in detail in section 3.2.3. The difficulty arises in which terms and between

which species are to be used. Focusing on the associates model, the choice remains on which Q-species associates to include, in addition to the arbitrarily large number of possible R-K terms between the associates. The choice of which R-K terms and associates to include follows some basic rules. The minimum number of terms required to gain a good fit is preferable as it simplifies interpretation and extension. In addition, lower-order interaction terms, i.e., small k , are preferred over higher-order terms as they are less likely to induce spurious features. Finally, the values of the coefficients are also bounded by experience. For example, the term $s_{\alpha,\beta,k}$ directly affects the entropy of the phase at absolute zero, thus its use can introduce a thermodynamic inconsistency and odd behaviour at low temperatures. While liquid phases in many applications are rarely extrapolated to very low temperatures this may happen numerically during the solution to equilibrium leading to spurious re-entrant liquid phases. In addition, the $s_{\alpha,\beta,k}$ term becomes more important in the free energy at high temperatures, thus positive values may lead to fictitious immiscibility gaps appearing. Even with this guidance, assessments typically proceed by trial and error, with researchers adding terms to address deficiencies in the calculated diagram after successive calculations. While experts can produce high-quality diagrams this way in short order, it is not deterministic, and it is difficult to know if the optimal choice has been made. Furthermore, for higher-order fitting to ternary systems such as CaO-Al₂O₃-SiO₂ or CaO-MgO-SiO₂ the problem of term selection and optimisation becomes factorially harder.

Automatic approach

To avoid the essential requirement of expert knowledge or “trial and error”, it is beneficial to develop a methodology that gives a better understanding of how different terms affect the model of the system. As part of the present work, an automatic mathematical optimisation approach was developed. This approach tests a variety of terms that could be added and selects the best ones, which is essential to avoid subjective modelling, as a better model may be easily overlooked by traditional methods. The fundamental aspect to this approach is the Akaike Information criterion which is used to test and select the terms as well as to prevent overfitting. The objective function that is optimised as part of this approach is the corrected Akaike information criteria,

$$AiCc = 2k - 2\ln(L) + (2k^2 + 2k)/(n - k - 1), \quad (4.3.4)$$

where AiCc the corrected Akaike information criteria, k is the number of parameters, n is the number of experimental data points, and L is the maximum of the likelihood function when the parameters are optimised to fit the experimental data. The log-likelihood is the sum of the error terms in Eqn. (4.3.1). The corrected equation is used to avoid overfitting in cases where the number of samples is sparse. Using the AICc, the model with the lowest score is the model that fits the data the best when traded against the complexity

of the model. This approach is entirely inspired by ESPEI which is used by others for thermochemical data fitting (i.e. stoichiometric solids). To find the globally optimal parameterisation according to (4.3.4) would require optimising all possible model variations and their coefficients against the experimental dataset to determine their likelihoods, before ranking them by (4.3.4). This is computationally infeasible at this time as it's a factorially hard problem and the optimisation in this system takes minutes per parameterisation to complete; however, a model with a low number of terms is the likely solution thus exploring the full range of possible parameterisations is not required. A gradient-descent type of approach from an initial zero-parameter model seems to be a sensible approach. While it might not guarantee a globally optimal solution, it will at least provide a local optimum which may be sufficient for practical purposes. Proving this is beyond the scope of this work and would require examination of the results across many thermodynamic assessments, so the results presented here will only be evaluated by comparing against previous parameterisations for this system later. The method proceeds from an initial parameterisation (i.e. an ideal system) in a stage-by-stage manner. At each stage, all zero interaction terms are individually enabled and optimised with the current set of enabled terms. All R-K terms up to an order of $k = 3$ are tested avoiding higher-order terms possible. At the end of each stage, the interaction term that is enabled permanently is the term that decreases the $AICc$ parameter the most. These stages continue until enabling any additional parameter no longer decreases the $AICc$. The optimisation of all interaction parameters against the experimental data is carried out using ESPEI, which uses a Bayesian approach that finds the maximum likelihood at each stage (more details on this technique can be found in [5]). A visualisation of the fitting algorithm described above is presented in Figure 4.1.

4.4 Overall approach with application to the CaO-MgO system.

Now that the fitting methodologies have been described for the solid phases, solid solution phases and melt phases. These methods are combined to produce a thermodynamic workflow from the solid fitting up to the melt phase and phase diagram:

- Gather and organise all experimental thermodynamic data for single phases, including experimental uncertainties.
- Organise all the compounds within the system of interest.
- Simultaneously fit all solid and pure liquid species within the system (adjusting uncertainties if necessary).
- Write out a phase model for the system of interest, at this stage the solid solutions are described using the CEF model, and an initial liquid associate model is

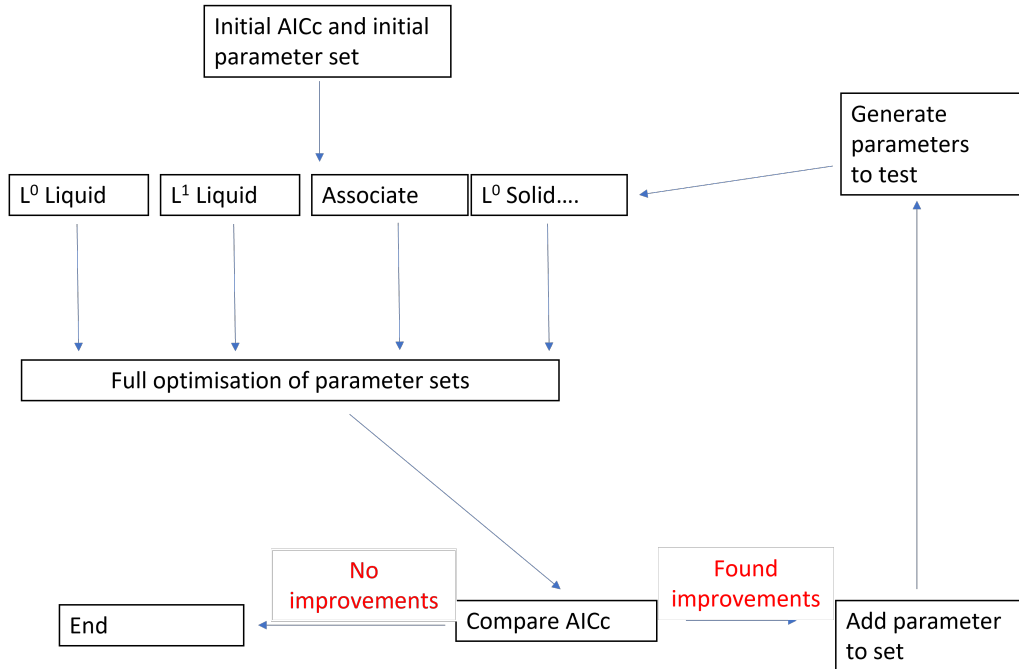


Figure 4.1: Flow diagram of the automatic fitting approach for the melt phase and solid solution. *AiCc* is the corrected Akaike information criterion which is used to determine how well the model parameters fit the experimental data, with a penalty for overfitting.

described.

- Generate possible parameters (associate, binary and ternary interactions).
- Test parameters against the phase diagram data using ESPEI's MCMC.
- Add parameters if they reduce the *AiCc* score.
- Output final phase diagram, in TDB format.

An example of the overall approach is presented through the modelling of the CaO-MgO system. This system was chosen due to its simplicity, only containing a solid solution of CaO and MgO. As per the approach, first, the single-phase data was gathered to fit the solid and liquid phases. Due to the simplicity of the system, the only species that required fitting at this stage were CaO and MgO (solid and liquid). Furthermore, the CaO solid and liquid phase was recently assessed by Deffrennes et al. [10] using the 3rd generation function and the two-state liquid model respectively. In this assessment, an exponent anharmonic term was used to avoid the use of near-zero values, which can cause issues in thermodynamic packages.

$$G_{solid} = H + 1.5R \sum \alpha_i \theta_i + 3RT \sum \alpha_i \ln(1 - \exp(\frac{-\theta_i}{T})) - \frac{a}{2}T^2 - \frac{\exp(b + cT)}{c^2} \quad (4.4.1)$$

The above equation is valid to the melting point of the oxide (3222 K and 3098 K for CaO and MgO respectively). Additionally, above the melting point a custom solid function

was used to fit the up to 6000 K,

$$G = H' - S'T + AT(1 - \ln(T)) + \frac{1}{2C^2(B + CT)}. \quad (4.4.2)$$

Similarly, the MgO solid was modelled using these functions. The full parameters for the CaO and MgO solid and liquid phases are presented in Table 4.1 and Table 4.2 respectively. Once the expressions for the solid and liquid phases were gathered, the monoxide

Table 4.1: Parameters for the solid MgO and CaO functions, according to Equation 4.4.1 and 4.4.2.

CaO(Solid)
$\alpha_1 = 0.9465361807, \theta_1 = 314.8272896$
$\alpha_2 = 0.05193351134, \theta_2 = 125.12812657$
$\alpha_3 = 1.001522312, \theta_3 = 598.37301449$
$H = -652625.815$
$a = -0.00174450265, b = -14.85294988, c = 0.00298095$
$H' = -727925.76111$
$S' = -486.19356495 A = 80.5, B = -281.8126077, C = 0.09083109344$
MgO(Solid)
$\alpha_1 = 1.04609077, \theta_1 = 475.5615692$
$\alpha_2 = 0.831024371, \theta_2 = 775.50257671$
$\alpha_3 = 0.122996143, \theta_3 = 259.55358863$
$H = -621095.005$
$a = -0.00184931485, b = -15.81600803, c = 0.00327218470$
$H' = -683262.3811$
$S' = -467.52323656 A = 76.5, B = -70.973453808, C = 0.025713125847$

Table 4.2: Parameters for the liquid MgO and CaO functions, according to Equation 3.1.9.

CaO(Liquid)
$\alpha_1 = 1.002336891, \theta_1 = 629.27558$
$\alpha_2 = 0.9976541127, \theta_2 = 234.0578$
$H = -652625.815$
$a = -0.00184186045$
G^{diff}
$A = 2*63019.5887, B = 2*-6.2358, C = 2*-0.997138715$
MgO(Liquid)
$\alpha_1 = 1.066915801, \theta_1 = 802.97139$
$\alpha_2 = 0.9330752028, \theta_2 = 316.655056$
$H = -583817.9035$
$a = -0.002702806$
G^{diff}
$A = 2*57951.4061, B = 2*-6.2358, C = 2*-0.62402962815$

solution was modelled using the sublattice (CaO, MgO). This gives the Gibbs energy ex-

pression for the monoxide solution as functions of the solid end-members CaO and MgO

$$G_{CaO}^{Monoxide} = G_{CaO}^{solid} \quad (4.4.3)$$

$$G_{MgO}^{Monoxide} = G_{MgO}^{solid} \quad (4.4.4)$$

At this point, this results in an ideally mixed phase diagram that can be seen in Fig. 4.2. The ideal mixed phase diagram does not reproduce the experimental data. To overcome this issue, terms are added using the automatic approach to fit the phase diagram data. The final optimised phase diagram is presented in Fig. 4.3 and compared against the assessment of Hillert and Wang [11].

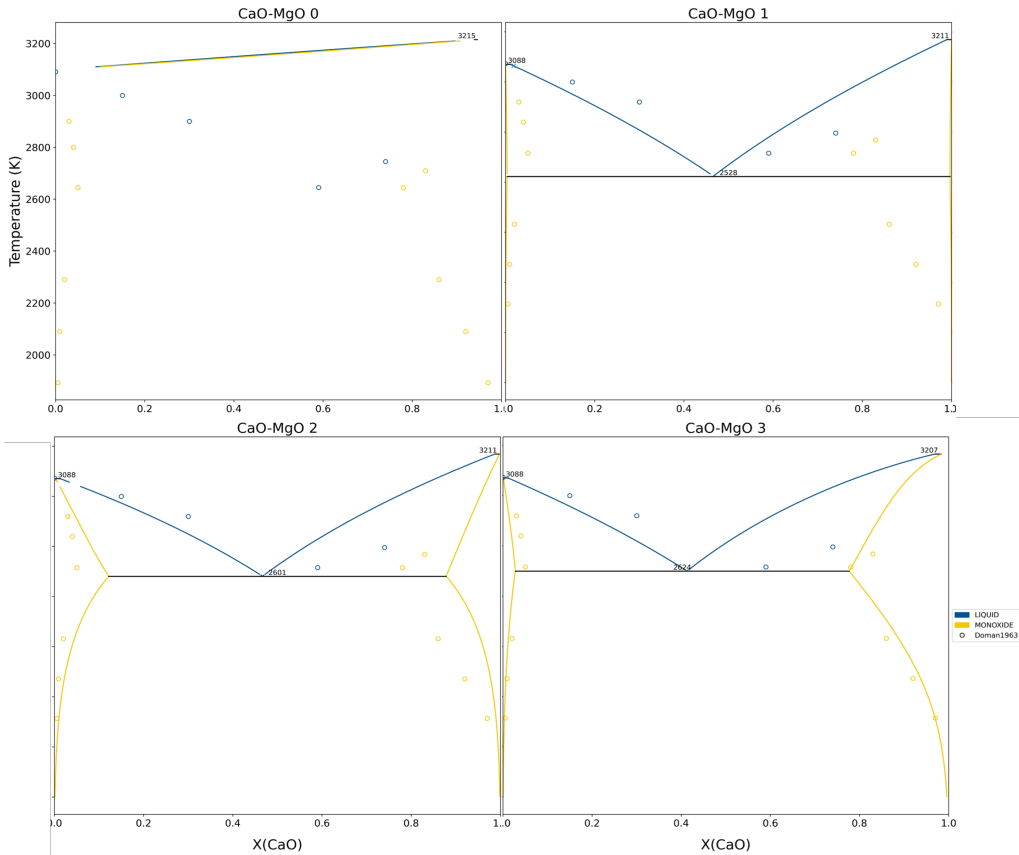


Figure 4.2: Sequential CaO-MgO phase diagrams, optimised using the developed automatic approach. The first phase diagram is ideally-mixed, with zero terms. Monoxide terms were added over melt phase terms in the subsequent fits, as they reduced the AiCc score the most.

In the resultant phase diagram, the approach chose one term for the melt phase and three terms for the solid solution phase, with the full melt model for the CaO-MgO system presented in Table 4.3. A direct comparison with the ionic two-sublattice model can be made using the work of Hillert and Wang [11], who achieved an equally well-fit diagram but used an additional parameter (two terms in the melt and three terms in the solid solution phase).

The difference in parameter sets is likely due to the tendency for the fitting approach to utilise T terms in the excess model. This can often model complex behaviours with a

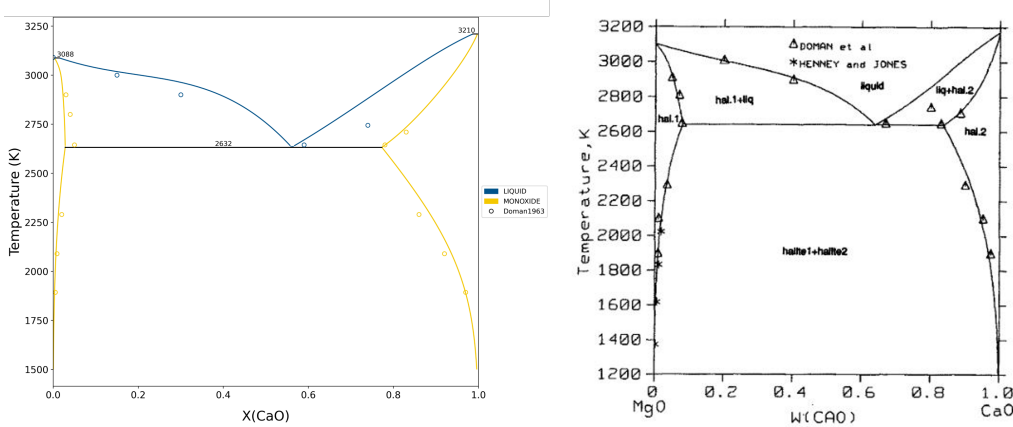


Figure 4.3: (left) Optimised phase diagram of the CaO-MgO from the present work the final term that was added was an L^1 for the melt phase. Results are compared against the phase diagram of Hillert and Wang (right).

Table 4.3: Resultant gibbs energy expression for the melt (labelled “liquid”) and the monoxide solid solution in CaO-MgO system.

Liquid(CaO,MgO)
$G_{CaO}^{Melt} = G_{CaO}^{Liquid}$
$G_{MgO}^{Melt} = G_{MgO}^{Liquid}$
Excess terms
$L^1(CaO, MgO) = -10.415 * T$
Monoxide(CaO,MgO)
$G_{CaO}^{Monoxide} = G_{CaO}^{Liquid}$
$G_{MgO}^{Monoxide} = G_{MgO}^{Liquid}$
Excess terms
$L^0(CaO, MgO) = 119445 - 24.2 * T$
$L^1(CaO, MgO) = -9.13 * T$

single term, but has the drawback of causing unintended features in the phase diagram. This is easily adjusted by penalising the addition of T terms, forcing them to be added only when necessary; however, in the CaO-MgO system, this is not an issue and the simplicity of the resultant model compared to Hillert and Wang is a success for the approach developed in this work.

4.4.1 Weighting of phase diagram data.

Important parameters that should be controlled when fitting the phase diagram are the weights applied to the experimental data. In ESPEI, each data point is assumed to have a residual with a Gaussian centred at zero, ($\mu = 0$), with a standard deviation σ_i . This can be adjusted using the weight factor w_i (more details on this can be found in [5]),

$$p_i(D|\theta) \sim N(\mu = 0, \sigma = \frac{\sigma_i}{w_i}), \quad (4.4.5)$$

The weight factor is dependent on the phase diagram data and is directly inputted to the likelihood function that is used to fit the diagram. For phase diagram (ZPF) data (which is expressed as Gibbs free energy driving forces), the default standard deviation is 1000 J/mol, this is a reasonable starting value but may be higher than the uncertainty on the data. Increasing the weight factor, increases the likelihood of residuals thus affecting the AiCc score which in turn affects the type, amount and value of parameters chosen in the approach. It is therefore important to adjust this weight factor, to ensure a good fit. A low weight results in underfitting (the phase diagram data is not well reproduced) and a high weight results in overfitting of the data (inserting more parameters than necessary to reproduce the phase diagram).

In the first instance, it is always suggested to input the experimental uncertainty; however, this is not always true (the reported uncertainty may be different to the actual uncertainty when fitting multiple datasets). Additionally, it is not intuitive to quantify uncertainty in the phase diagram as driving forces. This means, different weight factors have to be tested to get a mix of a good fit with the least complexity, whilst also trying to maintain the uncertainty on the phase diagram data.

Figure 4.4 shows the results of the effects of different weights, from these results there is a point of diminishing returns, where increasing the weight, will add parameters and reduce the AiCc score resulting in a mathematically 'better' fit; however, after a

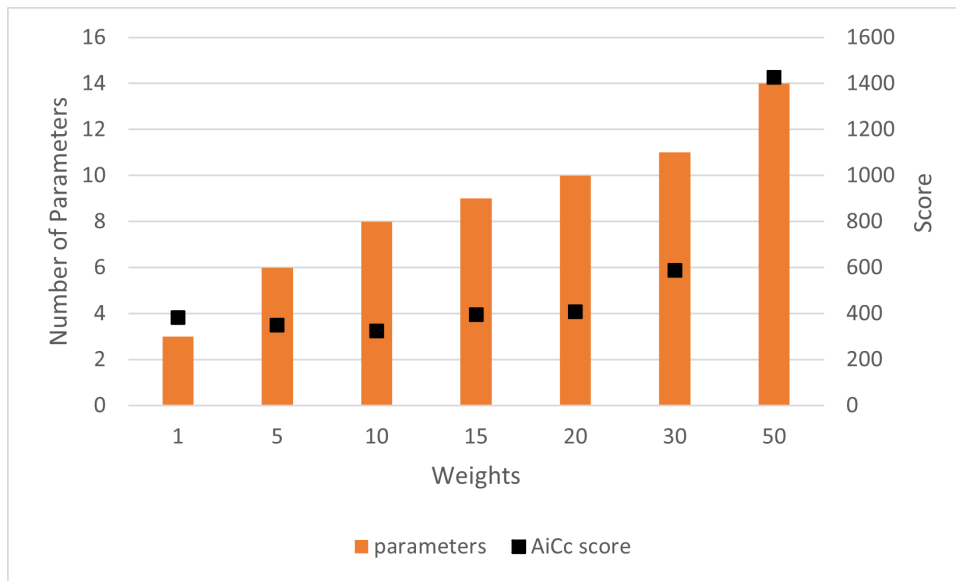


Figure 4.4: Graph of the number of parameters added with changing the weight factor of the phase diagram data, also plotted is the resultant AiCc score.

weight factor of 15, the number of parameters added reduces greatly but the AiCc score increases greatly, which could mean a poorer fit of the phase diagram as well as greater penalization of adding more parameters in the AiCc score (which is a feature of the AiCc score equation to prevent overfitting). Therefore, for this particular system, a max weight factor of 10 is the ideal balance of fitting results and complexity of the resulting model. Moving forward for the other systems, a weight factor of 10 will be used as a starting

point, although this is dependent on the quality of the data, number of points and reported uncertainty of the data and is adjusted on a per-system basis, where necessary.

4.5 Conclusions

In this chapter, the CALPHAD approach and its benefits when developing thermodynamic databases was discussed. It provides a guideline to develop thermodynamic databases from the ground up to accurately model higher-order interactions. Part of the CALPHAD approach is based on experience and the modeller's subjectivity, often in the most important parts of the modelling stages. In the first step of evaluating the literature, the uncertainties applied, have a major effect on the Gibbs free energy expressions for the phases and in this effort, the least squares simultaneously fitting approach was developed to continuously test the uncertainties to provide ideal fits for the single phases. Once that is achieved there is an issue in the melt or solid solutions phases, which is the choice in excess terms, which is a major contributor to the phase diagram re-calculation. At this stage, an automatic fitting approach was developed to overcome the subjective modelling of the phase diagram. This approach progressively tests and adds parameters, theoretically resulting in an optimal phase diagram with the least number of parameters.

Combining these two methods, results in a robust fitting methodology that envisions the CALPHAD approach but is also mathematically justified in achieving optimal results. An example of the approach was shown in this chapter on the CaO-MgO system and showed great success. In the following chapter, the results of the developed approach will be shown in the most important binary system: CaO-SiO₂, which will form part of the main ternary system CaO-Al₂O₃-SiO₂.

4.6 References

- [1] P.J. Spencer. ‘A brief history of CALPHAD’. In: *Calphad* 32.1 (2008), pp. 1–8. DOI: [10.1016/j.calphad.2007.10.001](https://doi.org/10.1016/j.calphad.2007.10.001).
- [2] J-O Andersson, Thomas Helander, Lars Höglund, Pingfang Shi and Bo Sundman. ‘Thermo-Calc and DICTRA, computational tools for materials science’. In: *Calphad* 26.2 (2002), pp. 273–312. DOI: [10.1016/S0364-5916\(02\)00037-8](https://doi.org/10.1016/S0364-5916(02)00037-8).
- [3] S. L. Chen, S. Daniel, F. Zhang, Y. A. Chang, X. Y. Yan, F. Y. Xie, R. Schmid-Fetzer and W. A. Oates. ‘The PANDAT software package and its applications’. In: *Calphad: Computer Coupling of Phase Diagrams and Thermochemistry* 26.2 (2002), pp. 175–188. DOI: [10.1016/s0364-5916\(02\)00034-2](https://doi.org/10.1016/s0364-5916(02)00034-2).

- [4] C. W. Bale, E. Bélisle, P. Chartrand, S. A. Dechterov, G. Eriksson, A. E. Gheribi, K. Hack, I. H. Jung, Y. B. Kang, J. Melançon, A. D. Pelton, S. Petersen, C. Robelin, J. Sangster, P. Spencer and M. A. Van Ende. ‘FactSage thermochemical software and databases, 2010-2016’. In: *Calphad* 54 (2016), pp. 35–53. DOI: [10.1016/j.calphad.2016.05.002](https://doi.org/10.1016/j.calphad.2016.05.002).
- [5] Brandon Bocklund, Richard Otis, Aleksei Egorov, Abdulmonem Obaied, Irina Roslyakova and Zi-Kui Liu. ‘ESPEI for efficient thermodynamic database development, modification, and uncertainty quantification: application to Cu-Mg’. In: *MRS Communications* 9.2 (2019), pp. 618–627. DOI: [10.1557/mrc.2019.59](https://doi.org/10.1557/mrc.2019.59).
- [6] John L. Haas Jr., Glipin R. Robinson Jr. and Bruce S. Hemingway. ‘Thermodynamic tabulations for selected phases in the system CaO-Al₂O₃-SiO₂-H₂ at 1 atm between 273.15 and 1800 K’. In: *Journal of Physical and Chemical Reference Data* 10.3 (1981), pp. 575–670. DOI: [10.1063/1.555645](https://doi.org/10.1063/1.555645).
- [7] S. Zomorodpoosh, B. Bocklund, A. Obaied, R. Otis, Z.-K. Liu and I. Roslyakova. ‘Statistical approach for automated weighting of datasets: Application to heat capacity data’. In: *Calphad* 71 (2020), p. 101994. DOI: [10.1016/j.calphad.2020.101994](https://doi.org/10.1016/j.calphad.2020.101994).
- [8] Andreas Wächter and Lorenz T Biegler. ‘On the implementation of an interior-point filter line-search algorithm for large-scale nonlinear programming’. In: *Mathematical Programming* 106.1 (2006), pp. 25–57. DOI: [10.1007/s10107-004-0559-y](https://doi.org/10.1007/s10107-004-0559-y).
- [9] ‘Bayesian strategies for uncertainty quantification of the thermodynamic properties of materials’. In: *International Journal of Engineering Science* 142 (2019), pp. 74–93. DOI: [10.1016/j.ijengsci.2019.05.011](https://doi.org/10.1016/j.ijengsci.2019.05.011).
- [10] Guillaume Deffrennes, Noël Jakse, Cecilia M.S. Alvares, Ioana Nuta, Alain Pasturel, Alexandra Khvan and Alexander Pisch. ‘Thermodynamic modelling of the Ca-O system including 3rd generation description of CaO and CaO₂’. In: *Calphad* 69 (2020), p. 101764. DOI: [10.1016/j.calphad.2020.101764](https://doi.org/10.1016/j.calphad.2020.101764).
- [11] ‘Thermodynamic calculation of the CaO-MgO system’. In: *Calphad* 13.3 (1989), pp. 267–271. DOI: [10.1016/0364-5916\(89\)90006-0](https://doi.org/10.1016/0364-5916(89)90006-0).

CHAPTER
FIVE

MODELLING THE CAO-SIO₂ SYSTEM

This chapter has been submitted as a journal article titled “CaO-SiO₂ Assessment: 3rd generation modelling of thermodynamic properties”. The author of this thesis was the primary author of the journal article and completed all the thermodynamic modelling. Dr Alexander Pisch carried out the DFT calculations and Chancel Malawala carried out the relative enthalpy measurements. Their respective methods are not discussed here, (more information on this can be found in the appended article) however for the benefit of the discussion, the experimental results will be presented in this chapter.

5.1 Introduction

Looking at ordinary Portland cement (OPC) clinker, the major cementitious constituents are alite (Ca_3SiO_5 with dissolved minor elements) and belite (Ca_2SiO_4 with dissolved minor elements). This leads to the CaO-SiO₂ binary system being one of the most critical assessments, as it contains the alite and belite phases. The solid compounds contained within this system include the four polymorphs of C₂S (β , γ , α' and α), three polymorphs of C₃S (triclinic, monoclinic, and rhombohedral), the two polymorphs of CS (wollastonite and pseudo-wollastonite) and finally C₃S₂ (rankinite) which is important for solidia [1] type cement (inorganic binders hardening by reaction with CO₂). Fortunately, cement production is carried out in oxidising conditions, thus for the CaO-SiO₂ system there is no need to model the metallic sub-system and oxygen as a separate component.

The first comprehensive assessment and modelling of the thermodynamic properties of the solid compounds in the CaO-SiO₂ system was carried out by Haas et al. [2]. The results of their study and the experimental data it reviews are often chosen as the basis of all modern assessments for the CaO-SiO₂ system. While seminal and largely correct, the study by Haas et al. contains typographical errors in the equations [3] which become obvious when comparing against the tabulated data. This, coupled with the availability of new experimental data justifies a review of the solids again. Commercial databases such as FACTSAGE [4] and SGTE [5] also contain extensive information for the calcium

silicates; however, recent advances in modelling, regression, and updates to the CaO [6] and SiO₂ [7] end-members have not yet been incorporated. Furthermore, a shortage of experimental data in the literature for high temperature calcium silicates, makes it harder for a complete and detailed model of this system. For example, it is often the case to only include the hatrurite high-temperature stable polymorph of C₃S but other meta-stable low-temperature polymorphs do exist and are very important for Portland cements [8]. Additionally, the C₃S₂ solid lacks thermodynamic data at higher temperatures, with data previously only available up to 300 K [9], making fits speculative. Likewise, the high-temperature polymorphs of C₂S: α and α' , lack data at low temperatures which was found to be essential in fitting the parameters to the new CALPHAD models and correctly calculating the phase diagram.

Previous assessments in the CaO-SiO₂ system have all used polynomial models to fit the experimental data, such as the popular Shomate [10] polynomials. This approach, although simple, is unreliable when extrapolating or interpolating far from experimental measurements. This makes connecting low and high-temperature data difficult; however, this is vital for cement which is produced at high temperatures but utilised/reacted closer to room temperature. In addition, there is a lot of data available at low temperatures for fitting, while high-temperature data is more limited, thus extrapolation is vital. As described in Section 4.4, the latest development in CALPHAD modelling attempts to overcome these issues through the use of a so-called 3rd generation approach which makes use of Einstein terms for the low-temperature data and one or more polynomial corrections to take into account the anharmonic contributions at high temperature (see Eqn. (3.1.5)). This combination yields a single function which can be used to model data over the full temperature range from 0 K to the melting point with no junction points, thanks to the Einstein model terms capturing the underlying vibrational nature of the internal energy.

The CaO-SiO₂ liquid phase has previously been modelled using a variety of models including the two-sublattice ionic model [11, 12], the modified quasi-chemical model [13, 14], the associates model [15, 16], and the cellular model [17]. The main difficulty within this system is the modelling of the miscibility gap in the silica-rich region which is important for the extension to higher-order systems. Many previous assessments overestimate the temperature at the onset of miscibility due to limitations in the model chosen. Regarding extensions to higher order systems, Pelton and Blander (modified quasi-chemical model) and Hillert et al. (two-sublattice) were able to extend their binary models to the CaO-FeO-SiO₂ and CaO-SiO₂-Al₂O₃ systems respectively, making their models promising choices for this system; however, in this work the associates model is employed as described in Barry et al. [15] but utilizing fewer parameters thanks to an information-theory led approach. The model for this binary system will be used to extend to the important cement system, CaO-Al₂O₃-SiO₂ in later work. To overcome, the lack of high temperature data for the C₂S polymorphs and C₃S₂, novel experiments and DFT calculations were carried out and added to the fitting procedure and modelling work.

5.2 Literature review of the solid phases

In the CaO-SiO₂ system, all solid compounds are considered stoichiometric; however, many of the stoichiometric phases have multiple polymorphs. For example, C₂S has 5 polymorphs: β -C₂S (which is a meta-stable, pressure-stabilized compound which appears in higher-order systems and real cement), γ -C₂S, α'_L -C₂S, α'_H -C₂S and α -C₂S. This section first considers each compound and its transitions before then considering the existing literature data used to fit the 3rd generation model described in the previous section. The structural properties of Ca₃SiO₅ are complex [8]. The available literature was reviewed by Regourd [18] and more recently by Dunstetter et al., [19]. Ca₃SiO₅ exists in seven polymorphic modifications but only the high-temperature rhombohedral structure is stable [20, 21]. The low-temperature triclinic modifications (designated TI, TII and TIII in the literature [20, 22]) and the intermediate monoclinic ones (designated MI and MII in the literature [21, 23, 24]) are all meta-stable but are important as they are observed in cement clinkers. All observed phase transformations are of the displacive type in which a small shift of atoms leads to orientation disorder between SiO₄ tetrahedral units and distorted CaO₆ polyhedra. Therefore, the observed heat of transitions, as measured by quantitative thermal analysis, are small [25]. In this assessment, the polymorphs of C₃S have been simplified to monoclinic, triclinic and rhombohedral, as this captures the fundamental structural changes where sufficient data exists to distinguish them in this system.

Calcium orthosilicate Ca₂SiO₄ exists in five modifications. The space groups, lattice parameters, and atomic positions of all modifications are known with precision thanks to a careful study by Mumme et al. [26] using high-temperature neutron diffraction combined with Rietveld analysis. The stable modification at room temperature, γ -Ca₂SiO₄ sometimes also called calcio-olivine, transforms to α'_L -Ca₂SiO₄ at 880°C [27]. This transformation is of the reconstructive type and accompanied by a considerable contraction of the cell volume [27]. Other transition temperatures for this have been reported in the literature. This is because the kinetics of this transformation is very sluggish and in addition, affected by a small solubility range of +0.4 wt % CaO on the lime-rich side and +0.2 wt % SiO₂ on the silica-rich side [27]. α'_L -Ca₂SiO₄ transforms into α'_H -Ca₂SiO₄ with increasing temperature. This transition is second order and of the displacive type [26]. Following this, α'_H -Ca₂SiO₄ transforms into the high temperature α -Ca₂SiO₄ modification above 1425°C [27] through a semi-reconstructive transition [26]. The fifth and last modification, β -Ca₂SiO₄ (larnite), is meta-stable at atmospheric pressure but can be fully stabilized by the addition of small amounts of minor elements (e.g. 0.4% of B₂O₃ [28]) or by quenching bulk sample from high temperature with a minimum particle size [27]. The α'_L - β transformation is of the displacive type which is kinetically favoured over the stable α'_L - γ transition. The metastable transition temperature was determined by dilatometry [27] and derived from an experimental p-T phase diagram [29]. The third compound considered here, Ca₃Si₂O₇, exists in two modifications: high-temperature rankinite [30] and

low-temperature kilchoanite [31] (sometimes called Z-Phase in the literature). The transition is irreversible for kinetic reasons and takes place in the temperature interval 954–1090°C [30]. Wollastonite CaSiO₃ exists in two general modifications with a series of derived superstructures due to modified stacking sequences. The low-temperature wollastonite compound [32] transforms into the pseudo-wollastonite modification [33–35] (sometimes also called cyclo-wollastonite in the literature).

The structural information of all compounds is summed up in Table 5.1. The available data on the phase transition temperatures and enthalpies are presented in Table 5.2.

Table 5.1: Table showing the structures of the compounds and their respective polymorphs within the CaO-SiO₂ system.

Compound	Designation	Space Group	Reference
Ca ₃ SiO ₅	T1	P-1	[20, 22]
	T2	-	[19, 25]
	T3	-	[19, 25]
	M1	Pc	[24]
	M2		[18, 19]
	M3	Cm (Am)	[23, 36]
Ca ₂ SiO ₄	R	R3m	[20, 21]
	γ (olivine)	Pnma	[26]
	β (larnite)	P21/c	[26]
	α' _H	Pna21	[26]
	α' _L	Pnma	[26]
Ca ₃ Si ₂ O ₇	α	P63/mmc	[26]
	kilchoanite	Ima2	[31]
	rankinite	P21/c	[30]
CaSiO ₃	wollastonite	P21/c	[32]
	pseudo-wollastonite	C21/c	[33]
		C-1	[34]

Heat capacity data for Ca₂SiO₄ β and γ were previously measured by Todd [38], King [9], and Grevel et al. [39], with these experiments being at low temperature thus allowing for the entropy at 298 K to be derived; however, no low-temperature data exists for the high-temperature polymorphs: α and α'. The relative enthalpy for the 4 polymorphs of Ca₂SiO₄ measured by Coughlin [37] is used to aid fitting of the C_p for the high-temperature polymorphs. Similarly, heats of formations at 298 K only exist for the low-temperature polymorphs [40, 41]. For the Ca₃SiO₅ solid, the heat capacity was also measured by Todd [38] and the relative enthalpy was measured by Gronow and Schwiete [42]. The heat of formation is often taken from the heat of decomposition as measured by Brunauer [43]. To overcome the lack of data surrounding the monoclinic and rhombohedral Ca₃SiO₅ polymorphs, each was given identical heat capacities derived from the triclinic form but are then individually corrected using their respective inversion temperatures and enthalpies as measured by Bigare et al. [8]. For Ca₃Si₂O₇ only the low-temperature heat capacity was measured by King [9]. The heat of formation measurement by Wilford [44] and EMF measurements by Benz and Wagner [45] are also used to calcu-

Table 5.2: Table showing the transition temperatures and enthalpies of the polymorphs the CaO-SiO₂ system.

Compound	Transition reaction	Transition temperature [°C]	Transition heat [kJ/mol]	Experimental technique
Ca ₃ SiO ₅	TI → TII	620	0.57	DTA [25]
	TII → TIII	920	0.96	DTA [25]
	TIII → MI	980	0.48	DTA [25]
	MI → MII	990	0.05	DTA [25]
	MII → R	1050	0.048	DTA [8, 25]
Ca ₂ SiO ₄	γ → α' _L	847	7.757-15.460 14.393	DTA [27] drop calorimetry [37]
	β → α' _L	711 680	13.020 1.439 1.841	DTA, at 0.34GPa [29] DTA [26] drop calorimetry [26]
	γ → β	711	1.780 4.678 4.48	DTA, at 0.34GPa [29] DTA [27] soln. calorimetry 20°C [28]
	α' _H → α	1425	11.250 0.720 13.305 14.184	DTA [27] DTA [27] drop calorimetry[37]
	Ca ₃ Si ₂ O ₇	kilch → rank	954-1090	[29]
	CaSiO ₃	woll → p-woll	1125	[35]

late the heat of formation and fix the absolute enthalpy; however, there is significant disagreement with the fit model around the Benz measurements so not all data was used [12]. The heat capacity of both polymorphs of CaSiO₃ was measured by Wagner [46] and the relative enthalpy for wollastonite was measured by Gronow [42], Courtial [47], and Pascal and Fiquet [48] for cyclov wollastonite. The heat of formation for both polymorphs was also measured by Charlu et al. [49].

The end-members in this system are the oxides CaO and SiO₂. CaO exists as a single polymorph which exists as a halite (rock salt) structure [50]. SiO₂ is more interesting as it exists as many structures in normal pressures: quartz, cristobalite and tridymite [51], with many more structures being observed at higher pressures [52]. Within the quartz and cristobalite structures, additional polymorphs have been observed with α-quartz, β-quartz, α-cristobalite and β-quartz. The thermodynamic properties of CaO and SiO₂ have been well studied [53, 54] and for the present work the latest assessments by Deffrennes et al. [6] (CaO) and Bajenova et al. [7] (SiO₂), was used without any need for corrections as they proved to be fully compatible with the present work. It is to be noted that in the SiO₂ assessment, tridymite was ignored as it was found not to be stable in the Si–O system [54], this differs from previous assessments which include the tridymite structure.

5.3 Literature review of the liquid phase.

The thermodynamic properties of the liquid end-members CaO and SiO₂ were recently assessed by Deffrennes et al. [6] and Bajenova et al. [7] respectively with a 3rd generation CALPHAD model, thus a reassessment of these is not required and instead

their expressions, which incorporate a two-state model for the liquid phase, are adopted here unmodified. The Phase Diagram for Ceramists [55] contains a complete study of the phase diagram of the CaO-SiO₂ system and lists the majority of the experimental liquidus points to be found for this system in the literature. Rankin and Wright [56] is the primary source and determined the melting points of C₂S and CS as well as the CS-C₃S₂ eutectic. However, corrections for the CaO side are required due to the dramatic change in the melting point of CaO. Modelling of the miscible region of the phase diagram was most recently investigated by Tehwey and Hess [57] with similar results from Greig [58]. It should also be noted that the activities of SiO₂ and CaO in the liquid phase of the CaO-SiO₂ system has been extensively studied in the range of 1773-1873 K through a variety of different techniques [59-62].

5.4 Methodology

The thermodynamic modelling of this system will follow the approaches described in the previous chapters. In the first instance, the solid phases were fit, with all the relevant data, including the new experimental data and DFT results gathered by colleagues at Grenoble. The experimental uncertainties were adjusted on the experimental data, to achieve a satisfactory fit as described in Section 4.4. To aid in the changing of these values, diagnostic plots were produced (an example of such a plot can be seen in Figure 5.1). The full experimental data fit, alongside their reported and fitted uncertainties are given in the Appendix of the submitted article. Unfortunately, this approach currently struggles to optimise miscibility gaps when the initial guess does not capture the experimental data points well. Thus, for this assessment the optimisation for the CaO-SiO₂ system is begun by including $h_{(CS,S,0)}$, $h_{(CS,S,1)}$, $h_{(CS,S,2)}$, $s_{(CS,S,0)}$, $s_{(CS,S,1)}$ and $s_{(CS,S,2)}$ with an initial hand-fit. Anecdotally, the automatic approach appears to function well in systems where there is no miscibility gap, and the issue appears to only be one of local/global convergence, thus it is expected to work with further improvements to ESPEI.

5.5 Results and Discussion

The following sections discuss the results of the experiments, fitting, and overall phase diagram in comparison to the literature.

5.5.1 Calorimetric measurements

The results of the heat content measurements for rankinite are summarised in Table 5.3. No experimental data exists in the literature on the heat capacity or heat content of rankinite at these high temperatures, thus this data is compared to the estimated data of Haas et al. [2] and the commercial FTOX database [4]. The estimated heat content

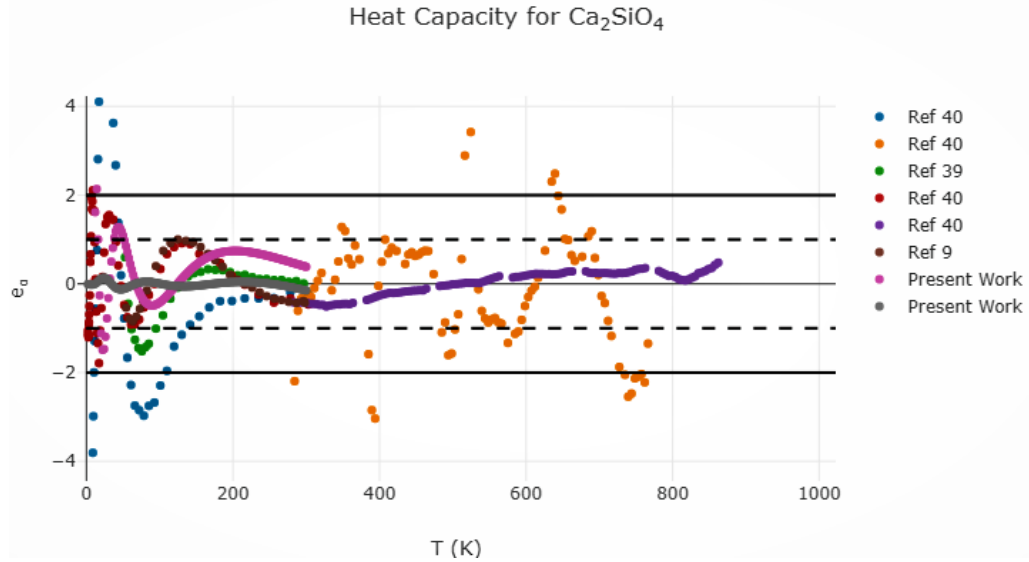


Figure 5.1: An example diagnostic plot displaying the error of all experimental heat capacity measurements considered while fitting C₂S polymorphs. Outer horizontal lines indicate the 2σ deviation limit that should contain 95% of the data set, while the dashed horizontal lines indicate the 1σ deviation. These guidelines are held true by adjusting the error estimates.

Table 5.3: Heat content measurements for rankinite (C₃S₂) compound. The uncertainty corresponds to a 95% confidence interval.

Heat Contents Ca₃Si₂O₇ (mol. wt. 288.42)				
T	T	H _T -H _{298 K}	uncertainty	
°C	K	J mol ⁻¹	J mol ⁻¹	%
25	298.15	-	-	-
599.3	872.45	147433	3570.3	2.4
699.8	972.95	180036.6	4109.9	2.3
799.2	1072.35	206085.9	5517.3	2.7
899	1172.15	233439.6	6032.1	2.6
998.8	1271.95	264146.9	6983.6	2.6
1097.7	1370.85	293304.5	7690.3	2.6
1198.5	1471.65	322841.2	6913.1	2.2

together with the experimental values from 298.15°K to 1471.65 K is presented in Figure 5.2. There is some agreement with the estimation of Haas but the calculated values using FTOX overestimate the heat content compared with the experimental results. The DSC results for C₃S₂ were only interpretable on heating due to the peritectic nature of its melting reaction. On cooling, the sample contained γ -C₂S and CS which did not completely convert to C₃S₂. However, the melting temperature obtained is 1737±5 K, which is identical to the value reported by Levin [55].

The results of the heat content measurements for belite are summed up in Table 5.4. The heat content measurements of $\gamma \rightarrow \alpha'$ -Ca₂SiO₄ have not been available previously. Coughlin O'Brien [37] measured the β , α' -Ca₂SiO₄ heat contents by an inverse drop calorimeter technique. The temperature of transition $\gamma \rightarrow \alpha'$ is situated near

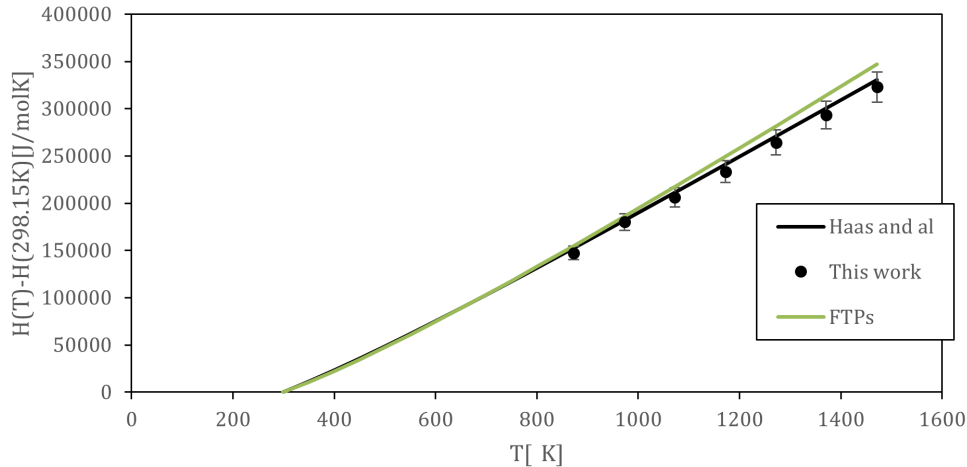


Figure 5.2: Heat content measurements for the rankinite compound compared to the values extrapolated from the FTOX database [4] and Haas et al. [2].

1120 K. Therefore, in this present work, the measured heat contents values include the $\gamma\text{-Ca}_2\text{SiO}_4\text{-}\alpha'\text{-Ca}_2\text{SiO}_4$ in the temperature range 972.86–1471.65 K. The obtained results compared to experimental and calculated values are plotted in Figure 5.3.

Table 5.4: Ca₂SiO₄ heat contents measurements in the temperature range 972.86–1471.05 K. Transition from γ to α' occurs at 1170 K.

Heat Contents (γ , α') - Ca ₂ SiO ₄ (mol. wt. 172.24)				
T	T	H _T -H _{298 K}	Uncertainty	
C	K	J mol-1	J mol-1	%
25	298.15	-	-	-
699.7	972.86	108430.8	3617.9	3.3
798.9	1072.09	123306.7	3251.5	2.6
898.2	1171.39	148801.8	3879.2	2.6
998.5	1271.67	171305.2	4185.5	2.4
1097.9	1371.05	187889.9	4479.1	2.4
1197.9	1471.05	212360.1	6444.6	3

Above 1072 K, γ and $\alpha'\text{-Ca}_2\text{SiO}_4$ measurements do not agree with calculated values using FTOX. For $\alpha'\text{-Ca}_2\text{SiO}_4$, the measured values are 24 to 32 kJ lower. However, there is good agreement with Haas' [2] data and Coughlin's [37] values. The measured values for $\gamma\text{-Ca}_2\text{SiO}_4$ in the temperature range 972–1072 K are in agreement with the calculated ones from FTOX [4] but also those of Haas [2] and Coughlin [37].

5.5.2 DFT Calculations

The ground state energies of all considered compounds are summarised in Table 5.5 together with the calculated transition energies at 0 K for the various Ca₂SiO₄ and CaSiO₃

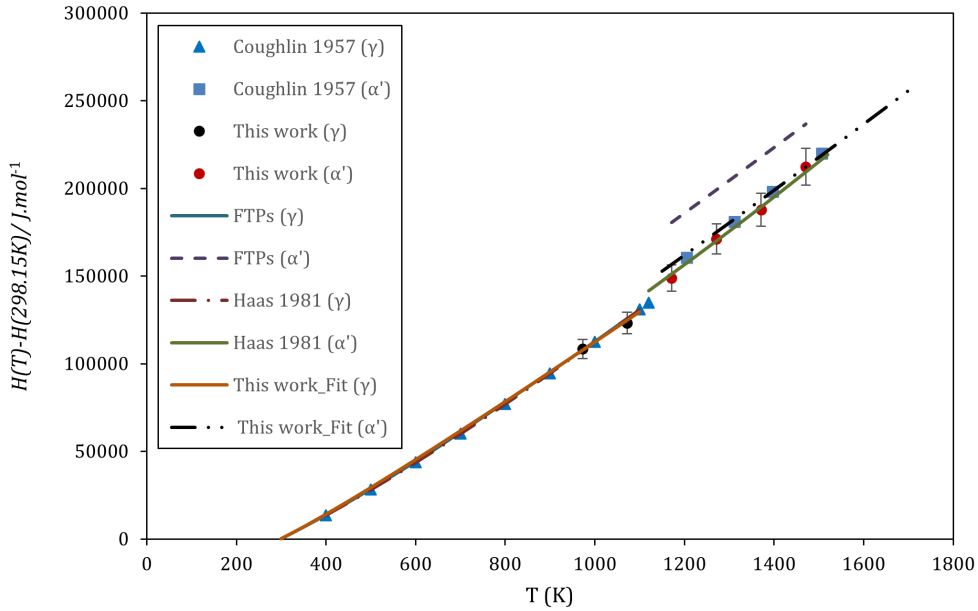


Figure 5.3: γ - and α' - Ca_2SiO_4 heat content measurements, compared against the experimental values of Coughlin [37] (corrected from the enthalpy values of γ - β transition values) and the calculated values of the present work, FTOX [4] and Haas et al. [2].

Table 5.5: Calculated ground state energies at 0 K in eV per formula unit.

Compound	$E^0(0\text{K}) (\text{eV mol}^{-1})$	$dE(0\text{K}) (\text{eV mol}^{-1})$
CaO	-27.36219	Ground state
α quartz- SiO_2	-31.66647	Ground state
monoclinic- Ca_3SiO_5	-114.97448	Ground state
γ - Ca_2SiO_4	-87.74651	Ground state
β - Ca_2SiO_4	-87.65976	0.08675
α' - Ca_2SiO_4	-87.63451	0.112
$\text{Ca}_3\text{Si}_2\text{O}_7$	-147.61658	Ground state
CaSiO_3 -wollastonite	-59.91709	Ground state
CaSiO_3 -cyclowollastonite	-59.8318	0.085

modifications. All data are given in eV per formula unit. For Ca_3SiO_5 , only the monoclinic modification is calculated as it is the only modification with completely occupied lattice sites. For Ca_2SiO_4 , the γ , β and α' modifications are calculated. The high temperature α -modification has a more complicated crystal structure with partially occupied lattice sites and could therefore not be calculated with sufficient precision. The calculated heat of formation at 0 K is summed up in Table 5.6. The data for Ca_2SiO_4 have an additional contribution from the zero point energy calculations (-0.4 kJ/mol for γ - Ca_2SiO_4 and -2.5 kJ/mol for β - Ca_2SiO_4 and α' - Ca_2SiO_4).

5.5.3 Thermodynamic modelling

The resultant coefficients for the solid phases in the CaO-SiO₂ system are given in the Appendix (Table A.1) alongside a table showing the full set of experimental data along

Table 5.6: Calculated heat of formation at 0 K in kJ/mol relative to the oxides CaO and α -SiO₂ (low quartz) and calculated heat of transitions for the different Ca₂SiO₄ and CaSiO₃ modifications.

Compound	$E_{for}(0K)$ (kJ mol ⁻¹)	$E_{trans}(0K)$ (kJ mol ⁻¹)
monoclinic-Ca ₃ SiO ₅	-117.9	-
γ -Ca ₂ SiO ₄	-131.2	-
β -Ca ₂ SiO ₄	-124.8	6.2
α' -Ca ₂ SiO ₄	-122.4	8.8
Ca ₃ Si ₂ O ₇	-212	-
CaSiO ₃ -wollastonite	-85.7	-
CaSiO ₃ -cyclowollastonite	-77.5	8.2

with their reported and calculated uncertainties. These fits allow for an evaluation of the new data for C₃S₂ and α' , α -C₂S. A comparison of the H₂₉₈ and S₂₉₈ values between the new fit and the values of Haas et al. [2] is given in Table 5.7. Most of the values are within the expected error of each other; however, disagreement exists for the H₂₉₈ of rankinite-Ca₃Si₂O₇. This is expected and the discrepancy in Haas was previously reported by Hillert et al. [12]. The H₂₉₈ and S₂₉₈ of α' -Ca₂SiO₄ also disagree with the Haas values, this is explained by the use of new data for both the enthalpy and heat capacity presented in this assessment.

Table 5.7: H₂₉₈ and S₂₉₈ of the compounds in the C-S system as calculated by the model presented here and compared to values from Haas et al. [2].

Compound	H ₂₉₈ (kJ mol ⁻¹)		S ₂₉₈ (J mol ⁻¹ K ⁻¹)	
	Calc.	Haas.	Calc.	Haas.
monoclinic-Ca ₃ SiO ₅	-2932	-	166.4	-
triclinic-Ca ₃ SiO ₅	-2933	-2933	166.5	168.6
rhombohedral-Ca ₃ SiO ₅	-2932	-	166.4	-
rankinite-Ca ₃ Si ₂ O ₇	-3951	-3973	207.6	210.6
wollastonite-CaSiO ₃	-1634	-1634	79.6	81
cyclowollastonite-CaSiO ₃	-1627	-1627	87.6	87.2
α -Ca ₂ SiO ₄	-2293	-2548*	132.7	84.91*
α' -Ca ₂ SiO ₄	-2304	-2198	130.4	116
β -Ca ₂ SiO ₄	-2307	-2306	126.1	126.7
γ -Ca ₂ SiO ₄	-2316	-2316	119	120.5

*This value is extrapolated beyond the temperature limits of the curve.

Figure 5.4 shows the calculated enthalpy of formation relative to the oxides for the compounds within this system (for which experimental data exists) and compares them against the experimental data. There is generally a good agreement between these values with the only discrepancy being the C₃S-triclinic phase ($x = 0.25$). This is due to the incorporation of the value of Brunauer et al. [43] which conflicts with the value of King [40].

The resulting optimised phase diagram model parameters including the Gibbs energy terms of the associates is presented in Table 5.8 with the final calculated phase diagram

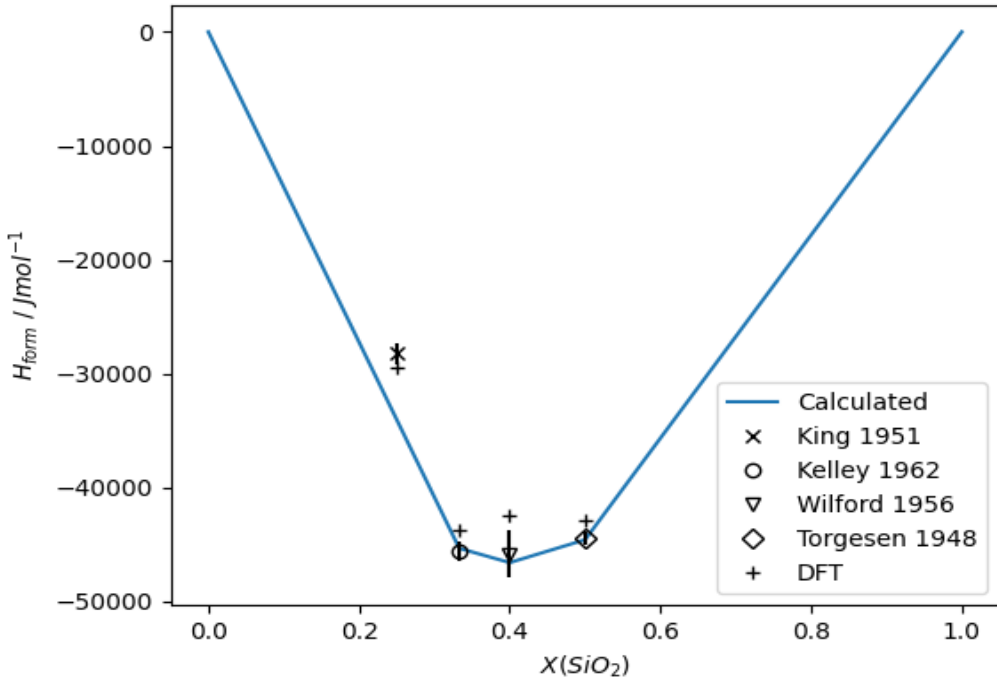


Figure 5.4: Graph of the enthalpy of formation at 298 K of the stable phases at room temperature with C_3S being metastable at room temperature. These values are relative to the single oxides and compared against the experimental data.

Table 5.8: Table showing the functions for the melt phase for the CaO-SiO₂ system, optimised in the present work.

Thermodynamic Properties of the C-S melt phase

$\mathbf{G}_{Liquid} (\mathbf{C}, \mathbf{C}_2\mathbf{S}, \mathbf{CS}, \mathbf{S})$:

$$G_C = G_{CaO,Liquid} [6]$$

$$G_C = G_{SiO_2,Liquid} [7]$$

$$G_{C_2S} = 2G_{CaO,Liquid} + G_{SiO_2,Liquid} - 183422.297315552 - 2.28483183782731T$$

$$G_{CS} = G_{CaO,Liquid} + G_{SiO_2,Liquid} - 116624.5108961 + 3.86841542916429T$$

$$L_{CS,S,0} = 251273.138042155 - 132.4131763105T$$

$$L_{CS,S,1} = -76026.8593265931 + 22.9753135769968T$$

$$L_{CS,S,2} = 117268.159674298 - 40.3850726577932T$$

$$L_{C,C_2S,2} = 8.99637059634927T$$

$$L_{C_2S,S,0} = 9.04086951648876T$$

presented in Figure 5.5. The calculated liquidus shows good agreement with the available experimental data. To facilitate the precise reading of key points of the phase diagram a summary of the invariant points is given in Table 5.9.

Whilst activity data was not fit in this assessment, the calculated model activities of SiO₂ and CaO alongside experimental comparisons can be seen in Figure 5.6 and 5.7 respectively. Furthermore, although the activity data is not fit, the calculated values are within the experimental error for the activity data and in line with the values calculated by previous models of the CaO-SiO₂ system [11, 14].

Direct comparisons of the model reported here can be made with the assessment conducted by Besmann and Spear [16] who also made use of an associates model for the C-S

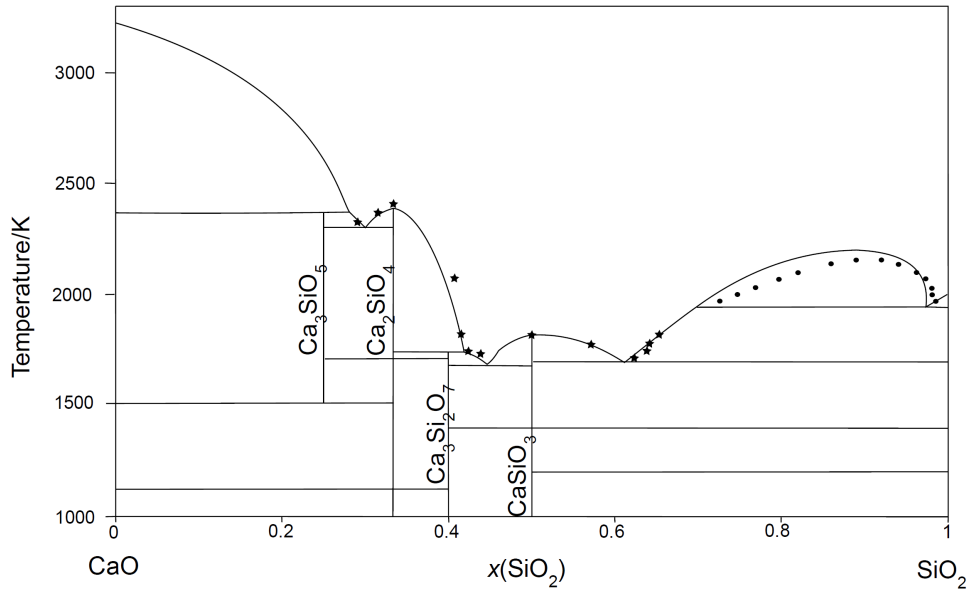


Figure 5.5: CaO-SiO₂ phase diagram calculated in this assessment plotted with experimental points obtained from Ref [55].

Table 5.9: Summary of transitions and invariant reactions in the C-S system from the calculated phase diagram compared to experimental data in parentheses. The composition values correspond to the liquid phase.

Transition	T (K)	H_{transition} (kJ mol⁻¹)
$\gamma - \text{Ca}_2\text{SiO}_4 \rightarrow \alpha' - \text{Ca}_2\text{SiO}_4$	1120 (1120) [63]	14.3 (14.3) [37]
$\beta - \text{Ca}_2\text{SiO}_4 \rightarrow \alpha' - \text{Ca}_2\text{SiO}_4$	970 (970) [63]	2.17 (1.84) [37]
$\alpha' - \text{Ca}_2\text{SiO}_4 \rightarrow \alpha - \text{Ca}_2\text{SiO}_4$	1710 (1710) [63]	16.2 (14.1) [37]
wollastonite \rightarrow cyclo-CaSiO ₃	1397 (1398) [35]	8.68 (5.85) [49]
triclinic \rightarrow monoclinic-Ca ₃ SiO ₅	1254 (1253) [8]	0.477 -0.477
monoclinic \rightarrow rhombohedral-Ca ₃ SiO ₅	1317 (1323) [8]	0.047 -0.047
Invariant	T (K)	X(SiO₂) in Liquid
Liquid + CaO \rightarrow Ca ₃ SiO ₅	2423 (2423) [55]	0.27 (0.27)
Liquid \rightarrow Ca ₃ SiO ₅ + α -Ca ₂ SiO ₄	2305 (2323) [55]	0.3 (0.29)
Liquid + α -Ca ₂ SiO ₄ \rightarrow Ca ₃ Si ₂ O ₇	1746 (1737) [55]	0.41 (0.43)
Liquid \rightarrow Ca ₃ Si ₂ O ₇ + CaSiO ₃	1739 (1733) [55]	0.43 (0.44)
Liquid \rightarrow SiO ₂ + CaSiO ₃	1709 (1709) [55]	0.62 (0.61)
Compound	T_{melting} (K)	H_{fusion} (kJ mol⁻¹)
α -Ca ₂ SiO ₄	2390 (2403) [56]	62.1 (61.0)[64]
cyclo-CaSiO ₃	1822 -1817	61.3 (57.3) [65]

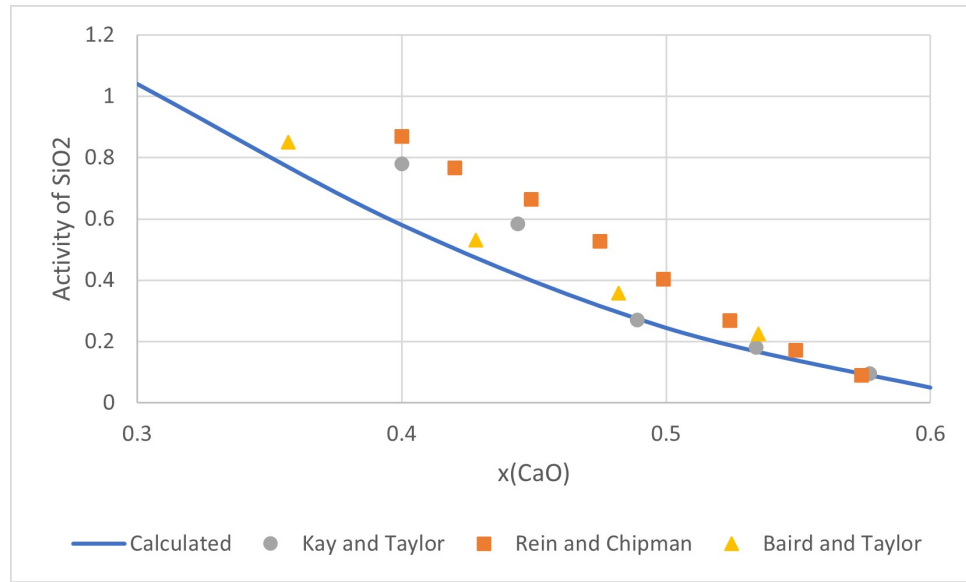


Figure 5.6: Activity of SiO_2 (at 1823 K, reference; cristobalite) calculated from the model compared with experimental data.

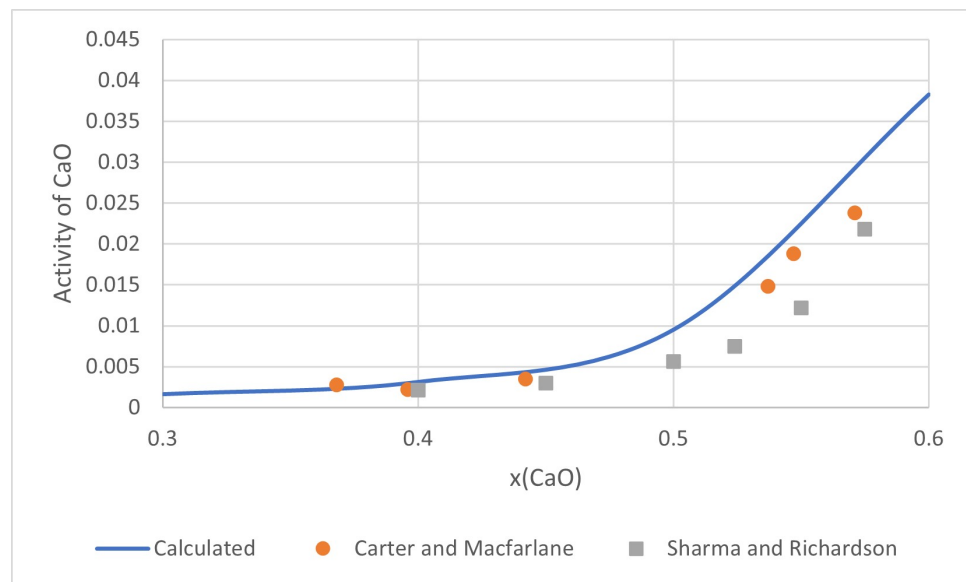


Figure 5.7: Activity of CaO (1773 K, reference: solid CaO) calculated from the model compared with the experimental data.

system. They used an additional C_3S associate, which is unfavourable as it is not evidenced to exist via spectroscopic measurements [66, 67]. Furthermore, adding an associate adds additional complexity to the resulting corrections as well as possible complications in the higher-order system which is why it was avoided in this assessment. The agreement with the experimental data in the present work demonstrates this associate is not needed from a purely fitting perspective. Not enough information is given to compare the parameterisation further; however, it is estimated they used a total of 10 parameters to capture the melt by assuming the use of an enthalpy and entropy correction for each associate. The developed model uses two more parameters to capture the miscibility gap, thus the automatic selection process arrived at the same level of parameterisation

which is a great success considering the difficulty in selecting and optimising parameters given that 60 potential parameters were available for insertion. Hillert et al. carried out two assessments for the CaO-SiO₂ system using two variations of an ionic two-sublattice model [11, 12], which due to the choice in species to represent the melt phase is a comparable model to the associates model used in this work (i.e. (Ca⁺²), (SiO₄⁻⁴, SiO₃⁻², O⁻², SiO₂)). In one model they included SiO₃²⁻ while in the other it was removed. Their models use 6 interactions terms between their sublattice species and SiO₂ to capture the liquid; However, they use a clever trick to lower the parameterisation level by repeating coefficients to neutralise a drawback of the miscibility gap model outside the region of the gap. The optimiser does not attempt these variations as they are highly customised for the system, but an equivalent model in a standardised description would have 12 parameters, thus they are comparable in complexity; however, the developed approach also shows not all the species require interaction parameters between them to fit the phase diagram and avoids the use of higher-order ideal interactions (i.e., $k = 3$ R-K terms) used by Hillert et al. [11, 12]. These are both advantageous when extending to higher-order systems or higher temperatures, so this might be viewed again as a successful automatic fit.

The liquid model can also be compared against the spectroscopic data of Mysen et al. [66]. Point equilibrium calculations can be conducted to obtain the abundance of the associate species in the melt phase and the results are as follows: At the $x(\text{SiO}_2) = 0.5$ composition, Mysen et al. measure 80% abundance of SiO₃²⁻ species whilst a calculated abundance of 60% is observed in the present work. Furthermore, at $x(\text{SiO}_2) = 0.5$, a 15% abundance of SiO₄⁴⁻ species is reported, compared to the calculated value of 19% (see Figure 5.8). These values are in reasonable agreement given the uncertainties involved and

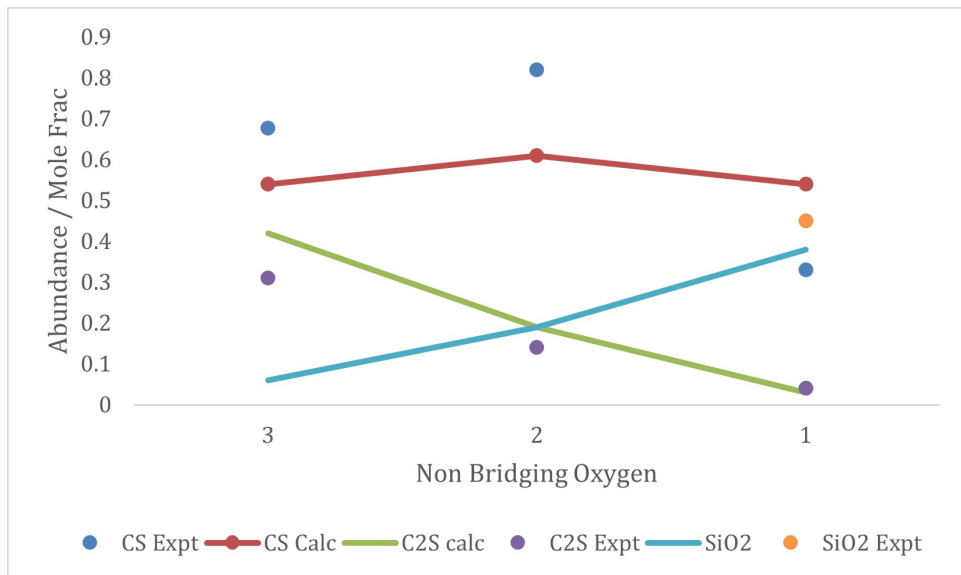


Figure 5.8: Abundance of C₂S and CS species in the melt compared against the spectroscopic data from [66].

the high experimentally measured abundances of those species in the C-S melt justifies the use of both the CS associate and C₂S associate. Furthermore, the low abundance of

CS species calculated at $x(\text{SiO}_2) = 0.5$ compared to the experimental data is most likely due to the interaction terms between CS and S associates required to fit the miscibility gap which was also described by Hillert et al. [11].

5.6 Conclusion

The CaO-SiO₂ is the most important system for Portland cement clinkers but modelling this system is challenging due to the miscibility gap, the large number of phases, and the polymorphs requiring revaluation, as well as the diversity of thermodynamic data. Novel results for the relative enthalpy of rankinite-Ca₃Si₂O₇ at high temperatures, the relative enthalpy of γ -Ca₂SiO₄ including the transition to the α' modifications, and phonon calculations to determine the low-temperature heat capacity of α' -Ca₂SiO₄ are presented here. This has led to a full re-evaluation of the solid compounds in this system, as well as the inclusion of updates to the CaO and SiO₂ end-members [6, 7] and the inclusion of the Ca₃SiO₅ polymorphs within the model, an important feature when extending the system. The produced model appears to accurately reproduce all known experimental data, including all solid and liquid phases. A modern fitting approach has been developed and tested in this paper with the use of the 3rd generation CALPHAD functions and the associate's model. The use of information criterion to select parameters appears to have been successful, although this is only a preliminary result in the development of these techniques. The resulting model has equal complexity in terms of parameter count to existing fits in the literature, while having fewer higher-order terms and better agreement. Further assessments to complete the cement clinker system will provide ample opportunity for further testing of this approach. These techniques will allow extensions with relative ease and further modelling and extensions are discussed in later sections complete the CaO-Al₂O₃-SiO₂-Fe₂O₃ system, which contains all the major clinker phases found in Portland cement.

5.7 References

- [1] Vincent Meyer, Nick de Cristofaro, Jason Bryant and Sada Sahu. ‘Solidia cement an example of carbon capture and utilization’. In: *Key Engineering Materials*. Vol. 761. 2018, pp. 197–203.
- [2] John L. Haas Jr., Glipin R. Robinson Jr. and Bruce S. Hemingway. ‘Thermodynamic tabulations for selected phases in the system CaO-Al₂O₃-SiO₂-H₂ at 1 atm between 273.15 and 1800 K’. In: *Journal of Physical and Chemical Reference Data* 10.3 (1981), pp. 575–670. DOI: 10.1063/1.555645.
- [3] Theodore Hanein, Fredrik P. Glasser and Marcus N. Bannerman. ‘Thermodynamic data for cement clinkering’. In: *Cement and Concrete Research* 132.106043 (2020). DOI: 10.1016/j.cemconres.2020.106043.

- [4] C. W. Bale, E. Bélisle, P. Chartrand, S. A. Dechterov, G. Eriksson, A. E. Gheribi, K. Hack, I. H. Jung, Y. B. Kang, J. Melançon, A. D. Pelton, S. Petersen, C. Robelin, J. Sangster, P. Spencer and M. A. Van Ende. ‘FactSage thermochemical software and databases, 2010-2016’. In: *Calphad* 54 (2016), pp. 35–53. DOI: 10.1016/j.calphad.2016.05.002.
- [5] A. T. Dinsdale. ‘SGTE data for pure elements’. In: *Calphad* 15.4 (1991), pp. 317–425. DOI: 10.1016/0364-5916(91)90030-n.
- [6] Guillaume Deffrennes, Noël Jakse, Cecilia M.S. Alvares, Ioana Nuta, Alain Pasturel, Alexandra Khvan and Alexander Pisch. ‘Thermodynamic modelling of the Ca-O system including 3rd generation description of CaO and CaO₂’. In: *Calphad* 69 (2020), p. 101764. DOI: 10.1016/j.calphad.2020.101764.
- [7] I. Bajenova, A. Khvan, A. Dinsdale and A. Kondratiev. ‘Implementation of the extended Einstein and two-state liquid models for thermodynamic description of pure SiO₂ at 1 atm’. In: *Calphad* 68.101716 (2020). DOI: 10.1016/j.calphad.2019.101716.
- [8] M Bigaré, A Guinier, C Mazières, M Regourd, N Yannaquis, W Eysbl, T.H Hahn and E Woermann. ‘Polymorphism of tricalcium silicate and its solid solutions’. In: *Journal of the American Ceramic Society* 50.11 (1967), pp. 609–619. DOI: 10.1111/j.1151-2916.1967.tb15009.x.
- [9] E. G. King. ‘Low Temperature Heat Capacities and Entropies at 298.15°K of Some Crystalline Silicates Containing Calcium’. In: *Journal of the American Chemical Society* 79.20 (1957), pp. 5437–5438. DOI: 10.1021/ja01577a028.
- [10] M. W. Chase. ‘NIST-JANAF Thermochemical Tables, 4th Edition’. In: (1998). DOI: 10.18434/t42s31.
- [11] Mats Hillert, Bo Sundman and Xizhen Wang. ‘An assessment of the CaO-SiO₂ system’. In: *Metallurgical Transactions B* 21.2 (1990), pp. 303–312. DOI: 10.1007/bf02664198.
- [12] Mats Hillert, Bo Sundman, Xizhen Wang and Tom Barry. ‘A re-evaluation of the rankinite phase in the CaO-SiO₂ system’. In: *Calphad* 15.1 (1991), pp. 53–58. DOI: 10.1016/0364-5916(91)90025-f.
- [13] Arthur D. Pelton and Milton Blander. ‘Thermodynamic analysis of ordered liquid solutions by a modified quasichemical approach-Application to silicate slags’. In: *Metallurgical Transactions B* 17.4 (1986), pp. 805–815. DOI: 10.1007/bf02657144.
- [14] Gunnar Eriksson, Ping Wu, Milton Blandert and Arthur D. Pelton. ‘Critical evaluation and optimization of the thermodynamic properties and phase diagrams of the MnO-SiO₂ and CaO-SiO₂ systems’. In: *Canadian Metallurgical Quarterly* 33.1 (1994), pp. 13–21. DOI: 10.1179/cmq.1994.33.1.13.

- [15] Thomas I. Barry, Alan T. Dinsdale and John A. Gisby. ‘Predictive thermochemistry and phase equilibria of slags’. In: *Journal of The Minerals, Metals & Materials Society* 45.4 (1993), pp. 32–38. DOI: 10.1007/bf03223284.
- [16] Theodore M. Besmann and Karl E. Spear. ‘Thermochemical Modelling of Oxide Glasses’. In: *Journal of the American Ceramic Society* 85.12 (2002), pp. 2887–2894. DOI: 10.1111/j.1151-2916.2002.tb00552.x.
- [17] J. R. Taylor and A. T. Dinsdale. ‘Thermodynamic and phase diagram data for the CaO-SiO₂ system’. In: *Calphad* 14.1 (1990), pp. 71–88. DOI: 10.1016/0364-5916(90)90041-w.
- [18] M Regourd. ‘Polymorphism Of Tricalcium Silicate - New X-Ray-Diffraction Data’. In: *Comptes Rendus Hebdomadaires Des Seances De L Academie Des Sciences Serie B* 289.1 (1979), pp. 17–20.
- [19] F. Dunstetter, M. N. De Noirlfontaine and M. Courtial. ‘Polymorphism of tricalcium silicate, the major compound of Portland cement clinker: 1. Structural data: Review and unified analysis’. In: *Cement and Concrete Research* 36.1 (2006), pp. 39–53. DOI: 10.1016/j.cemconres.2004.12.003.
- [20] J W Jeffery. ‘The Crystal Structure Of Tricalcium Silicate’. In: *Acta Crystallographica* 5.1 (1952), p. 26. DOI: 10.1107/s0365110x52000083.
- [21] Fumito Nishi and Yoshio Takéuchi. ‘The rhombohedral structure of tricalcium silicate at 1200°C’. In: *Zeitschrift für Kristallographie-Crystalline Materials* 168.1-4 (1984), pp. 197–212.
- [22] N I Golovastikov, R.G. Matveeva and N.V. Belov. ‘Crystal structure of tricalcium silicate’. In: *Kristallografiya* 20.4 (1975), pp. 721–729.
- [23] W. Mumme. ‘Crystal structure of tricalcium silicate from a Portland cement clinker and its application to quantitative XRD analysis’. In: *Neues Jahrbuch Für Mineralogie - Monatshefte* 1995.4 (1995), pp. 146–160.
- [24] Ángeles G De La Torre, Sebastián Bruque, Javier Campo and Miguel A G Aranda. ‘The superstructure of C₃S from synchrotron and neutron powder diffraction and its role in quantitative phase analyses’. In: *Cement and Concrete Research* 32.9 (2002), pp. 1347–1356.
- [25] Andre Guinier and Micheline Regourd. ‘Structure of Portland Cement Minerals’. In: *5th International Congress on the Chemistry of Cement. Part 1.* 1968.
- [26] W G Mumme, L Cranswick and B Chakoumakos. ‘Rietveld crystal structure refinement from high temperature neutron powder diffraction data for the polymorphs of dicalcium silicate’. In: *Neues Jahrbuch fuer Mineralogie. Abhandlungen (Band-Nr)* (1950-) 170 (1996), pp. 171–188.
- [27] J. Forest. ‘Knowledge Of Dicalcium Silicate’. In: *Bulletin De La Societe Francaise Mineralogie Et De Cristallographie* 94.2 (1971), p. 118.

- [28] W Lerch. ‘Approximate glass content of commercial Portland cement clinker’. In: *Journal Of Research Of The National Bureau Of Standards* 20.1 (1938), pp. 77–81. DOI: 10.6028/jres.020.045.
- [29] F Hanic, J Kamarad, J Stracelsky and I Kapralik. ‘The P-T Diagram of Ca₂SiO₄’. In: *British Ceramic Transactions And Journal* 86.6 (1987), pp. 194–198.
- [30] Shinsuke Saburi, Isao Kusachi, Chiyoko Henmi, Akira Kawahara, Kitinosuke Henmi and Isao Kawada. ‘Refinement of the structure of rankinite.’ In: *Mineralogical Journal* 8.4 (1976), pp. 240–246. DOI: 10.2465/minerj.8.240.
- [31] S O Agrell and P Gay. ‘Kilchoanite, a polymorph of rankinite’. In: *Nature* 189.4766 (1961). DOI: 10.1038/189743a0.
- [32] K. F. Hesse. ‘Refinement of the crystal structure of wollastonite-2M (parawollastonite)’. In: *Zeitschrift fur Kristallographie* 168.1 (1984), pp. 93–98. DOI: 10.1524/zkri.1984.168.1-4.93.
- [33] Hexiong Yang and Charles T. Prewitt. ‘Crystal structure and compressibility of a two-layer polytype of pseudowollastonite (CaSiO₃)’. In: *American Mineralogist* 84.11-12 (1999). DOI: 10.2138/am-1999-11-1217.
- [34] T. Yamanaka and H. Mori. ‘The structure and polytypes of α -CaSiO₃ (pseudowollastonite)’. In: *Acta Crystallographica Section B* 37.5 (1981). DOI: 10.1107/s0567740881004962.
- [35] Yu. K Voronko, A A Sobol, S N Ushakov, Jiang Guochang and You Jinglin. ‘Phase Transformations and Melt Structure of Calcium Metasilicate’. In: *Inorganic Materials* 38 (2002).
- [36] Fumito Nishi, Yoshio Takéuchi and Iwao Maki. ‘Tricalcium silicate: the monoclinic superstructure’. In: *Zeitschrift für Kristallographie-Crystalline Materials* 172.1-4 (1985), pp. 297–314.
- [37] J. P. Coughlin and C. J. O’Brien. ‘High Temperature Heat Contents of Calcium Orthosilicate’. In: *The Journal of Physical Chemistry* 61.6 (1957), pp. 767–769. DOI: 10.1021/j150552a016.
- [38] S. S. Todd. ‘Low-temperature Heat Capacities and Entropies at 298.16°K. of Crystalline Calcium Orthosilicate, Zinc Orthosilicate and Tricalcium Silicate’. In: *Journal of the American Chemical Society* 73.7 (1951), pp. 3277–3278. DOI: 10.1021/ja01151a084.
- [39] K. D. Grevel, F. Bellmann, J. Majzlan, E. Dachs, A. Benisek and H. M. Ludwig. ‘Thermodynamic data of belite polymorphs’. In: *Cement and Concrete Research* 152.106621 (2022). DOI: 10.1016/j.cemconres.2021.106621.
- [40] E G King. ‘Heats of Formation of Crystalline Calcium Orthosilicate, Tricalcium Silicate and Zinc Orthosilicate1’. In: *Journal of the American Chemical Society* 73.2 (1951), pp. 656–658. DOI: 10.1021/ja01146a046.

- [41] K K Kelley. ‘Heats and free energies of formation of anhydrous silicates’. In: *U.S Dept. of the Interior, Bureau of Mines* (1962).
- [42] H Elsner von Gronow and H E Schwiete. ‘Die spezifischen Wärmen von CaO, Al₂O₃, CaO.Al₂O₃, 3 CaO.Al₂O₃, 2 CaO.SiO₂, 3 CaO.SiO₂, 2 CaO.Al₂O₃.SiO₂ von 20° bis 1500° C’. In: *Zeitschrift für anorganische und allgemeine Chemie* 216.2 (1933), pp. 185–195. DOI: 10.1002/zaac.19332160212.
- [43] Stephen Brunauer, D. L. Kantro and C. H. Weise. ‘The heat of decomposition of tricalcium silicate into β -dicalcium silicate and calcium oxide’. In: *Journal of Physical Chemistry* 60.6 (1956), pp. 771–774. DOI: 10.1021/j150540a015.
- [44] Wilford F Weeks. ‘Heats of Formation of Metamorphic Minerals in the System CaO-MgO-SiO₂-H₂O and Their Petrological Significance’. In: *The Journal of Geology* 64.5 (1956), pp. 456–472.
- [45] Robert Benz and Carl Wagner. ‘Thermodynamics of the solid system CaO-SiO₂ from electromotive force data’. In: *The Journal of Physical Chemistry* 65.8 (1961), pp. 1308–1311. DOI: 10.1021/j100826a007.
- [46] Hubert Wagner. ‘Zur Thermochemie der Metasilikate des Calciums und Magnesiums und des Diopsids’. In: *Zeitschrift für anorganische und allgemeine Chemie* 208.1 (1932), pp. 1–22. DOI: 10.1002/zaac.19322080102.
- [47] P Courtial, C Tequi and P Richet. ‘Thermodynamics of diopside, anorthite, pseudo-wollastonite, CaMgGeO₄-olivine and akermanite up to near the melting point’. In: *Physics and Chemistry of Minerals* 27 (2000), pp. 242–250. DOI: 10.1007/s002690050253.
- [48] Pascal Richet and Guillaume Fiquet. ‘High-temperature heat capacity and premelting of minerals in the system MgO-CaO-Al₂O₃-SiO₂’. In: *Journal of Geophysical Research: Solid Earth* 96.B1 (1991), pp. 445–456. DOI: 10.1029/90JB02172.
- [49] T V Charlu, R C Newton and O J Kleppa. ‘Enthalpy of formation of some lime silicates by high-temperature solution calorimetry, with discussion of high pressure phase equilibria’. In: *Geochimica et Cosmochimica Acta* 42.4 (1978), pp. 367–375. DOI: 10.1016/0016-7037(78)90267-3.
- [50] Charles W. Bauschlicher and David R. Yarkony. ‘Electronic structure of CaO.’ In: *The Journal of Chemical Physics* 68.9 (1978), pp. 3990–3997. DOI: 10.1063/1.436312.
- [51] V Dmitriev, V Torgashev, P Toledano and EKH Salje. ‘Theory of SiO₂ polymorphs’. In: *Euro Physics Letters* 37.8 (1997), p. 553.
- [52] Przemyslaw Dera, John D Lazarz, Vitali B Prakapenka, Madison Barkley and Robert T Downs. ‘New insights into the high-pressure polymorphism of SiO₂ cristobalite’. In: *Physics and Chemistry of Minerals* 38.7 (2011), pp. 517–529.

- [53] Song-Mao Liang and Rainer Schmid-Fetzer. ‘Complete thermodynamic description of the Mg-Ca-O phase diagram including the Ca-O, Mg-O and CaO-MgO subsystems’. In: *Journal of the European Ceramic Society* 38.14 (2018), pp. 4768–4785.
- [54] S.M. Schnurre, J. Gröbner and R. Schmid-Fetzer. ‘Thermodynamics and phase stability in the Si-O system’. In: *Journal of Non-Crystalline Solids* 336.1 (2004), pp. 1–25. DOI: 10.1016/j.jnoncrysol.2003.12.057.
- [55] Ernest M. Levin, Carl R. Robbins and Howard F. McMurdie. *Phase diagrams for ceramists*. Columbus, Ohio: American Ceramic Society, 1964. ISBN: 0916094049.
- [56] G. A. Rankin and F. E. Wright. ‘The ternary system CaO-Al₂O₃-SiO₂’. In: *American Journal of Science* s4-39.229 (1915), pp. 1–79. DOI: 10.2475/ajs.s4-39.229.1.
- [57] Tehwey JD and Hess PC. ‘The Two Phase Region in the CaO-SiO₂ System: Experimental data and Thermodynamic analysis’. In: *Phys. Chem. Glasses* 20 (1979), pp. 41–52.
- [58] J W Greig. ‘Immiscibility in silicate melts’. In: *American Journal Of Science* 13.73 (1927), pp. 1–44.
- [59] Richard H Rein and John Chipman. ‘Activities in the liquid solution SiO₂-CaO-MgO-Al₂O₃ at 1600°C’. In: *Transactions of the Metallurgical Society* 233.2 (1965), pp. 415–425.
- [60] R A Sharma and F D Richardson. ‘Solubility of Calcium Sulphide and Activities in Lime-Silica Melts’. In: *Journal of the Iron And Steel Institute* 200.5 (1962).
- [61] J D Baird and J Taylor. ‘Reaction between silica and carbon and the activity of silica in slag solution’. In: *Transactions of the Faraday Society* 54 (1958), pp. 526–539.
- [62] D A R Kay and J Taylor. ‘Activities of silica in the lime + alumina + silica system’. In: *Transactions of the Faraday Society* 56 (1960), pp. 1372–1386.
- [63] M A Bredig. ‘Polymorphism of Calcium Orthosilicate’. In: *Journal of the American Ceramic Society* 33.6 (1950), pp. 188–192. DOI: 10.1111/j.1151-2916.1950.tb12789.x.
- [64] Ihsan. Barin, Fried. Sauert, Ernst. Schultze-Rhonhof and Wang. Shu Sheng. *Thermochemical data of pure substances*. Weinheim, Germany: VCH, 1989. ISBN: 9783527619825. DOI: 10.1002/9783527619825.
- [65] K Adamkovicova. ‘The heat of fusion of CaSiO₃’. In: *Silikaty* 24.3 (1980), pp. 193–201.
- [66] Bjørn O Mysen, David Virgo and Friedrich A Seifert. ‘The structure of silicate melts: Implications for chemical and physical properties of natural magma’. In: *Reviews of Geophysics* 20.3 (1982), pp. 353–383. DOI: 10.1029/RG020i003p00353.

- [67] John D. Frantza and Bjorn O. Mysen. ‘Raman spectra and structure of BaO-SiO₂ SrO-SiO₂ and CaO-SiO₂ melts to 1600°C’. In: *Chemical Geology* 121.1-4 (1995), pp. 155–176. DOI: 10.1016/0009-2541(94)00127-t.

CHAPTER
SIX

MODELLING CAO-AL₂O₃-SIO₂ FOR PORTLAND CEMENT CLINKERS

The assessment of the pure Al₂O₃ liquid and solid phases was carried out by a colleague Dr Alexander Pisch, who also provided the relevant DFT data for the calcium aluminates that are mentioned in this chapter. Additionally, the experiments for the compounds in the CaO-Al₂O₃ assessment were carried out by a colleague Chancel Malawala.

In the previous chapter, the details for modelling the most important binary CaO-SiO₂ were described. Additional binary phase diagrams that are relevant for the ternary system are the CaO-Al₂O₃ system which contains the clinker phase C₃A and the cementitious relevant phase C₁₂A₇, and the Al₂O₃-SiO₂ section which contains the solid solution mullite. Combining these binary systems allows for the modelling of the CaO-Al₂O₃-SiO₂ ternary. This is arguably the most important system as it contains information on 90% (by weight) of the clinker, thus it is favourable to accurately model the entire ternary, to avoid errors in the clinkering calculations as the ternary liquid melt is important in facilitating the clinkering reactions. For visualisation, the full phase diagram as calculated by Taylor is presented in Figure 6.1.

In this chapter, the models of the remaining binaries CaO-Al₂O₃ and Al₂O₃-SiO₂ will be presented first. Then the three binary systems will be combined resulting in an “extrapolated” ternary. Next, the fully assessed, CaO-Al₂O₃-SiO₂ ternary will be presented which will include newly assessed parameter values and comparisons will be made against previous assessments. Finally, initial calculations will be carried out at the clinkering composition and compared against experimental data, to validate the ternary system for OPC applications.

6.1 3rd Generation Al₂O₃

In the CaO-SiO₂ system, the thermodynamic description for the oxide end-member CaO was taken from the works of Deffrennes et al. [2]. Additionally, the thermodynamic

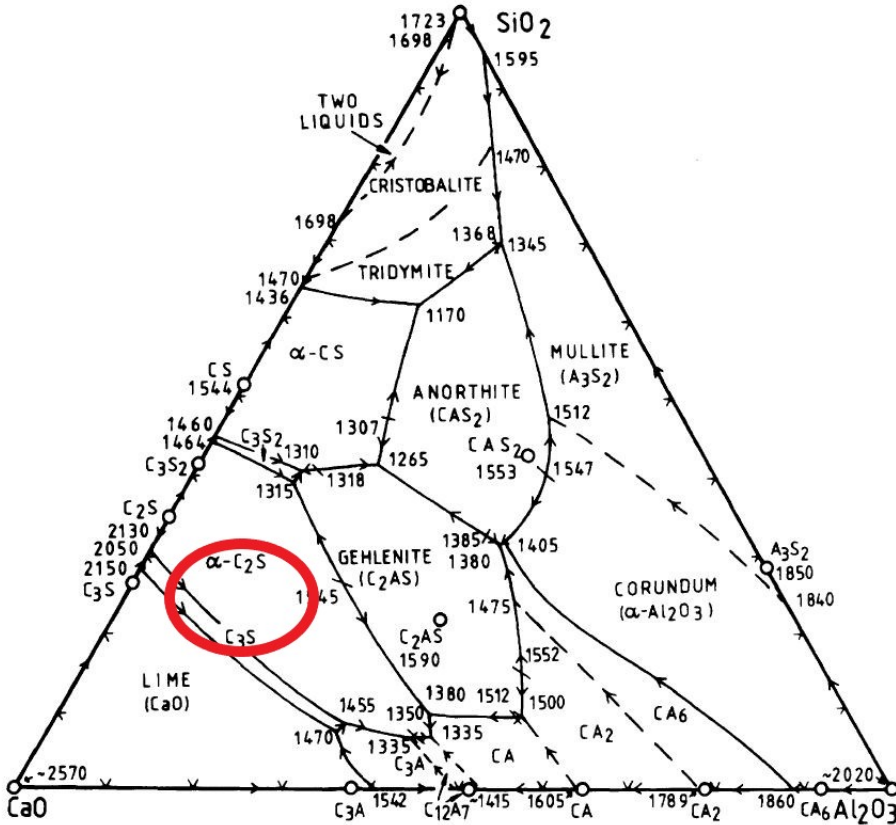


Figure 6.1: Established CaO - Al_2O_3 - SiO_2 phase diagram from literature. The red circle highlights the compositional area relevant to OPC. The phase diagram is taken from the work of Taylor cement chemistry from Ref [1].

descriptions of the SiO_2 end member (including all of its polymorphs) were taken from the works of Bajenova et al. [3]. These descriptions contained the latest data and were made by fitting the 3rd generation CALPHAD function for the solid phases and a two-state model for the pure liquid phase. These descriptions were found to be sufficient to accurately model the phase diagram and no further re-fitting of the oxide data was required. This was made possible by refitting all the other solid phases relative to the new oxide descriptions. Whilst descriptions of Al_2O_3 [4–6] do exist in the literature, they are modelled using a polynomial heat capacity (2nd generation models). Similar 3rd generation thermodynamic descriptions do not exist in the literature for the Al_2O_3 phase and thus must be fit in the present work before fitting can commence for systems containing the Al_2O_3 end member, for example Al_2O_3 - SiO_2 and CaO - Al_2O_3 . It is to be noted that any reliable and consistent description of the Al_2O_3 end-member can be used, it was just found desirable in the present work to use a new description of the Al_2O_3 phase.

Whilst many polymorphs for Al_2O_3 exist, many of them are metastable and are only stable at high pressures [7]. They can therefore be ignored and do not have to be fit. Thus, the only polymorph of interest is γ - Al_2O_3 , which is also known as corundum in the literature [8]. In addition, novel DFT data was used to provide more data to fit the Al_2O_3 solid and liquid phases. Using the methods and the novel expressions for the

high-temperature data presented by Deffrennes et al. [2], the thermodynamic properties of the corundum polymorph were refit using the 3rd generation and two-state model. The resultant expressions for the Gibbs free energy for the solid and liquid phases are presented in Table 6.1.

Table 6.1: Parameters for the solid Al_2O_3 functions optimised in the present work, according to Equation 4.4.1.

$Al_2O_3(Solid)$
$\alpha_1 = 5*0.31585708, \theta_1 = 1067.3396$
$\alpha_2 = 5*0.55886848, \theta_2 = 636.19021$
$\alpha_3 = 5*0.12527444, \theta_3 = 312.67623$
$H = 5*-347283.5$
$a = 5*-4.809835E-04, b = 5*-3.85040833E-08$
$Al_2O_3(Liquid)$
$H = 5*(-336231.946+2206.693149)$
G^{diff}
$A = 5*43735.7183, B = 5*-6.2358, C = 5*-0.2962085013$

6.2 $Al_2O_3-SiO_2$

Whilst the $Al_2O_3-SiO_2$ system is not directly important for cement clinker, it is important for modelling the ternary system as the mullite solid solution contained within this section extends far into the ternary melt.

In theory, this system is quite simple, containing only the end-members and the solid solution mullite, similar to the $CaO-MgO$ system. However, there is much debate on the sublattice model for mullite, with it initially being described as a stoichiometric solid with the composition $3(Al_2O_3) \cdot 2(SiO_2)$ by Grieg [9]; however, later revisions by Aramaki and Roy [10] corrected this and determined mullite existing as a solid solution.

6.2.1 Modelling mullite

The simplest model to use for mullite is made up of just the end-members Al_2O_3 and SiO_2 to produce the model (Al_2O_3, SiO_2) ; however, this is not ideal as it would make mullite stable all over the phase diagram and makes modelling harder. Experimentally, mullite exists in a narrow region of the phase diagram, which can be seen in the fully optimised binary phase diagram presented in Fig. 6.2. Within the literature, mullite has been successfully modelled by Hillert et al. [11] (which was published by MaO et al. [12]) using the sublattice model $Al_1Al_1(Al, Si)_1(O, Va)$. This gives rise to 4 end members: $Al_1Al_1Si_1O_5$, $Al_1Al_1Al_1O_5$, $Al_1Al_1Si_1Va$ and $Al_1Al_1Al_1Va$. The first end member corresponds to the high-pressure sillimanite phase, which is not stable in the phase diagram at normal pressures, making it an ideal “real” end member to model the limits of the solid solution. The last end member corresponds to an unstable Al_2O_3 , this sublattice model

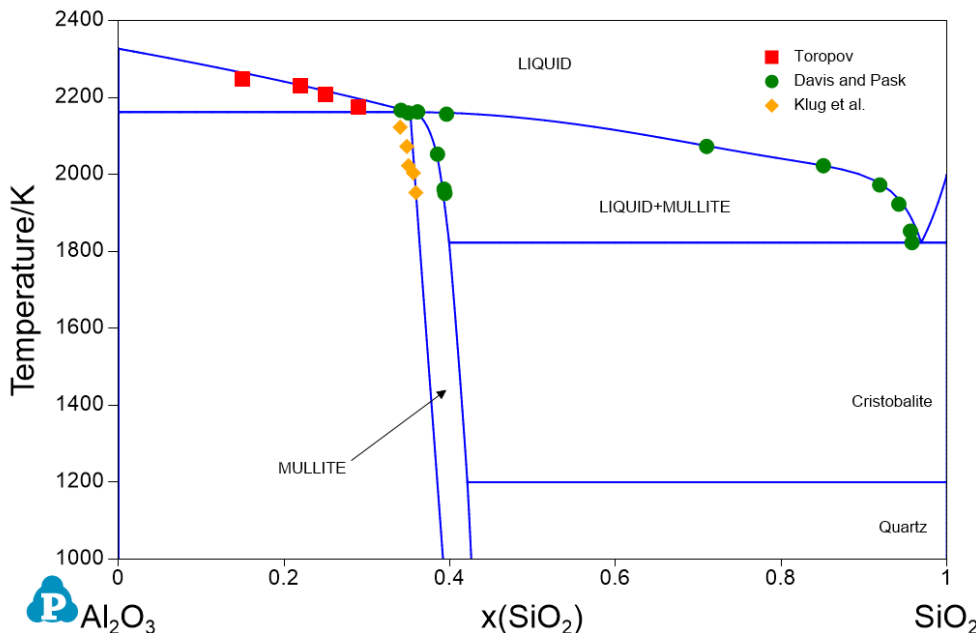


Figure 6.2: Diagram of the fully optimised Al_2O_3 - SiO_2 phase diagram carried out in the present work alongside the experimental points.

effectively makes a solid solution with limits from Al_2O_3 to silimanite. Other attempts by Eriksson and Pelton [13] used a solid solution based on the “stoichiometric” mullite $3(\text{Al}_2\text{O}_3) \cdot 2(\text{SiO}_2)$, but this places a hard limit on the solubility, as mullite has been observed to contain higher concentrations of SiO_2 as seen by Klug et al. [14]. Howald and Elziezer [15] also modelled the mullite solid solution and saw the need for the inclusion of silimanite phase which has the chemical formula Al_2SiO_5 in the sublattice model, to provide accurate limits on the solid solution. This was also done in the present work to produce the simplified model ($1.5\text{ Al}_2\text{O}_3$, silimanite). It is important to note that the Al_2O_3 in the solid solution of the mullite is not the same as corundum- Al_2O_3 , if this was the case, it would make the Al_2O_3 end-member in mullite stable outside the range of the solid solution. Instead, it is a fictive end-member of mullite and thus has a different Gibbs free energy to solid Al_2O_3 . This was achieved by adding an enthalpy correction of 4998.5 J/mol to this end-member making it only stable in the solid solution range.

The properties of the silimanite end member in the mullite are taken to be the same as the silimanite stoichiometric solid (without the modelling of the pressure dependence). This was fit using the 3rd generation model using heat capacity data [16] and an enthalpy of formation measurement [17]. The resultant coefficients for the 3rd generation model are presented in Appendix A.1, and the data used to fit the model is in the Appendix in Table A.3.

6.2.2 Phase diagram

Once the model for the solid solution is chosen, the interaction terms for the solution phases are fit in against the relevant experimental data. This was done by the automatic approach developed in this work. For the melt phase, it was found desirable to add a $(2/3) Al_2O_3 \cdot SiO_2$ associate, this was also done in the MTDATA oxide database [18]. This associate compositionally exists in the middle of the phase diagram and aids in the fitting of the liquidus experimental points. Previous attempts without this associate resulted in a poor fit for the eutectic point. The resultant parameters for the $Al_2O_3-SiO_2$ phase diagram are presented in Table 6.2.

Table 6.2: Table showing the functions and parameters optimised in the work for the melt phase in the $Al_2O_3-SiO_2$ system.

Thermodynamic Properties of the A-S melt phase	
Liquid ($A_{0.5}, A_{2/3}S_1, S$):	
$G_{A_{0.5}} = 0.5 * G_{Al_2O_3,Liquid}$	
$G_S = G_{SiO_2,Liquid}$ [3]	
$G_{A_{2/3}S} = 2/3 * G_{Al_2O_3,Liquid} + G_{SiO_2,Liquid} + 545197 - 3.51T$	
$L_{A_{0.5},S,0} = 6952 + 7.45T$	
$L_{A_{0.5},S,1} = -9798.4$	
$L_{A_{0.5},S,2} = 2893.01$	
Thermodynamic Properties of the mullite phase	
Mullite ($A_{1.5}, A_1S_1, S$):	
$G_{mullite,A_1S_1} = G_{Silimanite}$	
$G_{mullite,A_1S_1} = 1.5 * G_{Al_2O_3} + 4998.5$	
$L_{A_{1.5},A_1S_1,0} = 10573.05$	
$L_{A_{1.5},A_1S_1,1} = 85373.06$	
$L_{A_{1.5},A_1S_1,2} = 21.43T$	

A summary of the invariant point in the $Al_2O_3-SiO_2$ binary section is presented in Table 6.3. The experimental liquidus points on the silica-rich side were studied by Aramaki and Roy [10] and Davis and Pask [19], who also measured the silica-mullite eutectic at $x(Al_2O_3) = 0.033$ and $T = 1820$. This matches closely with the calculated values of $x(Al_2O_3) = 0.031$ and $T = 1822$. Furthermore, the measurements for the solid solution (including the invariant) by Klug et al. [14] were used to fit the phase diagram and are in close agreement with the optimised phase diagram.

Table 6.3: Summary of invariant points in the $Al_2O_3-SiO_2$ phase diagram. Values in parentheses are the experimental points [14, 19].

Reaction	T/K	x(Al_2O_3)
Liquid + $Al_2O_3 \rightarrow$ mullite	2162 (2163)	0.645 (0.659)
Liquid \rightarrow SiO ₂ + mullite	1822 (1820)	0.031 (0.033)

The $Al_2O_3-SiO_2$ was successfully fit in this section using the developed approach. This is whilst also using a simpler model for the mullite solid solution than previous

authors [11, 13]. This section, whilst not appearing in the OPC region, was important to fit as it provides additional constraints on the melt phase, which will be important when modelling the ternary CaO - Al_2O_3 - SiO_2 system.

6.3 CaO - Al_2O_3

The CaO - Al_2O_3 is an important system for modelling the cement clinker as it contains the major clinker phase C_3A , as well as the phase C_{12}A_7 . This phase is formed in the cement kiln and has been known to present in final clinker [1]. The other compounds within the system are important to assess in order to model the melt phase correctly. Present in the CaO - Al_2O_3 system are the stoichiometric compounds: CA (CaAl_2O_4), CA_6 ($\text{CaAl}_{12}\text{O}_{19}$), CA_2 (CaAl_4O_7), C_3A ($\text{Ca}_3\text{Al}_2\text{O}_6$) and C_{12}A_7 ($\text{Ca}_{12}\text{A}_{14}\text{O}_{33}$). In most assessments, the C_{12}A_7 phase is often removed, due to being stable in mainly anhydrous conditions [20] and whilst this is suitable for metallurgical and geological applications, this phase is quite important in the cement kiln. However, due to the lack of experimental data for this phase, it is important to first fit the phase diagram without this phase to get the correct liquid parameters and then this phase can then be entered in the section, resulting in a phase diagram that is suitable for cement applications.

6.3.1 Phase diagram

Experimentally, Rankin and Wright [21] reported the first CaO - Al_2O_3 binary section. In their phase diagram they identified four phases: C_3A , C_5A_3 , CA and C_3A_5 , with C_5A_3 and C_3A_5 later being renamed to C_{12}A_7 and CA_2 respectively. Later studies by Nurse et al. [20] and Jerebtsov and Makhailov [22] further improved the experimental information in the phase diagram and identified the CA_6 compound. The CA_6 is often troublesome due to the lack of experimental data on this phase [23]. In addition, aside from the compounds stated above, additional compounds such as the C_5A_3 and the high pressure CA_2 have also been known to exist in this section [22]. However, they are often removed from the modelling of the section due to the small stability range of these compounds.

Previous assessments of this system [13, 24, 25], are all quite similar but have varying liquid models with the most relevant assessment being carried out by Hallstedl [23]. Similar, to the previous assessments they excluded the C_{12}A_7 phase in the fully optimised phase diagram but did carry out the modelling of the C_{12}A_7 phase. The phase diagram assessed by Hallstedl can be seen in Figure 6.3.

6.3.2 Literature review of the solid phases

In the present work, only the compounds CA, CA_6 , CA_2 , and C_3A and C_{12}A_7 were considered as existing in the phase diagram, similar to previous assessments.

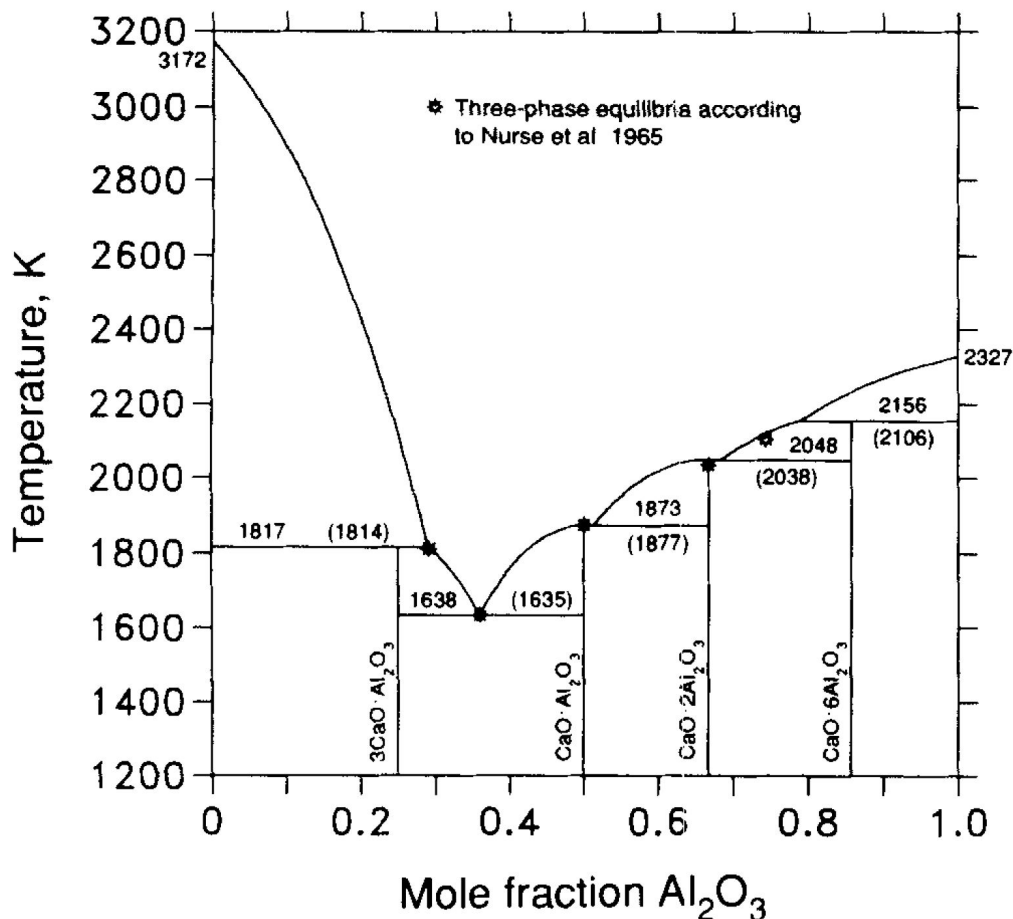


Figure 6.3: Assessed diagram of the CaO-Al₂O₃ system from Hallstedl [23].

For the CA compound, low-temperature heat capacity was measured by King [26]. The high-temperature relative enthalpy measurements were carried out by Gronow and Schwiete [27] and Bonnickson [28]. Similar heat capacity and relative enthalpy measurements were carried out by King [26] and Bonnickson [28] for the CA₂ and C₃A solid, with additional heat content data from Gronow and Schwiete measured for the C₃A compound [27]. The measurements by King are useful for the fitting of the solids as the low-temperature data helps to fit the S_{298} value for the compounds. In addition, the values from Bonnickson [28] were found to be experimentally consistent compared to the values by Gronow and Schwiete [27]. For the CA₆ phase, there is a lack of experimental data for the heat capacity. To supplement this relative enthalpy measurements were carried out and although not ideal, heat capacity measurements from previous assessments and the FTOX database were also taken but were only used to validate the fits.

There is an abundance of enthalpy of formation measurements for the compounds in the system, which is always beneficial, but there is a lack of agreement in the literature for many of the values. For the CA, CA₂ and C₃A compounds the same authors [29–31] measured the heat of formation values, with varying degrees of uncertainties in their values, therefore to supplement this DFT was used to provide a starting value to determine the fit uncertainties on all the experimental measurements. For the CA₆ compound, only

the heat of formation at 1063 K was measured by Geiger [29], so DFT was used to provide a better fit by calculating an appropriate value at 298 K. In addition to this, Gibbs energy of formation measurements by Rog et al. [32] was used to fit the CA_6 compounds, although their values were largely ignored for the other compounds in the system due to their disagreement with the enthalpy values.

The $C_{12}A_7$ phase was modelled separately from the rest of the compounds. For this compound, again King [26] and Bonnickson [28] measured the heat capacity and the relative enthalpy, respectively. The heat of formation was measured by Coughlin [31] at 298 K and Ayed et al. [33] at 1173 K. The value by Ayed et al. was in disagreement with the other measurements for this compound, so were excluded from the fit.

The thermodynamic properties of these compounds were evaluated and assessed and were fit using the 3rd generation model. The coefficients and the data used to fit the thermodynamic properties of the compounds in this system are presented in Appendix A.1.

6.3.3 Melt model

To fit the melt phase of the system, the associate model was used with associates of the oxide end-members CaO and $Al_1O_{1.5}$ (to represent the Al_2O_3 species). In addition to this, it was necessary to make use of the C_3A associate, which differs slightly from the assessment by Hallstedl, who made use of an CA species in the melt. In addition, to needing this associate in the binary melt, this associate makes the fitting of the $CaO-Al_2O_3-SiO_2$ system easier by providing a good “anchor” point for the alumina rich regions. The full parameter set can be seen in Table 6.4.

Table 6.4: Table showing the functions optimised in the present work for the melt phase in the $CaO-Al_2O_3$ system.

Thermodynamic Properties of the C-A melt phase

Liquid ($A_{0.5}, C_3A_1, C$):

$$G_{A_{0.5}} = 0.5 * G_{Al_2O_3,Liquid}$$

$$G_C = G_{CaO,Liquid}$$

$$G_{C_3A} = 1 * G_{Al_2O_3,Liquid} + 3 * G_{Al_2O_3,Liquid} - 150837.716392695$$

$$L_{A_{0.5},C_3A,1} = -267094 + 55.68T$$

$$L_{A_{0.5},C,0} = -108365.44 + 2.99T$$

$$L_{C_3A_1,C,0} = -73232 + 45.95T$$

The optimised phase diagram excluding the $C_{12}A_7$ solid phase is presented in Fig. 6.4 and shows excellent agreement with the experimental data, as well as the agreement with the phase diagram presented by Hallstedl [23]. A summary of invariant points in the $CaO-Al_2O_3$ system are presented in Table 6.5.

With the melt phase of the $CaO-Al_2O_3$ modelled, the newly fit $C_{12}A_7$ compound was added to the optimised system. The optimised phase diagram including the $C_{12}A_7$ compound is presented in Fig. 6.5. Inclusion of the assessed $C_{12}A_7$ phase exhibits an increase in the liquidus temperature, roughly on the order of 50 K, when compared to the phase

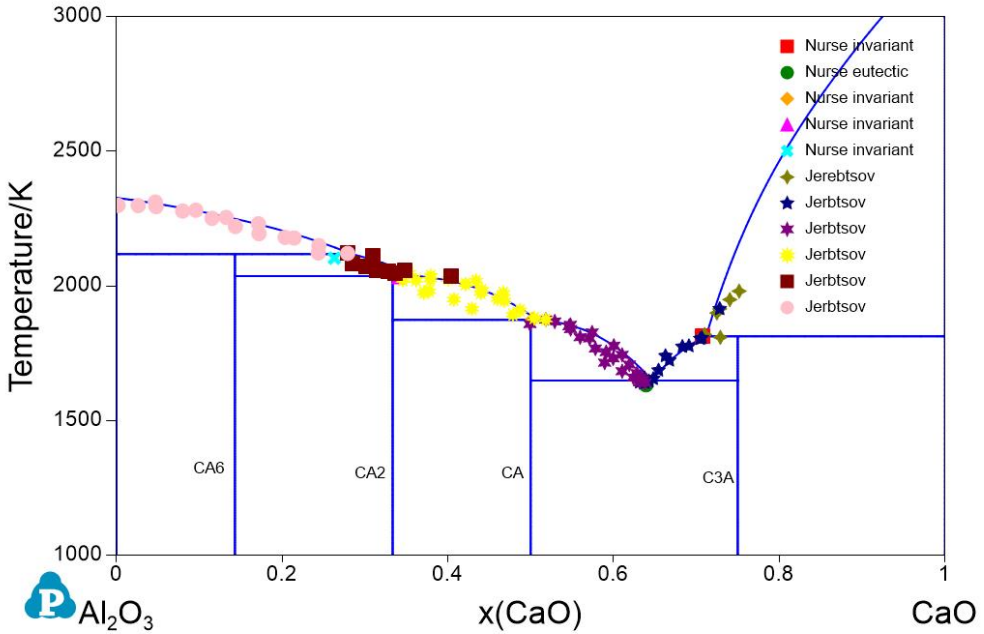


Figure 6.4: Phase diagram of the optimised $\text{CaO}-\text{Al}_2\text{O}_3$ compared against the experimental points from Jerebtsov [22] and Nurse [20].

Table 6.5: Summary of the invariant points in the $\text{CaO}-\text{Al}_2\text{O}_3$ phase diagram. Values in parentheses are experimental points from Nurse et al.

Equilibrium	T/K	$x(\text{Al}_2\text{O}_3)$ in liquid
Liquid + $\text{Al}_2\text{O}_3 + \text{C}_3\text{A}$	1813 (1814)	0.28 (0.29)
Liquid + CA + C_3A	1649 (1635)	0.35 (0.36)
Liquid + CA + CA ₂	1873 (1877)	0.49 (0.50)
Liquid + CA ₂ + CA ₆	2036 (2038)	0.63 (0.66)
Liquid + CA ₆ + Al_2O_3	2117 (2106)	0.71 (0.74)

diagram of Hallstedl. This change corresponds to the new heat of formation used to fit the C_{12}A_7 . For better results, the melt phase should be refit, with the inclusion of the C_{12}A_7 , however experimental data is lacking in this section. Despite this, a satisfactory phase diagram is achieved for OPC applications.

The $\text{CaO}-\text{Al}_2\text{O}_3$, is very important for OPC clinkers, as it contains the C_3A major clinker phase. The solid compounds were re-fit with new DFT data, and the melt phase was well modelled when compared against experimental values and the results of previous assessments [23]. This work will play a major role in the modelling of the ternary $\text{CaO}-\text{Al}_2\text{O}_3-\text{SiO}_2$ system and more importantly the melt phase.

6.4 $\text{CaO}-\text{Al}_2\text{O}_3-\text{SiO}_2$

The three binary systems: $\text{CaO}-\text{SiO}_2$, $\text{Al}_2\text{O}_3-\text{SiO}_2$, and $\text{CaO}-\text{Al}_2\text{O}_3$ have been optimised and have produced satisfactory recalculations of the experimental data. In the next

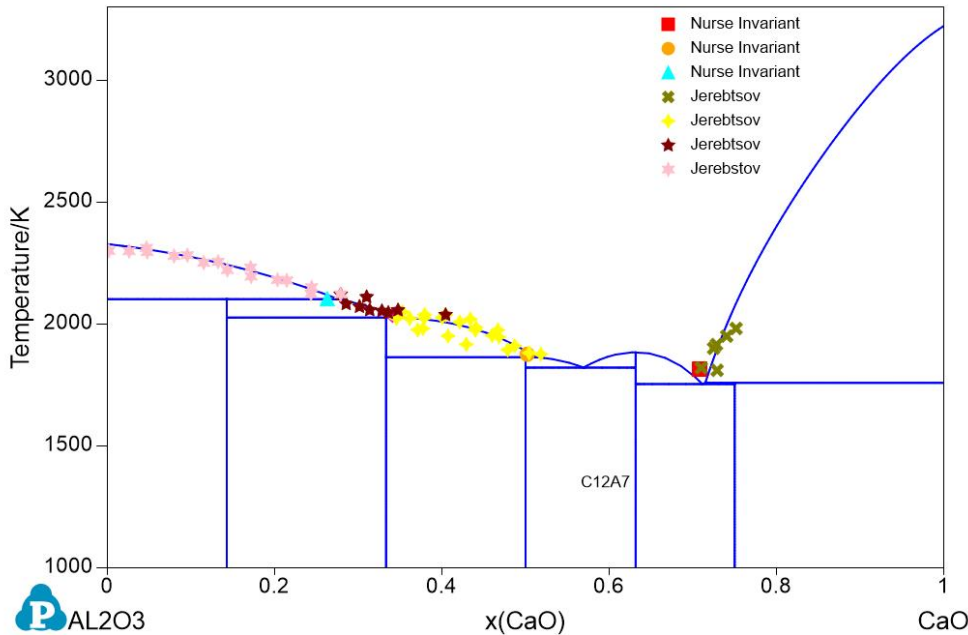


Figure 6.5: CaO- Al_2O_3 phase diagram including the $C_{12}A_7$, optimised in the present work.

instance, the modelling of the ternary CaO- Al_2O_3 - SiO_2 system can begin. At first, the extrapolative nature of CALPHAD is presented by simply combining the binary systems, then the ternary system can be optimised, including the ternary compounds which exist in the system: anorthite ($CaAl_2Si_2O_8$) and gehlenite ($Ca_2Al_2SiO_7$) also known as CAS_2 and C_2AS respectively.

6.4.1 Extrapolation of the binary systems

Simply combining the three optimised binaries, results in a Mugginue extrapolation of the ternary. This extrapolation calculation is described in detail in Section 4.1, but it is built into all thermodynamic packages. The extrapolative nature of the CALPHAD is useful, resulting in a reasonably well-fit ternary phase diagram. It was found by De Noirlfontaine et al. [34] that the extrapolation of the binary systems models the ternary melt in the clinkering zone (for OPC) well and can be used to carry out calculations at the OPC clinker composition and temperature, with results being within experimental uncertainty. Additionally, the extrapolation step allows us to see if there are any errors in the models of binary systems. If there are any errors with the binary models, irregular features would be observed e.g. miscibility gaps or binary solids being re-stabilised or too stable. This provides a “check” that the binary systems were modelled correctly. The extrapolated ternary is presented in Fig 6.6 and shows a good starting point in the region of interest and agreement with the results of [34].

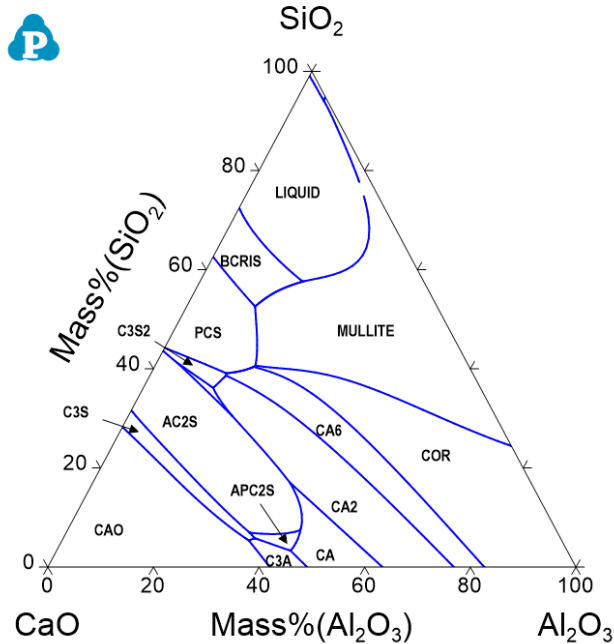


Figure 6.6: Ternary CaO-SiO₂-Al₂O₃ liquidus projection, extrapolated from the binary section, i.e. does not contain ternary phases/parameters.

6.4.2 Modelling the ternary system

Once satisfied with the initial phase diagram and the binary descriptions, the ternary is optimised further against the experimental phase diagram data. This first involves assessing the ternary compounds CAS₂ and C₂AS using the 3rd generation model. Two other compounds also exist in the ternary: grossular and clinopyroxene, but are only stable at high pressure so were not included in the optimisation for relevance to cement applications. The low-temperature heat capacity was measured by Hemingway and Robie for gehlenite [35] and by King for anorthite [36]. High-temperature measurements were carried out by Pankratz and Kelly [37] for the gehlenite solid, with the enthalpy of formation measured by Charlu et al. [38]. For the anorthite phase, high-temperature relative enthalpy data was measured by Courtial et al. [39] and the heat of formation was again measured by Charlu et al. [38]. The resulting parameters for the 3rd generation fit of the gehlenite and anorthite phases are presented in Table A.2 in the Appendix.

At this stage, additional parameters are added to the ternary melt phase. The choice in this has increased complexity as there is a choice between adding new binary parameters between different systems or adding ternary parameters. It is ideal to leave the optimised parameters of the binary systems “frozen”. There is great difficulty in reducing the size of the liquid miscibility gap which forms from the CaO-SiO₂ system, which was also found by previous assessments from MaO et al. [24] and Eriksson and Pelton [13]. In both cases, large positive parameters were used in that region to suppress the miscibility gap to reproduce the experimental points. This proved difficult to optimise in the present work, mainly due to equilibrium errors in that region, so that region was left unfit, which isn’t an issue for cement applications which are never that silica rich [1, 34]. Instead, the

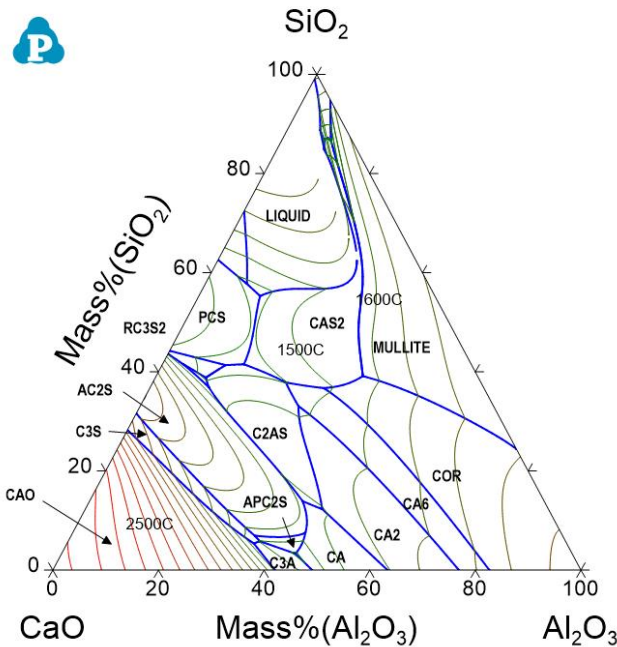


Figure 6.7: Ternary liquidus projection of the optimised CaO - Al_2O_3 - SiO_2 system, with isotherm lines calculated at every 100°C .

main area of concern that was fit was the liquidus temperature in the clinkering zone (see Figure 6.1). In this effort, a $\text{C}_{0.5}\text{A}_{0.5}\text{S}_1$ associate was added to represent the CAS_2 species in the melt. This associate was optimised to the enthalpy of fusion of CAS_2 and the congruent melting temperature measured by Weill [40]. The expression for the $\text{C}_{0.5}\text{A}_{0.5}\text{S}_1$ associate is as follows,

$$G_{\text{C}_{0.5}\text{A}_{0.5}\text{S}_1,liquid} = 0.5 * G_{C,liquid} + 0.5 * G_{A,liquid} + 1 * G_{S,liquid} - 85250 + 15 * T. \quad (6.4.1)$$

This was combined with the binary melt phase parameters and no additional parameters were added to the CaO - Al_2O_3 - SiO_2 ternary system. The resultant ternary projection can be seen in Figure 6.7. A comparison of experimental and calculated invariant points is also presented in Table 6.6 and shows reasonable agreement within a few degrees and mass %. This is to be expected due to the poor fitting of the miscibility as well as the inclusion of the C_{12}A_7 phase within the experimental measurements. The maximum discrepancy in the temperature is roughly 50°C , which is similar to the error reported by MaO et al. [24]. Whilst the phase diagram does not entirely agree with previous assessments due to the miscibility gap, the zone of interest for OPC clinkers is well captured. To verify this, the optimised ternary system was used for equilibrium calculations at the clinkering temperature for a typical Portland cement composition, similar to the calculations carried out by De Noirfontaine et al. [34]. This results in proportions that are close to the experimental data, which are presented in Table 6.7. The results show better agreement with the experimental data at 1500°C than the previously calculated values, but overpredicts the value of the C_2S at 1400°C compared with the experimental values.

Table 6.6: Table of the invariant points within the CaO-Al₂O₃-SiO₂ system. The experimental values from Osborn and Muan [41] are in parentheses.

Phases	T/C	Liquid Composition/ wt %		
		CaO	Al ₂ O ₃	SiO ₂
CA ₂ + C ₂ AS + CA ₆	1473 (1472)	36.9 (31.2)	29.9 (44.6)	33.06 (24.2)
C ₂ AS + Al ₂ O ₃ + mullite	1552 (1514)	21.7 (15.5)	39.1 (36.7)	39.1 (47.8)
C ₂ AS + CAS ₂ + PCS	1309 (1267)	43.0 (37.9)	15.4 (20.1)	41.5 (42.0)
PCS + C ₃ S ₂ + C ₂ AS	1315 (1312)	46.5 (47.3)	12.0 (12.0)	41.3 (40.7)
C ₂ S + C ₃ S ₂ + C ₂ AS	1330 (1317)	51.6 (48.9)	11.6 (11.8)	33.1 (39.3)
CA ₂ + CA + C ₂ AS	1492 (1502)	42.8 (53.1)	44.8 (37.5)	12.3 (9.4)
C ₂ AS + Al ₂ O ₃ + CA ₆	1478 (1446)	30.3 (27.5)	32.9 (39.6)	36.7 (32.9)
C ₂ AS + CA + C ₂ S	1472 (1461)	45.7 (49.3)	40.3 (37.0)	13.9 (13.6)
CaO + C ₃ S + C ₃ A	1426 (1472)	59.2	35.3 (32.8)	5.3 (7.5)
CA ₆ + CAS ₂ + C ₂ AS	1395 (1382)	36.9	25.1	37.8 (31.0)

Table 6.7: Table comparing the values of the weight % of the phases present in the equilibrium at a typical “white” OPC composition: 70% CaO, 25% SiO₂, 5% Al₂O₃. The values compared are from the present work, the calculated values from De Noirfontaine et al. [34] and experimental values from Rankin and Wright [21].

Phases	Present work	Noirfontaine et al.	Experimental
T=1400°C			
Liquid	13.8	15.7	13
α'-C ₂ S	17.5	14.8	16
C ₃ S	68.6	69.5	71
T=1500°C			
Liquid	15.5	18.6	14
α'-C ₂ S	16.7	12.1	16
C ₃ S	67.6	69.3	70

Additionally, the calculated composition of the melt phase at the 1400°C and 1500°C is presented in Table 6.8, with excellent agreement against the experimental data, but a disagreement in the SiO₂ value at 1400°C, which may account for the increased C₂S phase.

6.5 Conclusion

In this chapter, the step-by-step modelling of the most important ternary system CaO-Al₂O₃-SiO₂ was described. With just the information on the binary systems in this ternary, a favourable phase diagram was produced for Portland cement applications, due to the area of interest existing in a small compositional range of the ternary phase diagram. Finally, the ternary compounds and additional associates were added to fit the ternary system against the experimental phase diagram data, resulting in an optimised ternary melt.

The resulting CaO-Al₂O₃-SiO₂ phase diagram is satisfactory in modelling the thermo-

Table 6.8: Table comparing the values of the wt % of the components within the liquid phase present in the equilibrium with C_2S and C_3S . The values compared are from the present work, the calculated values from the assessment of Mao et al. [24] and experimental values from Rankin and Wright [21].

Components	Present work	Mao et al.	Experimental
T=1400°C			
CaO	57.9	57.7	55
Al_2O_3	36.1	31.8	37
SiO_2	5.9	10.5	8
T=1500°C			
CaO	59.2	59.5	59
Al_2O_3	32.0	26.9	32
SiO_2	8.6	13.6	9

dynamics of OPC clinkers. This is further supported by the initial calculations using the optimised system showing satisfactory results when compared against the experimental values and the calculated values of the previous assessment. It is, therefore, favourable to carry the information within this system forward to carry out further predictive calculations. However, whilst the majority of the information is captured by just this ternary system, conducting detailed calculations at this stage at the clinkering temperature does not result in accurate proportions of the phases due to the melt temperature being too high. Furthermore, the ferrite phase is not yet included in this system. Within the cement kiln, the lowering of the melt temperature is achieved by the presence of iron-containing compounds and the formation of the ferrite phase. This makes the next important component to be added to the thermodynamic database, Fe, which is discussed in the next chapter.

6.6 References

- [1] H.F.W. Taylor. *Cement chemistry*. 2nd edition. Thomas Telford Publishing, 1997. DOI: 10.1680/cc.25929.
- [2] Guillaume Deffrennes, Noël Jakse, Cecilia M.S. Alvares, Ioana Nuta, Alain Pasturel, Alexandra Khvan and Alexander Pisch. ‘Thermodynamic modelling of the Ca-O system including 3rd generation description of CaO and CaO_2 ’. In: *Calphad* 69 (2020), p. 101764. DOI: 10.1016/j.calphad.2020.101764.
- [3] I. Bajenova, A. Khvan, A. Dinsdale and A. Kondratiev. ‘Implementation of the extended Einstein and two-state liquid models for thermodynamic description of pure SiO_2 at 1 atm’. In: *Calphad* 68.101716 (2020). DOI: 10.1016/j.calphad.2019.101716.
- [4] ‘A Critical Assessment of Thermodynamic and Phase Diagram Data for the Al-O System’. In: *Calphad* 16.2 (1992), pp. 173–179. DOI: 10.1016/0364-5916(92)90005-I.

- [5] ‘Investigation of the thermodynamic properties of γ -Al₂O₃’. In: *Thermochimica Acta* 253 (1995), pp. 33–39. DOI: 10.1016/0040-6031(94)01969-N.
- [6] H A Wriedt. ‘The Al-O (Aluminum-Oxygen) system’. In: *Bulletin of Alloy Phase Diagrams* 6.6 (1985), pp. 548–553. DOI: 10.1007/bf02887157.
- [7] Igor Levin and David Brandon. ‘Metastable Alumina Polymorphs: Crystal Structures and Transition Sequences’. In: *Journal of the American Ceramic Society* 81.8 (1998), pp. 1995–2012. DOI: 10.1111/j.1151-2916.1998.tb02581.x.
- [8] Zhihui Zhang and Nan Li. ‘Effect of polymorphism of Al₂O₃ on the synthesis of magnesium aluminate spinel’. In: *Ceramics International* 31.4 (2005), pp. 583–589. DOI: 10.1016/j.ceramint.2004.06.025.
- [9] N. L. Bowen and J. W. Greig. ‘THE SYSTEM: Al₂O₃-SiO₂’. In: *Journal of the American Ceramic Society* 7.4 (1924), pp. 238–254. DOI: 10.1111/j.1151-2916.1924.tb18190.x.
- [10] Shigeo Aramaki and Rustum Roy. ‘Revised phase diagram for the system Al₂O₃-SiO₂’. In: *Journal of the American Ceramic Society* 45.5 (1962), pp. 229–242.
- [11] Mats Hillert, Bo Sundman and Xizhen Wang. ‘A Thermodynamic Evaluation of the Al₂O₃-SiO₂ System’. 1989.
- [12] Huahai Mao, Malin Selleby and Bo Sundman. ‘Phase Equilibria and Thermodynamics in the Al₂O₃-SiO₂ System-Modeling of Mullite and Liquid’. In: *Journal of the American Ceramic Society* 88.9 (2005), pp. 2544–2551. DOI: 10.1111/j.1551-2916.2005.00440.x.
- [13] Gunnar Eriksson and Arthur D Pelton. ‘Critical evaluation and optimization of the thermodynamic properties and phase diagrams of the CaO-Al₂O₃, Al₂O₃-SiO₂, and CaO-Al₂O₃-SiO₂ systems’. In: *Metallurgical Transactions B* 24.5 (1993), pp. 807–816. DOI: 10.1007/BF02663141.
- [14] Frederic J Klug, Svante Prochazka and Robert H Doremus. ‘Alumina-silica phase diagram in the mullite region’. In: *Journal of the American Ceramic Society* 70.10 (1987), pp. 750–759.
- [15] Reed A Howald and I Eliezer. ‘The thermodynamic properties of mullite’. In: *The Journal of Physical Chemistry* 82.20 (1978), pp. 2199–2204.
- [16] Bruce S. Hemingway, Richard A. Robie, Howard T. Evans and Derrill M. Kerrick. ‘Heat capacities and entropies of sillimanite, fibrolite, andalusite, kyanite, and quartz and the Al₂SiO₅ phase diagram’. In: *American Mineralogist* 76.9-10 (Oct. 1991), pp. 1597–1613.
- [17] J. L. Holm and O. J. Kleppa. ‘The thermodynamic properties of the aluminum silicates’. In: *The Journal of Physical Chemistry* 70.5 (1966), p. 1690. DOI: 10.1021/j100877a519.

- [18] John Gisby, Pekka Taskinen, Jouni Pihlasalo, Zushu Li, Mark Tyrer, Jonathan Pearce, Katri Avarmaa, Peter Björklund, Hugh Davies, Mikko Korpi, Susan Martin, Lauri Pesonen and Jim Robinson. ‘MTDATA and the Prediction of Phase Equilibria in Oxide Systems: 30 Years of Industrial Collaboration’. In: *Metallurgical and Materials Transactions B* 48.1 (2017), pp. 91–98. DOI: 10.1007/s11663-016-0811-x.
- [19] Robert F. Davis and Joseph A. Pask. ‘Diffusion and Reaction Studies in the System Al_2O_3 - SiO_2 ’. In: *Journal of the American Ceramic Society* 55.10 (1972), pp. 525–531. DOI: 10.1111/j.1151-2916.1972.tb13421.x.
- [20] RW Nurse, JH Welch and Amalendu Jyoti Majumdar. ‘The CaO - Al_2O_3 system in a moisture-free atmosphere’. In: *Transactions of the Ceramic Society B* 64.9 (1965), pp. 409–418.
- [21] G. A. Rankin and F. E. Wright. ‘The ternary system CaO - Al_2O_3 - SiO_2 ’. In: *American Journal of Science* s4-39.229 (1915), pp. 1–79. DOI: 10.2475/ajs.s4-39.229.1.
- [22] DA Jerebtsov and GG Mikhailov. ‘Phase diagram of CaO - Al_2O_3 system’. In: *Ceramics International* 27.1 (2001), pp. 25–28.
- [23] Bengt Hallstedl. ‘Assessment of the CaO - Al_2O_3 system’. In: *Journal of the American ceramic society* 73.1 (1990), pp. 15–23.
- [24] Huahai Mao, Mats Hillert, Malin Selleby and Bo Sundman. ‘Thermodynamic assessment of the CaO - Al_2O_3 - SiO_2 system’. In: *Journal of the American Ceramic Society* 89.1 (2006), pp. 298–308.
- [25] Huahai Mao, Malin Selleby and Bo Sundman. ‘A re-evaluation of the liquid phases in the CaO - Al_2O_3 and MgO - Al_2O_3 systems’. In: *Calphad* 28.3 (2004), pp. 307–312.
- [26] E G King. ‘Heat Capacities at Low Temperatures and Entropies at 298.16°K. of Crystalline Calcium and Magnesium Aluminates’. In: *The Journal of Physical Chemistry* 59.3 (1955), pp. 218–219. DOI: 10.1021/j150525a005.
- [27] H Elsner von Gronow and H E Schwiete. ‘Die spezifischen Wärmen von CaO , Al_2O_3 , $\text{CaO} \cdot \text{Al}_2\text{O}_3$, $3 \text{CaO} \cdot \text{Al}_2\text{O}_3$, $2 \text{CaO} \cdot \text{SiO}_2$, $3 \text{CaO} \cdot \text{SiO}_2$, $2 \text{CaO} \cdot \text{Al}_2\text{O}_3 \cdot \text{SiO}_2$ von 20° bis 1500° C’. In: *Zeitschrift für anorganische und allgemeine Chemie* 216.2 (1933), pp. 185–195. DOI: 10.1002/zaac.19332160212.
- [28] K R Bonnickson. ‘High Temperature Heat Contents of Aluminates of Calcium and Magnesium’. In: *The Journal of Physical Chemistry* 59.3 (1955), pp. 220–221. DOI: 10.1021/j150525a006.

- [29] Charles A. Geiger, Ole Jakob Kleppa, Bjorn O. Mysen, James M. Lattimer and Lawrence Grossman. ‘Enthalpies of formation of CaAl_4O_7 and $\text{CaAl}_{12}\text{O}_{19}$ (hibonite) by high temperature, alkali borate solution calorimetry’. In: *Geochimica et Cosmochimica Acta* 52 (1988), pp. 1729–1736. DOI: 10.1016/0016-7037(88)90241-4.
- [30] Isaac Eliezer, Naomi Eliezer, Reed A Howald and Puligandla Viswanadham. ‘Thermodynamic properties of calcium aluminates’. In: *The Journal of Physical Chemistry* 85.19 (Sept. 1981), pp. 2835–2838. DOI: 10.1021/j150619a028.
- [31] James P Coughlin. ‘Heats of Formation of Crystalline $\text{CaO} \cdot \text{Al}_2\text{O}_3$, $12\text{CaO} \cdot 7\text{Al}_2\text{O}_3$, and $3\text{CaO} \cdot \text{Al}_2\text{O}_3$ ’. In: *Journal of the American Chemical Society* 78.21 (Nov. 1956), pp. 5479–5482. DOI: 10.1021/ja01602a005.
- [32] G. Róg, A. Kozlowska-Róg, K. Zakula-Sokól and G. Borchardt. ‘Determination of the standard Gibbs free energies of formation of the calcium aluminates from the oxides by e.m.f. measurements’. In: *The Journal of Chemical Thermodynamics* 25.7 (1993), pp. 807–810. DOI: 10.1006/jcht.1993.1078.
- [33] F. Ayed, F. Sorrentino and R. Castanet. ‘Determination par calorimetrie de dissolution des enthalpies de formation de quelques silicates, alumates et alumino-silicates de calcium’. In: *Journal of Thermal Analysis and Calorimetry* 41.4 (1994), pp. 755–766. DOI: 10.1007/bf02547157.
- [34] M. N. De Noirlfontaine, S. Tusseau-Nenez, C. Girod-Labianca and V. Pontikis. ‘CALPHAD formalism for Portland clinker: Thermodynamic models and databases’. In: *Journal of Materials Science* 47.3 (2012), pp. 1471–1479. DOI: 10.1007/s10853-011-5932-7.
- [35] Bruce S Hemingway and Richard A Robie. ‘Heat capacity and thermodynamic functions for gehlenite and staurolite: with comments on the Schottky anomaly in the heat capacity of staurolite’. In: *American Mineralogist* 69.3-4 (1984), pp. 307–318.
- [36] E. G. King. ‘Low Temperature Heat Capacities and Entropies at 298.15°K of Some Crystalline Silicates Containing Calcium’. In: *Journal of the American Chemical Society* 79.20 (1957), pp. 5437–5438. DOI: 10.1021/ja01577a028.
- [37] Louis B Pankratz and Kenneth Keith Kelley. *High-temperature heat contents and entropies of akermanite, cordierite, gehlenite, and merwinite*. Vol. 6555. US Department of the Interior, Bureau of Mines, 1964.
- [38] T V Charlu, R C Newton and O J Kleppa. ‘Enthalpy of formation of some lime silicates by high-temperature solution calorimetry, with discussion of high pressure phase equilibria’. In: *Geochimica et Cosmochimica Acta* 42.4 (1978), pp. 367–375. DOI: 10.1016/0016-7037(78)90267-3.

- [39] P Courtial, C Tequi and P Richet. ‘Thermodynamics of diopside, anorthite, pseudo-wollastonite, $CaMgGeO_4$ -olivine and akermanite up to near the melting point’. In: *Physics and Chemistry of Minerals* 27 (2000), pp. 242–250. DOI: 10.1007/s002690050253.
- [40] ‘The enthalpy of fusion of anorthite’. In: *Contributions to Mineralogy and Petrology* 74.1 (1980), pp. 95–102. DOI: 10.1007/bf00375493.
- [41] E. F. Osborn and A. Muan. *Phase Equilibrium Diagrams of Oxide Systems. The System CaO- Al_2O_3 - SiO_2* . Ed. by Edward Orton. American Ceramic Society, 1960.

CHAPTER
SEVEN

MODELLING FERRITE: CAO-AL₂O₃-FE-O

Fe₂O₃ is an important component in the modelling of OPC clinkers. Iron is first essential in modelling the ferrite clinker phase C₄AF. The addition of iron in the system also allows a melt to be formed at the appropriate clinker temperature which is roughly 1450°C. Without iron, the CaO-Al₂O₃-SiO₂ system does not produce a melt at a low enough temperature facilitating the appropriate solid precipitations [1].

However, with the addition of Fe₂O₃, an issue was realised. Up until this point, the effects of oxygen were ignored and each component of the database made use of only oxides. This was possible due to the fact that the oxides: CaO, Al₂O₃ and SiO₂ do not structurally change with changing oxygen partial pressures i.e., only one oxidation state exists for the metallic ions. In Fig. 7.1, an example of the Ca-O phase diagram can be seen, the CaO solid is stoichiometric up until melting and exists in all parts of the phase diagram, there is a small section at very high oxygen concentrations that forms CaO₂, but this can be ignored due to the small area of stability in conditions not critical for OPC application, this allows us to ignore the effects of oxygen on Ca. This is not the case for iron. Fe (iron) can exist as Fe²⁺ and Fe³⁺ and the concentration of these are very dependent on the partial pressure of oxygen, with Fe²⁺ forming a solid solution of FeO that can also contain Fe³⁺ ions. Whilst, the main species of interest is Fe₂O₃, in reality modelling iron without the inclusion of the Fe²⁺ ions and therefore FeO may cause great errors in the resulting calculation, as Fe₂O₃ (hematite) phase melts into the magnetite phase (see Fig. 7.2), removing this results in a higher Fe₂O₃ melting temperature.

This results in modelling iron as a combination of Fe and O, which is then added to the CaO-Al₂O₃-SiO₂ database. This drastically increases the size of the problem as more binary and ternary phase diagrams have to be optimised; however, because OPC clinkers exist within small areas in the full thermodynamic system, some thermodynamic sections outside the clinker composition can be ignored.

Therefore, only the modelling of the important sections containing iron, is attempted, which includes the CaO-Fe₂O₃ section. This section includes the ferrite end member C₂F, allowing for the modelling of the C₂F-C₂A section. This will complete the model of the ferrite clinker phase for OPC applications. For additional benefit, the Fe₂O₃-SiO₂ system

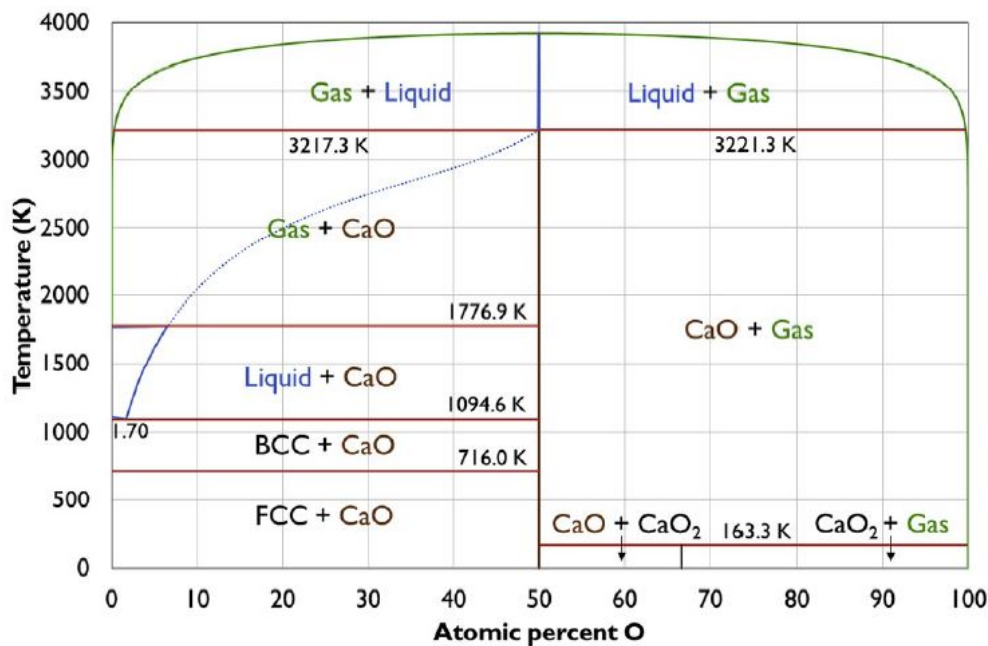


Figure 7.1: Ca-O phase diagram taken from the assessment carried out by Deffrennes et al[2].

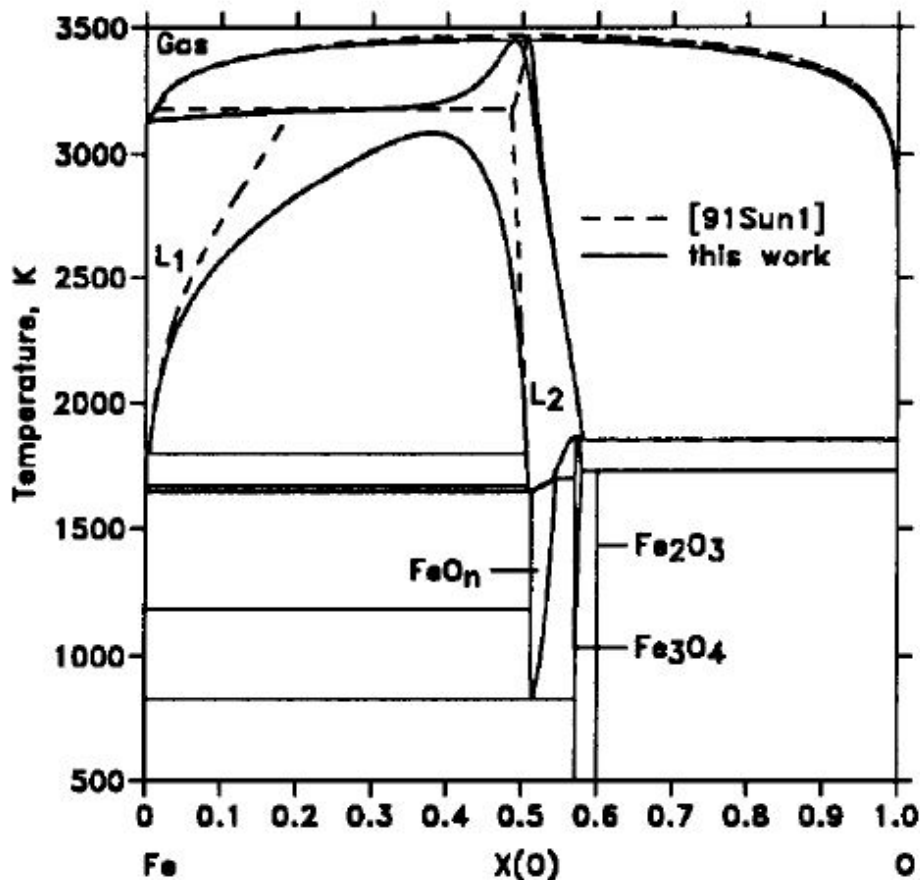


Figure 7.2: Fe-O phase diagram taken from the assessment carried out by Kowalski and Spencer[3].

is modelled which helps constrain the melt phase. Ideally modelling the $\text{Al}_2\text{O}_3\text{-Fe}_2\text{O}_3$ would provide a greater model for the overall melt, but it was found to not be needed to produce an accurate clinker model.

7.1 Fe-O model

To model these sections and the ferrite phase, first a Fe-O model which includes the solids of FeO and Fe_2O_3 was included. Instead of refitting the Fe-O system, it was decided to use the model parameters calculated by Kowalski and Spencer [3], who used an associates model to model the Fe-O system. This model is compatible with the models current thermodynamic database, and even though it is not a 3rd generation model (which was attempted in the first instance), the functions calculated by Kowalski and Spencer [3] reproduced the experimental data well. However, in their model, they ignored the magnetic properties of the iron phases. To overcome this, the magnetic properties discussed in the Fe-O assessment carried out by Sundman [4] was added in the final Fe-O assessment.

In the associates model for this system, Kowalski and Spencer [3] made use of the FeO and $\text{FeO}_{1.5}$ (this is chosen to represent Fe_2O_3) associates as well as a Fe and an O associate in the melt phase. The important associates and parameters for the present work were the FeO and $\text{FeO}_{1.5}$ species. The Fe-O model as optimised by Kowalski and Spencer is presented in Table 7.1. For the solid spinel (Fe_3O_4), wüstite (FeO) and hematite (Fe_2O_3) in the Fe-O system, the thermodynamic functions and parameters, were taken from the work of Sundman [4], as was suggested by Kowalski and Spencer [3].

7.2 CaO- Fe_2O_3

In this work, the $\text{CaO}\text{-}\text{Fe}_2\text{O}_3$ pseudo-binary section was computed from the $\text{CaO}\text{-Fe-O}$ ternary system. The $\text{CaO}\text{-}\text{Fe}_2\text{O}_3$ section is very important in modelling the ferrite clinker phase, as this section contains the ferrite end-member C_2F . Modelling this end-member accurately reduces the degrees of freedom in the ferrite phase which in theory makes the modelling easier. In addition to the C_2F phase, this section also includes the stoichiometric compounds CF and CF_2 .

7.2.1 Literature review of the solid phases

At normal pressures, three stoichiometric compounds exist in the $\text{CaO}\text{-}\text{Fe}_2\text{O}_3$ system: $\text{Ca}_2\text{Fe}_2\text{O}_5$ (C_2F), CaFe_2O_4 (CF) and CaFe_4O_7 (CF_2) (which at normal pressures exists in a very small region of the phase diagram). The low-temperature heat capacity was measured by King [5] for both the C_2F and CF compounds. Similarly, the high-temperature relative enthalpy was measured by Bonnickson [6] for both compounds. The enthalpy of formation from the oxides was measured at 1125 K for the C_2F and CF compounds by

Table 7.1: Table of the parameters and thermodynamic functions for the liquid and pure iron phases in the Fe-O system taken from Kowalski and Spencer [3].

Phase	Model
Liquid	(Fe, FeO, FeO1.5)
G(Fe) = GFELIQ	
G(FeO) = GFEO +34008 -20.969*T	
G(FeO1.5) = 0.5 GFE2O3 + 39712 - 20.007*T	
L(Fe, FeO, 0) = 109625.2 - 20.050*T	
L(Fe, FeO, 1) = 26317.9 - 11.072*T	
L(Fe, FeO1.5, 0) = 81541.2	
L(FeO, FeO1.5, 0) = -13353.8	
L(FeO, FeO1.5, 1) = 6707.07	
FCC	(Fe)1(O, Va)1
G(Fe:Va) = GFEFCC	
G(Fe:O) = GFECC + GOSOL	
L(Fe:O, Va, 0) = -168758 + 19.17*T	
BCC	(Fe)1(O, Va)3
G(Fe:Va) = GHSERFE	
G(Fe:O) = GHSERFE + 3*GOSOL	
L(Fe:O, Va, 0) = -517549 + 71.83*T	
GAS	(O1, O2, O3, Fe, FeO)
G(O1) = GO1GAS	
G(O2) = GO2GAS	
G(O3) = GO3GAS	
G(Fe) = GFEGAS	
G(FeO) = GFEOGAS	
Thermodynamic functions	
<i>The thermodynamic functions for the gas phase components taken from the SGTE database</i>	
GFEO3 298.15 - 3000	-858683 + 827.946*T -137.0089*T*LN(T) +1453810/T
GFEO 298.15-3000	- 279318 + 252.848*T - 46.12826*T*LN(T) - 5.7402984E^-3*T^2
GFELIQ 298.15 - 1811	12040.17 - 6.55843*T - 3.6751551E^-21*T^7 + GHSERFE
GFELIQ 1811- 6000	- 10839.7 + 291.302*T - 46*T*LN(T)
GHSERFE 298.15 - 1811	1225.7 + 124.134*T - 23.5143*T*LN(T) - 0.00439752*T^2 - 5.89269E^-8*T^3 + 77358.5*T^-1
GHSERFE 1811- 6000	- 25383.451 + 299.31255 T - 46 T*LN(T) + 2.2960305E+31*T^-9
GFEFCC 298.15 - 1811	- 1462.4 + 8.282*T - 1.15*T*LN(T) + 6.4E-4*T^2+ GHSERFE
GFEFCC 1811- 6000	- 27098.26 + 300.25256*T - 46*T*LN(T) + 2.7885E+31*T^-9

Jacob [7], with an additional measurement from Newman and Hoffman at 298 K for the C₂F compound [8]. The thermodynamic properties of the C₂F and CF compounds were fit with the 3rd generation model and the full parameters are presented in the Appendix in Table A.1.

The CF₂ is difficult to discuss and fit, due to a lack of thermodynamic data present in the literature. This is mostly due to the changing stability of the compound due to the pressure. At normal pressures Phillip and Muan [9] found the CF₂ existing from 1503-1453 K, with Bergman [10] reporting stability down to 1398 K, however, this is not a generally agreed value and the values of Phillip and Muan [9] were used in the present work. Due to the lack of thermodynamic measurements, the CF₂ compounds were fit using Neumann-Kopp [11] rule from the solid oxides with additional enthalpy and entropy parameters to fit the stability of the compound. The following expression was used to model the CF₂ compound,

$$G_{CF_2} = G_{CaO} + 2 * G_{Fe_2O_3} + A + B * T, A = 12500, B = -30 \quad (7.2.1)$$

where A is the enthalpy parameter and B is the entropy parameter used for fitting. The resultant heat capacity and enthalpy values were then compared against the values in the FTOX database [12].

7.2.2 Phase diagram

The phase diagram for the CaO-Fe₂O₃ pseudo section was measured by Phillips and Muan [9] in air and pure oxygen at 1 atm. While these measurements are not truly in the CaO-Fe₂O₃ section as the iron in their measurements is not fully oxidised to Fe³⁺, the measurements at 1 atm oxygen are close to the desired section and were used to fit the phase diagram.

Hillert et al. [13] carried out an assessment of the Ca-Fe-O system using a two-sublattice model, with a reassessment of their parameters carried out by Selleby and Sundman [14]. In the reassessment, the authors found it necessary to use a species to represent the Fe₂O₃ species present in the melt, This was necessary to avoid miscibility gaps in the quarternary system Ca-Fe-O-Si [15]. Hidayat et al. [16] used a MQM model for their assessment of the Ca-Fe-O system and had similar results for their calculation of the CaO-Fe₂O₃ section. A comparison of the two assessments is presented in Fig. 7.3. In the present work, the associates model was used to fit the phase diagram data from Phillips and Muan [9]. The optimised phase diagram is presented in Figure 7.4, with the optimised parameters presented in Table 7.2. The section optimised in the present work matches closely with experimental values and the values of the previous assessment. The calculated congruent melting point of C₂F is at 1720 K which matches the observations of Phillips and Muan [9]. Furthermore, stability of the CF₂ is closely matched to the experimental values [9, 17]. The only difference between the previous assessments and

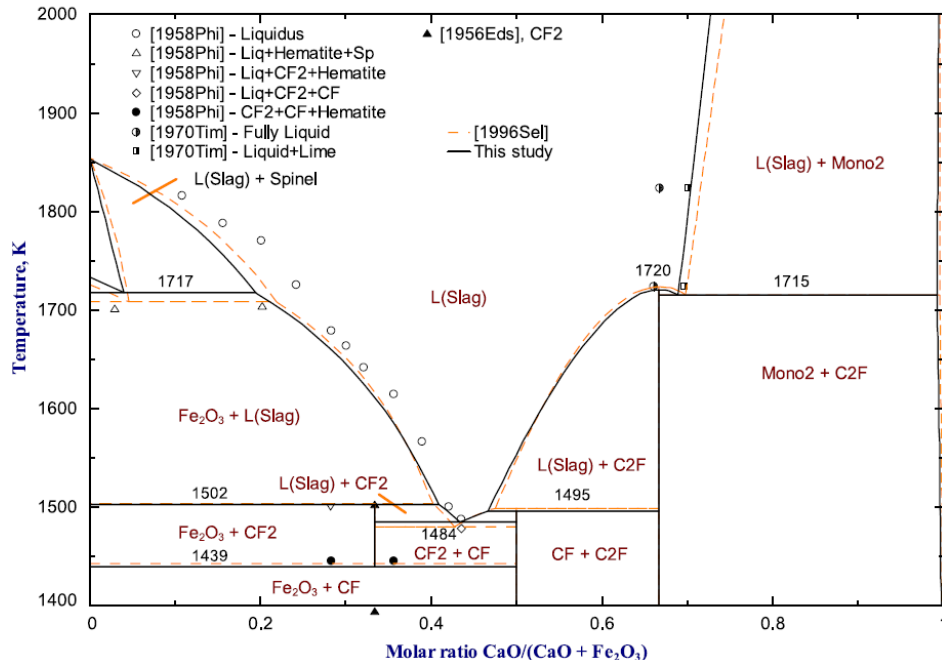


Figure 7.3: Phase diagram from the assessment from Hidayat et al. [16], alongside the phase diagram of Selleby and Sundman [14]. The experimental points [9, 17] are also displayed on the graph. The figure is adapted from Hidayat et al. [16].

the present work is the position of the eutectic point between the CF_2 and CF phases. The temperature is in good agreement but the compositional value for the eutectic differs by roughly 5 % compared to the assessment of Hillert et al. [13], which is within the uncertainty of the measurements by Phillips and Muan [9].

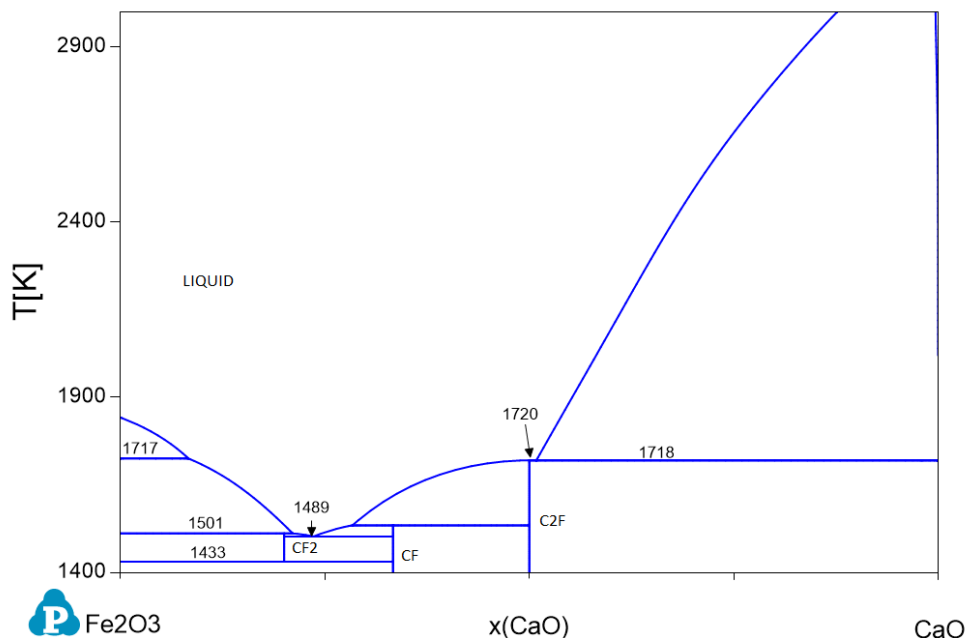


Figure 7.4: Optimised phase diagram of the $\text{CaO}-\text{Fe}_2\text{O}_3$ section, calculated in the present work.

Table 7.2: Table showing the functions found for the melt phase for the CaO- Fe_2O_3 section in the Ca-Fe-O system. These are the parameters used to fit the experimental data in the CaO- Fe_2O_3 section, therefore do not include parameters outside this section, the values of Fe-O parameters are present in Table 7.1.

Thermodynamic Properties of the CaO- Fe_2O_3 melt phase.

GLiquid (CaO,Fe,FeO, $FeO_1 \cdot 5$)

$$L_{CaO,FeO_1 \cdot 5,0} = -62800 - 8.4 * T$$

$$L_{CaO,FeO_1 \cdot 5,2} = -30000$$

The results of the optimised phase diagram are in good agreement with the experimental values. It is to be noted that the main features of the section to fit accurately are the melting point of the C_2F compound and the melting behaviour of the Fe_2O_3 compound. This is because these properties will be used to model the ferrite phase, with other compounds in the section being iron-rich and therefore not relevant for OPC clinker.

7.3 $Fe_2O_3-SiO_2$

Modelling the $Fe_2O_3-SiO_2$ pseudo section is not necessary for modelling OPC clinker phases, as it is either too iron-rich or too silica-rich. The $Fe_2O_3-SiO_2$ section is a simple system with no intermediate compounds and modelling the melt phase of this system will help to constrain the melt phase in the CaO- $Al_2O_3-SiO_2-Fe_2O_3$ system. Therefore, due to its simplicity and added melt constraint it was decided to model the pseudo section in the present work.

The Fe-O-Si ternary has been assessed by Selleby [18] and Fabrichnaya and Sundman [19] using the two-sublattice model, with the work of Fabrichnaya and Sundman [19] focusing on the high-pressure systems. Jak et al. [20] and Hidayat et al. [21] assessed the $FeO-Fe_2O_3-SiO_2$ using the MQM model. In both models, the $Fe_2O_3-SiO_2$ pseudo section was fit with a good agreement to the experimental data, of which there is little directly in the section. A comparison of the $Fe_2O_3-SiO_2$ section (in equilibrium with air) is presented in Figure 7.5. Experimentally, the section has been studied by Muan [22] and Liu et al. [23] on the iron-rich side, with Greig [24] carrying out measurements in the miscibility gap region. As stated above the $Fe_2O_3-SiO_2$ section contains no intermediate compounds, with only the compound Fe_2SiO_4 (FS also known as fayalite) existing at normal pressures in the $FeO-SiO_2$ section [19].

The melt phase of the $Fe_2O_3-SiO_2$ pseudo section in the present work was optimised with the associates model, with no additional associates i.e. only the existing end-member associates are present in the work. It was found sufficient to use the interaction terms calculated by Selleby [15] for the section. The optimised $Fe_2O_3-SiO_2$ section (in air) is presented in Figure 7.6. The invariant points in the present work are in good agreement with the experimental values, with some disagreement in the miscibility gap region, this is acceptable due to the difficulty in carrying out measurements in this region and thus are

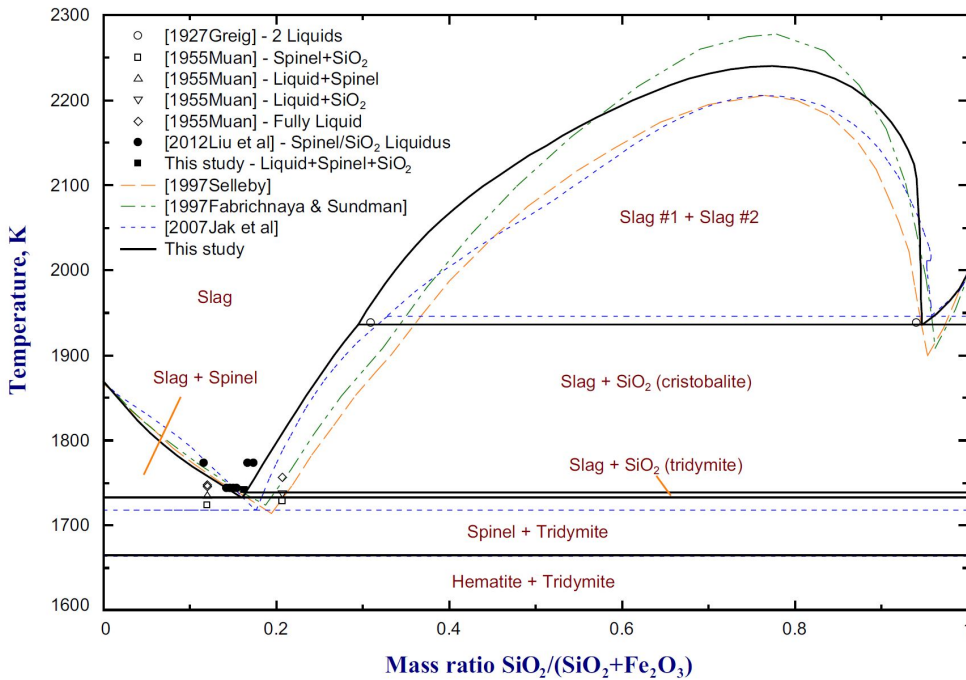


Figure 7.5: Computed phase diagram of the Fe_2O_3 - SiO_2 pseudo section (in air) from Hidayat et al. [21], compared against the previous assessments [18–20] plotted alongside the experimental points [22–24]. The figure is adapted from Hidayat et al. [21].

within the uncertainty of the experimental values from Grieg [24]. Using the parameters

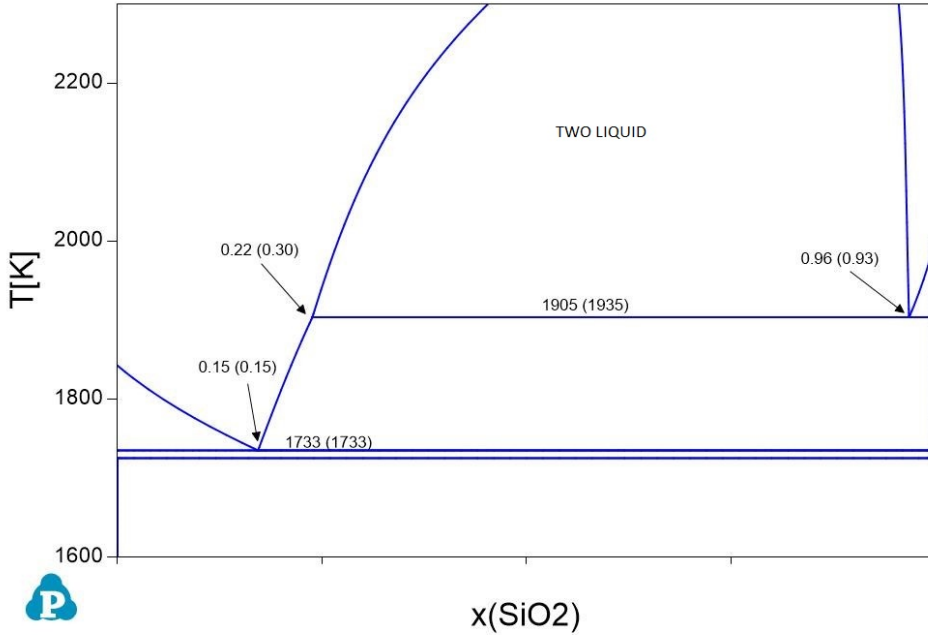


Figure 7.6: Optimised Fe_2O_3 - SiO_2 phase diagram in the present work, with the calculated points of the invariant labelled. The values in the parentheses are the experimental values [22, 24].

for this system, a “true” Fe_2O_3 - SiO_2 pseudo section which contains no Fe^{2+} is computed and presented in Fig. 7.7 and matches the “true” section calculated by Selleby [18] (see Fig. 7.8).

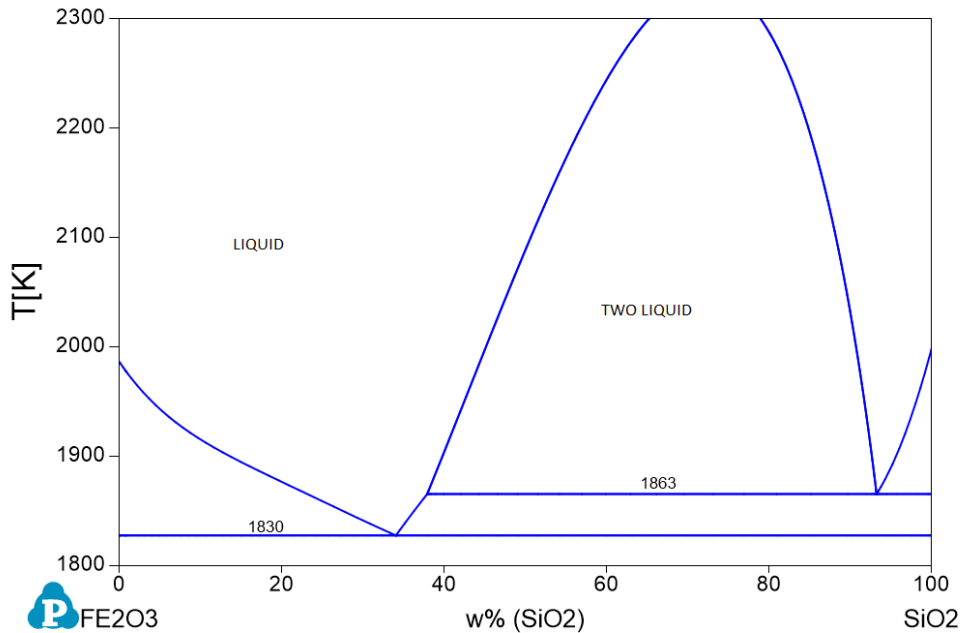


Figure 7.7: Optimised phase diagram of the “true” $Fe_2O_3-SiO_2$ pseudo section. It is considered a true pseudo-section as it contains no Fe^{2+} and the calculation is computed at infinite oxygen.

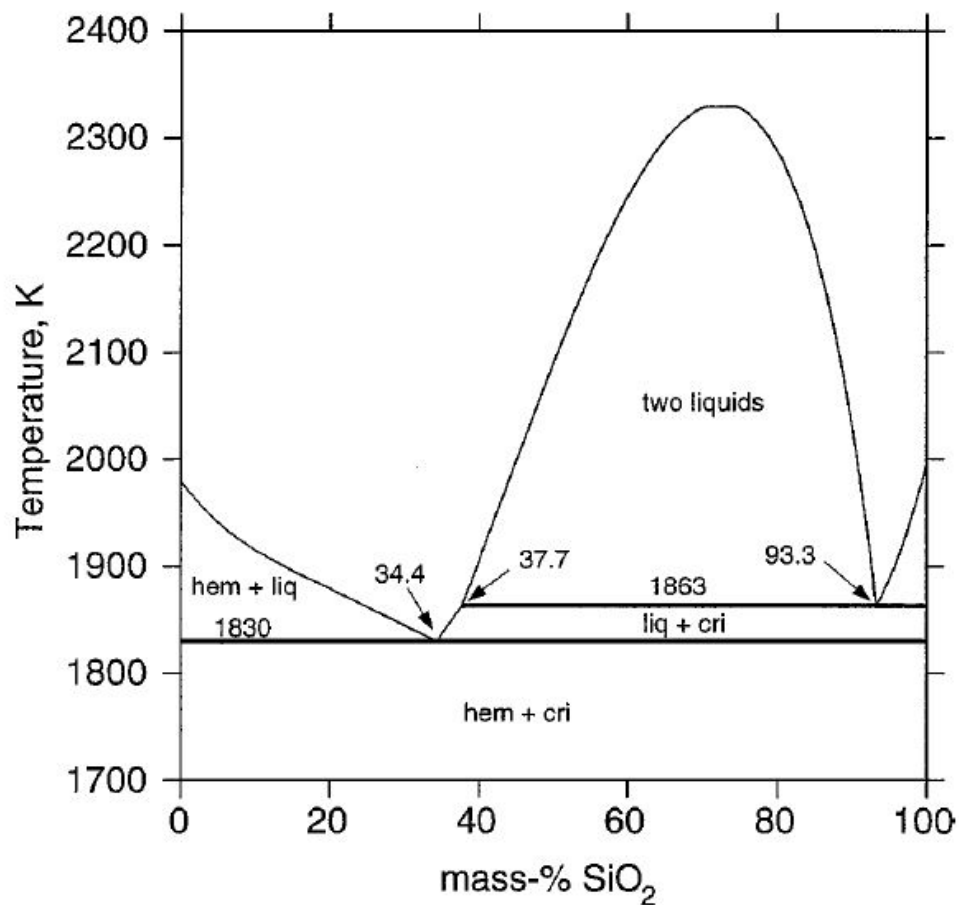


Figure 7.8: Phase diagram of the “true” pseudo section of the $Fe_2O_3-SiO_2$ as calculated by Selleby [18]. Figure is adapted from Selleby [18].

7.4 Modelling of the ferrite solid solution

The last major clinker phase to model in the present work is the ferrite solid solution also known as C₄AF or brownmellirite in the literature. The ferrite solid solution is complex, even when using a simplified CEF model. Magnetic transitions and structural polymorphism has been determined in the C₂A-C₂F pseudo section, including in the ferrite solid solution [25–28]. This information is valuable in accurately modelling ferrite, but is complex to model and requires a different approach, whilst it does not drastically improve the results of the ferrite prediction. This is the reason these structural effects are ignored in the Factsage [12] and MTDATA [29] databases. Similar to their approach, the ferrite was modelled as follows,

$$G_{Ferrite} = (C_2A, C_2F). \quad (7.4.1)$$

In the first instance, the thermodynamic properties of the end members have to be determined. The Gibbs energy of the C₂F end-member can be given the same Gibbs energy of the C₂F solid. This is not the case for the C₂A, which is not stable at normal pressures in the CaO-Al₂O₃ system. Thus, the Gibbs free energy of this end-member was first set to the Nueemann-Kopp of the oxides CaO and Al₂O₃ as follows,

$$G_{C_2A} = 2 * G_{CaO} + G_{Al_2O_3}. \quad (7.4.2)$$

The heat of formation of the C₂A phase was measured by Kojitani et al. [25], which was used in the present work to fit the L^0 parameter for the ferrite solid solution.

Furthermore, experimentally, little data exists in the literature for the ferrite solid solution or the C₂A-C₂F pseudo section. It is generally accepted that the solid solution exists from C₂F and 2/3 C₂A [1] (see Fig. 7.9). Phase diagram studies in the CaO-Al₂O₃-Fe₂O₃ ternary system have been carried out by Hansen et al. [30] and McMurdie [31], with Newkirk and Thwaite [32] carrying out measurements in the CA-C₂F pseudo section. Their results have been generally accepted and have been used to model the section. In the present work, experimental measurements that are close to the section will also be used to fit the C₂A-C₂F pseudo section. The heats of formation of C₂A_{0.5}F_{0.5} (which corresponds to C₄AF) and C₆A₂F have been measured [8, 33]. These were used in the present work to further fit the solid solution parameters in the ferrite phase. The parameters for the ferrite solid solution model are presented in Table 7.3. A comparison of the calculated enthalpies against the experimental values is presented in Table 7.4. Good agreement between the experimental and calculated are seen, given that the experimental uncertainties are 2 kJ/mol for Ayed et al. [33] and 3 kJ/mol for Newman [8].

Melt phase parameters from the binary systems CaO-Fe₂O₃ and CaO-Al₂O₃ were extrapolated to the C₂A-C₂F pseudo section and were not changed. Additional melt phase parameters in the pseudo-section were not added to avoid adding additional complexity to

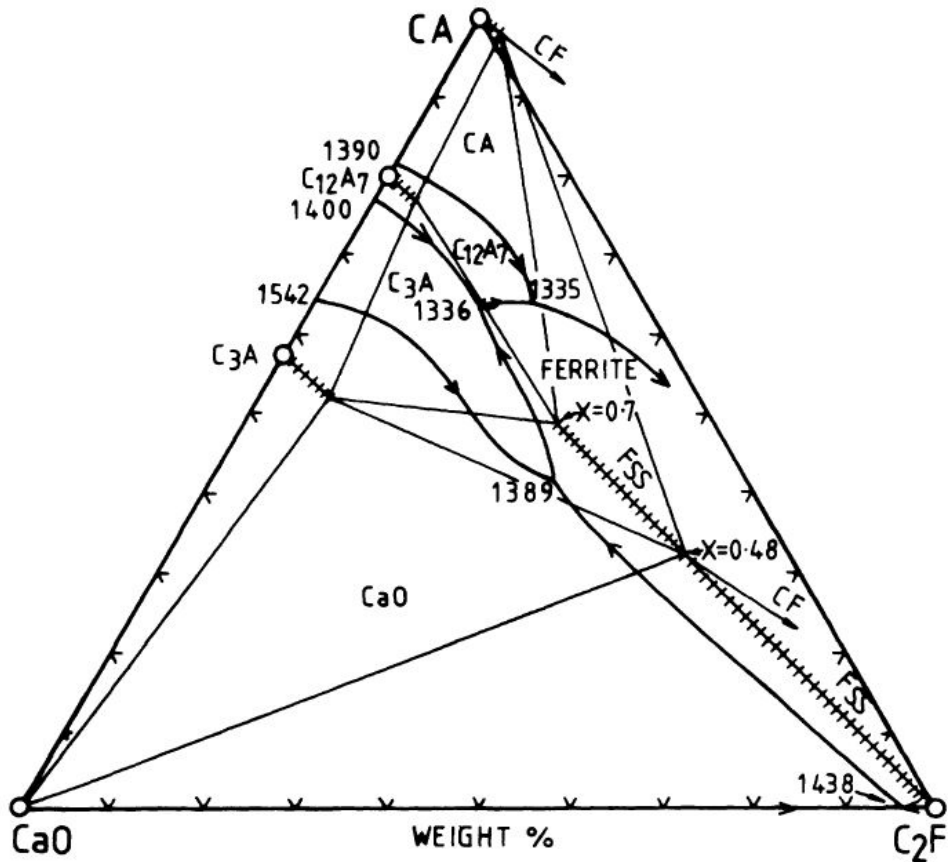


Figure 7.9: Pseudo section of the ternary system $\text{CaO}-\text{Al}_2\text{O}_3-\text{Fe}_2\text{O}_3$. Figure is adapted from Taylor [1].

Table 7.3: Table of the parameters for the ferrite solid solution calculated in the present work. “GC₂F” is the Gibbs free energy of the C_2F solid from the $\text{CaO}-\text{Fe}_2\text{O}_3$ system. The Gibbs free energy of the oxides is from the $\text{CaO}-\text{Al}_2\text{O}_3$ system.

Ferrite ($\text{C}_2\text{A}, \text{C}_2\text{F}$)
$G(\text{C}_2\text{F}) = \text{GC2F}$
$G(\text{C}_2\text{A}) = 2*\text{GCaO} + \text{GAl}_2\text{O}_3$
$L(\text{C}_2\text{A}, \text{C}_2\text{F}, 0) = -130000$
$L(\text{C}_2\text{A}, \text{C}_2\text{F}, 1) = -25000$

Table 7.4: Enthalpy of formation (from oxides) calculated in the present work and compared against the experimental measurements for ferrite solid solution compounds.

Phase	Calculated/kJmol^-1	Experiment/kJmol^-1
$\text{C}_2\text{A}_{0.5}\text{F}_{0.5}$	-47.9	-47 [33]
$\text{C}_6\text{A}_2\text{F}$	-73.2	-76.5 [8]

the section, which does not contain a lot of experimental information. The fully optimised section is presented in Figure 7.10. As there is no direct experimental information in this section, it is hard to make a direct comparison, with experimental information. There is good agreement with the melting point of C_4AF and the liquidus relations between C_2F and C_4AF as determined by McMurdie [31]. Whilst it is unknown whether the C_2A-C_2F pseudo section melt phase is well determined, there is confidence in the ferrite solid solution due to the excellent agreement with the heat of formation values for the ferrite compounds. Thus, the ferrite solid solution developed in this work is taken forward to accurately model the major clinker phases.

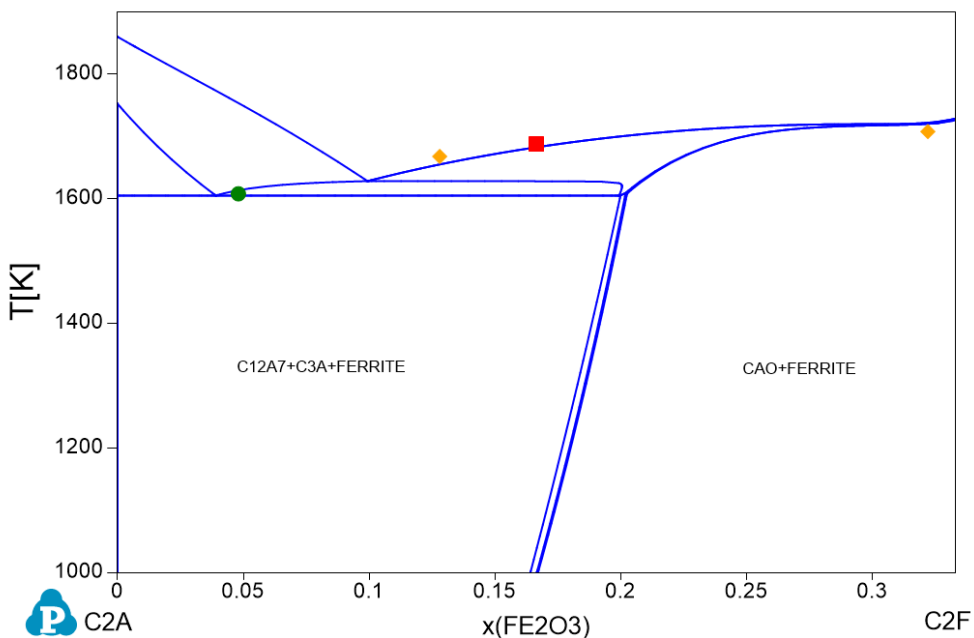


Figure 7.10: Optimised C_2A-C_2F pseudo section carried out in the present work, plotted with experimental liquidus points for comparison [8, 31].

7.5 Conclusion

In this chapter, iron was successfully added to the presently developed $CaO-Al_2O_3-SiO_2$ system. In the first instance, it was important to first define how to model iron due to its varying oxidation state. This was done using the assessment by Kowalski and Spencer [3]. This results in the addition of Fe and O into the thermodynamic database. The added complexity was reduced by the specific focus on OPC clinker, thus resulting in the focus on only the $CaO-Fe_2O_3$ section, which was modelled in the present work with good agreement against the experimental values. The section was then used to model the ferrite solid solution using the presently assessed parameters from the $CaO-Al_2O_3$ section and the $CaO-Fe_2O_3$ section, with the ferrite solid solution being fit using experimental heat of formation values. Whilst not the most accurate model due to exclusion of structural and magnetic transitions, the resulting ferrite model will be satisfactory in modelling the

clinker phase. In addition to the modelling of ferrite, the Fe_2O_3 - SiO_2 section was also presented which helps to further constrain the melt phase in the full system.

Whilst the modelling of the clinker phases is now possible due to the accurate modelling of the CaO - Al_2O_3 - SiO_2 - Fe-O system, it is desirable to start adding minor elements into the database at this point to further model clinker solubility and minor element substitution.

7.6 References

- [1] H.F.W. Taylor. *Cement chemistry*. 2nd edition. Thomas Telford Publishing, 1997. DOI: [10.1680/cc.25929](https://doi.org/10.1680/cc.25929).
- [2] Guillaume Deffrennes, Noël Jakse, Cecilia M.S. Alvares, Ioana Nuta, Alain Pasturel, Alexandra Khvan and Alexander Pisch. ‘Thermodynamic modelling of the Ca-O system including 3rd generation description of CaO and CaO_2 ’. In: *Calphad* 69 (2020), p. 101764. DOI: [10.1016/j.calphad.2020.101764](https://doi.org/10.1016/j.calphad.2020.101764).
- [3] M Kowalski and PJ Spencer. ‘Thermodynamic reevaluation of the Cr-O, Fe-O and Ni-O systems: Remodelling of the liquid, BCC and FCC phases’. In: *Calphad* 19.3 (1995), pp. 229–243.
- [4] B Sundman. ‘An assessment of the Fe-O system’. In: *Journal of phase equilibria* 12.2 (1991), pp. 127–140.
- [5] EG King. ‘Heat Capacities at Low Temperatures and Entropies at 298.16°K . of Calcium and Magnesium Ferrites’. In: *Journal of the American Chemical Society* 76.22 (1954), pp. 5849–5850.
- [6] K R Bonnickson. ‘High Temperature Heat Contents of Calcium and Magnesium Ferrites’. In: *Journal of the American Chemical Society* 76.6 (Mar. 1954), pp. 1480–1482. DOI: [10.1021/ja01635a006](https://doi.org/10.1021/ja01635a006).
- [7] KT Jacob, N Dasgupta and Y Waseda. ‘Thermodynamic properties of the calcium ferrites CaFe_2O_4 and $\text{Ca}_2\text{Fe}_2\text{O}_5$ ’. In: *Zeitschrift für Metallkunde* 90.7 (1999), pp. 486–490.
- [8] Edwin S. Newman and Roald Hoffman. ‘Heats of formation of hexacalcium dialumino ferrite and dicalcium ferrite’. In: *Journal of research of the National Bureau of Standards* 56 (1956), p. 313.
- [9] Bert R. Phillips and Arnulf Muan. ‘Phase Equilibria in the System CaO-Iron Oxide in Air and at 1 atm. O_2 Pressure’. In: *Journal of the American Ceramic Society* 41 (1958), pp. 445–454.
- [10] Bill Bergman. ‘Solid-State Reactions between CaO powder and Fe_2O_3 ’. In: *Journal of the American Ceramic Society* 69.8 (1986), pp. 608–611.

- [11] H. Kopp. ‘Investigations of the specific heat of solid bodies’. In: *Philosophical Transactions of the Royal Society* 155 (1865), pp. 71–202.
- [12] C. W. Bale, E. Bélisle, P. Chartrand, S. A. Dechterov, G. Eriksson, A. E. Gheribi, K. Hack, I. H. Jung, Y. B. Kang, J. Melançon, A. D. Pelton, S. Petersen, C. Robelin, J. Sangster, P. Spencer and M. A. Van Ende. ‘FactSage thermochemical software and databases, 2010-2016’. In: *Calphad* 54 (2016), pp. 35–53. DOI: 10.1016/j.calphad.2016.05.002.
- [13] Mats Hillert, Malin Selleby and B. Sundman. ‘An assessment of the Ca-Fe-O system’. In: *Metallurgical Transactions A* 21 (1990), pp. 2759–2776.
- [14] Malin Selleby and Bo Sundman. ‘A reassessment of the Ca-Fe-O system’. In: *Calphad* 20.3 (1996), pp. 381–392. DOI: 10.1016/S0364-5916(96)00039-9.
- [15] Malin Selleby. ‘An assessment of the Ca-Fe-O-Si system’. In: *Metallurgical and Materials Transactions B* 28.4 (1997), pp. 577–596. DOI: 10.1007/s11663-997-0030-6.
- [16] Taufiq Hidayat, Denis Shishin, Sergei Dechterov and Evgueni Jak. ‘Thermodynamic Optimization of the Ca-Fe-O System’. In: *Metallurgical and Materials Transactions B* 47 (Nov. 2016), pp. 256–281. DOI: 10.1007/s11663-015-0501-0.
- [17] Muharrem Timucin and AE Morris. ‘Phase Equilibria and Thermodynamic Studies in the System CaO-FeO- Fe_2O_3 - SiO_2 ’. In: *Metallurgical Transactions 1* (1970), pp. 3193–3201.
- [18] Malin Selleby. ‘An assessment of the Fe-O-Si system’. In: *Metallurgical and Materials Transactions B* 28.4 (Aug. 1997), pp. 563–576. DOI: 10.1007/s11663-997-0029-z.
- [19] O.B. Fabrichnaya and B. Sundman. ‘The assessment of thermodynamic parameters in the Fe-O and Fe-Si-O systems’. In: *Geochimica et Cosmochimica Acta* 61.21 (1997), pp. 4539–4555. DOI: 10.1016/S0016-7037(97)00256-1.
- [20] E. Jak, P. Hayes, A. Pelton and S. Dechterov. ‘Thermodynamic optimisation of the FeO- Fe_2O_3 - SiO_2 (Fe-O-Si) system with FactSage’. In: *International Journal of Materials Research* 98.9 (2007), pp. 847–854. DOI: doi:10.3139/146.101541.
- [21] Taufiq Hidayat, Denis Shishin, Sergei A Dechterov and Evgueni Jak. ‘Experimental Study and Thermodynamic Re-optimization of the FeO- Fe_2O_3 - SiO_2 System’. In: *Journal of Phase Equilibria and Diffusion* 38.4 (2017), pp. 477–492. DOI: 10.1007/s11669-017-0535-x.
- [22] Muan Arnulf. ‘Phase equilibria in the system FeO- Fe_2O_3 -SiO’. In: *Journal of The Minerals, Metals & Materials Society* 203 (1955), pp. 965–976. DOI: 10.1007/BF03377595.

- [23] Xijing Gloria Liu. ‘Experimental phase equilibria studies in oxide systems for copper smelting slags’. In: *School of Chemical Engineering* (2013).
- [24] J W Greig. ‘Immiscibility in silicate melts’. In: *American Journal Of Science* 13.73 (1927), pp. 1–44.
- [25] Hiroshi Kojitani, Yutaka Wakabayashi, Yasuko Tejima, Chikage Kato, Maiko Haraguchi and M. Akaogi. ‘High-pressure phase relations in Ca₂AlSiO_{5.5} and energetics of perovskite-related compounds with oxygen defects in the Ca₂Si₂O₆-Ca₂Al₂O₅ join’. In: *Physics of the Earth and Planetary Interiors* 173 (Apr. 2009), pp. 349–353. DOI: 10.1016/j.pepi.2009.02.001.
- [26] Koichiro Fukuda and Hisashi Ando. ‘Determination of the Pcmn/Ibm2 phase boundary at high temperatures in the system Ca₂Fe₂O₅-Ca₂Al₂O₅’. In: *Journal of the American Ceramic Society* 85.5 (2002), pp. 1300–1302. DOI: 10.1111/j.1551-2916.2002.tb00263.x.
- [27] Matthias Zötzl and Herbert Pöllmann. ‘Stability and properties of brownmillerites Ca₂(Al, Mn, Fe)₂O₅ and perovskites Ca(Mn, Fe)O_{3-x} in the system Ca₂Fe₂O₅-Ca₂Mn₂O₅-Ca₂Al₂O₅’. In: *Journal of the American Ceramic Society* 89.11 (2006), pp. 3491–3497. DOI: 10.1111/j.1551-2916.2006.01242.x.
- [28] The Long Phan, Ngo Tran, Deok Hyeon Kim, Pham T. Tho, Bui T. Huy, Toan N. Dang, Dong Seok Yang and Bowha Lee. ‘Electronic structure and magnetic properties of Al-doped Ca₂Fe₂O₅ brownmillerite compounds’. In: *Journal of the American Ceramic Society* 101.5 (2018), pp. 2181–2189. DOI: 10.1111/jace.15357.
- [29] John Gisby, Pekka Taskinen, Jouni Pihlasalo, Zushu Li, Mark Tyrer, Jonathan Pearce, Katri Avarmaa, Peter Björklund, Hugh Davies, Mikko Korpi, Susan Martin, Lauri Pesonen and Jim Robinson. ‘MTDATA and the Prediction of Phase Equilibria in Oxide Systems: 30 Years of Industrial Collaboration’. In: *Metallurgical and Materials Transactions B* 48.1 (2017), pp. 91–98. DOI: 10.1007/s11663-016-0811-x.
- [30] W C Hansen, L T Brownmiller and R H Bogue. ‘Studies On The System CaO-Al₂O₃-Fe₂O₃’. In: *Journal of the American Chemical Society* 50.2 (Feb. 1928), pp. 396–406. DOI: 10.1021/ja01389a023.
- [31] Howard F McMurtrie. ‘Studies on a portion of the system: CaO-Al₂O₃-Fe₂O₃’. In: *Journal of Research of the National Bureau of Standards* 18 (1937).
- [32] Terry F Newkirk and RD Thwaite. ‘Pseudoternary System CaO.Al₂O₃-2 CaO.Fe₂O₃’. In: *Journal of Research of the National Bureau of Standards* 61.4 (1958), p. 233.

- [33] F. Ayed, F. Sorrentino and R. Castanet. ‘Determination par calorimetrie de dissolution des enthalpies de formation de quelques silicates, aluminautes et alumino-silicates de calcium’. In: *Journal of Thermal Analysis and Calorimetry* 41.4 (1994), pp. 755–766. DOI: 10.1007/bf02547157.

CHAPTER
EIGHT

MODELLING MINOR ELEMENTS: CAO-MGO-SIO₂

The main oxide systems containing CaO, SiO₂, Al₂O₃ and iron have all been described and modelled. However, these are not the only oxides that are present in the cement kiln and therefore not the only oxides that may appear in the final clinker. Whilst not all minor elements were modelled in this project, due to their small presence in the clinker, it is important to include the minor element oxide MgO due to it being present in significant amounts.

MgO is present in cement clinkers by up to 5% by weight in the final clinker product [1], with the amount of MgO increasing in modern-day clinkers due to the scarcity of pure materials and the increasing diversity of the raw feed. Mg²⁺ is especially interesting to the clinker chemistry as it has the same charge and size as calcium ions, allowing for it to often substitute for calcium ions in the clinker phases [2]. This is especially evident in the ternary phase diagram CaO-MgO-SiO₂, where the calcium ions in CS, C₂S and CaO form a solid solution series with MS, M₂S and MgO, with the MgO substituting for CaO with increasing MgO concentration, this can be seen in a previously assessed ternary phase diagram in Fig. 8.1.

8.1 MgO-SiO₂

The binary sections required to model this ternary system are the CaO-SiO₂, CaO-MgO and the MgO-SiO₂ systems. The first two were presented in detail in the previous chapters, with the remaining MgO-SiO₂ section presented here. The MgO-SiO₂ system is interesting due to its similarity to CaO-SiO₂. It contains the compounds M₂S and MS and like the CaO-SiO₂ system it also contains a miscibility gap at high concentrations of SiO₂ (this can be seen in the fully optimised phase diagram in Fig. 8.2).

8.1.1 Literature review of the solid phases

The compounds found within the MgO-SiO₂ system at normal pressures are MgSiO₃ (MS) and Mg₂SiO₄ (M₂S). Whilst the compounds M₂S and MS can be seen as equivalent

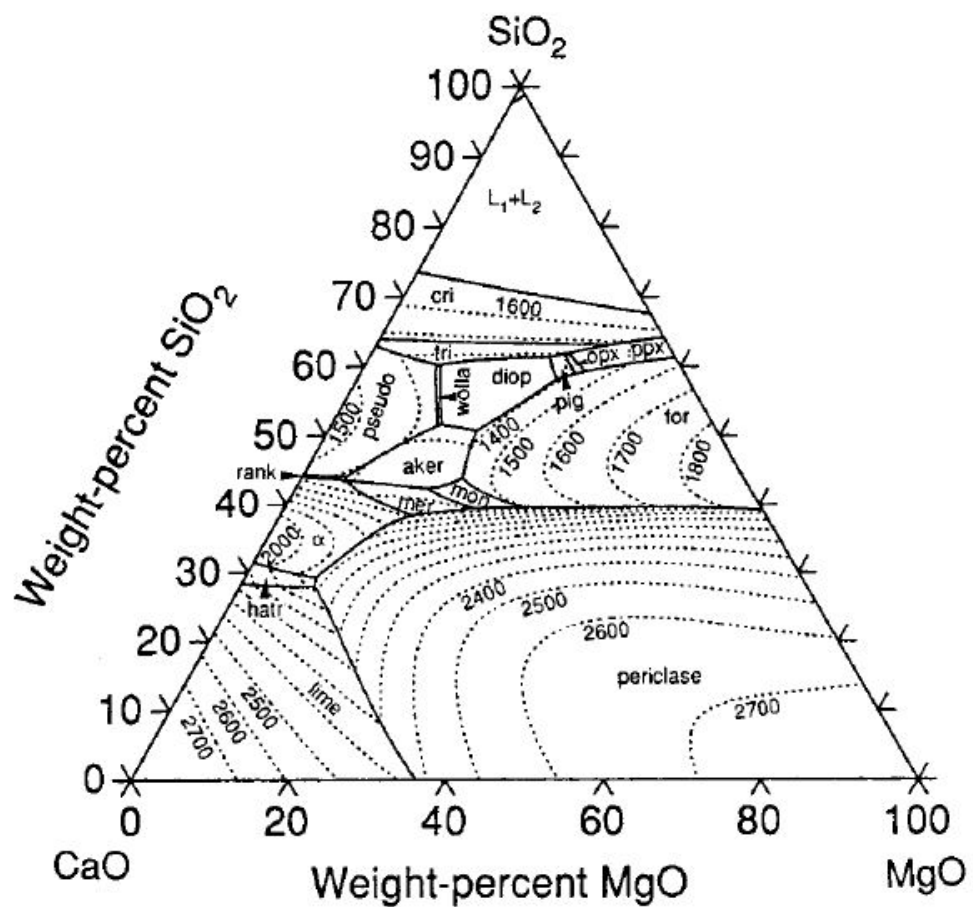


Figure 8.1: Ternary liquidus projection of the CaO-MgO-SiO₂ system assessed by Huang et al. [3].

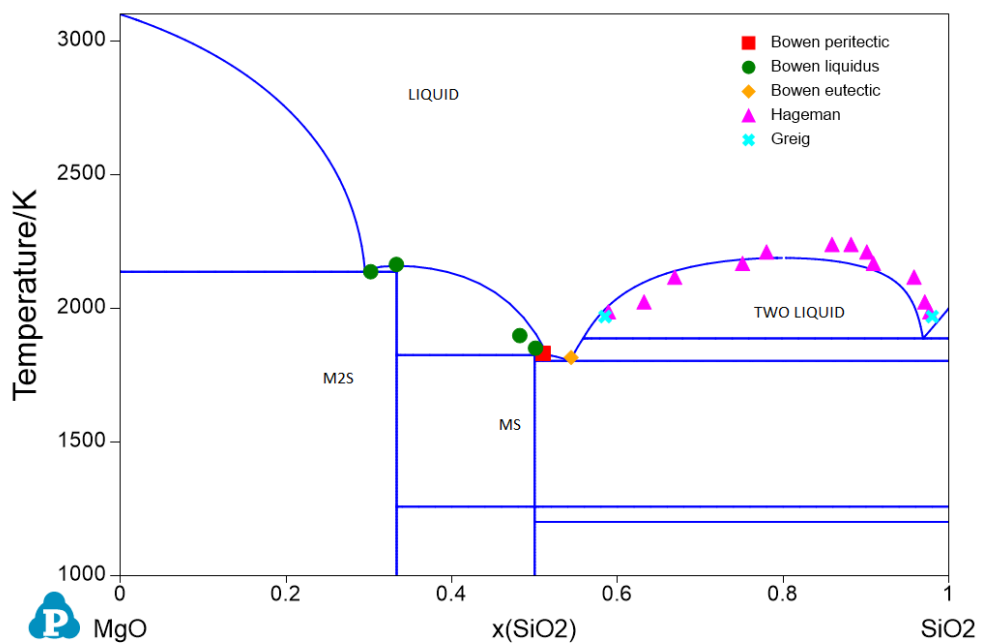


Figure 8.2: Phase diagram of the optimised MgO-SiO₂ compared against the experimental points [4, 5].

to the C₂S and CS respectively, the structural polymorphs are quite different.

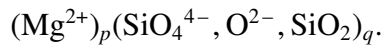
M₂S only exists as a single polymorph at normal pressures. This polymorph is known as forsterite and has the olivine structure which is similar to γ -C₂S. The low-temperature heat capacity of forsterite (M₂S) was measured by Robie et al. [6]. In these measurements, they calculated a S_{298} value of 94.11 J/K/mol. Akaogi et al. [7] also carried out low-temperature heat capacity measurements but at high pressures for the α , β and γ polymorphs [8]. For the high-temperature data, Orr [9] carried out relative enthalpy measurements from 398–1807 K. The heat of formation of forsterite has been measured by King et al. [10] (298–900 K), Torgsen and Shahama [11] (298 K), Charlu et al. [12] (970 K) and Kiseleva et al. [13] (1170 K). All authors carried out their measurements using acid-solution calorimetry.

The MS compound has a pyroxene structure, which has 3 stable polymorphs at normal pressures. These are known as enstatite (also known as ortho-enstatite), clino-enstatite and proto-enstatite. Additional polymorphs for the M₂S and MS compounds exist, but they are only stable at high pressures. Thermodynamic data around the MS compound is more complex as it is difficult to determine the polymorph being measured and there is a lack of measurements for high-temperature polymorphs ortho-enstatite and proto-enstatite. For clino-enstatite, heat capacity measurements were carried out by various authors [14–16], with enthalpy measurements carried out by Wagner [17]. Similar to forsterite, the heat of formation was measured by Charlu et al. [12] and Kiseleva et al. [13]. For the clino-enstatite and proto-enstatite phases, assessed values for the heat capacity and heat of formation values from the assessment of Robinson et al. [18] were used to fit the phases. This is similar to the approach carried out by Hillert and Wang [19], in their assessment of the MgO-SiO₂ system. The resultant coefficients and the data used to fit the solids are presented in Table A.1 in the Appendix.

8.1.2 Phase diagram

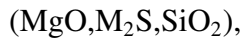
The first experimental determinations of the MgO-SiO₂ system were carried out by Bowen and Andersen [4], in which they determined the melting points of Mg₂SiO₄ and MgSiO₃. Schlaudt and Roy [20] further studied the system and determined the MgSiO₄-MgO eutectic. They found extensive solubility of SiO₂ in MgO, however further SEM studies did not corroborate these results [21]. Therefore, in the present work, all solids were assumed to be stoichiometric. Studies on the miscibility gap were carried out by Greig [22] and Hageman and Oonk [5].

The MgO-SiO₂ system has been previously modelled by Hillert and Wang [19], using the two-ionic sublattice model. The sublattice model used in the assessment of Hillert and Wang is as follows,



The parameters used in their assessment were similar to the parameters calculated in their

assessment of the CaO-SiO₂ system [23]. Hudon et al. [24] carried out thermodynamic measurements and assessed the MgO-SiO₂ system at high pressures and whilst not relevant, it is interesting to see the pressure dependence on the system. The MQM was employed in the assessment carried out by Wu et al. [25]. In their assessment, they fit the solid phases with the assessment values from Berman [26] but did achieve similar results to Hillert and Wang [19], if their modelled solubility of SiO₂ in MgO is ignored. In the present work, the melt phase was modelled with the associates model using the oxide end-members MgO and SiO₂. Additionally, it was found necessary to use the M₂S associate to properly model the miscibility. This gives a resulting melt phase model,



which is equivalent to the sub-lattice model used by Hillert and Wang [19]. The full model parameters are presented in Table 8.1, with the phase diagram optimised in the present work presented in Fig. 8.2.

Table 8.1: Table showing the functions optimised in the present work for the melt phase in the MgO-SiO₂.

Thermodynamic Properties of the MgO-SiO₂ melt phase.

Liquid (M,M₂S,S)

$$G_{M,liquid} = G_{M,liquid}$$

$$G_{S,liquid} = G_{S,liquid}$$

$$G_{\text{M}_2\text{S},liquid} = 2 * G_{M,liquid} + 1 * G_{S,liquid} - 11578 + 13.850 * T$$

$$L_{M,S,0} = 43199 - 22.75 * T$$

$$L_{M,S,1} = 8428$$

$$L_{M,S,2} = 455254 - 186.68 * T$$

$$L_{M,S,3} = -4993$$

From the phase diagram, there is good agreement around the invariant points in the system. The miscibility gap is well produced when accounting for the experimental uncertainties of the measurements [22]. The model parameters used in the present work, are similar to the interaction terms used by Hillert and Wang [19], except for lack of interaction terms between the end-member associates MgO and SiO₂. In the present work, it was found that the interaction terms between those species were not needed to reproduce the experimental data.

8.2 CaO-MgO-SiO₂

With the binary sections CaO-SiO₂, CaO-MgO and MgO-SiO₂ assessed and computed, the modelling of the ternary CaO-MgO-SiO₂ system can be attempted. The ternary system is interesting as it will include information on the substitution of MgO, into the CaO containing compounds, notably C₂S and CS. As a result of this, the modelling of the ternary system is complex due to the variety of solid solutions present within the ternary.

8.2.1 Phases within the ternary system

In this system, there are 2 stoichiometric ternary compounds, akermanite ($\text{Ca}_2\text{MgSi}_2\text{O}_7$) and merwenite ($\text{Ca}_3\text{MgSi}_2\text{O}_8$). High-temperature enthalpy measurements were carried out by Courtial et al [27] and Weller and Kelly [28] conducted heat capacity measurements for the akermanite and merwenite solids. The heat capacity of akermanite was also recorded by Hemingway et al. [29] from low temperature to high temperature, however, they recorded a sharp peak in the heat capacity at 379 K. This was excluded in the present work as further studies have not verified this. Kelley and Pankratz [30] conducted high-temperature measurements for the merwenite phase. Heats of formation of both ternary compounds have been measured by Neuveon and Brousse et al. [31]. The experimental measurements for these phases were used to fit a 3rd generation model and the resulting parameters are presented in the Appendix in Table A.2.

Several other phases also exist in the ternary system, but they were all considered solid solutions, so were fit using the CEF model. A table of the solid solution (including their respective sublattice model) and stoichiometric phases that exist in the ternary system is presented in Table 8.2.

Table 8.2: The ternary solid solutions and compounds found within CaO-MgO-SiO₂.

Phase	Formula	End-member
alpha	$(\text{C}, \text{M})_2(\text{S})$	$\alpha\text{-C}_2\text{S}$
		$\alpha\text{-M}_2\text{S}$
alpha prime	$(\text{C}, \text{M})_2(\text{S})$	$\alpha'\text{-C}_2\text{S}$
		$\alpha'\text{-M}_2\text{S}$
olivine	$(\text{C}, \text{M})(\text{C}, \text{M})(\text{S})$	$\gamma\text{-C}_2\text{S}$
		monticellite'
		monticellite
clino	$(\text{C}, \text{M})(\text{M})(\text{S})_2$	$\gamma\text{-M}_2\text{S}$
		clino-MS
		clino-diopside
low clino	$(\text{C}, \text{M})(\text{M})(\text{S})_2$	low clino-MS
		low clino-diopside
ortho	$(\text{C}, \text{M})(\text{M})(\text{S})_2$	ortho-MS
		ortho-diopside
proto	$(\text{C}, \text{M})(\text{S})$	proto-MS
		wollastonite-CS
woll	$(\text{C}, \text{M})(\text{S})$	clino-MS
		wollastonite-CS
akermanite	-	-
merwenite	-	-

8.2.2 Phase diagram

Although the end-members for the various solid solutions are clearly defined, in reality, a lot of them are fictive end-members. This is mainly due to the underlying end-

members and polymorphs only existing in the solid solution. This is true for most end-members except for the structurally similar ones e.g. in the olivine solid solution the M₂S and C₂S end-members are of the gamma polymorph which exists in the respective binary systems. Therefore, it is necessary to discuss in detail the modelling of the solid solutions.

To make the optimisation of the CaO-MgO-SiO₂ ternary easier, it was decided to split the optimisation process into two distinct sections: orthosilicate section (C₂S-M₂S) and the metasilicate section (CS-MS). This follows the approach of the work of Huang et al. [3] and In Ho Jung et al. [32].

Orthosilicate section

In the orthosilicate section, six distinct solid compounds exist α -C₂S, α' -C₂S, γ -C₂S, merwenite, monticellite and forsterite. Merwenite is the only stoichiometric compound in the section. The olivine solid solution exists with a miscibility gap caused by the monticellite phase and also exists in the system as γ -C₂S and forsterite (M₂S). The C₂S-CMS sub section was studied by Gutt [33] and Schlaudt and Roy [34]. Gutt established the high-temperature liquidus points, but it is generally accepted that the resulting phase diagram is incorrect [3, 32]. Schlaudt and Roy measured the solubility of Mg in the α' -C₂S and α -C₂S. Ricker and Osborn [2] studied the liquidus points in the remainder of the section and also determined the phases in the CMS-M₂S subsection. Biggar and O Hara [35] and Yang [36] further studied the monticellite phase in the middle of the section, including the tie-lines with forsterite.

The assessed sections by Huang et al. [3] (two-sublattice model) and In Ho Jung et al. [32] (MQM), differ by quite a bit. The work of In Ho Jung et al. reproduces the experimental data by Yang [36] and Biggar and O'Hara [35] far greater than the work of Huang et al. This results in an incorrectly described monticellite phase in the work of Huang et al. The orthosilicates sections computed by the previous assessments are presented in Figure 8.3.

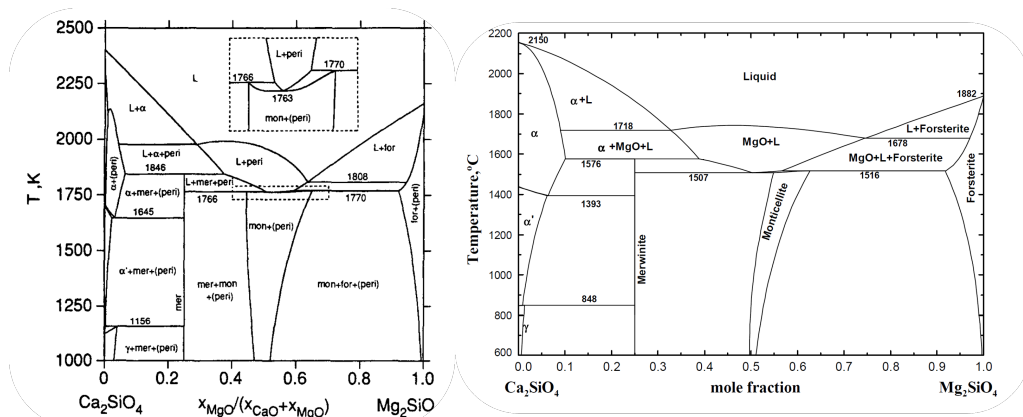


Figure 8.3: Orthosilicate section computed by the previous assessments, Huang et al. [3] (left) and In Ho Jung et al. [32] (right).

There are 4 end-members in the olivine solid solution and these are described in

Table 8.3, alongside the optimised parameters. The M₂S and C₂S end-members are simply the Gibbs free energies of M₂S and γ -C₂S respectively. The monticellite phase was decided to be described by the (C)₁(M)₁(S)₁ and given the Gibbs free energy of monticellite. In the assessment of Huang et al., the monticellite phase was described with the N-K rule from the oxides. In the present work, the monticellite phase was fit to experimental thermodynamic data [31, 37], using the 3rd generation model plus a correction for the configurational entropy. The remaining end-member is known as “unstable monticellite” and was given the Gibbs free energy of monticellite plus a large positive enthalpy to make it unstable in the section. The interaction terms for the olivine solid solution were required to produce the appropriate miscibility gap.

Table 8.3: Parameters for the olivine solid solution in the CaO-MgO-SiO₂.

Olivine (C, M)₁(C, M)₁S₁
* The colon is a separator for the sublattices
$G_{(C:C:S, \text{olivine})} = G_{\gamma-\text{C}_2\text{S}}$
$G_{(M:M:S, \text{olivine})} = G_{\text{M}_2\text{S}}$
$G_{(C:M:S, \text{olivine})} = G_{\text{monticellite}} + 2.4362T$
$G_{(M:C:S, \text{olivine})} = G_{\text{monticellite}} + 146440$
$L_{(C,M:M:S,0)} = 32235.53$
$L_{(C,M:M:S,1)} = -4079.92$
$L_{(C:C,M:S,0)} = 28032.8$

The “alpha” and “alpha prime” solid solutions are described with the same sublattice models as each other: (C, M)₂(S)₁, and models the solubility of MgO in the α and α' C₂S phases. The α -M₂S solid does not exist and is instead made by adding an enthalpy correction to the Gibbs free energy of M₂S to form that end-member, this is the same for the “alpha prime” solid solution. The Gibbs free energy of the solid solution phases and parameters are presented in Table 8.4.

Table 8.4: Description of the alpha and alpha prime solid solutions in the CaO-MgO-SiO₂ system.

Alpha (C, M)₂S₁
$G_{(C:S, \text{alpha})} = G_{\alpha-\text{C}_2\text{S}}$
$G_{(M:S, \text{alpha})} = G_{\text{M}_2\text{S}} + 83680$
$L_{(C,M:S,0)} = -35564$
Alpha Prime (C, M)₂S₁
$G_{(C:S, \text{alphaprime})} = G_{\alpha'-\text{C}_2\text{S}}$
$G_{(M:S, \text{alphaprime})} = G_{\text{M}_2\text{S}} + 85772$
$L_{(C,M:S,0)} = -35564$

The interaction parameters for the olivine, alpha, and alpha prime solid solutions were initially taken from the assessment of In Ho Jung et al. [32] and optimised further. The optimised section is presented in Fig. 8.4. The composition data is well reproduced, within experimental uncertainty and matches well with the section of In Ho Jung et al. The only disagreement is the melting temperature of the liquid, which is roughly 100 K

higher, this is due to the stability of the merwenite phase. However, melt interaction terms in the section could be added to further fit the section but is not necessary to fit accurately for OPC applications, where the main feature is the solubility of MgO, which is well reproduced. Therefore, the optimised work is taken to be acceptable.

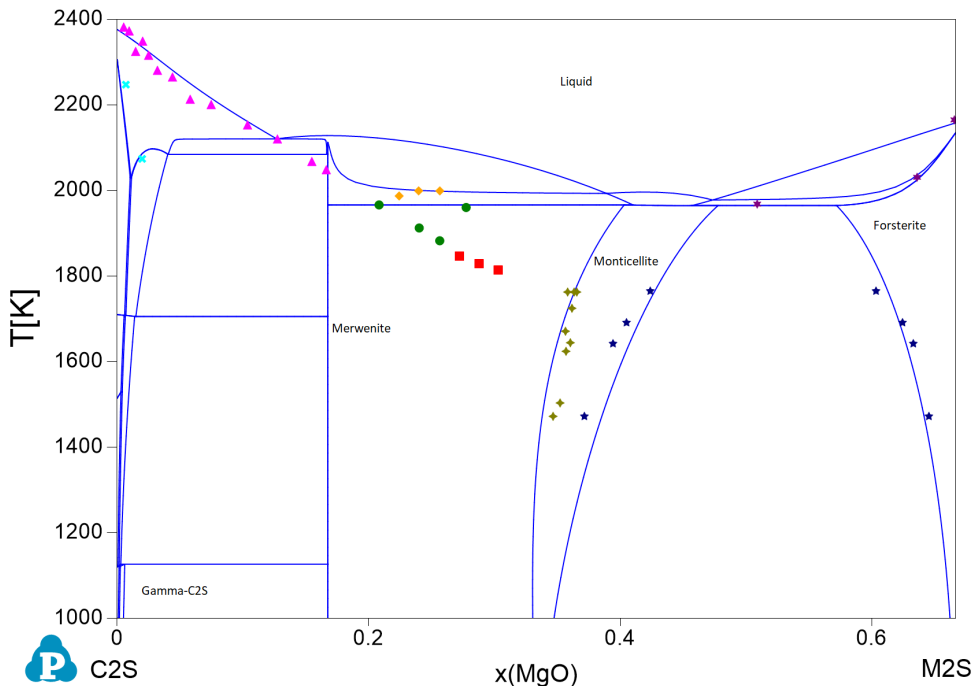


Figure 8.4: Optimised C₂S-M₂S orthosilicate section carried out in the present work.

Metasilicate section

The metasilicate section (CS-MS pseudo section) is complex with many solid solutions of CS and the various polymorphs of MS. The diopside phase (CaMgSi₂O₆), which is a stable end-member of the “clino” solid solution is also present in the section. The CS-diopside subsection was studied by Schraier and Bowen [38], who determined the solubility of MgO in the wollastonite solid solution. No further experiments exist for this section as it was well-measured by Schraier and Bowen. The other subsection contains much more information, with the diopside-enstatite liquidus first studied by Bowen [39], with further quenching studies by Boyd and Schraier [40]. The diopside and pyroxene equilibria were studied extensively by Carlson [41] and provided a lot of information on the solid solutions. The results of Carlson were also supported by further studies [42, 43]. For the sake of visualisation, Fig. 8.5, shows the diopside-enstatite section from the assessment of In Ho Jung et al., with experimental points overlaid.

All the parameters for the solid solutions and the metasilicate section (including the Gibbs free energy of the end-members) were taken from the assessment of Huang et al., with no additional parameters used. Full details of the solid solutions and parameters are therefore not presented in this work and the reader is referred to read the work of Huang

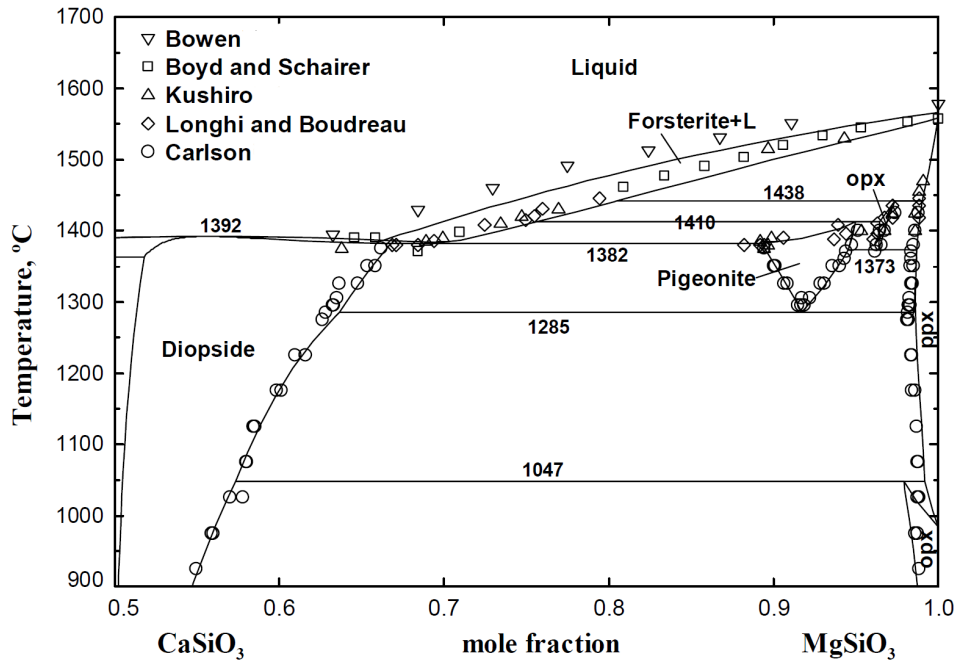


Figure 8.5: Diopside-enstatite subsection as calculated by the work of In Ho Jung et al., overlaid with experimental data [40–43]. Figure is adapted from [32].

et al [3]. The optimised metasilicate section is presented in Figure 8.6. The optimised section matches the sections of the previous assessments, with a slight disagreement in the melt temperature.

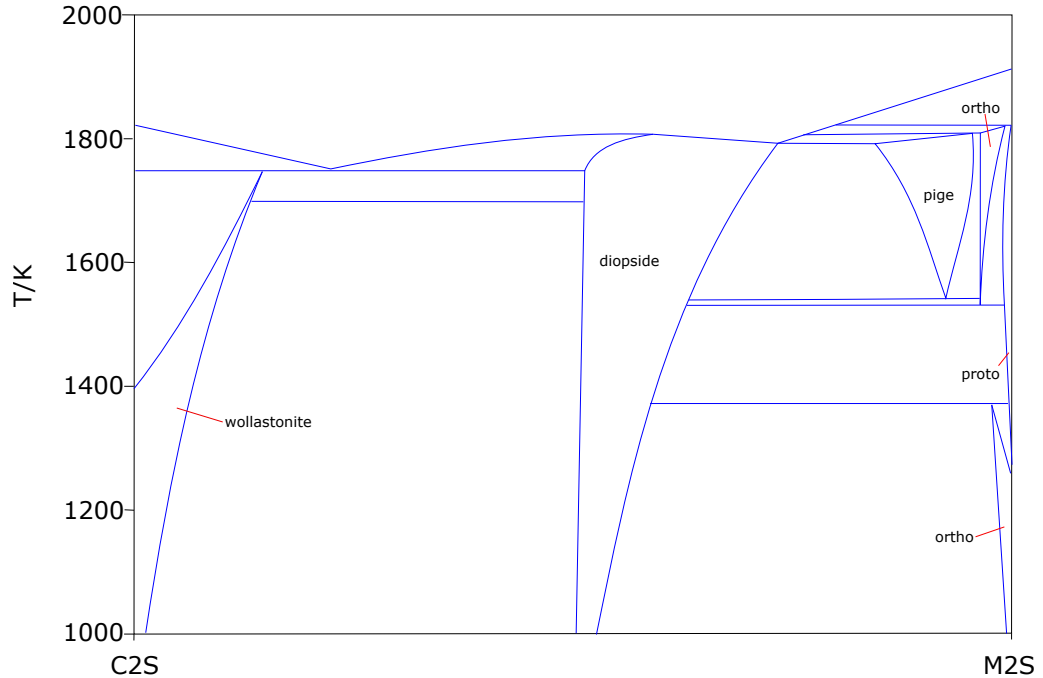


Figure 8.6: Optimised CS-MS metasilicate section carried out in the present work.

Ternary phase diagram

Combining the optimised orthosilicate and metasilicate sections, the ternary CaO-MgO-SiO₂ system can be produced. The resulting optimised ternary liquidus projection is presented in Figure 8.7.

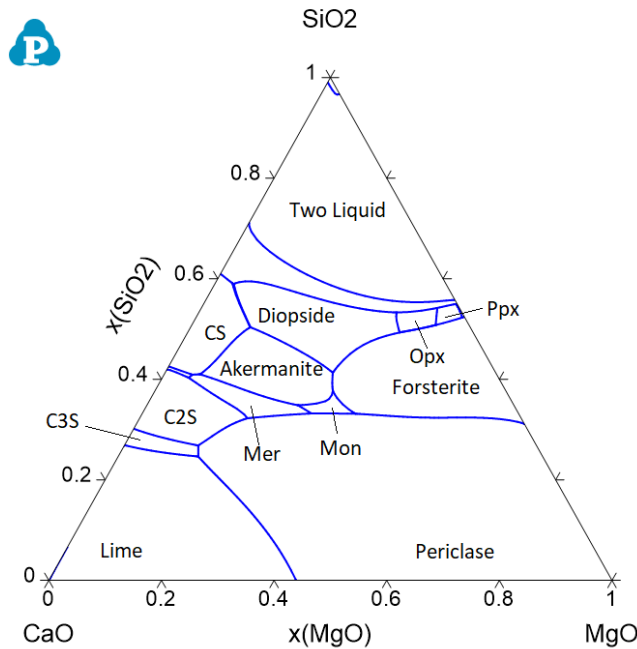


Figure 8.7: Optimised liquidus projection of the CaO-MgO-SiO₂ ternary carried out in the present work.

Compared with the ternary phase diagram calculated by Huang et al. [3], there is a discrepancy in the centre of the diagram, with the calculated merwinitic phase being calculated as too stable and the akermanitic phase less stable. Whilst this isn't an accurate representation of the ternary system, the main feature necessary to capture for OPC application is the CaO rich sections of the system, which are well reproduced. The invariant points in the CaO rich and low MgO sections are presented in Table 8.5.

Table 8.5: Invariant points in the CaO rich corner of the CaO-MgO-SiO₂ ternary, which is relevant for OPC clinkers. Values in parentheses are estimated experimental values from Ricker and Osborn [2].

Phases	T/K	w% (MgO)	w% (SiO ₂)
CaO + C ₃ S + MgO	2096 (~2123)	10.32 (~13.5)	26.7 (~25.5)
C ₃ S + MgO + alpha	2029 (~2063)	9.32 (~13.5)	28.7 (~29)

8.3 Conclusion

MgO is known as a “major” minor element i.e., a minor element that is present in significant quantities, thus modelling the MgO oxide and its substitution is important in

accurately modelling OPC clinkers. Whilst not accurately modelled in the present work, the substitution of MgO in C₂S was well modelled. Furthermore, the amount of MgO in the cement kiln is in such small quantities, accuracy in the full ternary system isn't required and emphasis is put on the CaO rich section. Therefore, it can be concluded that the adding of MgO was successfully achieved in the present work, leading to the modelling of the CaO-MgO-SiO₂ ternary, which allows for the modelling of the substitution of MgO into the belite phase.

With the ternary modelled, the system can be combined with the previously modelled database, with the idea of modelling the 4 clinker phases and the effect of the minor oxide MgO. At this stage, more minor elements can be added. These can be added simply compared to the modelling of MgO, as the majority of the minor elements exist in such low quantities that entire systems don't need to be modelled. However, it is to be noted that the modelling of the MgO substitution in the C₃S is not included in all assessments, even though it has been found in the alite (C₃S) phase [44]. This would affect the predicted values of the alite phases, when carrying subsequent calculations.

In the following chapter, the higher-order systems that were optimised in the present work will be used to predict the clinker compositions against the real clinkers that were analysed as a part of this project. This will allow for the application and display of the effectiveness and need of such a thermodynamic database.

8.4 References

- [1] H.F.W. Taylor. *Cement chemistry*. 2nd edition. Thomas Telford Publishing, 1997. DOI: 10.1680/cc.25929.
- [2] RW Ricker and EF Osborn. ‘Additional phase equilibrium data for the system CaO-MgO-SiO₂’. In: *Journal of the American Ceramic Society* 37.3 (1954), pp. 133–139.
- [3] Weiming Huang, Mats Hillert and Xizhen Wang. ‘Thermodynamic assessment of the CaO-MgO-SiO₂ system’. In: *Metallurgical and Materials Transactions A* 26.9 (1995), pp. 2293–2310.
- [4] Norman Levi Bowen and Olaf Andersen. ‘The binary system MgO-SiO₂’. In: *American Journal of Science* 37.222 (1914), pp. 487–500. DOI: 10.2475/ajs.s4-37.222.487.
- [5] V.B.M. Hageman and H.A.J. Oonk. ‘Liquid immiscibility in the SiO₂-MgO, SiO₂-SrO, SiO₂-La₂O₃ and SiO₂-Y₂O₃ systems’. In: *Physics and Chemistry of Glasses* 27.5 (1986), pp. 194–198.
- [6] Richard A Robie and Bruce S Hemingway. ‘Heat capacities and entropies of Mg₂SiO₄, Mn₂SiO₄, and Co₂SiO₄ between 5 and 380 K’. In: *American Mineralogist* 67.5-6 (1982), pp. 470–482.

- [7] M. Akaogi, M. Yano, Y. Tejima, M. Iijima and H. Kojitani. ‘High-pressure transitions of diopside and wollastonite: Phase equilibria and thermochemistry of CaMgSi₂O₆, CaSiO₃ and CaSi₂O₅-CaTiSiO₅ system’. In: *Physics of the Earth and Planetary Interiors* 143.1-2 (2004), pp. 145–156. DOI: 10.1016/j.pepi.2003.08.008.
- [8] Akaogi M., Takayama H., Kojitani H., Kawaji H. and Atake T. ‘Low-temperature heat capacities entropies and enthalpies of Mg₂SiO₄ polymorphs and α - β - γ and post-spinel phase relations at high pressure’. In: *Physics and Chemistry of Minerals* 34 (2007), pp. 169–187. DOI: 10.1007/s00269-006-0137-3.
- [9] Raymond L Orr. ‘High Temperature Heat Contents of Magnesium Orthosilicate and Ferrous Orthosilicate’. In: *Journal of the American Chemical Society* 75.3 (Feb. 1953), pp. 528–529. DOI: 10.1021/ja01099a005.
- [10] E G King, R Barany, W Weller and L B Pankratz. ‘Thermodynamic Properties of Forsterite and Serpentine’. In: *U.S Bureau of Mines* (1967). DOI: <https://digital.library.unt.edu/ark:/67531/metadc100853/m1/5/>.
- [11] D R Torgeson and Th. G Sahama. ‘A Hydrofluoric Acid Solution Calorimeter and the Determination of the Heats of Formation of Mg₂SiO₄, MgSiO₃, and CaSiO₃’. In: *Journal of the American Chemical Society* 70.6 (1948), pp. 2156–2160. DOI: 10.1021/ja01186a048.
- [12] T.V Charlu, R.C Newton and O.J Kleppa. ‘Enthalpies of formation at 970 K of compounds in the system MgO-Al₂O₃-SiO₂ from high temperature solution calorimetry’. In: *Geochimica et Cosmochimica Acta* 39.11 (1975), pp. 1487–1497. DOI: 10.1016/0016-7037(75)90150-7.
- [13] I.A. Kiseleva, L.P. Ogorodova, N.D. Topor and O.G. Chigareva. ‘Thermochemical Study of the CaO-MgO-SiO₂ System’. In: 12.12 (1979), pp. 1811–1825.
- [14] V A Drebushchak, Yulia A Kovalevskaya, I E Paukov and N V Surkov. ‘Low-temperature heat capacity of monoclinic enstatite’. In: *Journal of Thermal Analysis and Calorimetry* 94.2 (2008), pp. 493–497. DOI: 10.1007/s10973-007-8443-7.
- [15] K K Kelley. ‘Specific Heats at Low Temperatures of Magnesium Orthosilicate and Magnesium Metasilicate1’. In: *Journal of the American Chemical Society* 65.3 (1943), pp. 339–341. DOI: 10.1021/ja01243a012.
- [16] Kenneth M. Krupka, Richard A. Robie, Bruce S. Hemingway, Derrill M. Kerrick and Jun Itô. ‘Low-temperature heat capacities and derived thermodynamic properties of anthophyllite, diopside, enstatite, bronzite, and wollastonite’. In: *American Mineralogist* 70 (1985), pp. 249–260.
- [17] Hubert Wagner. ‘Zur Thermochemie der Metasilikate des Calciums und Magnesiums und des Diopsids’. In: *Zeitschrift für anorganische und allgemeine Chemie* 208.1 (1932), pp. 1–22. DOI: 10.1002/zaac.19322080102.

- [18] Gilpin R Robinson, Constance M Schafer and John L Haas. *Thermodynamic and Thermophysical Properties of Mineral Components of Basalts*. US Geological Survey, 1982.
- [19] Mats Hillert and Xizhen Wang. ‘A study of the thermodynamic properties of MgO-SiO₂ system’. In: *Calphad* 13.3 (1989), pp. 253–266. DOI: 10.1016/0364-5916(89)90005-9.
- [20] Charles M. Schlaudt and Della M. Roy. ‘Crystalline Solution in the System MgO-MgSiO₄-MgAl₂O₄’. In: *Journal of the American Ceramic Society* 48.5 (1965), pp. 248–251. DOI: 10.1111/j.1151-2916.1965.tb14730.x.
- [21] AF Henriksen and WD Kingery. ‘The Solid Solubility of Sc₂O₃, Al₂O₃, Cr₂O₃, SiO₂ and ZrO₂ in MgO’. In: *Ceramurgia International* 5.1 (1979), pp. 11–17.
- [22] J W Greig. ‘Immiscibility in silicate melts’. In: *American Journal Of Science* 13.73 (1927), pp. 1–44.
- [23] Mats Hillert, Bo Sundman and Xizhen Wang. ‘An assessment of the CaO-SiO₂ system’. In: *Metallurgical Transactions B* 21.2 (1990), pp. 303–312. DOI: 10.1007/bf02664198.
- [24] Pierre Hudon, In Ho Jung and Don R. Baker. ‘Experimental investigation and optimization of thermodynamic properties and phase diagrams in the systems CaO-SiO₂, MgO-SiO₂, CaMgSi₂O₆-SiO₂ and CaMgSi₂O₆-Mg₂SiO₄ to 1.0 GPa’. In: *Journal of Petrology* 46.9 (2005), pp. 1859–1880. DOI: 10.1093/petrology/egi037.
- [25] Ping Wu, Gunnar Eriksson, Arthur D Pelton and Milton Blander. ‘Prediction of the thermodynamic properties and phase diagrams of silicate systems-evaluation of the FeO-MgO-SiO₂ system’. In: *ISIJ international* 33.1 (1993), pp. 26–35.
- [26] R. G. Berman, M. Engi, H. J. Greenwood and T. H. Brown. ‘Derivation of Internally-Consistent Thermodynamic Data by the Technique of Mathematical Programming: a Review with Application to the System MgO-SiO₂-H₂O’. In: *Journal of Petrology* 27 (Dec. 1986), pp. 1331–1364. DOI: 10.1093/petrology/27.6.1331.
- [27] P Courtial, C Tequi and P Richet. ‘Thermodynamics of diopside, anorthite, pseudowollastonite, CaMgGeO₄-olivine and akermanite up to near the melting point’. In: *Physics and Chemistry of Minerals* 27 (2000), pp. 242–250. DOI: 10.1007/s002690050253.
- [28] William W Weller and Kenneth Keith Kelley. *Low-temperature Heat Capacities and Entropies at 298.15 K of Akermanite, Cordierite, Gehlenite, and Merwinite*. Vol. 6343. US Department of the Interior. Bureau of Mines, 1963.

- [29] B S Hemingway, H T Evans Jr., G L Nord Jr., H T Haselton Jr., R A Robie and J J McGee. ‘Akermanite: phase transitions in heat capacity and thermal expansion, and revised thermodynamic data.’ In: *Canadian Mineralogist* 24.3 (1986), pp. 425–434.
- [30] Louis B Pankratz and Kenneth Keith Kelley. *High-temperature heat contents and entropies of akermanite, cordierite, gehlenite, and merwinite*. Vol. 6555. US Department of the Interior, Bureau of Mines, 1964.
- [31] C. Brousse, Robert C. Newton and Ole Jakob Kleppa. ‘Enthalpy of formation of forsterite, enstatite, akermanite, monticellite and merwinite at 1073 K determined by alkali borate solution calorimetry’. In: *Geochimica et Cosmochimica Acta* 48.5 (1984), pp. 1081–1088. DOI: doi.org/10.1016/0016-7037(84)90198-4.
- [32] In-Ho Jung, Sergei A. Decterov and Arthur D. Pelton. ‘Critical thermodynamic evaluation and optimization of the CaO-MgO-SiO₂ system’. In: *Journal of the European Ceramic Society* 25.4 (2005), pp. 313–333. DOI: 10.1016/j.jeurceramsoc.2004.02.012.
- [33] W Gutt. ‘The System Dicalcium Silicate-Merwinite’. In: *Nature* 207.4993 (1965), pp. 184–185. DOI: 10.1038/207184a0.
- [34] C.M. Schlaudt and Della M. Roy. ‘The Join Ca₂SiO₄-CaMgSiO₄’. In: 49.8 (1966), pp. 430–432. DOI: 10.1111/j.1151-2916.1966.tb15410.x.
- [35] GM Biggar and MJ O’Hara. ‘Monticellite and forsterite crystalline solutions’. In: *Journal of the American Ceramic Society* 52.5 (1969), pp. 249–252. DOI: 10.1111/j.1151-2916.1969.tb09177.x.
- [36] Houng-Yi Yang. ‘New data on forsterite and monticellite solid solutions’. In: *American Mineralogist: Journal of Earth and Planetary Materials* 58.3-4 (1973), pp. 343–345.
- [37] ZD Sharp, Eric J Essene, Lawrence M Anovitz, Guy W Metz, Edgar F Westrum Jr, Bruce S Hemingway and John W Valley. ‘The heat capacity of a natural monticellite and phase equilibria in the system CaO-MgO-SiO₂-CO₂’. In: *Geochimica et Cosmochimica Acta* 50.7 (1986), pp. 1475–1484.
- [38] John Frank Schairer and Norman Levi Bowen. ‘The binary system CaSiO₃-diopside, and the relations between CaSiO₃ and akermanite’. In: *American Journal of Science* 240.10 (1942), pp. 725–742.
- [39] N.L. Bowen. ‘The ternary system diopside-forsterite-silica’. In: *American Journal of Science* 38.225 (1914), pp. 207–264. DOI: 10.2475/ajs.s4-38.225.207.
- [40] F.R. Boyd and J.F. Schairer. ‘The system MgSiO₃-CaMgSi₂O₆’. In: *Journal of Petrology* 5.2 (1964), pp. 275–309. DOI: 10.1093/petrology/5.2.275.

- [41] William D Carlson. ‘Subsolidus phase equilibria on the forsterite-saturated join $\text{Mg}_2\text{Si}_2\text{O}_6$ - $\text{CaMgSi}_2\text{O}_6$ at atmospheric pressure’. In: *American Mineralogist* 73.3-4 (1988), pp. 232–241.
- [42] Ikuo Kushiro. ‘Determination of liquidus relations in synthetic silicate systems with electron probe analysis: the system forsterite-diopside-silica at 1 atmosphere’. In: *American Mineralogist: Journal of Earth and Planetary Materials* 57.7-8 (1972), pp. 1260–1271.
- [43] John Longhi and AE Boudreau. ‘The orthoenstatite liquidus field in the system forsterite-diopside-silica at one atmosphere’. In: *American Mineralogist* 65.5-6 (1980), pp. 563–573.
- [44] A. Palomo and F. P. Glasser. ‘Solubility of magnesium oxide in selected cement clinker phases’. In: *Advances in Cement Research* 2.6 (1989), pp. 55–59. DOI: 10.1680/adcr.1989.2.6.55.

CHAPTER
NINE

CLINKER ANALYSIS AND CALCULATIONS

The XRD, XRF, and EDX mapping clinker analysis presented in this chapter was carried out by a colleague Dr Christiane Rößler from Bauhaus-Universität Weimar. For this reason, the experimental methods will not be explained here. The collation of the results, evaluation and statistical analysis of the results of the XRD, XRF, and EDX data was carried out by the present author resulting in the graphs and discussions presented in this chapter

Now that the relevant phases, sections and systems have been assessed and modelled successfully, the information contained within the developed database can be used to carry out important calculations that will provide predictive results compared to technical clinkers.

The power of these calculations was demonstrated by Barry and Glasser [1], when they conducted equilibrium and scheil cooling calculations for Portland cement clinkers using the oxide database developed by MTDATA [2]. They proved that such databases are a great tool for predicting clinker and melt compositions at clinker temperatures and beyond. Their work has gone on to inspire similar work using a variety of oxide databases including minor elements [3, 4] with great success. This chapter will provide an update on the heat of clinkering values determined from the solid thermodynamic properties optimised in the present work. The chapter will then follow the methods and calculations carried out by Barry and Glasser [1] and will present results of equilibrium calculations as well as scheil cooling calculations, which are a more accurate representation of the cement kiln. These calculations alongside the full thermodynamic database (including the minor element MgO) will be used to predict the compositions of real industrial clinkers and the results of these will be compared against the XRD values of these clinkers, as well as results of other calculations. Finally, preliminary minor element predictions will be made using the thermodynamic database and compared against analysed EDX values. This will show the power of the thermodynamic modelling carried out in this work.

9.1 Heat of Clinkerization

It is ideal to estimate the energy required to carry out the clinker reactions, this is known as the heat of clinkerization and is determined by summing the enthalpy changes of reactions in the clinkering process. Previously, this has been well documented by Taylor [5] and these values have remained largely unchanged since their publication. They were determined using the enthalpy values from various compilations of thermodynamic data such as NIST [6] and Haas et al. [7]. It is therefore interesting to provide an update on the heat of clinkerization given that there is now an abundance of thermodynamic data since the publication by Taylor, which has been used in the current thermodynamic database to fit the relevant clinker phases. Taylor presented a value of 1757 kJ/kg for the enthalpy of formation for 1 kg of OPC (see Table 9.1).

Table 9.1: Enthalpy of formation of 1 kg of Portland cement clinker, as presented by Taylor. The products are assumed to be: C_3S , 0.673 kg; C_2S , 0.133 kg; C_3A , 0.118 kg; $\text{C}_6\text{A}_2\text{F}$, 0.064 kg; CaO (free), 0.010 kg.

Component of reaction	$\Delta H/\text{kJ kg}$
$\text{CaCO}_3 \rightarrow \text{CaO} + \text{CO}_2$	+2138
$\text{AS}_4\text{H} \rightarrow \text{Al}_2\text{O}_3 + 4 \text{SiO}_2 + \text{H}_2\text{O}$	+34
$\text{AS}_2\text{H}_2 \rightarrow \text{Al}_2\text{O}_3 + 2 \text{SiO}_2 + 2 \text{H}_2\text{O}$	+21
$2 \text{FeO} \cdot \text{OH} \rightarrow \text{Fe}_2\text{O}_3 + \text{H}_2\text{O}$	+8
$3 \text{CaO} + \text{SiO}_2 \rightarrow \text{C}_3\text{S}$	-333
$2 \text{CaO} + \text{SiO}_2 \rightarrow \text{C}_2\text{S}$	-98
$3 \text{CaO} + \text{Al}_2\text{O}_3 \rightarrow \text{C}_3\text{A}$	-3
$6 \text{CaO} + 2 \text{Al}_2\text{O}_3 + \text{Fe}_2\text{O}_3 \rightarrow \text{C}_6\text{A}_2\text{F}$	-10
Total	+1757

Using the newly calculated enthalpy of formation values for the C_3S , C_2S , C_3A and $\text{C}_6\text{A}_2\text{F}$ phases a new value of 1743.2 kJ/kg is calculated (presented in Table 9.2). The updates to the solid clinker phases represent a 1% change in the value provided by Taylor and whilst not significant, the heat of formation of the clinker compounds represents a small aspect of the update to the solids. In the present work, polymorphs of C_3S and updates to the polymorphs of C_2S were added to the thermodynamic database, which is vital for the modelling of OPC clinkers.

Table 9.2: Heat of formation for selected clinker phases contributing to the formation of 1 kg of Portland cement. The values in the parentheses are the values from Taylor and the total enthalpy of formation includes the values from Taylor for the other phases.

Compound	$H/\text{kJ kg}$
$\beta\text{-C}_2\text{S}$	-98.8 (-98)
C_3S	-349 (-333)
C_3A	-3.3 (-3)
$\text{C}_6\text{A}_2\text{F}$	-6.7 (-10)
Enthalpy of formation of OPC	1743.2 (1757)

9.2 Equilibrium and Scheil cooling

Equilibrium calculations are a set of calculations used to determine the concentrations of components present at specific temperatures and composition. At equilibrium, the Gibbs free energy difference of the reaction in equilibrium is 0. This leads to (when temperature and pressure are held at constant), a maximum of entropy via the second law of thermodynamics,

$$(\Delta S_{total})_{T,p} = -dG/T, \quad (9.2.1)$$

Therefore to determine the concentration of phases at equilibrium one can maximise the system entropy or minimise the Gibbs free energy of the system. In reality, it is far easier to minimise the Gibbs free energy, however, a mass balance constraint has to be added to avoid products and reactants disappearing or being added to the system by the minimiser. This is followed by all Gibbs energy minimization tools and has also been described by Hanein et al. [8].

In carrying out these types of calculations, there are however some assumptions that are not valid for the cement kiln or other industrial applications. For the results of the equilibrium calculations to be accurate the process must be kinetically fast and the system well mixed. These assumptions are not valid mainly due to formation of the melt and its rapid cooling rates. In this case, it has been found better to use Scheil-Gulliver solidification/cooling equations to determine the phase concentrations [9, 10]. This calculation is very similar to carrying out an equilibrium calculation but has the assumption that the liquid has rapid diffusion while the precipitated solids do not. This means that the solids that are precipitated out of the melt are frozen and do not react further approximating what occurs in a rapid cooling process. This makes this set of calculations more applicable to industrial applications such as the cement kiln [11]. Scheil cooling values are calculated through the following algorithm,

- Solve for equilibrium at temperature T , if melt phase is not present in equilibrium then increase T until melt phase is found.
- Any solid phases found are removed from the melt phase and the amount is added to an accumulator.
- Decrease T and solve for equilibrium with new melt phase composition.
- Remove solids, decrease T and solve for equilibrium until no more melt phase is found.
- Sum phases in accumulator to calculated phase fraction of the precipitated phases.

For a visualisation of this algorithm the results of a scheil cooling calculation using the thermodynamic database for the Barry and Glasser clinker composition is shown in Fig. 9.1.

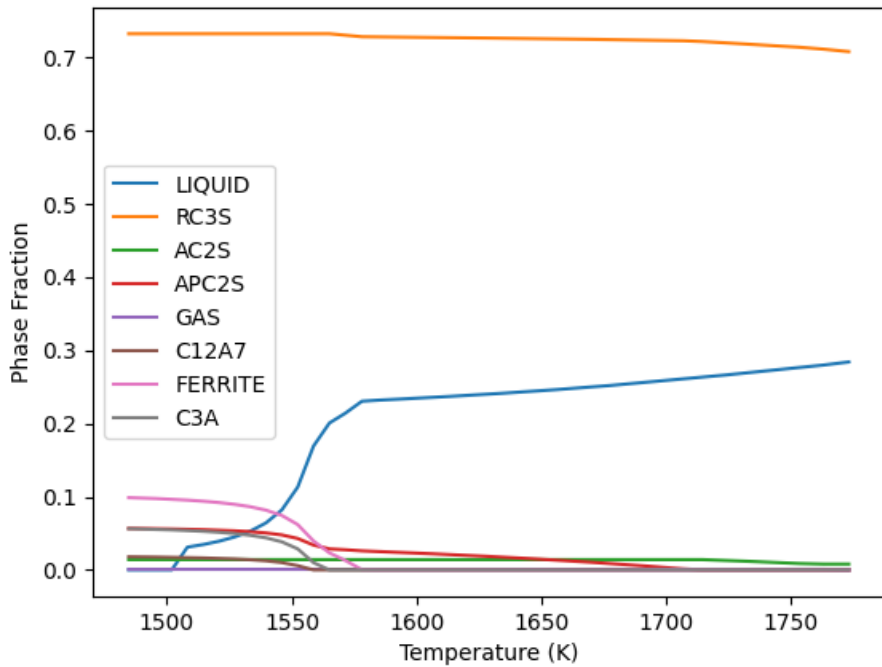


Figure 9.1: Graph of the scheil cooling computed for the composition: CaO 69 wt %, Fe₂O₃ 3.6 wt %, Al₂O₃ 5.4 wt %, SiO₂ 22 wt %.

Both equilibration and scheil cooling are powerful tools that can provide predictions of the final clinker composition for a given raw input. As a test for the database that was developed in this work, the conditions that were used in the calculations by Barry and Glasser [1] are reproduced. In their work they assumed a starting composition of: CaO 69(wt %), CaO 69(wt %), SiO₂ 22(wt %), Al₂O₃ 5.4(wt %) and Fe₂O₃ 3.6(wt %) and a clinker temperature of 1327°C for their equilibrium calculations and found a liquid existing down to 1280°C in their respective scheil cooling calculations. A comparison of the values of the calculations is presented in Table 9.3. It is to be noted that the clinker composition is representative of a “virtual” clinker for which there is no experimental data to compare against. The values compared are solely calculated between the current work and the work of Barry and Glasser. The equilibrium results for C₃A and ferrite are in close agreement with the values from Barry and Glasser. The discrepancy in the C₂S values likely arises from the new thermodynamic functions for the C₂S and C₃S solids.

Table 9.3: Table of the fractional amounts of phases calculated for the composition: CaO 69 wt %, Fe₂O₃ 3.6 wt %, Al₂O₃ 5.4 wt %, SiO₂ 22 wt %. The equilibrium is calculated at 1327°C with the scheil cooling results accumulated from 1500°C to 1227°C. The values in parentheses are from Barry and Glasser.

Calculation	C ₃ S	C ₂ S	C ₃ A	Ferrite	C ₁₂ A ₇	CA
Equilibrium	0.701 (0.720)	0.096 (0.087)	0.085 (0.086)	0.115 (0.105)	-	-
Scheil Cooling	0.749 (0.755)	0.060 (0.060)	0.045 (0.48)	0.123 (0.126)	0.023 (0.0087)	- (0.0003)
Bogue	0.710	0.094	0.085	0.109	-	-

Despite the differences in the equilibrium results, the results of the scheil cooling

closely match the results from Barry and Glasser, with the only difference being the precipitation of the $C_{12}A_7$ phase, this also causes a lack of precipitation of the CA phase. A graph of the scheil cooling for the composition is presented in Figure 9.1. As expected in the first instance C_3S is precipitated from the melt alongside C_2S . At 1710 K the α' - C_2S is precipitated. Massive precipitation of the ferrite phases occurs around 1600 K, which corresponds to the value also found by Barry and Glasser. The liquid continues to exist below 1600 K and exists down to 1500 K which is 53 K lower than the liquid crystallisation temperature of Barry and Glasser.

Furthermore, the composition of the ferrite that is precipitated out from the melt can be deduced, this is presented in Table 9.4. This allows the determination of the average composition of the ferrite phase, i.e., whether it exists as C_4AF as commonly denoted. The results show that the precipitated ferrite is close to the C_4AF composition and precipitates as $C_2A_{0.4}F_{0.6}$, which disagrees with the more alumina-rich composition of the ferrite determined by Barry and Glasser. In the following sections, these calculations will be carried out against real clinkers, where comparisons can be made against the EDX mapping, that more accurately determine the composition of the ferrite phase.

Table 9.4: Table of the mass fractions of the components of the ferrite phase (including the mole fractions of the end members of the ferrite solid solution model) calculated for the composition: CaO 69 wt %, Fe_2O_3 3.6 wt %, Al_2O_3 5.4 wt %, SiO_2 22 wt % at 1327°C. The values in the parentheses are from Barry and Glasser [1].

CaO	Al_2O_3	Fe_2O_3	$x(C_2A)$	$x(C_2F)$
0.450 (0.467)	0.163 (0.236)	0.385 (0.295)	0.401	0.598

These results are in good agreement, given the complexity of the database used by Barry and Glasser [1], who also modelled $C_{12}A_7$ and C_3A as solid solutions, which is not the case in the present database. Furthermore, Tazuddin et al. [3] used the TCOX database to use the CALPHAD method to predict clinker compositions. In their work they carried out clinker equilibrium calculations at 1400°C and 1200°C for the determination of the C_2S , C_3S and the C_3A , C_2F (ferrite) phases respectively. They then compared the results against XRD and the Bogue equation and found good agreement with the XRD values against the predicted Thermo-calc values, except in the case of C_3A . Using the same starting conditions, a comparison of the results from the work of Tazuddin et al. [3] and the results of the scheil cooling calculation using the current database are presented in Table 9.5. In the calculated results, close agreement with the previous work [3] is shown, but with a better agreement in the C_2S phase in the scheil cooling results using the current database. There is a poor prediction in the C_3A for both the current and previous works, but there is a closer agreement in the current work compared to the XRD values.

These results are favourable towards the presently developed database when compared to the results of two commercial oxide databases [2, 12]. It is therefore promising to carry the work forward as a tool for clinker predictions.

Table 9.5: Comparison of the weight % of the phases found in the clinker for the raw input: CaO 66.7, Al₂O₃ 5.68, SiO₂ 21.84, Fe₂O₃ 4.65 and MgO 1.06. Results from “equilibrium” were conducted at 1400°C and 1200°C. Scheil cooling calculation started from 1450°C, which is in line with the heating microscopy results of Tazuddin et al. [3].

	C ₃ S	C ₂ S	C ₃ A	C ₂ F (Ferrite)
Tazuddin et al.	62.18	8.30	4.13	16.41
Equilibrium	63.3	9.9	4.41	14.8
Scheil Cooling	56.4	7.0	6.7	14.4
Bogue	60.89	16.7	7.18	14.15
XRD	60.1	5.57	18	14

9.3 Comparison against clinkers

As part of this project, industrial partners sent a variety of different clinker products for analysis. The clinkers are first analysed by XRF to verify the oxide compositions provided by the manufacturers. These oxide compositions will provide the initial values for the calculations. The clinkers presented here are also analysed by XRD-Reitveld to determine the phase composition of the clinkers, this in itself is valuable information as it experimentally determines the amount of alite, belite, C₃A, and ferrite in the final product accurately.

In total 27 clinkers were received from the industrial partners, with 26 of the clinkers analysed by XRF, XRD, and EDX. The collated results are presented in the Appendix. Shim et al. [13] conducted a similar analysis of the clinker oxide composition, with the majority of their clinkers coming from the 1977 Holderbank/Holcim database [14]. A comparison of the oxide compositions in the present work and the work by Shim et al. [13] is presented in Table 9.6.

Table 9.6: Comparison of the average clinker oxide compositions (in wt %) measured by XRF in the present work and the work of Shim et al. [13]. The typical values as presented by Taylor [5] are also presented for comparison.

Source	CaO	SiO ₂	Al ₂ O ₃	Fe ₂ O ₃	MgO	SO ₃	K ₂ O	Na ₂ O	P ₂ O ₅	TiO ₂	Mn ₂ O ₃
Present	65.8	21.36	4.8	3.35	1.93	0.8	0.75	0.17	0.22	0.29	0.05
[13]	65.29	22.11	5.14	2.91	1.88	0.91	0.47	0.54	0.18	0.2	0
[5]	67	22	5	3				3			

This comparison is interesting as it allows the comparison of historical clinkers, with more modern compositions, and the changes in oxide composition over the last 50 years. There is an increase in Fe₂O₃ content and a decrease in alkali (Na₂O) content, with all other oxides in agreement on average. For further comparison, the distribution of the oxide compositions between the current clinker data set, and the data set of Shim et al. is presented in Figure 9.2. This detailed analysis shows, that the distribution of the SiO₂ content is more varied in the work of Shim et al. In general, there are fewer extremes in the current work for the main oxides with a greater diversity in the alkali content when compared against the previous data set.

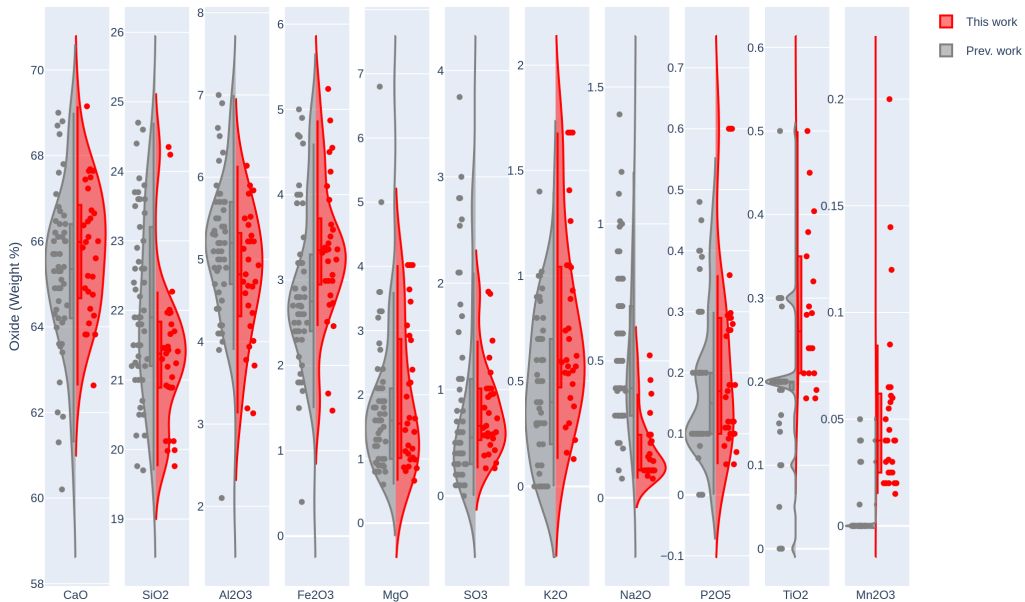


Figure 9.2: Violin plot of the distribution of the oxide composition between the clinkers in the current work and the clinkers collated by Shim et al. [13]. The horizontal line in the box plot is the median value and the box represents the interquartile range (the range between the 1st quartile and the 3rd quartile). The vertical lines outside the box are the $1.5 \times$ interquartile range, which is a simple measure for determining outliers.

These changes as well as the difference in the distribution of the SiO_2 content result in differences in major clinker phases. A comparison of the clinker phases is presented in Table 9.7. From the average clinker phase compositions, there is a great increase in alite %, which corresponds to a significant decrease in belite %. The change was expected as alite is responsible for the early development in OPC [15], making it a desirable change in OPC. Additionally, there is an observed increase in the aluminate and ferrite composition compared to the study by Shim et al. These changes give us an insight into the desires and priorities of clinker manufacturers over the last few decades, which is reflected in the final clinker.

Table 9.7: Comparison of the average clinker phase composition measured from XRD, values are in wt %.

Phase (wt %)	Alite	Belite	Aluminate	Ferrite
Present work	67.55	10.7	8.02	10.34
Shim et al.	62.32	17.63	6.59	9.02

9.3.1 Clinker prediction

The major clinker phases can be calculated by the Bogue equation [16] and the modified Bogue equation [17] using the oxide composition as the initial conditions for the calculations. The modified Bogue was developed by Taylor to try and account for the minor element substitutions that exists in OPC clinkers by modifying the conventional Bogue equations. Both sets of equations are a simple mass conversion, where the mass of

the oxides is converted to the clinker phases by multiplying by a coefficient matrix, i.e., a set of simultaneous equations. The difference between the experimental clinker phase values and the calculated values for the current clinker data set and the data-set of Shim et al. [13] using the Bogue and the modified Bogue equation is shown in Figure 9.3.

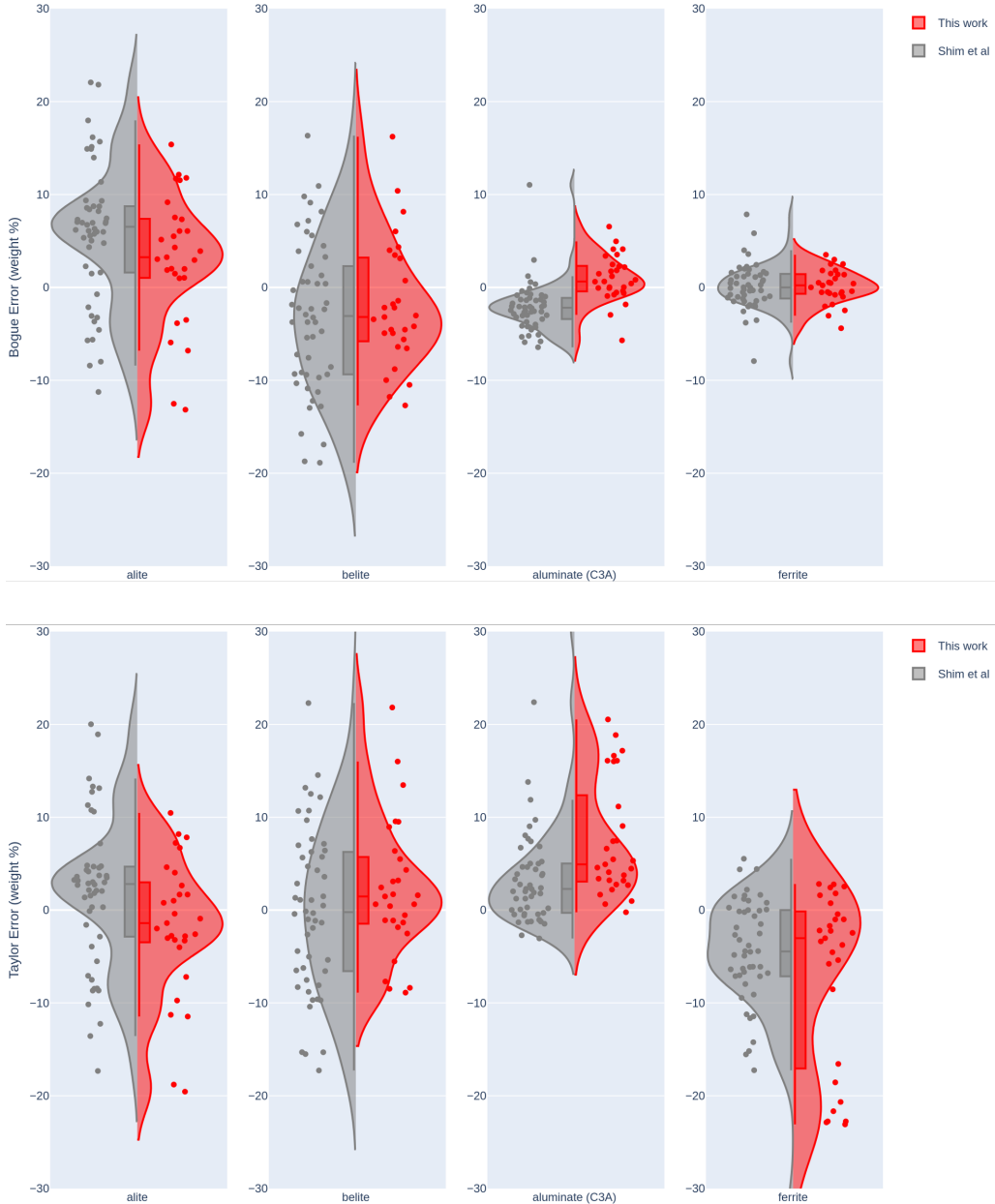


Figure 9.3: Violin plots of the error % between the experimental values and the calculated values using the Bogue equation (top) and the modified Bogue equation (bottom).

From the comparison between the two forms of the equations, a general trend can be seen in the results. The alite phase is over-predicted and the belite phase is under-predicted in the belite phase for the Bogue equation, which is a common observation of the Bogue equation [13, 17]. Furthermore, in general, the alite and belite phase are better predicted in the modified Bogue, with the aluminate and ferrite better predicted in the conventional Bogue. This could suggest an adjusted equation be developed that takes advantage of both forms of the equations to better predict the major clinker phases, i.e.

the alite and belite coefficients taken from the modified Bogue and the coefficients for the aluminate and ferrite from the conventional Bogue to form a new set of coefficients.

Additionally, aside from these two calculations, the approach by Hanein et al. [8] (which utilises the thermodynamic information for the solid phases to conduct equilibrium calculations, without substitutions), can also be used to predict the major clinker phases. The results of these calculations for the different clinker data sets are presented in Figure 9.4. These calculations are more robust than the forms of the Bogue equation by enforcing the non negativity constraint of the mass balance. This is important to enforce because in the modified Bogue equation negative masses were often seen in the aluminate and ferrite phases, which is physically impossible. This approach generally has good agreement with the experimental values, with only some discrepancy in the values of the aluminate phase for only the current clinker data set.

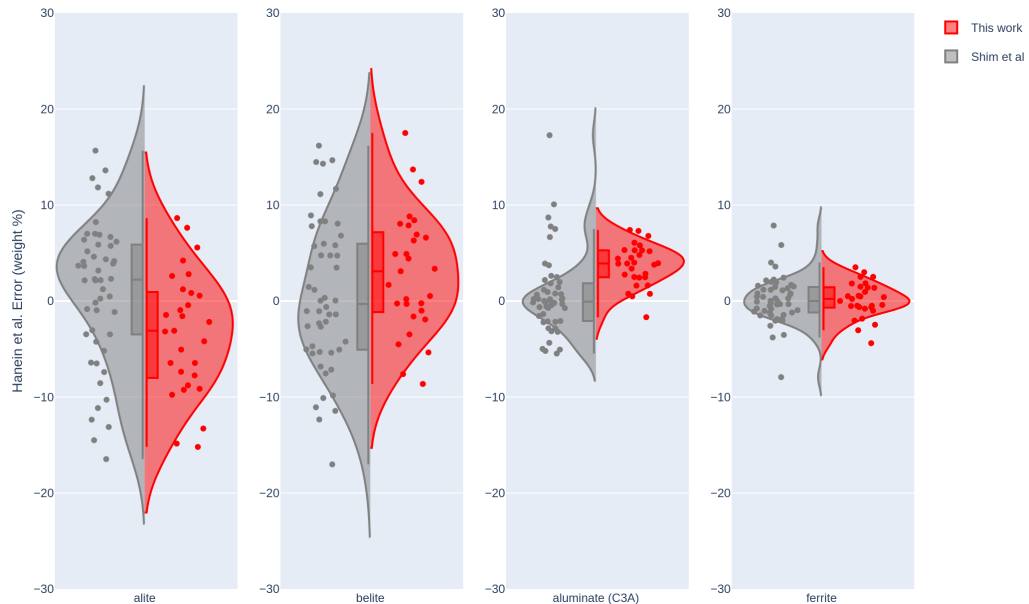


Figure 9.4: Violin plots of the error % between the experimental values and the calculated values using the approach of Hanein et al. [8].

Finally, the currently developed thermodynamic model for the $\text{CaO}-\text{SiO}_2-\text{Al}_2\text{O}_3-\text{MgO}-\text{Fe-O}$ system was used to conduct scheil cooling calculations to predict the major clinker phases in both clinker data-sets, this is presented in Figure 9.5. This calculation differs from the calculations presented thus far, with the biggest difference being the inclusion of the melt phase and the solid precipitation from it. From the results using the current thermodynamic modelling, there is generally good agreement in the values of the experimental and calculated values for all the major clinker phases. There is a tendency to over-predict the alite phase, which is similar to the Bogue equation, but there is excellent agreement in the belite phase (especially for the data set of Shim et al.). This is to be expected, as the belite phase is well modelled by including the Mg substitution, whereas the same is not done for the alite phase. There is good agreement for the aluminate phase content, with excellent agreement for the values of the ferrite phase. This is similar to the trend seen in the approach by Hanein et al. [8].

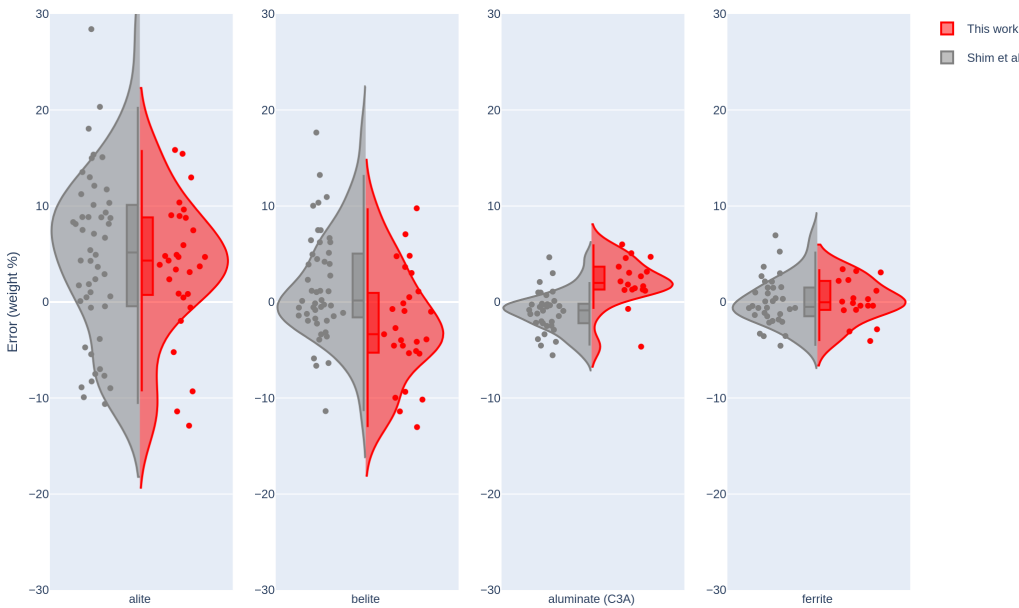


Figure 9.5: Violin plots of the error % between the experimental values and the calculated values using the currently developed thermodynamic database to conduct scheil cooling calculations from 1500°C.

A summary of the average error % of the clinker phases achieved by each calculation method is presented in Table 9.8. The summary reinforces the earlier conclusions that were made about the prediction trends of each calculation but also shows a large difference between the clinker data sets. It is observed that generally, the calculations agree more with the experimental results of the clinkers within the work Shim et al. (excluding the Bogue calculation). This could suggest that there is a discrepancy in the analysis of the two clinker data sets. It is known that the present work was analysed to study a greater diversity of minor elements, which may result in more substitutions that are not accounted for by the various calculations. The scheil cooling calculations conducted in the present work with the newly developed thermodynamic database are shown to be favourable against the more “traditional” calculations, exhibiting a generally smaller standard deviation and good agreement against the experimental data for all the major clinker phases.

Table 9.8: Summary of the average error in wt % (alongside the standard deviation) for the calculations conducted on the present clinker data set, and the data set of Shim et al.

Calculation	Bogue	Modified Bogue	Hanein et al.	This work
Alite (Present)	3.11 ± 6.95	-1.64 ± 7.38	-3.32 ± 6.32	3.62 ± 7.03
Alite (Shim et al.)	5.84 ± 7.50	-1.80 ± 8.04	0.911 ± 7.46	4.68 ± 8.63
Belite (Present)	-1.93 ± 6.75	2.18 ± 7.28	2.92 ± 6.26	-2.40 ± 5.69
Belite (Shim et al.)	-3.14 ± 8.10	-0.12 ± 8.75	0.569 ± 7.79	1.63 ± 5.49
Aluminate (Present)	0.981 ± 2.47	7.45 ± 6.21	3.70 ± 2.15	2.20 ± 2.40
Aluminate (Shim et al.)	-2.10 ± 2.67	3.73 ± 6.04	0.614 ± 4.20	-0.982 ± 2.11
Ferrite (Present)	0.130 ± 1.83	-6.88 ± 9.40	0.130 ± 1.83	0.179 ± 2.15
Ferrite (Shim et al.)	0.15 ± 2.43	-5.64 ± 8.84	0.152 ± 2.43	0.038 ± 2.49

It should be mentioned that the differing results seen in the calculations with the present clinker data set could be due to the discrepancy in the XRD and XRF values i.e., the XRD does not pick up all the compositions or phases that are present in the final clinker. To try and account for this difference the XRD wt % was used to back calculate the oxides. The results of the scheil cooling calculations against the back-calculated values for selected poorly predicted clinkers are shown in Figure 9.6.

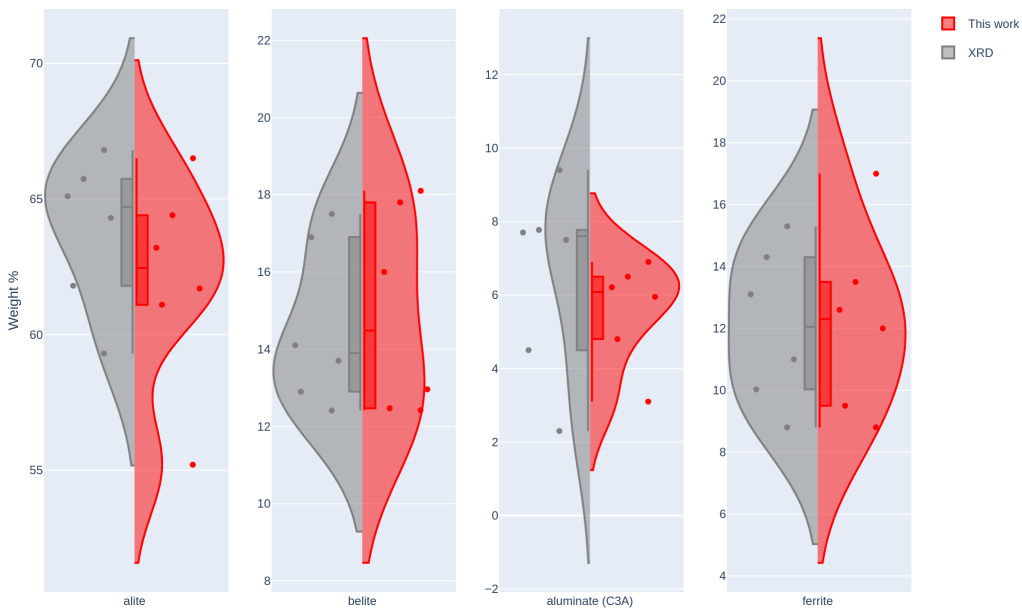


Figure 9.6: Weight % of the calculated clinker phases within selected clinkers compared against the XRD values.

The results of the “back-calculated” scheil cooling results for the clinkers that were not very well predicted are now observed to be in much better agreement with the XRD values. A reason for this could be due to the discrepancies between the XRF and XRD values, which results in the incorrectly calculated oxide compositions for the clinkers. This could also arise from the sensitivity of the XRF, meaning more phases are present in the XRD than are detected. This would mean the values of the oxides that are calculated by the XRD to be more representative of the analysed XRD phases (but not necessarily the true clinker phases), resulting in a far better prediction.

9.3.2 Minor element substitution

The EDX mapping data that was gathered in the current clinker data set, gives an insight into the elements within the major clinker phases. Figure 9.7 is an example of the EDX mapping data for the belite phase in all the clinkers. It is observed that there is an ideal range of the amount of oxides that can exist in the belite phase, this is denoted by the peaks in the violin plots. These ranges correspond to the substitution of those oxides for other oxides, which in turn corresponds to the site fractions in the clinker phase. From this, the co-substitution between the different oxides in belite was studied and is presented in Figure 9.8.

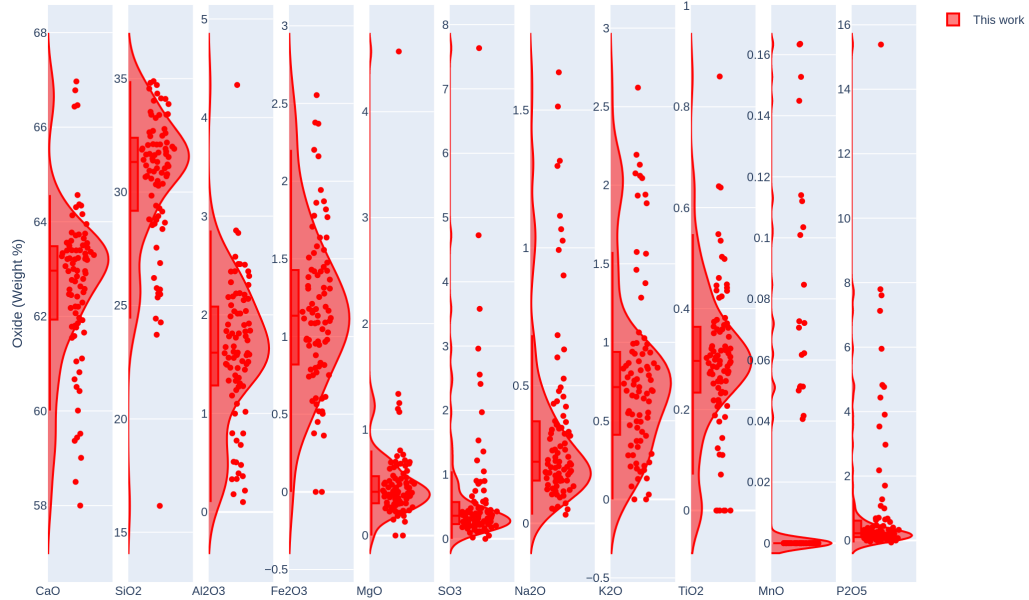


Figure 9.7: Oxide composition of the belite phase present in the clinkers within the clinker data-set. Results were determined using EDX mapping.

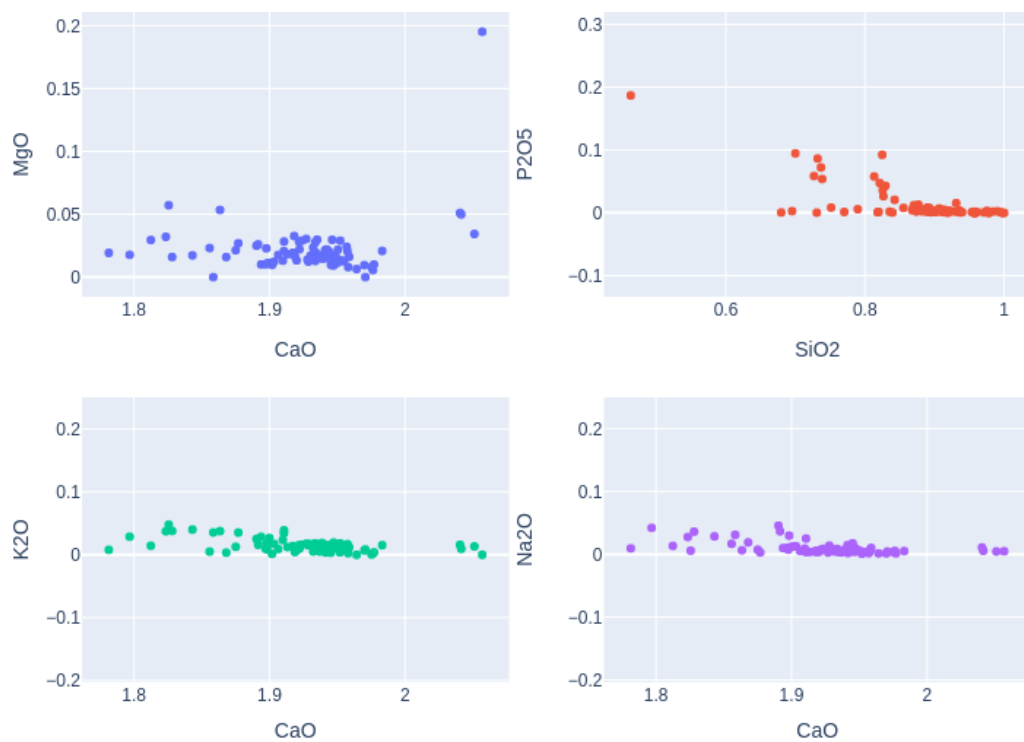


Figure 9.8: Molar amounts of oxides present in the belite phase within the present data set, plotted against various oxides to determine the co-substitution.

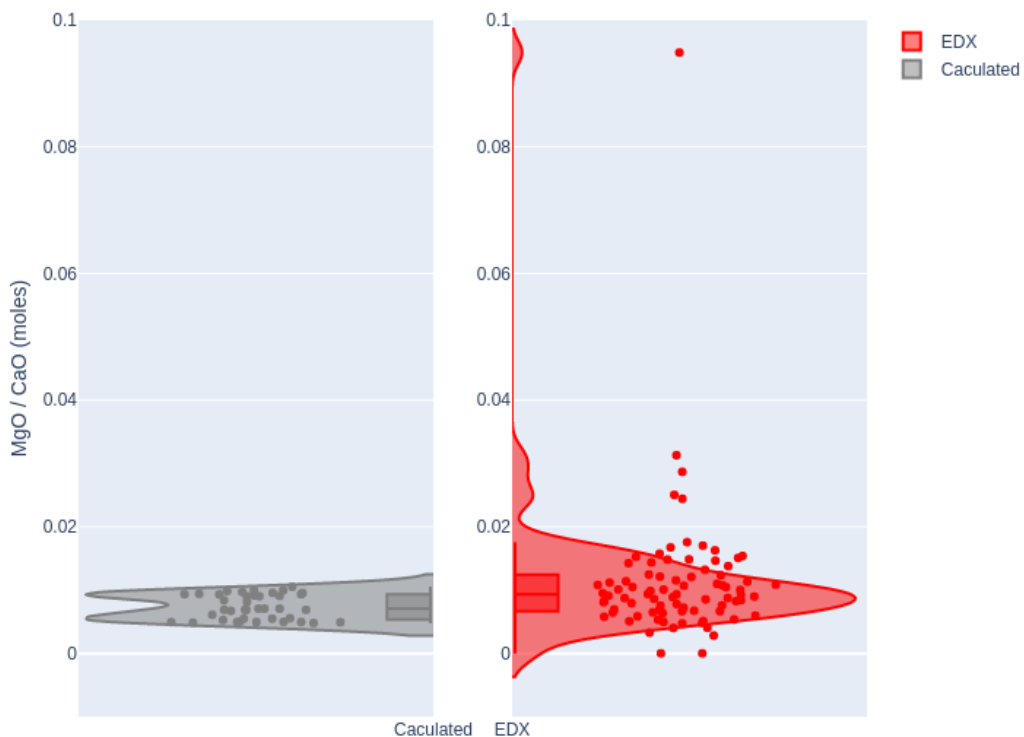


Figure 9.9: Violin plots of the moles of MgO/CaO in the belite phase calculated from scheil cooling, compared with the EDX values measured in the clinker data-set. The EDX contains more points due to the detection of multiple belite phases in the clinkers.

This analysis provides a great insight into the role of minor elements by showing which of the major oxides can be substituted for which minor oxide including in their respective amounts, with these values largely agreeing with the approximate values given by Taylor [5].

With the thermodynamic modelling of the MgO substitution into the belite phase carried out in the present work, it is also possible to calculate the amount of CaO and MgO using the thermodynamic database. Conducting an equilibrium at a fixed temperature of 1327°C (the chosen temperature from Barry and Glasser [1]) results in a value of 1.98 CaO and 0.01 MgO , which matches the average value seen in the EDX data. Using the scheil cooling calculations, the amount of MgO in the precipitated phases can be determined. A graph of the plot of the ratio of MgO/CaO found in the belite phase is presented in Figure 9.9.

The calculations result in approximate values of the molar amounts of CaO and MgO that are very close to the majority of the clinkers seen in the EDX data Figure 9.8. The scheil cooling resulted in the precipitation of up to two belite phases, corresponding to the high temperature polymorphs of C_2S , however within some clinkers the EDX detected more distinct structures of belite. The variation and scatter in the experimental values suggest that MgO or CaO is substituted by other oxides, not accounted for in the model.

It is difficult to directly compare the results of the calculations against the EDX values for individual clinkers, due to the difference in belite phases detected at different magnifications. An attempt to compare the results of individual clinkers is presented in

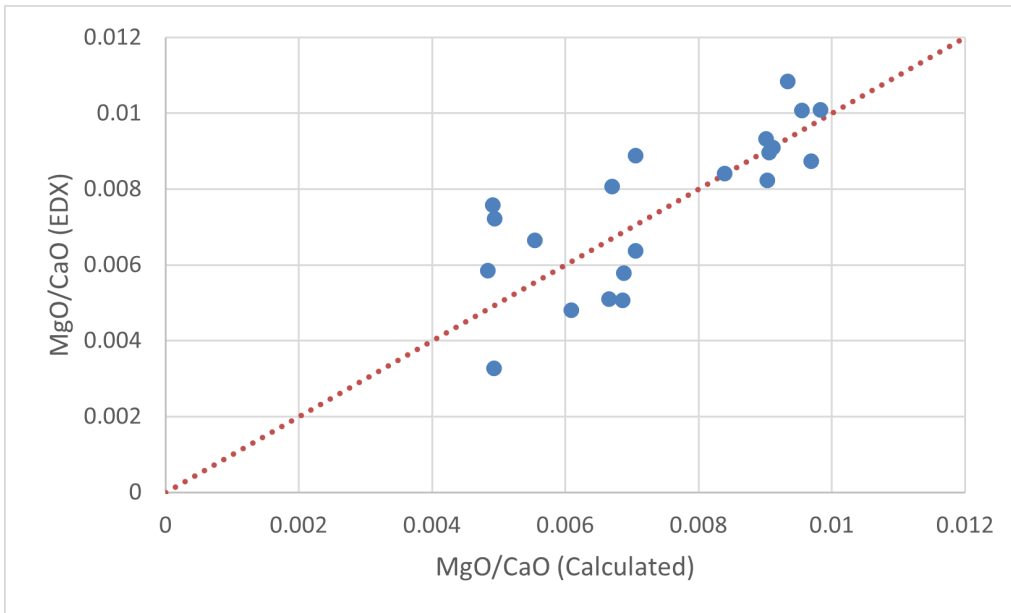


Figure 9.10: Cross-plot of MgO/CaO ratio in the belite phase in individual clinkers, with the calculated ratio compared against the EDX values. A linear dashed-line is plotted to compare the calculated values against the EDX values.

Figure 9.10, where comparisons are made against only the high magnification results for selected clinkers, where two different belite clinker phases were detected. From these results, there is general agreement between EDX values and the calculated values using the thermodynamic database, with the cross-point values existing close to a $y = x$ relationship. Furthermore, Tazuddin et al. [4] measured a synthesised clinker sample by EDX for their work and found an average MgO/CaO ratio of 0.0112, this value closely matches the average ratio of 0.0102 calculated using the thermodynamic database developed in the present work for their synthetic clinker composition. These preliminary results show that the scheil cooling calculations using the developed database are promising in being able to predict the ratio of MgO/CaO ratio within the belite phase, this is a very useful tool for clinker modelling and research.

Similar statistical analysis can be done with the ferrite phase, which is a known solid solution existing over a range of compositions [5, 18]. By looking at the $\text{Al}_2\text{O}_3/\text{Fe}_2\text{O}_3$ ratio, the average composition of the ferrite solid solution within the present data set is observed to be close to $\text{C}_6\text{A}_2\text{F}$ (see Fig 9.11). However, looking at the $\text{Al}_2\text{O}_3/\text{CaO}$ ratio suggests the ferrite composition is close to the C_4AF composition. This difference in the supposed ferrite solid solution could be due to a decrease in Fe_2O_3 which arises from the substitution of the Fe_2O_3 with other oxides. If this is the case this would cause the $\text{Al}_2\text{O}_3/\text{Fe}_2\text{O}_3$ ratio to appear alumina rich. From this theory, it is therefore assumed that the average ferrite phase composition is close to the C_4AF , but with a decrease in Fe_2O_3 . This closely matches with the average composition presented by Taylor [5], $\text{C}_4\text{AF}_{0.6}\text{M}_{0.2}\text{S}_{0.15}\text{Ti}_{0.05}$.

Furthermore, similar to the belite phase, the thermodynamic database developed in this work can be used to try and predict the composition of the ferrite phase, with the

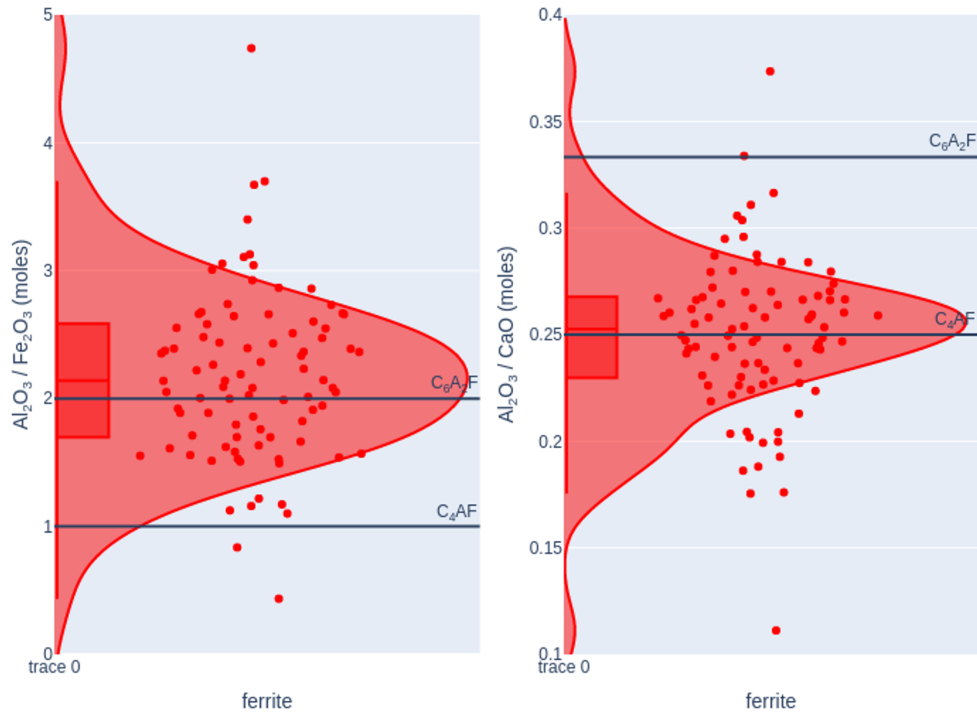


Figure 9.11: (left) Ratios of $\text{Al}_2\text{O}_3/\text{Fe}_2\text{O}_3$ and $\text{Al}_2\text{O}_3/\text{CaO}$ (right) within the ferrite phase for all clinkers within the clinker data set. Marked lines represent the $\text{C}_6\text{A}_2\text{F}$ and C_4AF solid composition.

results of the $\text{Al}_2\text{O}_3/\text{CaO}$ ratio shown in Fig. 9.12. The results of the calculation suggest $\text{Al}_2\text{O}_3/\text{CaO}$ ratio ($x = 0.2$) close to the C_4AF composition ($x = 0.25$) but not exact, like the EDX data suggests. This may be due to the current model of the ferrite phase, which only includes C_2A and C_2F in the solid solution sublattice. This would therefore calculate a C_2F -rich ferrite, which is caused by the iron oxide in the input conditions only being able to form ferrite in the present work i.e, the other clinker phases do not contain a possible substitution for Fe_2O_3 in the present thermodynamic model. However, in real clinkers it is known that iron exists in large quantities in the other clinker phases, for example, 1% is present on average in belite, with existence up 2.5% (see Figure 9.7). Therefore, to better predict the composition of ferrite, it is necessary to model the substitution of iron within the other clinker phases, as well as the substitution of other oxides (that can replace iron) in the ferrite phase.

Figure 9.13 shows a cross plot of the calculated $\text{Al}_2\text{O}_3/\text{CaO}$ values using the current database compared against the $\text{Al}_2\text{O}_3/\text{CaO}$ determined by EDX for selected clinkers. In the comparison, it is shown that the prediction of the $\text{Al}_2\text{O}_3/\text{CaO}$ ratio is in excellent agreement for the clinker with lower alumina content, but it is poor at predicting the ratios greater than 0.22, this is supported by the earlier conclusions of the need to model further substitutions but shows that the developed thermodynamic database is useful in its ability to be able to predict at least some compositions of ferrite within clinkers.

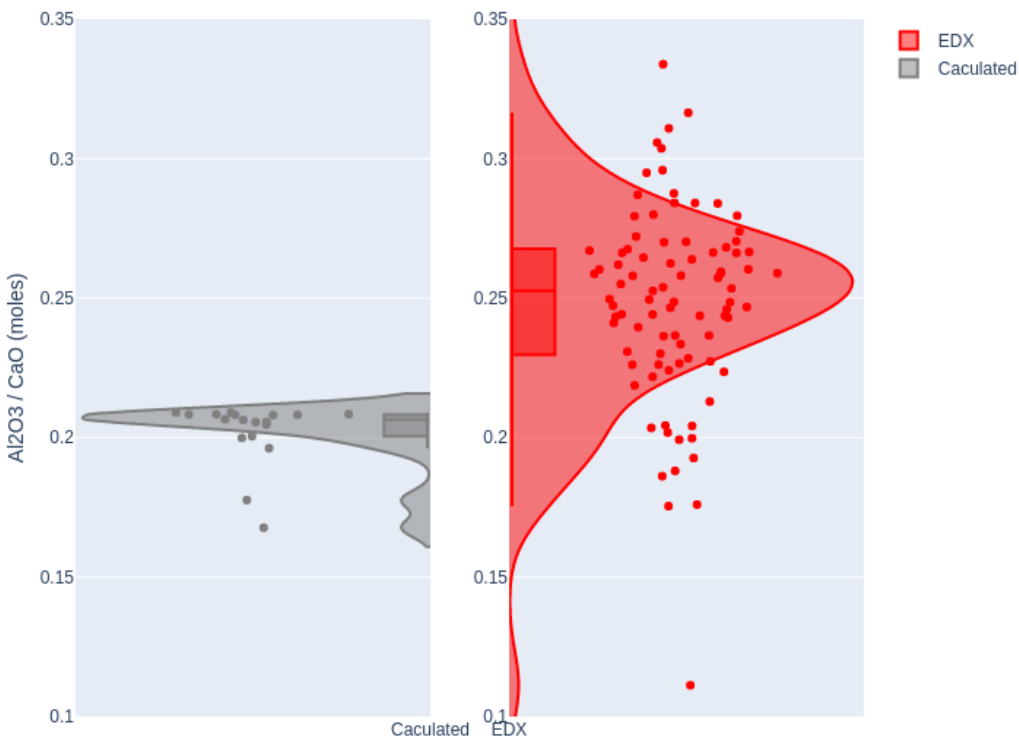


Figure 9.12: Violin plots of the $\text{Al}_2\text{O}_3/\text{CaO}$ ratio in the ferrite phase calculated using scheil cooling calculations, compared against the EDX values measured in the clinker data-set. The EDX plots contains more data-point due to the detection of multiple ferrite phases, within the clinkers.

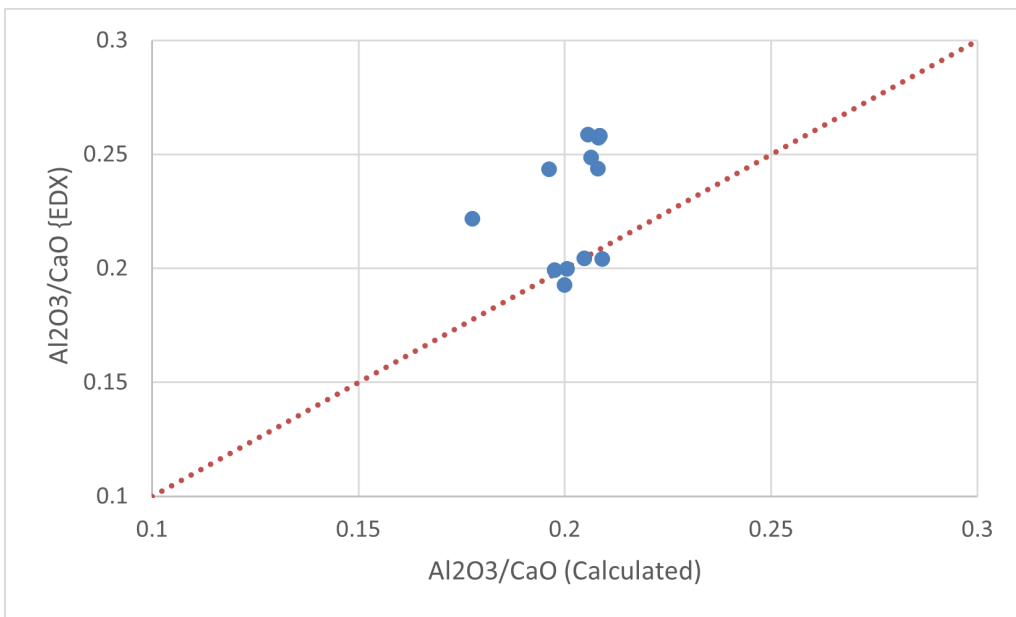


Figure 9.13: Cross-plot of the calculated ratio of $\text{Al}_2\text{O}_3/\text{CaO}$, within the ferrite phase for individual clinkers, compared against the EDX values. A linear dashed-line is plotted to compare the calculated values against the EDX values.

9.4 Conclusions

In this chapter, the thermodynamic database that was developed in this work was used as a tool for clinker predictions. This approach was first demonstrated by Barry and Glasser [1] and the results of the scheil cooling calculations were in close agreement with their work. Comparison against the work of Tazuddin et al. [3] were also favourable, where they used the commercial database to model the CaO-SiO₂-Al₂O₃-Fe₂O₃-MgO system in their work.

A clinker data-set was presented in this work that included 27 clinkers that were received from industry and contained XRF, XRD, and EDX analysis. This provided an insight into industry trends when compared against the work of Shim et al. [13] and much-needed information on minor element substitution. The clinker data set was used to test and compare various predictive tools including scheil cooling calculations using the CaO-Al₂O₃-SiO₂-MgO-Fe-O that was developed in this thesis. The results of the clinker phases predicted by the developed thermodynamic database, showed good agreement with the experimental and performed better than the previous methods at predicting all clinker phases except for in the case of alite. This is due to the lack of modelling of MgO into alite, which is often ignored in many thermodynamic assessments but is essential for cement clinker and therefore should be studied further.

Finally, the EDX analysis in the presented clinker data set allowed for the analysis of the minor element substitution, with a focus on the belite phase and the possible composition of the ferrite phase. This analysis was compared against the results of the scheil cooling calculations and whilst only preliminary calculations at this stage, the results of the belite phase are in good agreement and show the power of the thermodynamic modelling and the resultant calculations that were carried out in this work. Furthermore, even though the predicted ferrite composition didn't exactly match all the EDX data, there was some ability to predict the ferrite compositions within certain clinkers. These calculations suggest other substitutions in the ferrite phase have to be modelled, to avoid an iron rich ferrite prediction.

Currently, the prediction of these substitutions cannot be achieved by the more traditional prediction tools such as the Bogue equation, due to their modelling of the clinker phases as purely stoichiometric which is far from the true clinker composition. The ability to predict minor elements within OPC cement is a powerful tool and is data that can currently be only achieved experimentally with accuracy. However, it has been shown here, that the developed thermodynamic database is a stepping stone to better predict and model the clinker phases (including minor elements).

9.5 References

- [1] T I Barry and Fredrik Glasser. ‘Calculation of Portland cement clinkering reactions’. In: *Advances in Cement Research* 12 (2000), pp. 19–28. DOI: 10.1680/adcr.2000.12.1.19.
- [2] John Gisby, Pekka Taskinen, Jouni Pihlasalo, Zushu Li, Mark Tyrer, Jonathan Pearce, Katri Avarmaa, Peter Björklund, Hugh Davies, Mikko Korpi, Susan Martin, Lauri Pesonen and Jim Robinson. ‘MTDATA and the Prediction of Phase Equilibria in Oxide Systems: 30 Years of Industrial Collaboration’. In: *Metallurgical and Materials Transactions B* 48.1 (2017), pp. 91–98. DOI: 10.1007/s11663-016-0811-x.
- [3] Tazuddin, Hemantkumar N. Aiyer and Amit Chatterjee. ‘Phase equilibria studies of CaO-SiO₂-Al₂O₃-Fe₂O₃-MgO system using CALPHAD’. In: *Calphad* 60 (2018), pp. 116–125. DOI: 10.1016/j.calphad.2017.12.003.
- [4] A Tazuddin, Hemantkumar Aiyer and Amit Chatterjee. ‘Thermodynamic simulation in evaluating the role of minor oxides and mineralizers in Portland cement clinker phase formation’. In: *SN Applied Sciences* 2.10 (2020), pp. 17–37. DOI: 10.1007/s42452-020-03548-7.
- [5] H.F.W. Taylor. *Cement chemistry*. 2nd edition. Thomas Telford Publishing, 1997. DOI: 10.1680/cc.25929.
- [6] M. W. Chase. ‘NIST-JANAF Thermochemical Tables, 4th Edition’. In: (1998). DOI: 10.18434/t42s31.
- [7] John L. Haas Jr., Glipin R. Robinson Jr. and Bruce S. Hemingway. ‘Thermodynamic tabulations for selected phases in the system CaO-Al₂O₃-SiO₂-H₂ at 1 atm between 273.15 and 1800 K’. In: *Journal of Physical and Chemical Reference Data* 10.3 (1981), pp. 575–670. DOI: 10.1063/1.555645.
- [8] Theodore Hanein, Fredrik P. Glasser and Marcus N. Bannerman. ‘Thermodynamic data for cement clinkering’. In: *Cement and Concrete Research* 132.106043 (2020). DOI: 10.1016/j.cemconres.2020.106043.
- [9] Erich Scheil. ‘Bemerkungen zur schichtkristallbildung’. In: *International Journal of Materials Research* 34.3 (1942), pp. 70–72.
- [10] GH Gulliver. ‘The quantitative effect of rapid cooling upon the constitution of binary alloys’. In: *Journal of the Institute of Metals* 13 (1915), pp. 263–291.
- [11] Tanai Marin. ‘Modelling Scheil Cooling of a Metal Alloy - Thermodynamic and Multiphysics Solidification’. In: Oct. 2016.
- [12] J-O Andersson, Thomas Helander, Lars Höglund, Pingfang Shi and Bo Sundman. ‘Thermo-Calc and DICTRA, computational tools for materials science’. In: *Calphad* 26.2 (2002), pp. 273–312. DOI: 10.1016/S0364-5916(02)00037-8.

- [13] Sang-Hyo Shim, Tae-Hee Lee, Seong-Joon Yang, Norhazilan Bin Md. Noor and Jang-Ho-Jay Kim. ‘Calculation of Cement Composition Using a New Model Compared to the Bogue Model’. In: *Materials* 14.16 (2021). DOI: 10.3390/ma14164663.
- [14] M. Kristmann. ‘Portland cement clinker mineralogical and chemical investigations: Part II electron microprobe analysis’. In: *Cement and Concrete Research* 8.1 (1978), pp. 93–102. DOI: 10.1016/0008-8846(78)90062-5.
- [15] T Staňek and P Sulovský. ‘The influence of the alite polymorphism on the strength of the Portland cement’. In: *Cement and Concrete Research* 32.7 (2002), pp. 1169–1175. DOI: 10.1016/S0008-8846(02)00756-1.
- [16] R. H. Bogue. ‘Calculation of the Compounds in Portland Cement’. In: *Industrial and Engineering Chemistry - Analytical Edition* 1.4 (1929), pp. 192–197. DOI: 10.1021/ac50068a006.
- [17] H. F. W. Taylor. ‘Modification of the Bogue calculation’. In: *Advances in Cement Research* 2.6 (1989), pp. 73–77. DOI: 10.1680/adcr.1989.2.6.73.
- [18] Peter del Strother. *Lea’s Chemistry of Cement and Concrete (Fifth Edition)*. Ed. by Peter C. Hewlett and Martin Liska. Butterworth-Heinemann, 2019. ISBN: 978-0-08-100773-0. DOI: 10.1016/B978-0-08-100773-0.00002-2.

CHAPTER
TEN

CONCLUSION

In conclusion, in this project, a thermodynamic database with specific relevance for Portland cement clinkers was developed. In this thesis, the need for such a database was discussed which arises from the complexity of the chemistry of the cement clinker production and the lack of a single source of information for Portland cement clinkers. In the first instance, the consolidation and remodelling of the thermodynamic data surrounding clinker phases were required. This included the use of the latest in CALPHAD modelling, through the 3rd generation models and the two-state model. The complexity of such modelling required the strict use of the CALPHAD approach and in this effort, new tools were developed to mathematically assess solid and liquid parameters using a least squares approach and an automatic approach, which has successfully been used in assessing many systems in the database. In this effort, a preliminary thermodynamic database for OPC application was developed, being made of CaO, SiO₂, Al₂O₃, Fe-O and finally the minor element MgO. Calculations using this database were favourable against simulated clinkers produced by Barry and Glasser [1] and Tazuddin et al. [2]. An industrial clinker database was presented as a part of this work, which included a detailed analysis of 27 clinkers using XRF, XRD, and EDX. The presently developed work was used to predict the clinkers with the presented clinker database and the database of Shim et al. [3], where the calculated results were in general agreement. Furthermore, with the addition of MgO in the thermodynamic modelling, the main substitution within the belite phase could be studied, and the resulting calculations showed good agreement with the EDX results within the clinker database. Finally, the composition of the ferrite phase was determined using the thermodynamic database and showed good agreement in clinkers that contained alumina-poor ferrite phases. The initial application and results look promising and show the importance of such work and allow for further extensions to the thermodynamic database produced in this thesis.

10.1 Future work

The first work required to improve the presently developed thermodynamic modelling is to include the modelling of the MgO and Fe₂O₃ substitution within the alite, ferrite and aluminate phases to properly account for the effect of varying MgO and Fe₂O₃ content. The role of MgO and other minor elements was studied by [2, 4], who used the FTOX [5] and TXOC [6] database. In their work, a large effect on the precipitation of the major clinker phases is observed when minor elements are varied. This was also seen in the current work, with results of the calculations for the belite and ferrite compositions. Therefore, it is essential to model the uptake of Fe₂O₃ and MgO into other phases, to dramatically improve the ability of the current thermodynamic database to predict alite but also to predict minor elements within specific clinker phases. This modelling work could also be developed further to look at other cement compositions or “extreme” clinker compositions.

Furthermore, it is also desirable to add other minor elements such as F, Zn, and Ti. This modelling is far less complex due to the trace amounts of these elements in the cement kiln and could be done with ease as the underlying database has been developed and whole systems containing these minor elements don't have to be developed [7]. This is theoretically enough to model the minor element behaviour in the clinker and if needed the wider systems on minor elements can be assessed. Additionally, SO₃ can be added to the database, but this will have to be modelled with oxygen dependency as well as including the potential sulfate phases that can appear in the cement kiln [8].

For the fitting approach and tools developed in this project, it is desirable to test other systems and models such as the two-ionic sublattice and the modified quasichemical model. A global optimiser for this routine would be desirable and would drastically increase reliability, calculation of miscibility gaps and reduce computational costs. Work is underway to include such an optimisation routine through the use of interval arithmetic methods inside the Julia programming language. This will allow for fast and accurate optimisation of Gibbs free energy expressions as well as the melt model parameters.

10.2 Impact

The impact of this work on cement research is in the resulting thermodynamic database, which has been modelled from the ground up and includes much-needed updates to the underlying phases that form OPC clinker. This thermodynamic database is the first open-access database specific to Portland cement clinkers, with full database provided in the Appendix. Furthermore, in this work, a detailed industrial clinker data set was presented in this work, which would prove very useful to those carrying out calculations or other forms of analysis. The CaO-SiO₂-Al₂O₃-Fe-O-MgO thermodynamic system that was developed in this work, largely contains updates to the underlying compounds and new models and modelling techniques. It was designed as a single source of thermodynamic

information specific for OPC use. The resulting database has also proven successful in predicting synthetic clinker compositions and real clinkers with good agreement to the experimental values as well as the ability to attempt to predict minor elements within the clinker phases. At a smaller scale, this work and the resulting database will provide a framework for researching clinker compositions. This is more important now, given the increasing diversity in cement clinkers, due to a decrease in raw materials in certain parts of the world. On a larger scale, this work could be used to optimise the industrial clinker production process, with manufacturers having the ability to accurately predict clinker phases and compositions for a given raw oxide mix. Furthermore, the developed thermodynamic work could be used to develop a kiln model and with the inclusion of the melt phase could help to improve the mechanical processes within the cement kiln. In addition, combining this work, with kinetic data and models could help to produce advanced thermal models for kilns or digital twins. This tool and the database are a far more thermodynamically consistent predictor of clinker compositions and have the potential of aiding manufacturers in reducing material and energy losses as well as aiding in the reduction of CO₂ emissions from the clinker production process.

Additionally, the fitting methodologies that were developed in this work could prove useful in aiding the CALPHAD community. Even though they are in the initial stages of development and have only been used for oxide systems, the tools developed in this work could be used to fit a range of solid and liquid Gibbs free energy expressions, including various polynomial and 3rd generation models. The uncertainty approach in this work makes it quick and easy to change and apply uncertainties to experimental data, which is a big part of the CALPHAD approach. For those modellers using an associates model for the melt and CEF model for solid solutions, the automatic approach provides a good starting point in deciding which parameters to use, of which there is often an abundance of choice. This will hopefully make it easier for new modellers to quickly optimise systems of interest.

10.3 References

- [1] T I Barry and Fredrik Glasser. ‘Calculation of Portland cement clinkering reactions’. In: *Advances in Cement Research* 12 (2000), pp. 19–28. DOI: 10.1680/adcr.2000.12.1.19.
- [2] Tazuddin, Hemantkumar N. Aiyer and Amit Chatterjee. ‘Phase equilibria studies of CaO-SiO₂-Al₂O₃-Fe₂O₃-MgO system using CALPHAD’. In: *Calphad* 60 (2018), pp. 116–125. DOI: 10.1016/j.calphad.2017.12.003.
- [3] Sang-Hyo Shim, Tae-Hee Lee, Seong-Joon Yang, Norhazilan Bin Md. Noor and Jang-Ho-Jay Kim. ‘Calculation of Cement Composition Using a New Model Compared to the Bogue Model’. In: *Materials* 14.16 (2021). DOI: 10.3390/ma14164663.

- [4] A Tazuddin, Hemantkumar Aiyer and Amit Chatterjee. ‘Thermodynamic simulation in evaluating the role of minor oxides and mineralizers in Portland cement clinker phase formation’. In: *SN Applied Sciences* 2.10 (2020), pp. 17–37. DOI: [10.1007/s42452-020-03548-7](https://doi.org/10.1007/s42452-020-03548-7).
- [5] C. W. Bale, E. Bélisle, P. Chartrand, S. A. Decterov, G. Eriksson, A. E. Gheribi, K. Hack, I. H. Jung, Y. B. Kang, J. Melançon, A. D. Pelton, S. Petersen, C. Robelin, J. Sangster, P. Spencer and M. A. Van Ende. ‘FactSage thermochemical software and databases, 2010-2016’. In: *Calphad* 54 (2016), pp. 35–53. DOI: [10.1016/j.calphad.2016.05.002](https://doi.org/10.1016/j.calphad.2016.05.002).
- [6] J-O Andersson, Thomas Helander, Lars Höglund, Pingfang Shi and Bo Sundman. ‘Thermo-Calc and DICTRA, computational tools for materials science’. In: *Calphad* 26.2 (2002), pp. 273–312. DOI: [10.1016/S0364-5916\(02\)00037-8](https://doi.org/10.1016/S0364-5916(02)00037-8).
- [7] Thuan T Tran, Duncan Herfort, Hans J Jakobsen and Jørgen Skibsted. ‘Site Preferences of Fluoride Guest Ions in the Calcium Silicate Phases of Portland Cement from ^{29}Si (^{19}F) CP-REDOR NMR Spectroscopy’. In: *Journal of the American Chemical Society* 131.40 (Aug. 2009), pp. 14170–14171. DOI: [10.1021/ja905223d](https://doi.org/10.1021/ja905223d).
- [8] Roman Fediuk, Mugahed Amran, Mohammad Mosaberpanah, Aamar Danish, Mohamed El-Zeadani, Sergey Klyuev and Nikolai Vatin. ‘A Critical Review on the Properties and Applications of Sulfur-Based Concrete’. In: *Materials* 13 (Oct. 2020), p. 4712. DOI: [10.3390/ma13214712](https://doi.org/10.3390/ma13214712).

APPENDIX
A

APPENDIX: SUPPLEMENTARY MATERIAL

The following expression was used to describe the Gibbs free energy of the stoichiometric solids,

$$G_{solid,\alpha}(T) = H_0 + \sum_{j=1}^{N_P} C_j T^j + 3 R \sum_{i=1}^{N_E} D_{i,alpha} \left[\frac{\theta_{E,i,\alpha}}{2} + T \ln(1 - e^{-\theta_{E,i,\alpha}/T}) \right] \quad (\text{A.0.1})$$

Provided in Tables A.1 and A.2 are the coefficients for the 3rd generation function resulting from the experimental thermodynamic data in this work for the binary and ternary compounds, respectively.

Provided in Tables A.3, A.4, A.6 and A.5 are the evaluation of the experimental data that was used to fit the compounds in the Al_2O_3 - SiO_2 , CaO - Al_2O_3 , CaO - Fe_2O_3 and MgO - SiO_2 systems. Within the tables, the measurement, temperature range and reported uncertainty are presented. The fit uncertainty is the final uncertainty of the experimental data that was required to achieve a suitable fit. Not all of the experimental data was used for the fitting and these are marked with an asterisk.

Table A.1: Coefficients for the 3rd generation model for the stoichiometric solids in the binary systems according to Equation A.0.1.

$\alpha(\text{Compound})$	D_1	θ_1	D_2	θ_2	D_3	θ_3	$C\Gamma^2$	H_0
sillimanite-Al ₂ SiO ₅	0.409079	153.061491	3.33903	411.012608	4.250374	1030.533416	-0.000265	-2684355.273939
CaFe ₂ O ₄	6.998	401.0761	-	-	-	-	-0.00638	-1544867.118
Ca ₂ Fe ₂ O ₅	3.250271	215.33754	5.749947	569.493275	-	-	-0.009779	-2204596.507827
cyclowollastonite-CaSiO ₃	3.20933	398.726519	0.448513	113.639538	1.337919	1779.149444	-0.004177	-1686958.147895
monoclinic-Ca ₃ SiO ₅	2.721575	216.554568	4.322571	502.02771	1.955837	1253.079747	-0.013441	-3026014.386963
rankinite-Ca ₃ Si ₂ O ₇	3.262669	201.048711	5.228277	471.758995	3.509145	1114.209222	0.001345	-4081064.820333
rhombohedral-Ca ₃ SiO ₅	2.728885	216.897351	4.322171	502.823393	1.948978	1257.541676	-0.013504	-3026101.460607
triclinic-Ca ₃ SiO ₅	2.770329	217.322399	4.397009	511.911036	1.832799	1306.969635	-0.013446	-3026703.415132
wollastonite-CaSiO ₃	0.021926	39.983404	1.364237	180.16112	3.611497	777.592204	-0.00094	-1685783.296919
α -Ca ₂ SiO ₄	3.310467	427.508038	1.659827	174.273816	2.029525	1235.840109	-0.008061	-2368644.112281
α' -Ca ₂ SiO ₄	0.626679	122.320053	3.608269	315.618264	2.756109	1092.028025	-0.005737	-2377633.243328
β -Ca ₂ SiO ₄	0.452659	2585.222081	3.03791	835.357211	3.509071	259.231418	-0.008614	-2385856.23658
γ -Ca ₂ SiO ₄	0.151692	88.647382	2.689799	257.3199	4.158219	759.369678	-0.001096	-2384448.968068
Ca ₃ Al ₂ O ₆	2.736775	1020.13119	5.308183	480.050423	2.955042	195.44252	-0.005773	-3703855.550421
CaAl ₂ O ₄	2.751556	1047.38873	2.733077	458.837521	1.515367	178.6963	-0.00066	-2412710.719525
CaAl ₄ O ₇	4.690403	1109.65247	4.648185	508.764148	2.661412	209.974186	-0.005173	-4151607.924476
CaAl ₁₂ O ₁₉	6.808324	322.249714	12.343087	1228.630433	12.848596	509.837847	-0.022371	-11108541.2936
Ca ₁₂ Al ₁₄ O ₃₃	15.803145	1156.48654	27.045024	502.738546	16.151831	206.200874	-0.057413	-20074558.3798
fosterite-Mg ₂ SiO ₄	1.119246	242.335447	3.684162	521.005587	2.195919	1146.892162	-0.00398	-2248200.966899
ortho-MgSiO ₃	1.980721	294.361305	0.0	281.181868	3.019065	995.156035	-0.003885	-1601185.823182
clino-MgSiO ₃	3.7180	436.68	1.2818	1934.094	-	-	-0.0038364	-1608490.415
proto-MgSiO ₃	4.090088	587.941409	0.125477	0.02273	0.784447	2956.380561	-0.001736	-1601466.410408

Table A.2: Coefficients for the 3rd generation model for the stoichiometric solids in the ternary systems according to Equation A.0.1.

$\alpha(\text{Compound})$	D_1	θ_1	D_2	θ_2	D_3	θ_3	$C\Gamma^2$	H_0
anorthite-CaAl ₂ Si ₂ O ₈	3.096026	1550.569716	3.938197	218.711611	5.965741	658.27375	-0.006151	-4383831.217987
gehlenite-Ca ₂ Al ₂ SiO ₇	3.269467	203.55967	3.934145	1203.83153	4.796298	509.374611	-0.005641	-4116707.278225
merwinite-Ca ₃ MgSi ₂ O ₈	0.995845	8200.627974	5.963981	858.754919	7.040296	260.616429	-0.017234	-4795630.527432
monticellite-CaMgSiO ₄	0.628889	153.351406	3.439243	385.662661	2.930209	962.165316	-0.001494	-2333950.077639
akermanite-Ca ₂ MgSi ₂ O ₇	4.410228	220.33505	1.718215	1803.481006	5.871528	676.043141	-0.006461	-4009964.849678

Table A.3: Experimental data used to fit the sillimanite (Al_2SiO_5) phase.

Measurement	Chemistry	T(K)	Reported Uncertainty	Fitted Uncertainty	Ref
C_p	Al_2SiO_5	54.4→298.16	2.09	22.95%→1.71%	2.09
C_p	Al_2SiO_5	300.37→347.88	2.0	1.61%→1.45%	2.0
C_p	Al_2SiO_5	8.7→54.93	0.0→1.88	20.0%	0.0→1.88
C_p	Al_2SiO_5	60.03→170.72	1.0	8.76%→1.39%	1.0
C_p	Al_2SiO_5	176.0→270.0	1.0	1.35%→0.9%	1.0
C_p	Al_2SiO_5	257.18→310.26	1.5	1.37%→1.18%	1.5
ΔH	$\text{Al}_2\text{O}_3 + \text{SiO}_2 \rightarrow \text{Al}_2\text{SiO}_5$	968.0	627.6	9.93%	627.6
				9.93%	[2]

Table A.4: Experimental data used to fit the solid compounds within the CaO-Al₂O₃ system.

Measurement	Chemistry	T(K)	Reported Uncertainty	Fitted Uncertainty	Ref
C _p	CA ₆	298.15→1500.0	10.0 1.97%→1.19%	10.0 1.97%→1.19%	[3]*
C _p	CA ₆	298.0	10.0 1.93%	10.0 1.93%	[4]
H _T -H ₂ 98.15	CA ₆	300.0→1500.0	1000.0 106.25%→0.11%	1000.0 106.25%→0.11%	[3]*
ΔH	CaO+ 6 Al ₂ O ₃ →CA ₆	298.15	1000.0 5.65%	1000.0 5.65%	Present work
ΔH	CaO+ 6 Al ₂ O ₃ →CA ₆	1063.0	9700.0 29.39%	3700.0 10.39%	[5]
ΔG	CaO+ 6 Al ₂ O ₃ →CA ₆	1100.0	1000.0 1.65%	1000.0 1.65%	[6]*
C _p	C ₁₂ A ₇	53.89→298.16	5.02 3.42%→0.46%	5.02 3.42%→0.46%	[7]
H _T -H ₂ 98.15	C ₁₂ A ₇	394.4→1672.6	1000.0 0.91%→0.05%	2000.0 1.8%→0.1%	[8]
ΔH	12 CaO+ 7 Al ₂ O ₃ →C ₁₂ A ₇	1173.0	8000.0 4.02%	8000.0 4.02%	[9]*
ΔH	12 CaO+ 7 Al ₂ O ₃ →C ₁₂ A ₇	298.15	11130.0 14.02%	100 1%	[10]
ΔH	12 CaO+ 7 Al ₂ O ₃ →C ₁₂ A ₇	298.15	8000.0 9.65%	4000 4.5%	[11]
C _p	CA	53.52→298.16	6.28 36.83%→5.2%	6.28 36.83%→5.2%	[7]
H _T -H ₂ 93.15	CA	573.15→1673.15	2000.0 4.86%→0.85%	3000.0 4.86%→0.85%	[12]*
H _T -H ₂ 98.15	CA	402.6→1800.2	1800.0 13.24%→0.7%	1800.0 13.24%→0.7%	[8]
ΔH	CaO + Al ₂ O ₃ →CA	298.15	1000.0 7.45%	1000.0 7.45%	Present work
ΔH	CaO + Al ₂ O ₃ →CA	298.15	1464.4 9.49%	1464.4 9.49%	[10]
ΔH	CaO + Al ₂ O ₃ →CA	298.15	836.8 5.0%	836.8 5.0%	[11]
ΔH	CaO + Al ₂ O ₃ →CA	298.15	1046.0 6.16%	1046.0 6.16%	[13]
ΔH	CaO + Al ₂ O ₃ →CA	298.15	2000.0 13.25%	2000.0 13.25%	[14]
ΔH	CaO + Al ₂ O ₃ →CA	298.15	2000.0 12.9%	2000.0 12.9%	[15]

Measurement	Chemistry	T(K)	Reported Uncertainty	Fitted Uncertainty	Ref
ΔG	$\text{CaO} + \text{Al}_2\text{O}_3 \rightarrow \text{CA}$	1000.0→1200.0	500.0 1.4%→-1.5%	500.0 1.4%→1.52%	[6]*
C_p	CA_2	53.5→298.16	5.02 22.4%→2.52%	5.02 22.4%→2.52%	[7]
$H_T\text{-H}_298.15$	CA_2	403.7→1801.5	2000.0 8.58%→0.46%	2000.0 8.58%→0.46%	[8]
ΔH	$\text{CaO} + 2 \text{Al}_2\text{O}_3 \rightarrow \text{CA}_2$	298.15	1000.0 7.41%	1000.0 7.41%	Present work
ΔH	$\text{CaO} + 2 \text{Al}_2\text{O}_3 \rightarrow \text{CA}_2$	1063.0	4700.0 18.36%	4700.0 18.36%	[5]
ΔH	$\text{CaO} + 2 \text{Al}_2\text{O}_3 \rightarrow \text{CA}_2$	298.15	5000.0 39.68%	5000.0 39.68%	[14]
ΔH	$\text{CaO} + 2 \text{Al}_2\text{O}_3 \rightarrow \text{CA}_2$	298.15	2000.0 22.99%	4000.0 32.99%	[16]
ΔG	$\text{CaO} + 2 \text{Al}_2\text{O}_3 \rightarrow \text{CA}_2$	1100.0	1000.0 2.37%	1000.0 2.37%	[6]*
C_p	C_3A	53.86→298.16	5.02 17.08%→2.39%	5.02 17.08%→2.39%	[7]
$H_T\text{-H}_293.15$	C_3A	573.15→1573.15	1500.0 2.24%→0.44%	1500.0 2.24%→0.44%	[12]*
$H_T\text{-H}_298.16$	C_3A	373.6→1807.9	2928.8 17.59%→0.71%	2928.8 17.59%→0.71%	[8]
ΔH	$3 \text{CaO} + \text{Al}_2\text{O}_3 \rightarrow \text{C}_3\text{A}$	298.15	1000.0 8.93%	3000.0 20.93%	Present work
ΔH	$3 \text{CaO} + \text{Al}_2\text{O}_3 \rightarrow \text{C}_3\text{A}$	298.15	1380.72 20.75%	1380.72 20.75%	[10]
ΔH	$3 \text{CaO} + \text{Al}_2\text{O}_3 \rightarrow \text{C}_3\text{A}$	298.15	2000.0 27.78%	2000.0 27.78%	[11]
ΔH	$3 \text{CaO} + \text{Al}_2\text{O}_3 \rightarrow \text{C}_3\text{A}$	298.15	2000.0 23.81%	2000.0 23.81%	[14]
ΔH	$3 \text{CaO} + \text{Al}_2\text{O}_3 \rightarrow \text{C}_3\text{A}$	298.15	2000.0 29.41%	2000.0 29.41%	[15]
ΔG	$3 \text{CaO} + \text{Al}_2\text{O}_3 \rightarrow \text{C}_3\text{A}$	1000.0→1200.0	500.0 -1.35%→-1.16%	500.0 -1.35%→-1.16%	[6]*

Table A.5: Experimental data used to fit the solid compounds in the MgO-SiO₂ system.

Measurement	Chemistry	T(K)	Reported Uncertainty	Fitted Uncertainty	Ref
C _p	Mg ₂ SiO ₄	623→380.31	1.0 0.84%→17.09%	1.0 0.84%→17.09%	[17]
H _T -H _{298.15}	Mg ₂ SiO ₄	398.1→1807.6	1000.0 7.93%→0.77%	1000.0 7.93%→0.77%	[18]
ΔH	2 MgO + SiO ₂ →Mg ₂ SiO ₄	298.15	1255.2 2.16%	1255.2 2.16%	[19]
ΔH	2 MgO + SiO ₂ →Mg ₂ SiO ₄	970.0	1130.0 1.8%	1130.0 1.8%	[20]
ΔH	2 MgO + SiO ₂ →Mg ₂ SiO ₄	1170.0	1380.0 2.31%	1380.0 2.31%	[21]
ΔH	2 MgO + SiO ₂ →Mg ₂ SiO ₄	298.15	878.64 1.39%	878.64 1.39%	[22]*
C _p	clino-MgSiO ₃	6208→302.449	1.0 3154.57%→1.22%	1.0 3154.57%→1.22%	[23]*
C _p	clino-MgSiO ₃	52.7→295.3	4.18 66.31%→5.14%	4.18 66.31%→5.14%	[24]*
H _T -H _{Ref}	clino-MgSiO ₃	580.0→1174.0	1000.0 3.56%→1.03%	1000.0 3.56%→1.03%	[25]
ΔH	MgO + SiO ₂ →clino-MgSiO ₃	970.0	711.0 1.93%	711.0 1.93%	[20]
ΔH	MgO + SiO ₂ →clino-MgSiO ₃	1170.0	1130.0 3.23%	1130.0 3.23%	[20]
ΔH	MgO + SiO ₂ →clino-MgSiO ₃	298.15	627.6 1.73%	627.6 1.73%	[22]*
C _p	ortho-MgSiO ₃	349.9→999.9	1.0 1.1%→0.8%	1.0 1.1%→0.8%	[26]*
C _p	ortho-MgSiO ₃	400.0→1200.0	1.0 1.04%→0.77%	1.0 1.04%→0.77%	[27]
H _T -H _{273.15}	ortho-MgSiO ₃	415.6→1225.4	1000.0 7.91%→0.91%	1000.0 7.91%→0.91%	[27]*
ΔH	MgO + SiO ₂ →ortho-MgSiO ₃	298.15	1000.0 3.05%	1000.0 3.05%	[27]
T _{transition}	ortho-MgSiO ₃ →clino-MgSiO ₃	968.5	1.0 K -	1.0 K -	[27]
C _p	proto-MgSiO ₃	400.0→1800.0	1.0 1.1%→0.79%	1.0 1.1%→0.79%	[27]
H _T -H _{273.15}	proto-MgSiO ₃	1366.3→1811.4	1000.0 0.77%→0.52%	1000.0 0.77%→0.52%	[27]*
ΔH	MgO + SiO ₂ →proto-MgSiO ₃	298.15	1000.0 5.01%	1000.0 5.01%	[27]
T _{transition}	proto-MgSiO ₃ →ortho-MgSiO ₃	1257.4	1.0 K -	1.0 K -	[27]

Table A.6: Experimental data that was used to fit the compounds in the CaO-Fe₂O₃ system.

Measurement	Chemistry	T(K)	Reported Uncertainty	Fitted Uncertainty	Ref
C _p	CaFe ₂ O ₄	52.99→298.16	4.18 28.92%→2.72%	2.09 14.40%→1.31%	[28]
C _p	CaFe ₂ O ₄	298.15→1500.0	10.0 6.44%→5.15%	10.0 6.44%→5.15%	[3]*
ΔH	CaO + Fe ₂ O ₃ →CaFe ₂ O ₄	1125.0	1000.0 2.67%	1000.0 2.67%	[29]
C _p	Ca ₂ Fe ₂ O ₅	53.29→298.16	4.18 16.29%→2.17%	4.18 16.29%→2.17%	[28]
C _p	Ca ₂ Fe ₂ O ₅	298.15→1500.0	10.0 5.19%→4.0%	10.0 5.19%→4.0%	[3]*
ΔH	2 CaO + Fe ₂ O ₃ →Ca ₂ Fe ₂ O ₅	1125.0	1300.0 2.87%	1300.0 2.87%	[29]
ΔH	2 CaO + Fe ₂ O ₃ →Ca ₂ Fe ₂ O ₅	298.15	418.4 1.35%	418.4 1.35%	[30]

A.1 References

- [1] Bruce S. Hemingway, Richard A. Robie, Howard T. Evans and Derrill M. Kerrick. ‘Heat capacities and entropies of sillimanite, fibrolite, andalusite, kyanite, and quartz and the Al₂SiO₅ phase diagram’. In: *American Mineralogist* 76.9–10 (Oct. 1991), pp. 1597–1613.
- [2] J. L. Holm and O. J. Kleppa. ‘The thermodynamic properties of the aluminum silicates’. In: *The Journal of Physical Chemistry* 70.5 (1966), p. 1690. DOI: 10.1021/j100877a519.
- [3] C. W. Bale, E. Bélisle, P. Chartrand, S. A. Decterov, G. Eriksson, A. E. Gheribi, K. Hack, I. H. Jung, Y. B. Kang, J. Melançon, A. D. Pelton, S. Petersen, C. Robelin, J. Sangster, P. Spencer and M. A. Van Ende. ‘FactSage thermochemical software and databases, 2010–2016’. In: *Calphad* 54 (2016), pp. 35–53. DOI: 10.1016/j.calphad.2016.05.002.
- [4] Anne M Hofmeister. ‘Physical properties of calcium aluminates from vibrational spectroscopy’. In: *Geochimica et Cosmochimica Acta* 68.22 (2004), pp. 4721–4726.
- [5] Charles A. Geiger, Ole Jakob Kleppa, Bjorn O. Mysen, James M. Lattimer and Lawrence Grossman. ‘Enthalpies of formation of CaAl₄O₇ and CaAl₁₂O₁₉ (hibonite) by high temperature, alkali borate solution calorimetry’. In: *Geochimica et Cosmochimica Acta* 52 (1988), pp. 1729–1736. DOI: 10.1016/0016-7037(88)90241-4.
- [6] G. Róg, A. Kozlowska-Róg, K. Zakula-Sokól and G. Borchardt. ‘Determination of the standard Gibbs free energies of formation of the calcium aluminates from the oxides by e.m.f. measurements’. In: *The Journal of Chemical Thermodynamics* 25.7 (1993), pp. 807–810. DOI: 10.1006/jcht.1993.1078.
- [7] E G King. ‘Heat Capacities at Low Temperatures and Entropies at 298.16°K. of Crystalline Calcium and Magnesium Aluminates’. In: *The Journal of Physical Chemistry* 59.3 (1955), pp. 218–219. DOI: 10.1021/j150525a005.
- [8] K R Bonnickson. ‘High Temperature Heat Contents of Aluminates of Calcium and Magnesium’. In: *The Journal of Physical Chemistry* 59.3 (1955), pp. 220–221. DOI: 10.1021/j150525a006.
- [9] F. Ayed, F. Sorrentino and R. Castanet. ‘Determination par calorimetrie de dissolution des enthalpies de formation de quelques silicates, aluminates et alumino-silicates de calcium’. In: *Journal of Thermal Analysis and Calorimetry* 41.4 (1994), pp. 755–766. DOI: 10.1007/bf02547157.
- [10] James P Coughlin. ‘Heats of Formation of Crystalline CaO·Al₂O₃, 12CaO·7Al₂O₃, and 3CaO·Al₂O₃’. In: *Journal of the American Chemical Society* 78.21 (Nov. 1956), pp. 5479–5482. DOI: 10.1021/ja01602a005.

- [11] M F Koehler, R Barany and K K Kelley. ‘Heats and Free Energies of Formation of Ferrite and Aluminates of Calcium, Magnesium, Sodium, and Lithium’. In: *U.S Bureau of Mines. Report of Investigations* 5711 (1961).
- [12] H Elsner von Gronow and H E Schwiete. ‘Die spezifischen Wärmen von CaO, Al_2O_3 , $\text{CaO} \cdot \text{Al}_2\text{O}_3$, $3\text{CaO} \cdot \text{Al}_2\text{O}_3$, $2\text{CaO} \cdot \text{SiO}_2$, $3\text{CaO} \cdot \text{SiO}_2$, $2\text{CaO} \cdot \text{Al}_2\text{O}_3 \cdot \text{SiO}_2$ von 20° bis 1500° C’. In: *Zeitschrift für anorganische und allgemeine Chemie* 216.2 (1933), pp. 185–195. DOI: 10.1002/zaac.19332160212.
- [13] Alexandra Navrotsky, Gilles Peraudeau, Paul McMillan and Jean-Pierre Coutures. ‘A thermochemical study of glasses and crystals along the joins silica-calcium aluminate and silica-sodium aluminate’. In: *Geochim. Cosmochim. Acta* 46.11 (Nov. 1982), pp. 2039–2047. DOI: 10.1016/0016-7037(82)90183-1.
- [14] Bengt Hallstedl. ‘Assessment of the CaO-Al₂O₃ system’. In: *Journal of the American ceramic society* 73.1 (1990), pp. 15–23.
- [15] Isaac Eliezer, Naomi Eliezer, Reed A Howald and Puligandla Viswanadham. ‘Thermodynamic properties of calcium aluminates’. In: *The Journal of Physical Chemistry* 85.19 (Sept. 1981), pp. 2835–2838. DOI: 10.1021/j150619a028.
- [16] B S Hemingway. ‘Comment on "Thermodynamic properties of calcium aluminates"’. In: *The Journal of Physical Chemistry* 86.14 (July 1982), pp. 2802–2803. DOI: 10.1021/j100211a049.
- [17] Richard A Robie and Bruce S Hemingway. ‘Heat capacities and entropies of Mg_2SiO_4 , Mn_2SiO_4 , and Co_2SiO_4 between 5 and 380 K’. In: *American Mineralogist* 67.5-6 (1982), pp. 470–482.
- [18] Raymond L Orr. ‘High Temperature Heat Contents of Magnesium Orthosilicate and Ferrous Orthosilicate’. In: *Journal of the American Chemical Society* 75.3 (Feb. 1953), pp. 528–529. DOI: 10.1021/ja01099a005.
- [19] E G King, R Barany, W Weller and L B Pankratz. ‘Thermodynamic Properties of Forsterite and Serpentine’. In: *U.S Bureau of Mines* (1967). DOI: <https://digital.library.unt.edu/ark:/67531/metadc100853/m1/5/>.
- [20] T.V Charlu, R.C Newton and O.J Kleppa. ‘Enthalpies of formation at 970 K of compounds in the system MgO-Al₂O₃-SiO₂ from high temperature solution calorimetry’. In: *Geochimica et Cosmochimica Acta* 39.11 (1975), pp. 1487–1497. DOI: 10.1016/0016-7037(75)90150-7.
- [21] I.A. Kiseleva, L.P. Ogorodova, N.D. Topor and O.G. Chigareva. ‘Thermochemical Study of the CaO-MgO-SiO₂ System’. In: 12.12 (1979), pp. 1811–1825.
- [22] D R Torgeson and Th. G Sahama. ‘A Hydrofluoric Acid Solution Calorimeter and the Determination of the Heats of Formation of Mg_2SiO_4 , MgSiO_3 , and CaSiO_3 ’. In: *Journal of the American Chemical Society* 70.6 (1948), pp. 2156–2160. DOI: 10.1021/ja01186a048.

- [23] V A Drebushchak, Yulia A Kovalevskaya, I E Paukov and N V Surkov. ‘Low-temperature heat capacity of monoclinic enstatite’. In: *Journal of Thermal Analysis and Calorimetry* 94.2 (2008), pp. 493–497. DOI: 10.1007/s10973-007-8443-7.
- [24] K K Kelley. ‘Specific Heats at Low Temperatures of Magnesium Orthosilicate and Magnesium Metasilicate1’. In: *Journal of the American Chemical Society* 65.3 (1943), pp. 339–341. DOI: 10.1021/ja01243a012.
- [25] Hubert Wagner. ‘Zur Thermochemie der Metasilikate des Calciums und Magnesiums und des Diopsids’. In: *Zeitschrift für anorganische und allgemeine Chemie* 208.1 (1932), pp. 1–22. DOI: 10.1002/zaac.19322080102.
- [26] Kenneth M. Krupka, Richard A. Robie, Bruce S. Hemingway, Derrill M. Kerrick and Jun Itô. ‘Low-temperature heat capacities and derived thermodynamic properties of anthophyllite, diopside, enstatite, bronzite, and wollastonite’. In: *American Mineralogist* 70 (1985), pp. 249–260.
- [27] Mats Hillert and Xizhen Wang. ‘A study of the thermodynamic properties of MgO-SiO₂ system’. In: *Calphad* 13.3 (1989), pp. 253–266. DOI: 10.1016/0364-5916(89)90005-9.
- [28] EG King. ‘Heat Capacities at Low Temperatures and Entropies at 298.16° K. of Calcium and Magnesium Ferrites’. In: *Journal of the American Chemical Society* 76.22 (1954), pp. 5849–5850.
- [29] KT Jacob, N Dasgupta and Y Waseda. ‘Thermodynamic properties of the calcium ferrites CaFe₂O₄ and Ca₂Fe₂O₅’. In: *Zeitschrift für Metallkunde* 90.7 (1999), pp. 486–490.
- [30] Edwin S. Newman and Roald Hoffman. ‘Heats of formation of hexacalcium dialuminoferrite and dicalcium ferrite’. In: *Journal of research of the National Bureau of Standards* 56 (1956), p. 313.

APPENDIX
B

APPENDIX: TDB FILE

Provided here is a copy of the TDB (Thermodynamic database file) for the CaO-Al₂O₃-SiO₂-MgO-Fe-O system that was developed in the present work. This file has been tested to be compatible with the Pycalphad thermodynamic package for python, but should also be compatible with Thermo-calc and PANDAT.

```
$$$$$$$$$$$$$$$$$$$$$$$$$$$$$$$$$$$$$$$$$$$$$$$$$$$$$$$$$$$$$$$$$$$$$$$$$$$$$$$$$
$ TDB File for the CAO-AL2O3-SIO2-FE-O-MGO SYSTEM
$ FOR OPC CLINKERS
$ PRODUCED AS PART OF THESIS:
$ "THERMODYNAMIC MODELLING OF PORTLAND CEMENT CLINKERS"
$$$$$$$$$$$$$$$$$$$$$$$$$$$$$$$$$$$$$$$$$$$$$$$$$$$$$$$$$$$$$$$$$$$$$$$$$$$$
$ ELEMENT DEFINITIONS
$ A=AL2O3, Q=SIO2
$ L = CAO M=MGO
$$$$$$$$$$$$$$$$$$$$$$$$$$$$$$$$$$$$$$$$$$$$$$$$$$$$$$$$$$$$$$$$$$$$$$$$
ELEMENT A CORUNDUM 101.96 0.0000E+00 0.0000E+00!
ELEMENT /- ELECTRON_GAS 0.0000E+00 0.0000E+00 0.0000E+00!
ELEMENT VA VACUUM 0.0000E+00 0.0000E+00 0.0000E+00!
ELEMENT FE BCC_A2 5.5847E+01 4.4890E+03 2.7280E+01!
ELEMENT O 1/2_MOLE_O2(G) 1.5999E+01 4.3410E+03 1.0252E+02!
ELEMENT L BLANK 56.07 0.0 0.0 !
ELEMENT Q BLANK 60.08 0.0 0.0 !
ELEMENT M BLANK 40.3 0.0 0.0 !
$$$$$$$$$$$$$$$$$$$$$$$$$$$$$$$$$$$$$$$$$$$$$$$$$$$$$$$$$$$$$$$$$$$$$$$$
SPECIES ALL A0.5 !
SPECIES C3AL L3A1 !
SPECIES CAOL L1 !
SPECIES ASL A0.66666666666666Q1 !
SPECIES C2A L2.0A1.0 !
SPECIES C2F L2.0FE2O3 !
```

```

SPECIES SIL A1Q1 !
SPECIES COR A1.5 !
SPECIES FE+2           FE1/+2!
SPECIES FE+3           FE1/+3!
SPECIES FEO             FE1O1!
SPECIES FEO3/2          FE1O1.5!
SPECIES FE2O3           FE2O3 !
SPECIES M2SL M2Q1 !
SPECIES MGOL M1 !
SPECIES O-2             O1/-2!
SPECIES O2               O2!
SPECIES O1               O1!
SPECIES O3               O3!

SPECIES C2SL L2Q1 !
SPECIES CSL L1Q1 !
SPECIES SIO2L Q1 !
SPECIES CAS2L A0.5L0.5Q1 !

FUNCTION TEMP      0.1 +T**(-1); 6000 N !
FUNCTION RTEMP     0.1 +R#**(-1)*TEMP#; 6000 N !
FUNCTION TMLN      0.1 +1-LN(T); 6000 N !
FUNCTION TLNT      0.1 +T*LN(T); 6000 N !
$$$$$$$$$$$$$$$$$$$$$$$$$$$$$$$$$$$$$$$$$$$$$$$$$$$$$$$$$$$$$$$$
$-----
$           SOLID PHASE FUNCTIONS      $
$ solid functions use the 3rd generation function
$ function is split apart to implement maximum
$ compatibility with software.
$-----
$           ALPHA C2S                  $
$-----
$ Einstein Terms $
FUNCTION AC2S0 1 (1 - EXP(-427.508038/T)); 10000 N !
FUNCTION AC2S1 1 (1 - EXP(-174.273816/T)); 10000 N !
FUNCTION AC2S2 1 (1 - EXP(-1235.840109/T)); 10000 N !

FUNCTION GAC2S 1 -2316104.80639131
+ 50.6232292353224 * T *
LN(AC2S2)-0.008061 * T**2

```

```

+ 82.5742623603897 * T * LN(AC2S0) +
41.4017086323043 * T * LN(AC2S1); 3000 N !
$-----
$          ALPHA PRIME C2S                      $
$-----
FUNCTION APC2S0 1 (1 - EXP(-1092.028025/T)); 10000 N !
FUNCTION APC2S1 1 (1 - EXP(-315.618264/T)); 10000 N !
FUNCTION APC2S2 1 (1 - EXP(-122.320053/T)); 10000 N !

FUNCTION GAPC2S 1 -2324937.35232995
-0.005737 * T**2 + 15.631497357245 * T *
LN(APC2S2) + 68.7466957561671 * T * LN(APC2S0)
+ 90.0024531502235 * T * LN(APC2S1); 3000 N !
$-----
$          BETA   C2S                      $
$-----
FUNCTION BC2S0 1 (1 - EXP(-2585.222081/T)); 10000 N !
FUNCTION BC2S1 1 (1 - EXP(-835.357211/T)); 10000 N !
FUNCTION BC2S2 1 (1 - EXP(-259.231418/T)); 10000 N !

FUNCTION GBC2S 1 -2328266.62444862
-0.008614 * T**2 + 87.5281189618368 * T *
LN(BC2S2) + 11.2908490028119 * T * LN(BC2S0)
+ 75.7757673969417 * T * LN(BC2S1); 3000 N !

$-----
$          GAMMA  C2S                      $
$-----
FUNCTION GC2S0 1 (1 - EXP(-88.647382/T)); 10000 N !
FUNCTION GC2S1 1 (1 - EXP(-257.3199/T)); 10000 N !
FUNCTION GC2S2 1 (1 - EXP(-759.369678/T)); 10000 N !

FUNCTION GGC2S 1 -2336268.1787659
+ 103.720069300784 * T * LN(GC2S2)-0.001096 * T**2
+ 3.7837123904187 * T * LN(GC2S0)
+ 67.0926997075379 * T * LN(GC2S1); 3000 N !
$-----
$          ALPHA CRISTOBALITE                  $
$-----
FUNCTION ACRISO 1 (1 - EXP(-100.17/T)); 10000 N !

```

APPENDIX B. APPENDIX: TDB FILE

```
FUNCTION ACRIS1 1 (1 - EXP (-374.45/T)) ; 10000 N !
FUNCTION ACRIS2 1 (1 - EXP (-1134/T)) ; 10000 N !

FUNCTION GACRIS 1 -914067.250936864
+ 38.9116850529572 * T * LN(ACRIS2)
+ 7.23358247779332 * T * LN(ACRISO)
+ 28.6848960326287 * T * LN(ACRIS1); 6000 N !
$-----
$          BETA CRISTOBALITE           $
$-----

FUNCTION BCRISO 1 (1 - EXP (-125.65/T)) ; 10000 N !
FUNCTION BCRIS1 1 (1 - EXP (-966.5/T)) ; 10000 N !

FUNCTION GBCRIS 1 -912412.146717818
+ 55.2052048672473 * T * LN(BCRIS1)
+ 19.6249586961318 * T * LN(BCRISO); 6000 N !
$-----
$          ALPHA QUARTZ           $
$-----

FUNCTION AQUARTZ0 1 (1 - EXP (-159.2/T)) ; 10000 N !
FUNCTION AQUARTZ1 1 (1 - EXP (-524/T)) ; 10000 N !
FUNCTION AQUARTZ2 1 (1 - EXP (-1421/T)) ; 10000 N !
FUNCTION AQUARTZ3 1 (1 - EXP (-159.2/T)) ; 10000 N !
FUNCTION AQUARTZ4 1 (1 - EXP (-524/T)) ; 10000 N !
FUNCTION AQUARTZ5 1 (1 - EXP (-1421/T)) ; 10000 N !

FUNCTION GAQUARTZ 1 -917661.326977757
-1.076E-12 * T**5 + 13.3696558899904 * T * LN(AQUARTZ0)
+ 29.0341034625911 * T * LN(AQUARTZ2)
+ 32.4264042107976 * T * LN(AQUARTZ1); 847.1 Y
-914725.826977757
-9.16882E+33 * T**(-11)
+ 32.4264042107976 * T * LN(AQUARTZ1)
+ 13.3696558899904 * T * LN(AQUARTZ0)
+ 29.0341034625911 * T * LN(AQUARTZ2)
-2.72959E+16 * T**(-5) -3.87837 * T; 6000 N !
$-----
$          BETA QUARTZ           $
$-----

FUNCTION BQUARTZ0 1 (1 - EXP (-66.518134/T)) ; 10000 N !
```

```

FUNCTION BQUARTZ1 1 (1 - EXP(-1024.54773/T)); 10000 N !

FUNCTION GBQUARTZ 1 -913771.02970493
+ 59.8851830700525 * T * LN(BQUARTZ1)
+ 14.9449804933267 * T * LN(BQUARTZ0); 6000 N !
$-----
$          WOLLOSTONITE                      $
$-----

FUNCTION WCS0 1 (1 - EXP(-39.983404/T)); 10000 N !
FUNCTION WCS1 1 (1 - EXP(-180.16112/T)); 10000 N !
FUNCTION WCS2 1 (1 - EXP(-777.592204/T)); 10000 N !

FUNCTION GWCS 1 -1647683.13184533
-0.00094 * T**2
+ 90.0829704062177 * T * LN(WCS2)
+ 0.546908722096884 * T * LN(WCS0)
+ 34.0286926164046 * T * LN(WCS1); 6000 N !
$-----
$          p-WOLLOSTONITE                     $
$-----

FUNCTION PCS0 1 (1 - EXP(-398.726519/T)); 10000 N !
FUNCTION PCS1 1 (1 - EXP(-113.639538/T)); 10000 N !
FUNCTION PCS2 1 (1 - EXP(-1779.149444/T)); 10000 N !

FUNCTION GPCS 1 -1640676.04549942
-0.004177 * T**2
+ 33.3722325348509 * T * LN(PCS2)
+ 80.0515629429532 * T * LN(PCS0)
+ 11.1874337167673 * T * LN(PCS1); 6000 N !
$-----
$          m-C3S                           $
$-----

FUNCTION MC3S0 1 (1 - EXP(-216.554568/T)); 10000 N !
FUNCTION MC3S1 1 (1 - EXP(-502.02771/T)); 10000 N !
FUNCTION MC3S2 1 (1 - EXP(-1253.079747/T)); 10000 N !

FUNCTION GMC3S 1 -2961033.87273599
-0.013441 * T**2
+ 48.7852008711029 * T * LN(MC3S2)
+ 67.8853008000012 * T * LN(MC3S0)

```

APPENDIX B. APPENDIX: TDB FILE

```
+ 107.81956498144 * T * LN(MC3S1); 6000 N !
$-----
$          t-C3S                      $
$-----
FUNCTION TC3S0 1 (1 - EXP(-217.322399/T)); 10000 N !
FUNCTION TC3S1 1 (1 - EXP(-511.911036/T)); 10000 N !
FUNCTION TC3S2 1 (1 - EXP(-1306.969635/T)); 10000 N !

FUNCTION GTC3S 1 -2961247.66744604
+ 69.1013907314575 * T * LN(TC3S0)
-0.013446 * T**2
+ 45.7162163162659 * T * LN(TC3S2)
+ 109.67630088655 * T * LN(TC3S1); 6000 N !
$-----
$          r-C3S                      $
$-----
FUNCTION RC3S0 1 (1 - EXP(-216.897351/T)); 10000 N !
FUNCTION RC3S1 1 (1 - EXP(-502.823393/T)); 10000 N !
FUNCTION RC3S2 1 (1 - EXP(-1257.541676/T)); 10000 N !

FUNCTION GRC3S 1 -2961047.88690192
-0.013504 * T**2
+ 48.6141141738092 * T * LN(RC3S2)
+ 68.0676369652173 * T * LN(RC3S0)
+ 107.809587626298 * T * LN(RC3S1); 6000 N !
$-----
$          r-C3S2                     $
$-----
FUNCTION RC3S20 1 (1 - EXP(-201.04871/T)); 10000 N !
FUNCTION RC3S21 1 (1 - EXP(-471.7589/T)); 10000 N !
FUNCTION RC3S22 1 (1 - EXP(-1114.2092/T)); 10000 N !

FUNCTION GRC3S2 1 -3.9933593273921650E6
+ 0.001345157705172196 * T**2
+ 87.52997635528091 * T * LN(RC3S22)
+ 81.382016522242722 * T * LN(RC3S20)
+ 130.4109304207976 * T * LN(RC3S21); 6000 N !
$-----
$          CAO                      $
$-----
```

```

FUNCTION CAO0 1 (1 - EXP (-314.8272896/T)) ; 10000 N !
FUNCTION CAO1 1 (1 - EXP (-125.12812657/T)) ; 10000 N !
FUNCTION CAO2 1 (1 - EXP (-598.37301449/T)) ; 10000 N !

FUNCTION GCAO 1 (-641354.1762949
+ 23.6098190734791*T*LN(CAO0)
+ 1.2953977159976*T*LN(CAO1)
+ 24.9813594731112*T*LN(CAO2)
- 0.00174450265*T**2
- 112535.777764825*EXP (-14.85294988 + 0.00298095*T));
3222 Y (-727925.76111
+ 486.19356495*T
+ 80.5*T*(1 - LN(T))
+ 60.6039483894586*(-281.8126077 + 0.09083109344*T)**(-1))
; 6000 N !
$-----
$          C2F                      $
$-----
FUNCTION C2F0 1 (1 - EXP (-170155.53632209363/T)) ; 10000 N !
FUNCTION C2F1 1 (1 - EXP (-215.33754004091622/T)) ; 10000 N !
FUNCTION C2F2 1 (1 - EXP (-569.493275432429/T)) ; 10000 N !

FUNCTION GC2F 1.0 (-2.1550282235185245E6
+ 9.265379709115280E-11*T*LN(C2F0)
+ 81.07276569312136*T*LN(C2F1)
+ 143.42315186788068*T*LN(C2F2)
- 0.009779319700444069*T**2); 3000.0 N !
$-----
$          CF                      $
$-----
FUNCTION CFO 1 (1 - EXP (-401.0761361736441/T)) ; 10000 N !

FUNCTION GCF 1 (-1.506467891684749E6
+ 174.5590006453247*T*LN(CF0)
- 0.006385582537395782*T**2); 3000.0 N !
$-----
$          LIQUID PHASE FUNCTIONS           $
$ two-state function for liquid
$-----$
```

APPENDIX B. APPENDIX: TDB FILE

```

$           SiO2           $
$-----
FUNCTION SIO2L0 1 (1 - EXP(-1308.6/T)); 10000 N !
FUNCTION SIO2L1 1 (1 - EXP(-441.14/T)); 10000 N !
FUNCTION SIO2L2 1 (1 - EXP(-105.58/T)); 10000 N !

FUNCTION ZSIO2L0 1
(1 + EXP(0.120272355042726*(-33226 + 11.184*T)/T))
; 10000 N !

FUNCTION GSIO2L 1
-913715.638421418
-8.31446261815324 * T * LN(ZSIO2L0)
+ 33.5987434399572 * T * LN(SIO2L0)
+ 9.12927995473226 * T * LN(SIO2L2)
+ 32.1021401686897 * T * LN(SIO2L1); 6000 N !
$-----

$           CaO           $
$-----
FUNCTION CAOL0 1 (1 - EXP(-629.27558/T)); 10000 N !
FUNCTION CAOL1 1 (1 - EXP(-234.0578/T)); 10000 N !

FUNCTION GCAOL 1 (-602797.126970587
+ 25.0016778330463*T*LN(CAOL0)
+ 24.884873477673*T*LN(CAOL1)
- 16.6289252363065*T*LN(ZCAOL0)
- 0.00184186045*T**2); 6000 N !

FUNCTION ZCAOL0 1
(1 + EXP(0.120272355042726*(-63019.5887 + 6.2358*T
+ 0.997138715*T*LN(T))/T)); 10000 N !

$-----
$           GAS PHASE FUNCTIONS           $
$-----
FUNCTION GO2GAS 298.15 -6961.74451
-76729.7484*T**(-1)
-51.0057202*T-22.2710136*T*LN(T)
-0.0101977469*T**2+1.3236921E-06*T**3; 1000 Y
-13137.5203+525809.556*T**(-1)

```

```
+25.3200332*T-33.627603*T*LN(T)
-0.00119159274*T**2+1.3561111E-08*T**3; 3300 Y
-27973.4908+8766421.4*T**(-1)
+62.5195726*T-37.9072074*T*LN(T)
-8.50483772E-04*T**2+2.14409777E-08*T**3; 6000 N !
FUNCTION GO1GAS 298.15 243206.529
-42897.0876*T**(-1)
-20.7513421*T
-21.0155542*T*LN(T)+1.26870532E-4*T**2
-1.2313129E-8*T**3; 2950 Y
+252301.473
-3973170.33*T**(-1)
-51.974853*T-17.2118798*T*LN(T)
-5.41356254E-4*T**2+7.64520703E-9*T**3; 6000 N !
FUNCTION GO3GAS 298.15 133772.042
-11328.9959*T**(-1)
-84.8602165*T-19.8314069*T*LN(T)
-0.0392015696*T**2 + 7.90727187E-6*T**3; 600 Y
120765.524
+ 997137.156*T**(-1)
+ 120.113376*T
- 51.841015*T*LN(T)
-0.0035398314*T**2+3.2064014E-7*T**3; 1500 Y
115412.196
+ 1878139.02*T**(-1)
+164.67966*T-58.06974*T*LN(T)
-2.8439903E-4*T**2+5.9565028E-10*T**3; 6000 N !
FUNCTION GFEOGAS 298.15 241501.965
+ 57679.3688*T**(-1)-46.1742716*T
- 28.411703*T*LN(T)
-0.00855192864*T**2 + 1.5099707E-6*T**3; 800 Y
237160.413+446016.49*T**(-1)
+ 14.348854*T - 37.647297*T*LN(T)
+2.5380772E-4*T**2-7.0014359E-8*T**3; 3200 Y
247039.926
-1074034.89*T**(-1)
-45.0126518*T
```

```
-29.8873162*T*LN(T)
-0.00207289167*T**2+5.0880159E-8*T**3; 6000 N !
```

```
FUNCTION GFEGAS 298.15 405624.097
+ 112881.768*T**(-1) + 36.7995658*T
- 33.007881*T*LN(T)
+0.0092758129*T**2
-1.3799585E-6*T**3; 950 Y
414289.373
-996891.764*T**(-1)
- 53.3825193*T
-19.9029533*T*LN(T)
+ 1.3565310E-4*T**2-1.38830908E-7*T**3; 2350 Y
406336.639 + 2445907.82*T**(-1) - 32.8404885*T
-22.1593719*T*LN(T)
- 1.41918414E-4*T**2
-6.8989725E-8*T**3; 6000 N !
```

```
FUNCTION GOSOL 298.15 +GO2GAS +RLNP*T; 6000 N !
FUNCTION RLNP 298.15 +130; 6000 N !
```

```
$-----
$ Fe-O solid functions
$-----
FUNCTION GHSERFE 298.15
+1225.7+124.134*T-23.5143*T*LN(T)
-0.00439752*T**2
-5.89269E-08*T**3+77358.5*T**(-1); 1811 Y
-25383.581+
299.31255*T-46*T*LN(T)
+2.2960305E+31*T**(-9); 6000 N !
```

```
FUNCTION GFELIQ 298.15
+12040.17-6.55843*T-3.6751551E-21*T**7+GHSERFE; 1811 Y
-10839.7 + 291.302*T - 46*T*LN(T); 6000 N !
```

```
FUNCTION GFEFCC 298.15
-1462.4+8.282*T-1.15*T*LN(T)+6.4E-04*T**2+GHSERFE; 1811 Y
-27098.26+300.25256*T-46*T*LN(T)
+2.7885E+31*T**(-9); 6000 N !
```

```

FUNCTION GFE3O2 298.15
-858683+827.946*T
-137.0089*T*LN(T)+1453810*T**(-1); 3000 N !

FUNCTION GFEO 298.15
-279318+252.848*T
-46.12826*T*LN(T)-5.7402984E-3*T**2; 3000 N !

FUNCTION GFE2O3 298.15 +GFE3O2; 6000 N !

FUNCTION GWUSTITE 298.15
-279318+252.848*T-46.12826*T*LN(T)-
.0057402984*T**2; 3000 N !

FUNCTION AWUSTITE 298.15 -55384+27.888*T; 3000 N !

FUNCTION BFE3O4 298.15 +46826-27.266*T; 3000 N !
FUNCTION CFE3O4 298.15 +120730-20.102*T; 3000 N !
FUNCTION DFE3O4 298.15 +402520-30.529*T; 3000 N !

FUNCTION GFE3O4 298.15 -161731+144.873*T-24.9879*T*LN(T)
-.0011952256*T**2+206520*T**(-1); 3000 N !
FUNCTION RFE3O4 298.15 +156000-3.37*T; 3000 N !
FUNCTION SFE3O4 298.15 +46028.95
+38.73173*T-11.58574*T*LN(T)
+.006411774*T**2; 3000 N !

FUNCTION RR 298.15 +8.31451; 6000 N !
FUNCTION FLN6 298.15 +1.791759; 6000 N !
FUNCTION FLN5 298.15 +1.609438; 6000 N !
FUNCTION FLN3 298.15 +1.098612; 6000 N !
FUNCTION FLN2 298.15 +0.693147; 6000 N !

FUNCTION UN_ASS 298.15 0.0; 300 N !

$-----
$ Al2O3
$ new assessment
$-----
FUNCTION ALLO 1 (1 - EXP(-443.38125/T)); 10000 N !

```

```

FUNCTION ALL1 1 (1 - EXP (-165.9763/T)); 10000 N !
FUNCTION ALL2 1 (1 - EXP (-1092.388/T)); 10000 N !

FUNCTION ZALLO 1
(1 + EXP (0.120272355042726*(-43735.7183
+ 6.2358*T
+ 0.2962085013*T*LN(T))/T)); 10000 N !

FUNCTION GALL 1
(-1.6252622037652672E6 + 47.2689970856593*T*LN(ALLO)
+ 17.0909636655054*T*LN(ALL1)
+ 60.356978521133852*T*LN(ALL2)
- 41.5723130907662*T*LN(ZALLO) - 0.00369223705*T**2
+ 1.3242320350000002E-7*T**3); 6000 N !

FUNCTION COR0 1 (1 - EXP (-1067.3396/T)); 10000 N !
FUNCTION COR1 1 (1 - EXP (-636.19021/T)); 10000 N !
FUNCTION COR2 1 (1 - EXP (-312.67623/T)); 10000 N !

FUNCTION GCOR 1
(-1.690780842821017E6
+ 39.3927282650856*T*LN(COR0)
+ 69.7003662813618*T*LN(COR1)
+ 15.62384472585121*T*LN(COR2)
- 0.0024049175*T**2 - 1.925204165E-07*T**3); 3000 N !

$-----
$ Binary CaO-Al2O3 compounds
$-----  

$ Ca3Al2O6 = C3A
$-----  

FUNCTION C3A0 1 (1 - EXP (-1020.13119/T)); 10000 N !
FUNCTION C3A1 1 (1 - EXP (-480.050423/T)); 10000 N !
FUNCTION C3A2 1 (1 - EXP (-195.44252/T)); 10000 N !

FUNCTION GC3A 1
(-3.6265529844279119E6
+ 68.264428571996837*T*LN(C3A0)
+ 132.4040773488046*T*LN(C3A1)

```

```
+ 73.70876047825546*T*LN(C3A2)
- 0.005773438010000005*T**2); 6000 N !

$-----
$ C12A7
$-----
FUNCTION FEC12A7S1 0.1 +0.26784991; 6000 N !
FUNCTION TEC12A7S1 0.1 +1156.48654; 6000 N !
FUNCTION FEC12A7S2 0.1 +0.45839024; 6000 N !
FUNCTION TEC12A7S2 0.1 +502.7385460; 6000 N !
FUNCTION FEC12A7S3 0.1 +0.27375985; 6000 N !
FUNCTION TEC12A7S3 0.1 +206.200874; 6000 N !

FUNCTION TEC12A7S 0.1
+FEC12A7S1#*TEC12A7S1#+FEC12A7S2#*TEC12A7S2#
+FEC12A7S3#*TEC12A7S3#; 6000 N !

FUNCTION GC12A7S11 0.1
+1-1*EXP(-TEC12A7S1#*T**(-1)); 6000 N !
FUNCTION GC12A7S12 0.1
+1-1*EXP(-TEC12A7S2#*T**(-1)); 6000 N !
FUNCTION GC12A7S13 0.1
+1-1*EXP(-TEC12A7S3#*T**(-1)); 6000 N !

FUNCTION GEC12A7S2 0.1
+FEC12A7S1#*LN(GC12A7S11#)
+FEC12A7S2#*LN(GC12A7S12#)
+FEC12A7S3#*LN(GC12A7S13#); 6000 N !

FUNCTION G0C12A7S 0.1 -340246.7522; 6000 N !
FUNCTION GEC12A7S3 0.1 +3*R#*T*GEC12A7S2#; 6000 N !
FUNCTION GEC12A7S 0.1 +1.5*R#*TEC12A7S#+GEC12A7S3#;
6000 N !
FUNCTION GTC12A7S 0.1 -9.731079847457630E-04*T**2;
6000 N !
FUNCTION GHC12A7S 0.1
+G0C12A7S#+GEC12A7S#+GTC12A7S#; 6000 N !

$-----
```

```
$ CaAl2O4 = CA
$-----
FUNCTION CA0 1 (1 - EXP(-1047.38873/T)); 10000 N !
FUNCTION CA1 1 (1 - EXP(-458.837521/T)); 10000 N !
FUNCTION CA2 1 (1 - EXP(-178.6963/T)); 10000 N !

FUNCTION GCA 1 (-2.349750735736110E6
+ 68.6331374908854*T*LN(CA0)
+ 68.17219790106598*T*LN(CA1)
+ 37.79837958926666*T*LN(CA2)
- 0.000660288792999997*T**2
- 7.06344541E-07*T**3); 6000 N !

$-----
$ CaAl4O7 = CA2
$-----

FUNCTION CA20 1 (1 - EXP(-1109.65247/T)); 10000 N !
FUNCTION CA21 1 (1 - EXP(-508.764148/T)); 10000 N !
FUNCTION CA22 1 (1 - EXP(-209.974186/T)); 10000 N !

FUNCTION GCA2 1 (-4.0392333170626090E6
+ 116.99454471479561*T*LN(CA20)
+ 115.9414882584303*T*LN(CA21)
+ 66.38462128029035*T*LN(CA22)
- 0.005173192760000004*T**2); 6000 N !

$-----
$ CaAl12O19 = CA6
$-----

FUNCTION CA60 1 (1 - EXP(-420.6218761876267/T)); 10000 N !
FUNCTION CA61 1 (1 - EXP(-3359.6658182832766/T)); 10000 N !
FUNCTION CA62 1 (1 - EXP(-1101.1852843648976/T)); 10000 N !

FUNCTION GCA6 1 (-1.0812591475462691E7
+ 450.3133250660283*T*LN(CA60) +
26.02792788344765*T*LN(CA61)
+ 321.84737776464585*T*LN(CA62) -
```

```
0.02480194952447252*T**2); 6000 N !
$-----
$          CAS2
$-----
FUNCTION CAS20 1 (1 - EXP(-658.274391945986/T)); 10000 N !
FUNCTION CAS21 1 (1 - EXP(-1550.57097920/T)); 10000 N !
FUNCTION CAS22 1 (1 - EXP(-218.71174550/T)); 10000 N !

FUNCTION GCAS2 1 (-4.2642398308864581E6
+ 148.8058523578853*T*LN(CAS20) +
77.225227444567193*T*LN(CAS21)
+ 98.232082012479691*T*LN(CAS22) -
0.006150786253147202*T**2); 3000 N !

$-----
$          C2AS
$-----
FUNCTION C2AS0 1 (1 - EXP(-202.647055790/T)); 10000 N !
FUNCTION C2AS1 1 (1 - EXP(-505.519980529/T)); 10000 N !
FUNCTION C2AS2 1 (1 - EXP(-1197.96796582/T)); 10000 N !

FUNCTION GC2AS 1 (-4.0184623119067852E6
+ 80.712983752394474*T*LN(C2AS0) +
119.3772222870370*T*LN(C2AS1)
+ 99.22999860142122*T*LN(C2AS2) -
0.005751138264637631*T**2); 3000 N !

$-----
$          SIL
$-----
FUNCTION SILO 1 (1 - EXP(-153.06149123803786/T)); 10000 N !
FUNCTION SIL1 1 (1 - EXP(-411.0126080405844/T)); 10000 N !
FUNCTION SIL2 1 (1 - EXP(-1030.5334157523516/T)); 10000 N !

FUNCTION GSIL 1 (-2.6118305016655323E6
+ 10.2038161601145*T*LN(SILO) +
83.2867203476766*T*LN(SIL1)
+ 106.018727208511*T*LN(SIL2) -
0.00026505572690566217*T**2); 3000 N !
```

```

$-----
$          MGO
$-----
FUNCTION MGO0 1 (1 - EXP (-475.5615692/T)); 10000 N !
FUNCTION MGO1 1 (1 - EXP (-775.50257671/T)); 10000 N !
FUNCTION MGO2 1 (1 - EXP (-259.55358863/T)); 10000 N !

FUNCTION LMG00 1.0
1 - EXP (-802.97139*T**(-1)); 10000.0 N !
FUNCTION LMG01 1.0
1 - EXP (-316.655056*T**(-1)); 10000.0 N !
FUNCTION ZLMG00 1.0
EXP ((0.0750535129940371*T*LN(T)
+ 0.749994351575431*T -
6969.9520896844)*T**(-1)) + 1; 10000.0 N !

FUNCTION GMGO 1.0
-0.00184931485*T**2
+ 26.0930478070804*T*LN(MGO0#) +
20.7285632023614*T*LN(MGO1#)
+ 3.06794049945159*T*LN(MGO2#) -
0.0126333744160015*EXP (0.0032721847*T)
- 606454.905049196; 3098.0 Y
76.5*T*(1 - LN(T)) + 467.52323656*T
- 683262.3811 + (3.4001229515421E-5*T
- 0.0938503045793433)**(-1); 6000.0 N !
FUNCTION GMG01 1.0
-0.002702806*T**2
+ 26.6124946323946*T*LN(LMG00#) +
23.2740566808191*T*LN(LMG01#)
- 16.6289252363065*T*LN(ZLMG00#) -
569448.443736023; 6000.0 N !

$-----
$          M2S
$-----
FUNCTION M2S0 1 (1 - EXP (-242.33544682642355/T)); 10000 N !
FUNCTION M2S1 1 (1 - EXP (-521.0055871316241/T)); 10000 N !
FUNCTION M2S2 1 (1 - EXP (-1146.8921615705249/T)); 10000 N !

```

```

FUNCTION GM2S 1
(-2.1894694547503009E6 + 27.917791527833063*T*LN(M2S0) +
91.895489221328484*T*LN(M2S1)
+ 54.773668005547061*T*LN(M2S2) -
0.0039796137052090595*T**2); 2170 N !

$-----
$          MS
$-----

FUNCTION CMS0 1 (1 - EXP(-436.68607089282295/T)); 10000 N !
FUNCTION CMS1 1 (1 - EXP(-1934.0948767977611/T)); 10000 N !

FUNCTION OMS0 1 (1 - EXP(-294.36130457004157/T)); 10000 N !
FUNCTION OMS1 1 (1 - EXP(-281.1818681281586/T)); 10000 N !
FUNCTION OMS2 1 (1 - EXP(-995.1560351249022/T)); 10000 N !

FUNCTION PMS0 1 (1 - EXP(-587.941408967336/T)); 10000 N !
FUNCTION PMS1 1 (1 - EXP(-0.0227303680778/T)); 10000 N !
FUNCTION PMS2 1 (1 - EXP(-2956.3805608988832/T)); 10000 N !

FUNCTION GCLMGSIO 298.15
(-1584678 + 544.9199*T + 104.3011*T*(1 - LN(T)) +
1287726*T**(-1) - 0.009291338*T**2); 3000 N !

FUNCTION GCMS 1
(-1.5573200148785093E6 + 92.741911826035484*T*LN(CMS0) +
31.974491948419917*T*LN(CMS1)
- 0.0038364494166432546*T**2); 3000 N !

FUNCTION GOMS 1
(-1.5564437638799032E6
+ 49.405882892834079*T*LN(OMS0) +
9.503439739060052E-6*T*LN(OMS1)
+ 75.305714024248420*T*LN(OMS2) -
0.0038853173054983477*T**2); 3000 N !

FUNCTION GPMS 1
(-1.5425518874130727E6

```

```

+ 102.020640125967*T*LN(PMS0) +
3.1298114477056090*T*LN(PMS1)
+ 19.56676914813782*T*LN(PMS2) -
0.0017363618331370015*T**2); 3000 N !

$-----
$          DIOP, AKER, MER
$-----

FUNCTION GDIOP
298.15 (-3282503
+ 1095.5238*T + 210.1692*T*(1 - LN(T)) +
2517588*T**(-1) - 0.022135662*T**2); 3000 N !

FUNCTION GAKER 1 + (-4009964.8637490207)
+(3.0/2)*8.31446261815324*
(1.718214012820375)*(1803.4822162315852)
+3*8.31446261815324*T*
(1.718214012820375)*ln(1-exp(-(1803.4822162315852)/T))
+(3.0/2)*8.31446261815324*
(5.8715282086640945)*(676.0432747418508)
+3*8.31446261815324*T*
(5.8715282086640945)*ln(1-exp(-(676.0432747418508)/T))
+(3.0/2)*8.31446261815324*
(4.410228317926463)*(220.33507085331422)
+3*8.31446261815324*T*
(4.410228317926463)*ln(1-exp(-(220.33507085331422)/T))
+(-0.006461012014427301)*T**2); 3000 N !

FUNCTION GMER 1 (-4795630.118828734)
+(3.0/2)*8.31446261815324*
(5.963982025706537)*(858.7549774936704)
+3*8.31446261815324*T*
(5.963982025706537)*ln(1-exp(-(858.7549774936704)/T))
+(3.0/2)*8.31446261815324*
(0.995844162605323)*(8200.60360461208)
+3*8.31446261815324*T*
(0.995844162605323)*ln(1-exp(-(8200.60360461208)/T))
+(3.0/2)*8.31446261815324*
(7.040296106185939)*(260.61640988898563)
+3*8.31446261815324*T*

```

```
(7.040296106185939)*ln(1-exp(-(260.61640988898563)/T))
+(-0.01723427125059624)*T**2; 3000 N !

$ -----
$ Define phases - pure components
$ -----


PHASE AC2S % 2 2 1 !
CONSTITUENT AC2S :L:Q: !


PHASE ACRIS % 1 1 !
CONSTITUENT ACRIS :Q: !


PHASE APC2S % 2 2 1 !
CONSTITUENT APC2S :L:Q: !


PHASE AQUARTZ % 1 1 !
CONSTITUENT AQUARTZ :Q: !


PHASE BC2S % 2 2 1 !
CONSTITUENT BC2S :L:Q: !


PHASE BCRIS % 1 1 !
CONSTITUENT BCRIS :Q: !


PHASE BQUARTZ % 1 1 !
CONSTITUENT BQUARTZ :Q: !


PHASE GC2S % 2 2 1 !
CONSTITUENT GC2S :L:Q: !


PHASE MC3S % 2 3 1 !
CONSTITUENT MC3S :L:Q: !


PHASE PCS % 2 1 1 !
CONSTITUENT PCS :L:Q: !


PHASE RC3S % 2 3 1 !
CONSTITUENT RC3S :L:Q: !
```

APPENDIX B. APPENDIX: TDB FILE

PHASE RC3S2 % 2 3 2 !
CONSTITUENT RC3S2 :L:Q: !

PHASE TC3S % 2 3 1 !
CONSTITUENT TC3S :L:Q: !

PHASE WCS % 2 1 1 !
CONSTITUENT WCS :L:Q: !

PHASE CAS2 % 3 1 1 2 !
CONSTITUENT CAS2 :L:A:Q: !

PHASE C2AS % 3 2 1 1 !
CONSTITUENT C2AS :L:A:Q: !

PHASE PMS % 2 1 1 !
CONSTITUENT PMS :M:Q: !
PARAMETER G(PMS,M:Q;0) 1 GPMS#; 10000 N !

PHASE OMS % 2 1 1 !
CONSTITUENT OMS :M:Q: !
PARAMETER G(OMS,M:Q;0) 1 GOMS#; 10000 N !

PHASE CMS % 2 1 1 !
CONSTITUENT CMS :M:Q: !
PARAMETER G(CMS,M:Q;0) 1 GCMS#; 10000 N !

PHASE M2S % 2 2 1 !
CONSTITUENT M2S :M:Q: !
PARAMETER G(M2S,M:Q;0) 1 GM2S#; 10000 N !

PHASE AKER % 3 2.0 1.0 2.0 !
CONSTITUENT AKER :L:M:Q: !
PARAMETER G(AKER,L:M:Q;0) 298.15 GAKER ; 3000 N !

PHASE MER % 3 3.0 1.0 2.0 !
CONSTITUENT MER :L:M:Q: !
PARAMETER G(MER,L:M:Q;0) 0.1 GMER ; 6000 N !

FUNCTION ALPHA_H 1 83680; 10000 N !

```
FUNCTION ALPHA_L0 1 -35564; 10000 N !
FUNCTION ALPHA_LOT 1 0; 10000 N !

PHASE ALPHA % 2 2.0 1.0 !
CONSTITUENT ALPHA :L,M:Q: !
PARAMETER G(ALPHA,L:Q;0) 298.15
+GAC2S ; 6000 N !
PARAMETER G(ALPHA,M:Q;0) 298.15
+GM2S+ALPHA_H ; 6000 N !
PARAMETER L(ALPHA,L,M:Q;0) 298.15
ALPHA_L0 + ALPHA_LOT*T ; 6000 N !

FUNCTION ALPHA_PRIME_H 1 85772; 10000 N !
FUNCTION ALPHA_PRIME_L0 1 -35564; 10000 N !
FUNCTION ALPHA_PRIME_LOT 1 0; 10000 N !

PHASE ALPHA_PRIME % 2 2.0 1.0 !
CONSTITUENT ALPHA_PRIME :L,M:Q: !
PARAMETER G(ALPHA_PRIME,L:Q;0) 298.15 +GAPC2S ; 6000 N !
PARAMETER G(ALPHA_PRIME,M:Q;0) 298.15
+GM2S+ALPHA_PRIME_H ; 6000 N !
PARAMETER L(ALPHA_PRIME,L,M:Q;0) 298.15
ALPHA_PRIME_L0+ALPHA_PRIME_LOT*T ; 6000 N !

PHASE WOLL % 2 1.0 1.0 !
CONSTITUENT WOLL :L,M:Q: !
PARAMETER G(WOLL,L:Q;0) 298.15 +GWCS ; 6000 N !
PARAMETER G(WOLL,M:Q;0) 298.15
+GCLMGSIO+42443-12.523*T ; 6000 N !
PARAMETER G(WOLL,L,M:Q;0) 298.15 -10000 ; 6000 N !

FUNCTION MONOXIDE_L_M_L0 1 119445.732404441; 10000 N !
FUNCTION MONOXIDE_L_M_LOT 1 -24.2429471085131; 10000 N !
FUNCTION MONOXIDE_L_M_LT 1 -9.13219667432677; 10000 N !

PHASE MONOXIDE % 1 1.0 !
CONSTITUENT MONOXIDE :L,M: !
PARAMETER G(MONOXIDE,L;0) 1 +GCAO; 5000 N !
PARAMETER G(MONOXIDE,M;0) 1 +GMGO; 5000 N !
PARAMETER L(MONOXIDE,L,M;0) 1
```

APPENDIX B. APPENDIX: TDB FILE

```
T * MONOXIDE_L_M_LOT + MONOXIDE_L_M_L0; 10000 N !
PARAMETER L(MONOXIDE,L,M;1) 1
T * MONOXIDE_L_M_L1T; 10000 N !

PHASE CLINO % 3 1 1 2 !
CONSTITUENT CLINO :L,M:M:Q: !
PARAMETER G(CLINO,M:M:Q;0) 298.15
+2*GCLMGSIO+9389-7.3925*T ; 6000 N !
PARAMETER G(CLINO,L:M:Q;0) 298.15
+GDIOP ; 6000 N !
PARAMETER L(CLINO,L,M:M:Q;0) 298.15
25304 +2.358*T ; 6000 N !
PARAMETER L(CLINO,L,M:M:Q;1) 298.15
-3437 ; 6000 N !

PHASE ORTHO % 3 1 1 2 !
CONSTITUENT ORTHO :L,M:M:Q: !
PARAMETER G(ORTHO,M:M:Q;0) 298.15
2*GCLMGSIO-4103+50.186*T
-6.6828*T*LN(T) ; 6000 N !
PARAMETER G(ORTHO,L:M:Q;0) 298.15
GDIOP + 19740 + 0.02*T ; 6000 N !
PARAMETER L(ORTHO,L,M:M:Q;0) 298.15
26411-8.484*T ; 6000 N !

PHASE PROTO % 2 1.0 1.0 !
CONSTITUENT PROTO :L,M:Q: !
PARAMETER G(PROTO,M:Q;0) 298.15
+GCLMGSIO+11831-34.218*T
+3.1114*T*LN(T)+0.0017629728*T**2 ; 6000 N !
PARAMETER G(PROTO,L:Q;0) 298.15
+GWCS +31920 ; 6000 N !
PARAMETER L(PROTO,L,M:Q;0) 298.15
26411 - 8.484*T ; 6000 N !

PHASE LOW_CLINO % 3 1 1 2 !
CONSTITUENT LOW_CLINO :L,M:M:Q: !
PARAMETER G(LOW_CLINO,M:M:Q;0) 298.15
+2*GCLMGSIO ; 6000 N !
```

```

PARAMETER G(LOW_CLINO,L:M:Q;0) 298.15
GDIOP + 20000 ; 6000 N !
PARAMETER L(LOW_CLINO,L,M:M:Q;0) 298.15
(25304) +(2.358)*T ; 6000 N !
PARAMETER L(LOW_CLINO,L,M:M:Q;1) 298.15
-(3437) ; 6000 N !

FUNCTION GMONT 1
+(-2333950.0776404175)
+(3.0/2)*8.31446261815324
*(0.6288886419963274)*(153.35140646512613)
+3*8.31446261815324*T
*(0.6288886419963274)*ln(1-exp(-(153.35140646512613)/T))
+(3.0/2)*8.31446261815324
*(3.4392430255122903)*(385.6626614286263)
+3*8.31446261815324*T
*(3.4392430255122903)*ln(1-exp(-(385.6626614286263)/T))
+(3.0/2)*8.31446261815324
*(2.9302087654155162)*(962.1653157086014)
+3*8.31446261815324*T
*(2.9302087654155162)*ln(1-exp(-(962.1653157086014)/T))
+(-0.0014936167775075617)*T**2; 3000 N !

PHASE OLIVINE % 3 1 1 1 !
CONSTITUENT OLIVINE :L,M:L,M:Q: !
PARAMETER G(OLIVINE,L:L:Q;0) 0.1 GGC2S; 3000 N !
PARAMETER G(OLIVINE,M:M:Q;0) 0.1 GM2S; 3000 N !

PARAMETER G(OLIVINE,M:L:Q;0) 0.1
GMONT+146440+(1.9806+0.3576+0.0756+0.023)*T ; 3000 N !
PARAMETER G(OLIVINE,L:M:Q;0) 0.1
GMONT+(1.9806+0.3576+0.0756+0.023)*T ; 3000 N !

PARAMETER G(OLIVINE,L,M:M:Q;0) 298.15 +32235.53; 6000 N !
PARAMETER G(OLIVINE,L,M:M:Q;1) 298.15 -4079.92; 6000 N !
PARAMETER G(OLIVINE,L:L,M:Q;0) 298.15 +28032.8; 6000 N !

PHASE MULLITE % 1 1 !
CONSTITUENT MULLITE :COR, SIL: !

```

```
FUNCTION MULLITE_COR_SIL_L0 1 10573.0559222137; 10000 N !
FUNCTION MULLITE_COR_SIL_L1 1 85373.0647139828; 10000 N !
FUNCTION MULLITE_COR_SIL_L2T 1 21.4338330628626; 10000 N !

PARAMETER G(MULLITE,COR;0) 1
1.5*GCOR+4998.5299011052; 10000 N !
PARAMETER G(MULLITE,SIL;0) 1 GSIL; 10000 N !
PARAMETER L(MULLITE,COR,SIL;0) 1
MULLITE_COR_SIL_L0; 10000 N !
PARAMETER L(MULLITE,COR,SIL;1) 1
MULLITE_COR_SIL_L1; 10000 N !
PARAMETER L(MULLITE,COR,SIL;2) 1
T * MULLITE_COR_SIL_L2T; 10000 N !

PARAMETER G(ACRIS,Q;0) 1 GACRIS; 10000 N !
PARAMETER G(AQUARTZ,Q;0) 1 GAQUARTZ; 10000 N !
PARAMETER G(BCRIS,Q;0) 1 GBCRIS; 10000 N !
PARAMETER G(BQUARTZ,Q;0) 1 GBQUARTZ; 10000 N !

PARAMETER G(AC2S,L:Q;0) 1 GAC2S; 10000 N !
PARAMETER G(APC2S,L:Q;0) 1 GAPC2S; 10000 N !
PARAMETER G(BC2S,L:Q;0) 1 GBC2S; 10000 N !
PARAMETER G(GC2S,L:Q;0) 1 GGC2S; 10000 N !

PARAMETER G(MC3S,L:Q;0) 1 GMC3S; 10000 N !
PARAMETER G(RC3S,L:Q;0) 1 GRC3S; 10000 N !

PARAMETER G(RC3S2,L:Q;0) 1 GRC3S2; 10000 N !

PARAMETER G(WCS,L:Q;0) 1 GWCS; 10000 N !
PARAMETER G(PCS,L:Q;0) 1 GPCS; 10000 N !

PARAMETER G(C2AS,L:A:Q;0) 1 GC2AS; 10000 N !
PARAMETER G(CAS2,L:A:Q;0) 1 GCAS2; 10000 N !

PHASE C3A % 2 3 1 !
CONSTITUENT C3A :L:A: !
PARAMETER G(C3A,L:A;0) 1 GC3A; 10000 N !
```

```
PHASE CA % 2 1 1 !
CONSTITUENT CA :L:A: !
PARAMETER G(CA,L:A;0) 1 GCA; 10000 N !

PHASE CA2 % 2 1 2 !
CONSTITUENT CA2 :L:A: !
PARAMETER G(CA2,L:A;0) 1 GCA2; 10000 N !

PHASE CA6 % 2 1 6 !
CONSTITUENT CA6 :L:A: !
PARAMETER G(CA6,L:A;0) 1 GCA6; 10000 N !

PHASE C12A7 % 2 12 7 !
CONSTITUENT C12A7 :L:A: !
PARAMETER G(C12A7,L:A;0) 0.1 +59*GHC12A7S; 6000 N !

PHASE C2F % 2 2 1 !
CONSTITUENT C2F :L:FE2O3: !
PARAMETER G(C2F,L:FE2O3;0) 1 GC2F; 10000 N !

PHASE CAO % 1 1 !
CONSTITUENT CAO :L: !
PARAMETER G(CAO,L;0) 1 GCAO; 10000 N !

PHASE CF % 2 1 1 !
CONSTITUENT CF :L:FE2O3: !
PARAMETER G(CF,L:FE2O3;0) 1 GCF; 10000 N !

PHASE CF2 % 2 1 2 !
CONSTITUENT CF2 :L:FE2O3: !
FUNCTION A 1 -30; 10000 N !
FUNCTION B 1 12500; 10000 N !
PARAMETER G(CF2,L:FE2O3;0) 298.0
T*A# + B# + GCAO# + 2*GFE2O3#; 6000.0 N !

PHASE GAS:G % 1 1.0 !
CONSTITUENT GAS:G :O1,O2,O3,FE,FEO : !
PARAMETER G(GAS,O2;0) 298.15 +GO2GAS; 6000 N !
```

APPENDIX B. APPENDIX: TDB FILE

```
PARAMETER G(GAS,O1;0) 298.15 +GO1GAS; 6000 N !
PARAMETER G(GAS,O3;0) 298.15 +GO3GAS; 6000 N !
PARAMETER G(GAS,FE;0) 298.15 +GFEGAS; 6000 N !
PARAMETER G(GAS,FEO;0) 298.15 +GFEQOGAS; 6000 N !

PHASE LIQUID % 1 1 !
CONSTITUENT LIQUID :CAOL, MGOL, M2SL, CAS2L,
ALL, ASL, C3AL, FE, FEO, FEO3/2, C2SL, CSL, SIO2L : !

PARAMETER G(LIQUID,SIO2L;0) 1 GSIO2L; 10000 N !
PARAMETER G(LIQUID,CAOL;0) 1 GCAOL; 10000 N !
PARAMETER G(LIQUID,MGOL;0) 298.15 GMGOL#; 6000 N !
PARAMETER G(LIQUID,FE;0) 298.15 +GFELIQ; 6000 N !

PARAMETER G(LIQUID,FEO;0) 298.15
+GFEQ+34008-20.969*T; 6000 N !

PARAMETER G(LIQUID ,FEO3/2;0)
298.15 0.5*GFE2O3+39712-20.007*T; 6000 N !
PARAMETER G(LIQUID,ALL;0) 1 0.5 * GALL; 10000 N !

FUNCTION ASL_H 1 545197.227605748; 10000 N !
FUNCTION ASL_S 1 -3.51484617476168; 10000 N !
PARAMETER G(LIQUID,ASL;0) 1 -1 * T * ASL_S +
ASL_H + 0.66666666666667 * GALL
+ GSIO2L; 10000 N !

FUNCTION ALL_SIO2L_L0 1 6952.81065916526; 10000 N !
FUNCTION ALL_SIO2L_LOT 1 7.45929355884341; 10000 N !
FUNCTION ALL_SIO2L_L1 1 -9798.44151926753; 10000 N !
FUNCTION ALL_SIO2L_L2 1 2893.01383248282; 10000 N !
PARAMETER L(LIQUID,ALL,SIO2L;0) 1
T * ALL_SIO2L_LOT + ALL_SIO2L_L0; 10000 N !
PARAMETER L(LIQUID,ALL,SIO2L;1) 1
ALL_SIO2L_L1; 10000 N !
PARAMETER L(LIQUID,ALL,SIO2L;2) 1
ALL_SIO2L_L2; 10000 N !

FUNCTION C3AL_CAOL_L0 1 -73232.4694701268; 10000 N !
FUNCTION C3AL_CAOL_LOT 1 45.9571438918422; 10000 N !
```

```

FUNCTION C3AL_H 1 -150837.716392695; 10000 N !
FUNCTION ALL_C3AL_L1 1 -267094.165327997; 10000 N !
FUNCTION ALL_C3AL_L1T 1 55.6830981222739; 10000 N !
FUNCTION ALL_CAOL_L0 1 -108365.449831167; 10000 N !
FUNCTION ALL_CAOL_LOT 1 2.99851122675031; 10000 N !

PARAMETER G(LIQUID,C3AL;0) 1
C3AL_H + 3 * GCAOL + GALL; 10000 N !
PARAMETER L(LIQUID,ALL,C3AL;1) 1
T * ALL_C3AL_L1T + ALL_C3AL_L1; 10000 N !
PARAMETER L(LIQUID,ALL,CAOL;0) 1
T * ALL_CAOL_LOT + ALL_CAOL_L0; 10000 N !
PARAMETER L(LIQUID,C3AL,CAOL;0) 1
T * C3AL_CAOL_LOT + C3AL_CAOL_L0; 10000 N !

FUNCTION CAS2L_H 1 -85250; 10000 N !
FUNCTION CAS2L_S 1 -15; 10000 N !
PARAMETER G(LIQUID,CAS2L;0) 1
CAS2L_H + -CAS2L_S*T + GSIO2L + 0.5 * GCAOL
+ 0.5 * GALL; 10000 N !

FUNCTION C2SL_H 1 -183422.297315552; 10000 N !
FUNCTION C2SL_S 1 2.28483183782731; 10000 N !
PARAMETER G(LIQUID,C2SL;0) 1
-1 * T * C2SL_S + 2 * GCAOL + C2SL_H + GSIO2L;
10000 N !

FUNCTION CSL_H 1 -116624.5108961; 10000 N !
FUNCTION CSL_S 1 -3.86841542916429; 10000 N !
PARAMETER G(LIQUID,CSL;0) 1
CSL_H + GCAOL-1 * T * CSL_S + GSIO2L; 10000 N !

FUNCTION C2SL_SIO2L_LOT 1 9.04086951648876; 10000 N !
FUNCTION C2SL_CAOL_L2T 1 8.99637059634927; 10000 N !
FUNCTION CSL_SIO2L_L0 1 251273.138042155; 10000 N !
FUNCTION CSL_SIO2L_LOT 1 -132.4131763105; 10000 N !
FUNCTION CSL_SIO2L_L1 1 -76026.8593265931; 10000 N !
FUNCTION CSL_SIO2L_L1T 1 22.9753135769968; 10000 N !
FUNCTION CSL_SIO2L_L2 1 117268.159674298; 10000 N !
FUNCTION CSL_SIO2L_L2T 1 -40.3850726577932; 10000 N !

```

```
PARAMETER L(LIQUID,C2SL,CAOL;2) 1
T * C2SL_CAOL_L2T; 6000 N !
PARAMETER L(LIQUID,C2SL,SIO2L;0) 1
T * C2SL_SIO2L_LOT; 6000 N !
PARAMETER L(LIQUID,CSL,SIO2L;1) 1
T * CSL_SIO2L_L0T + CSL_SIO2L_L0; 6000 N !
PARAMETER L(LIQUID,CSL,SIO2L;2) 1
T * CSL_SIO2L_L1T + CSL_SIO2L_L1; 6000 N !
PARAMETER G(LIQUID,FE,FEO;0) 298.15
+109625.2-20.050*T; 3000 N !
PARAMETER G(LIQUID,FE,FEO;1) 298.15
-26317.9+11.072*T; 3000 N !
PARAMETER G(LIQUID,FE,FEO3/2;0) 298.15
81541.2; 3000 N !
PARAMETER G(LIQUID,FEO,FEO3/2;0) 298.15
-13353.8; 3000 N !
PARAMETER G(LIQUID,FEO,FEO3/2;1) 298.15
6707.07; 3000 N !

PARAMETER G(LIQUID,CAOL,FEO;0) 298.15
-119593+26.125*T; 3000 N !
PARAMETER G(LIQUID,CAOL,FEO;1) 298.15
-38729+25.427*T; 3000 N !
PARAMETER G(LIQUID,CAOL,FEO;2) 298.15
5370; 3000 N !

PARAMETER G(LIQUID,CAOL,FEO,FEO3/2;0) 298.15
91713; 3000 N !

FUNCTION L0 298.15 -62800; 10000 N !
FUNCTION LOT 298.15 -8.4; 10000 N !
FUNCTION L2 298.15 -30000; 10000 N !

PARAMETER L(LIQUID,CAOL,FEO3/2;0) 1.0
T*LOT# + L0#; 6000.0 N !
```

```

PARAMETER L(LIQUID,CAOL,FEO3/2;2) 1.0
L2#; 6000.0 N !

FUNCTION SL0 1 34642; 10000 N !
FUNCTION SLOT 1 0; 10000 N !
FUNCTION SL1 1 -7766; 10000 N !
FUNCTION SL1T 1 0; 10000 N !
FUNCTION SL2 1 9992; 10000 N !
FUNCTION SL2T 1 0; 10000 N !

PARAMETER L(LIQUID,FEO3/2,SIO2L;0) 1
T * SLOT + SL0; 10000 N !
PARAMETER L(LIQUID,FEO3/2,SIO2L;1) 1
T * SL1T + SL1; 10000 N !
PARAMETER L(LIQUID,FEO3/2,SIO2L;2) 1
T * SL2T + SL2; 10000 N !

FUNCTION CAOL_MGOL_L1T 1 -10.4155436539951; 10000 N !
FUNCTION M2SL_H 1 -111578.217113669; 10000 N !
FUNCTION M2SL_S 1 -13.8504048423601; 10000 N !
FUNCTION M2SL_SIO2L_L0 1 43199.4342511078; 10000 N !
FUNCTION M2SL_SIO2L_LOT 1 -22.7544714005804; 10000 N !
FUNCTION M2SL_SIO2L_L1 1 8428.95059316569; 10000 N !
FUNCTION M2SL_SIO2L_L2 1 455254.927413284; 10000 N !
FUNCTION M2SL_SIO2L_L2T 1 -186.680283524485; 10000 N !
FUNCTION M2SL_SIO2L_L3 1 -4993.17777002718; 10000 N !

PARAMETER G(LIQUID,M2SL;0) 1
-1 * T * M2SL_S + M2SL_H
+ 2 * GMGOL + GSIO2L; 10000 N !
PARAMETER L(LIQUID,M2SL,SIO2L;0) 1
T * M2SL_SIO2L_LOT
+ M2SL_SIO2L_L0; 10000 N !
PARAMETER L(LIQUID,M2SL,SIO2L;1) 1
M2SL_SIO2L_L1; 10000 N !
PARAMETER L(LIQUID,M2SL,SIO2L;2) 1
T * M2SL_SIO2L_L2T
+ M2SL_SIO2L_L2; 10000 N !
PARAMETER L(LIQUID,M2SL,SIO2L;3) 1
M2SL_SIO2L_L3; 10000 N !

```

APPENDIX B. APPENDIX: TDB FILE

```
PARAMETER L(LIQUID,CAOL,MGOL;1) 1
T * CAOL_MGOL_L1T; 10000 N !

TYPE_DEFINITION & GES A_P_D BCC_A2 MAGNETIC -1.0 0.4 !
PHASE BCC_A2 %& 2 1 3 !
CONSTITUENT BCC_A2 :FE,O : VA : !
PARAMETER G(BCC_A2,FE:VA;0) 298.15 +GHSERFE; 6000 N !
PARAMETER TC(BCC_A2,FE:VA;0) 298.15 +1043; 6000 N !
PARAMETER BMAGN(BCC_A2,FE:VA;0) 298.15 +2.22; 6000 N !
PARAMETER G(BCC_A2,O:VA;0) 298.15
+0.5*GO2GAS+30000; 6000 N !
PARAMETER G(BCC_A2,FE,O:VA;0) 298.15
-209794+84*T; 6000 N !

TYPE_DEFINITION ( GES A_P_D FCC_A1 MAGNETIC -3.0 0.28 !
PHASE FCC_A1 %( 2 1 1 !
CONSTITUENT FCC_A1 :FE,O : VA : !
PARAMETER G(FCC_A1,FE:VA;0) 298.15 +GFEFCC; 6000 N !
PARAMETER TC(FCC_A1,FE:VA;0) 298.15 -201; 6000 N !
PARAMETER BMAGN(FCC_A1,FE:VA;0) 298.15 -2.1; 6000 N !
PARAMETER G(FCC_A1,O:VA;0) 298.15
+0.5*GO2GAS+30000; 6000 N !
PARAMETER G(FCC_A1,FE,O:VA;0) 298.15
-199345.5+84*T; 6000 N !

PHASE HALITE % 2 1 1 !
CONSTITUENT HALITE :FE+2,FE+3,VA : O-2 : !
PARAMETER G(HALITE,FE+2:O-2;0) 298.15
+GWUSTITE; 3000 N !
PARAMETER G(HALITE,FE+3:O-2;0) 298.15
+1.25*AWUSTITE+1.25*GWUSTITE; 3000 N !
PARAMETER G(HALITE,VA:O-2;0) 298.15 +0; 6000 N !
PARAMETER G(HALITE,FE+2,FE+3:O-2;0) 298.15
-12324; 3000 N !
PARAMETER G(HALITE,FE+2,FE+3:O-2;1) 298.15
+20070; 3000 N !

FUNCTION GSPCA 298.15 -561218 -51.606*T ; 3000 N !
```

```
TYPE_DEFINITION ) GES A_P_D SPINEL MAGNETIC -3.0 0.28 !
PHASE SPINEL %) 4 1 2 2 4 !
CONSTITUENT SPINEL :FE+2,FE+3 : FE+2,FE+3,VA : FE+2,VA : O-2 : !
PARAMETER G(SPINEL,FE+2:FE+2:FE+2:O-2;0) 298.15
+9*GFE3O4+DFE3O4; 3000 N !
PARAMETER G(SPINEL,FE+3:FE+2:FE+2:O-2;0) 298.15
+9*GFE3O4+DFE3O4-BFE3O4; 3000 N !
PARAMETER G(SPINEL,FE+2:FE+3:FE+2:O-2;0) 298.15
+9*GFE3O4+DFE3O4-BFE3O4; 3000 N !
PARAMETER G(SPINEL,FE+3:FE+3:FE+2:O-2;0) 298.15
+9*GFE3O4+DFE3O4-2*BFE3O4; 3000 N !
PARAMETER G(SPINEL,FE+2:VA:FE+2:O-2;0) 298.15
+7*GFE3O4+DFE3O4+CFE3O4-BFE3O4; 3000 N !
PARAMETER G(SPINEL,FE+3:VA:FE+2:O-2;0) 298.15
+7*GFE3O4+DFE3O4+CFE3O4-2*BFE3O4; 3000 N !
PARAMETER G(SPINEL,FE+2:FE+2:VA:O-2;0) 298.15
+7*GFE3O4-BFE3O4; 3000 N !
PARAMETER G(SPINEL,FE+3:FE+2:VA:O-2;0) 298.15
+7*GFE3O4; 3000 N !
PARAMETER G(SPINEL,FE+2:FE+3:VA:O-2;0) 298.15
+7*GFE3O4; 3000 N !
PARAMETER G(SPINEL,FE+3:FE+3:VA:O-2;0) 298.15
+7*GFE3O4-BFE3O4; 3000 N !
PARAMETER G(SPINEL,FE+2:VA:VA:O-2;0) 298.15
+5*GFE3O4+CFE3O4; 3000 N !
PARAMETER G(SPINEL,FE+3:VA:VA:O-2;0) 298.15
+5*GFE3O4+CFE3O4-BFE3O4; 3000 N !
PARAMETER TC(SPINEL,FE+2:FE+2:FE+2:O-2;0) 298.15
848; 3000 N !
PARAMETER TC(SPINEL,FE+3:FE+2:FE+2:O-2;0) 298.15
848; 3000 N !
PARAMETER TC(SPINEL,FE+2:FE+3:FE+2:O-2;0) 298.15
848; 3000 N !
PARAMETER TC(SPINEL,FE+3:FE+3:FE+2:O-2;0) 298.15
848; 3000 N !
PARAMETER TC(SPINEL,FE+2:VA:FE+2:O-2;0) 298.15
848; 3000 N !
PARAMETER TC(SPINEL,FE+3:VA:FE+2:O-2;0) 298.15
848; 3000 N !
PARAMETER TC(SPINEL,FE+2:FE+2:VA:O-2;0) 298.15
```

```
848; 3000 N !
PARAMETER TC(SPINEL,FE+3:FE+2:VA:O-2;0) 298.15
848; 3000 N !
PARAMETER TC(SPINEL,FE+2:FE+3:VA:O-2;0) 298.15
848; 3000 N !
PARAMETER TC(SPINEL,FE+3:FE+3:VA:O-2;0) 298.15
848; 3000 N !
PARAMETER TC(SPINEL,FE+2:VA:VA:O-2;0) 298.15
848; 3000 N !
PARAMETER TC(SPINEL,FE+3:VA:VA:O-2;0) 298.15
848; 3000 N !

PARAMETER BMAGN(SPINEL,FE+2:FE+2:FE+2:O-2;0) 298.15
44.54; 3000 N !
PARAMETER BMAGN(SPINEL,FE+3:FE+2:FE+2:O-2;0) 298.15
44.54; 3000 N !
PARAMETER BMAGN(SPINEL,FE+2:FE+3:FE+2:O-2;0) 298.15
44.54; 3000 N !
PARAMETER BMAGN(SPINEL,FE+3:FE+3:FE+2:O-2;0) 298.15
44.54; 3000 N !
PARAMETER BMAGN(SPINEL,FE+2:VA:FE+2:O-2;0) 298.15
44.54; 3000 N !
PARAMETER BMAGN(SPINEL,FE+3:VA:FE+2:O-2;0) 298.15
44.54; 3000 N !
PARAMETER BMAGN(SPINEL,FE+2:FE+2:VA:O-2;0) 298.15
44.54; 3000 N !
PARAMETER BMAGN(SPINEL,FE+3:FE+2:VA:O-2;0) 298.15
44.54; 3000 N !
PARAMETER BMAGN(SPINEL,FE+2:FE+3:VA:O-2;0) 298.15
44.54; 3000 N !
PARAMETER BMAGN(SPINEL,FE+3:FE+3:VA:O-2;0) 298.15
44.54; 3000 N !
PARAMETER BMAGN(SPINEL,FE+2:VA:VA:O-2;0) 298.15
44.54; 3000 N !
PARAMETER BMAGN(SPINEL,FE+3:VA:VA:O-2;0) 298.15
44.54; 3000 N !

TYPE_DEFINITION % SEQ * !
```

```
PHASE FERRITE % 1 1.0 !
CONSTITUENT FERRITE :C2F,C2A: !
PARAMETER G(FERRITE,C2F;0) 298.15
GC2F; 3000.0 N !
PARAMETER G(FERRITE,C2A;0) 298.15
2*GCAO + 1*GCOR;10000.0 N !
FUNCTION FERRA 298.15
-130000; 10000.0 N !
FUNCTION FERRAT 1 0; 10000 N !
FUNCTION FERRB 1 -25000; 10000 N !
FUNCTION FERRBT 1 0; 10000 N !
PARAMETER G(FERRITE,C2A,C2F;0) 298.15
FERRA+FERRAT*T ;10000 N !
PARAMETER G(FERRITE,C2A,C2F;1) 298.15
FERRB+FERRBT*T ;10000 N !

TYPE_DEFINITION ^ GES A_P_D CORUNDUM MAGNETIC -3.0 0.28 !
PHASE CORUNDUM %^ 1 1 !
CONSTITUENT CORUNDUM :A,FE2O3: !
PARAMETER G(CORUNDUM,FE2O3;0) 298.15
+GFE2O3 ;6000 N !
PARAMETER G(CORUNDUM,A;0) 298.15
+GCOR ;6000 N !
PARAMETER TC(CORUNDUM,FE2O3;0) 298.15
-2867; 6000 N !
PARAMETER BMAGN(CORUNDUM,FE2O3;0) 298.15
-25.1; 6000 N !

$ END
```

APPENDIX
C

APPENDIX: CLINKER ANALYSIS

In this appendix, are the results of the XRF, XRD and EDX analysis of the clinker data set that was presented in this work. The analysis was carried out by Dr Christiane Rößler from Bauhaus-Universität Weimar.

Provided in Table C.1 are the oxide compositions in weight % of the clinkers within the data set, as measured by XRF. Clinkers were anonymised and thus given ID numbers.

Provided in Table C.2 are the compositions of the clinker in weight % in terms of the phases as measured by XRD.

Provided in Figures C.1, C.2, C.3 and C.4 are graphs of the oxide composition in weight % of the major clinker phases within the clinkers, as measured by EDX at the highest resolution. Graphs are provided instead of tables due to the abundance of data, which is better visualised in graphical form.

Table C.1: Table of oxide compositions of the clinkers measured via XRF. All masses are in weight %.

ID	SiO ₂	Al ₂ O ₃	Fe ₂ O ₃	CaO	MgO	Na ₂ O	K ₂ O	SO ₃	MnO	P ₂ O ₅	TiO ₂	Cl ⁻	LOI	Sum XRF	F
10	21.66	5.52	3.36	66.1	0.855	0.207	0.536	0.31	0.116	0.294	0.404	0.01	0.25	99.372	0.04
11	19.76	5.9	3.32	64.82	1.63	0.134	1.406	1.9	0.062	0.092	0.282	0.01	0.14	99.316	0.06
13	21.7	3.19	4.55	64.9	2.85	0.23	0.59	0.96	0.12	0.1	0.5		0.17	99.69	
14	21.38	5.13	3.24	64.08	3.45	0.14	1.04	0.64	0.08	0.29			0.1	99.47	
15_1N	21.3	4.67	3.43	69.15	1.16	0.1	0.28	0.39	0.1	0.18	0.24		0.12	101	
15_2H	21.46	4.73	3.22	67.23	1.02	0.08	0.22	0.26	0.09	0.18	0.28		0.42	98.77	
16	21.96	5.8	2.73	65.98	1.55	0.1	0.57	0.6	0.06	0.12	0.29		0.63	99.76	
17	22.27	5.42	1.67	67.44	0.99	0.23	0.74	0.57	0.03	0.26			0.21	99.62	
18	20.9	6.14	3.94	65.17	1.64	0.15	0.7	0.66	0.04	0.07			0.12	99.41	
19	20.89	5.84	3.38	65.19	2.19	0.1	1.05	0.73	0.05	0.28			0.17	99.7	
23	20.89	4.93	3.59	66.37	1.45	0.38	0.93	0.95	0.08	0.1			0.23	99.67	
26	21.8	5	3.36	66.72	1.21	0.1	0.42	0.54	0.4	0.11			0.25	99.66	
29-1H	22.01	3.13	4.5	64.26	2.92	0.1	0.62	0.93	0.11	0.05	0.45		1.3	99.08	
29-2N	19.99	4.35	3.06	64.42	3.08	0.31	1.26	1.46	0.08	0.05	0.32		0.43	98.38	
3	21.97	4.19	4.27	66	1.08	0.1	0.55	0.43	0.04	0.08	0.21		0.5	98.92	
30	20.12	5.22	2.99	63.82	4.02	0.1	1.68	1.01	0.13	0.6			0.28	99.69	
31	21.24	4.68	3.65	66.53	1.42	0.2	0.89	0.59	0.24	0.12			0.23	99.56	
32	21.41	4.44	2.71	67.64	1.97	0.07	0.54	0.58	0.08	0.12			0.19	99.56	
35	21.19	3.71	5.24	65.85	0.81	0.1	0.57	0.56	0.06	0.36	0.18		0.52	98.63	
37	20.92	5.29	4.1	66.65	1.12	0.43	0.16	0.78	0.04	0.27	0.18		0.38	99.94	
38	21.97	4.59	2.46	65.6	2.17	0.23	1.05	1.3	0.04	0.29	0.21		0.61	99.91	
5	21.43	4.82	3.51	64.75	2.39	0.1	0.75	0.83	0.28	0.17	0.24		0.26	99.27	
8	19.98	4.01	4.87	62.63	3.64	0.52	0.3	1.92	0.17	0.11	0.35		0.52	98.5	
9	21.48	5.5	3.35	66.46	0.868	0.231	0.486	0.26	0.122	0.298	0.379	0.01	0.19	99.444	0.05
a35	24.24	3.94	2.51	67.64	0.99	0.1	0.38	0.38	0.05	0.27	0.21		0.24	100.71	
a36	24.35	3.78	1.47	67.68	0.66	0.16	0.6	0.48	0.04	0.16	0.19		0.34	99.57	

Table C.2: Table of the clinker phase composition, measured via XRD. All values are in weight %.

ID	elite I	elite III	elite sum	belite	C ₃ A cubic	C ₃ A ortho	C ₃ A sum	ferrite	MgO	CaO	SiO ₂	Sum	C ₁₂ A ₇
10	1.7	61.7	63.4	10.84	5.3	8.6	13.9	10.7	0.15	0.2	0.3	100.69	
11	0	61.8	61.8	13.7	7.5	1.9	9.4	13.1	0.1	0.4	0.1	99	
13	2.3	65.7	68	7.1	2.6	4.7	7.3	10.8	3.4	0.9	0.1	101	
14	8	49.5	57.5	14.8	4.486	6.1	10.586	10.4	1.1	2.1	0.1	102.186	
15_IN	12.739	53	65.739	12.412	5.628	2.1416	7.7696	10.028	0.224	1.15866	0.155	99.5033	
15_2H	17.4	55.923	73.323	6.317	5.685	2.039	7.724	11.202	0.056	0.628	0.076	100.629	
16	16.803	44.454	61.257	15.791	9.534	3.052	12.586	7.677	0.963	0.422	0.273	100.423	
17	3.94	67	70.94	8.99	10.31	3.41	13.72	3.04	0.7	1.8	0.1	101.88	
18	1.9	69.8	70.94	5.3	4	2.8	13.72	12.4	0.7	0.9	0.2	107.86	
19	3.1	66.9	71.7	8.1	3.5	2.5	6.8	12.8	0.6	0.4	0.1	103.4	
23	2	68.6	70.6	6.6	2.3	4.3	6.6	12.3	0.1	1.1	0.1	100.8	
26	3.7	66.3	70	6.8	6	3.3	9.3	9.7	0.6	2.3	0.8	102.6	
29-1H	5.1	60.7	65.8	18.8	2.1	2.7	4.8	9.3	1.3	0.6	0.1	103.5	
29-2N	2.1	74.7	76.8	3.1	3.2	2.6	5.8	8.3	1.8	1.3	0.2	101.3	
3	1.5	67.6	69.1	10.2	3.4	1.3	4.7	13	1.2	0.1	0	100.2	
30_1	2	68	70	4.9	3.7	5.1	8.8	8.6	3.4	0.8	0.2	100.9	
30_2	1.8	66.9	68.7	6.3	3.8	4.9	8.7	8.3	3.5	0.5	0.3	100.6	
31	0.8	67.8	68.6	10.1	2.9	2.4	5.3	12.6	0	1.4	0.1	101.5	
32	3.2	70.9	74.1	4.9	7.5	0.3	7.8	9.2	0.8	1.8	0.1	101.9	
35		59.3	59.3	16.9	1.5	3	4.5	15.3	0.1	2	0	102.1	
36	0.9	64.2	65.1	17.5	6.1	1.6	7.7	8.8	0	0.2	0.2	99.9	
37	0.8	63.5	64.3	12.9	7.2	0.3	7.5	14.3	0.1	0.3	0.1	99	
38	36.8	30	66.8	14.1	2.4	0.4	2.3	11	0.6	0	0	95.9	1.1
5	2.1	68.4	70.5	8.6	4.5	0.5	5	13.2	1.1	0.4	0	100.5	
8	8.29	57.258	65.548	12.049	0.597	1.01	1.607	16.664	2.447	1.151	0.143	101.212	
9	0	68.3	68.3	7.4	4.4	7.9	12.3	10.7	0.2	0.2	0.3	100.4	
a35	0.5	55.9	56.4	28.3	6.1	2.35	8.45	5.8	0.5	0.2	0	100.15	
a36	2.6	71.7	74.3	12.6	3.7	5.3	9	2	0.2	0.1	0.3	100	

APPENDIX C. APPENDIX: CLINKER ANALYSIS

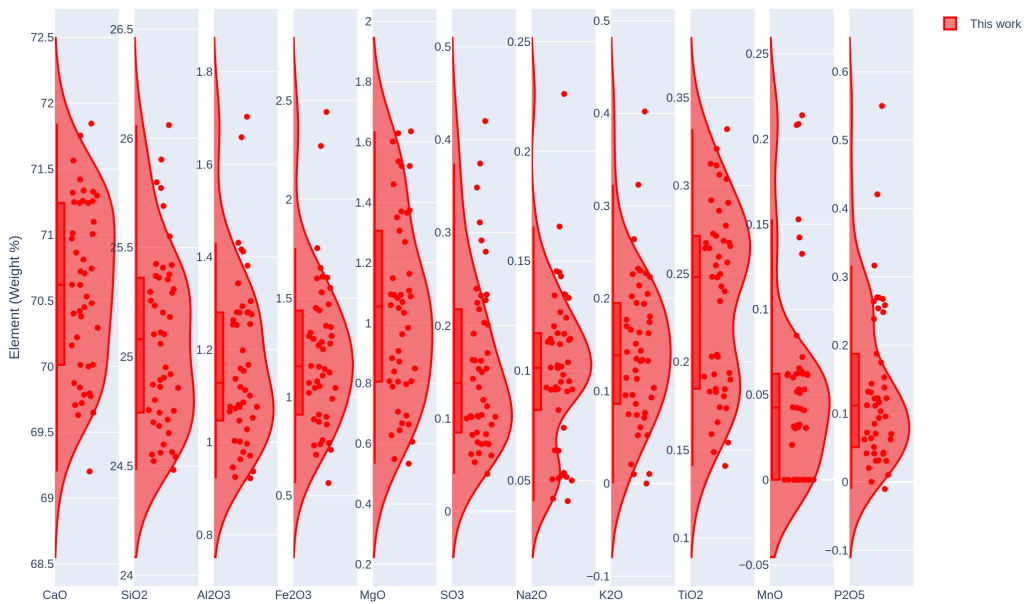


Figure C.1: Composition of the alite phase within the clinkers inside the clinker data-set determined by EDX.

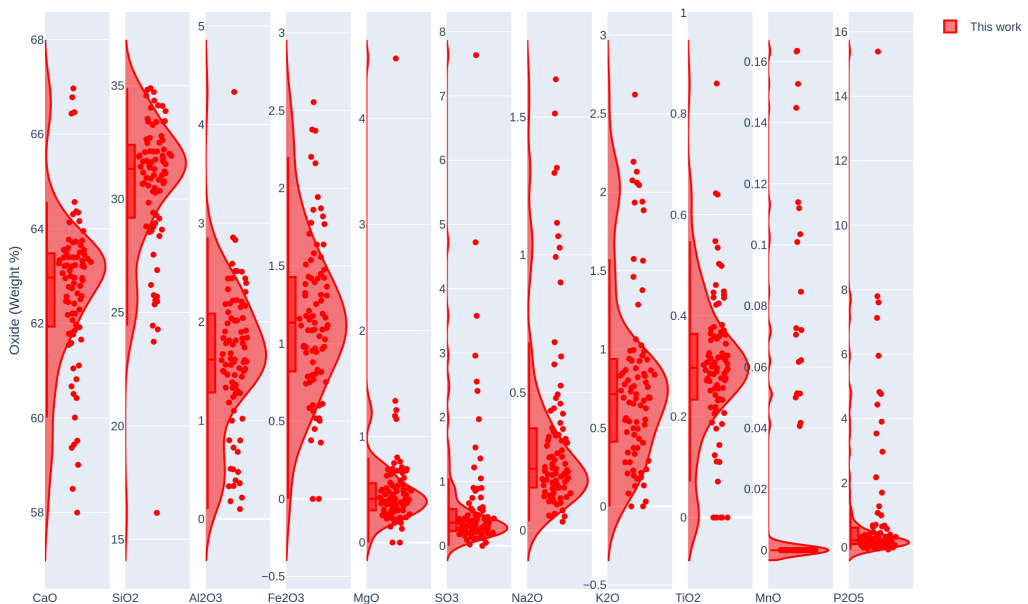


Figure C.2: Composition of the belite phase within the clinkers inside the clinker data-set determined by EDX.

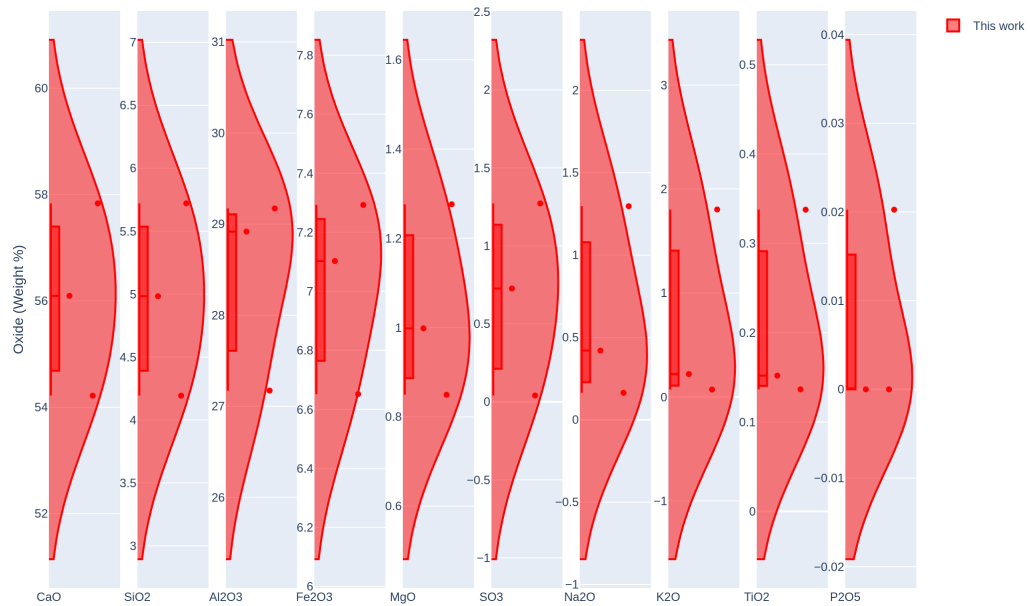


Figure C.3: Composition of the aluminate phase within the clinkers inside the clinker data-set determined by EDX.

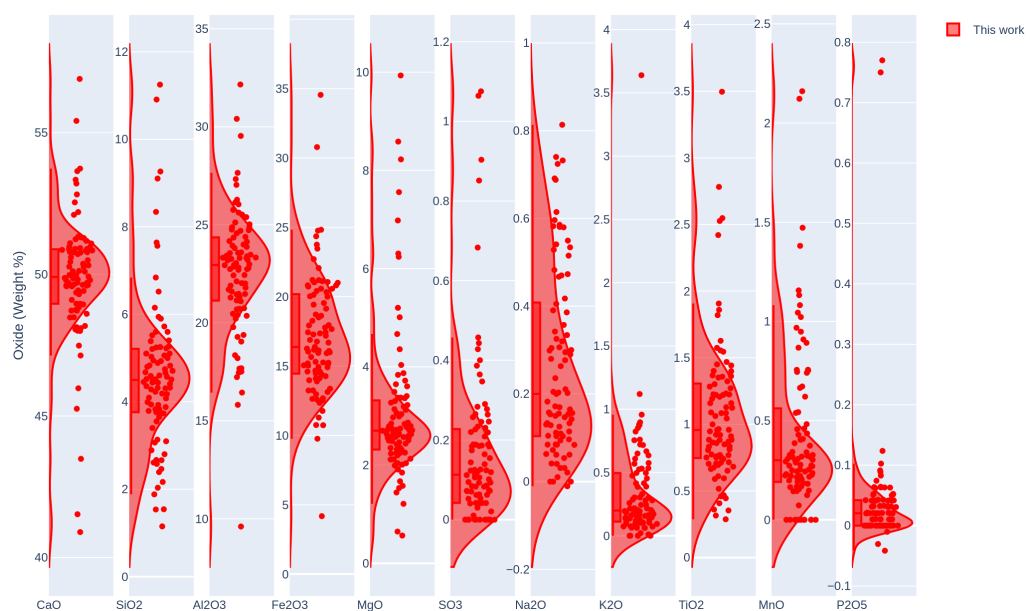


Figure C.4: Composition of the ferrite phase within the clinkers inside the clinker data-set determined by EDX.

APPENDIX
D

APPENDIX: SUBMITTED JOURNAL ARTICLES

Articles submitted to journals during the time this research was undertaken are presented in this section. It should be noted that at the time of writing these articles were yet to be published. The articles presented here are as follows:

- **W. Abdul.**, Ch. Mawalala., A. Pisch., M. N. Bannerman. “CaO-SiO₂ Assessment: 3rd generation modelling of thermodynamic properties”. *Cement and Concrete Research*, 2022.

CaO-SiO₂ Assessment: 3rd generation modelling of thermodynamic properties

W. Abdul^{*a}, Ch. Mawalala^b, A. Pisch^b, M. N. Bannerman^a

^aSchool of Engineering, University of Aberdeen, King's College, Aberdeen, AB24 3FX, United Kingdom

^b Univ. Grenoble Alpes, CNRS, Grenoble INP, SIMaP, F-38000, Grenoble, France

w.abdul.19@abdn.ac.uk

Keywords: Portland cement, Thermodynamic Calculations, Calorimetry.

Abstract

There is an urgent need for new accurate thermodynamic models for the cement clinker production process, especially as increasingly diverse raw materials, fuels, and other modifications are explored to reduce its environmental impact. This contribution reviews current best practices for thermodynamic model fitting in oxide systems and applies it to the most important binary oxide system for cement clinker, CaO-SiO₂. The thermodynamic properties of all solid phases are regressed simultaneously using the 3rd generation Einstein model to maximize accuracy and a new Akaike-Information-Criterion led approach is used to model the liquid phase. The result is comparable to previously published models which highlights the potential of this approach in simplifying and automating thermodynamic modelling. Simplicity is vital, both in techniques and in the model, as many higher-order systems will be built on this binary modelling to cover the full cement system. The solid phase modelling presented here contains new heat capacity measurements for C₃S₂ and the C₂S polymorphs as well as DFT calculations. It also includes the latest modelling of CaO which has recently had a significant adjustment in its melting point. Finally, it distinguishes between the polymorphs of alite (C₃S) even though data is limited, as this will also be important to capture in higher-order systems. The oxide melt is modelled using an associate model and the full phase diagram is computed which compares favourably with all available experimental data.

1. Introduction

Each year, 0.5 tons of cement is produced per person [1] worldwide, accounting for roughly 8% of humanity's annual CO₂ emissions [1]. For each ton of cement produced, 1.25 tons of CO₂ are released by the clinkerization process. Roughly half of the CO₂ released comes from the fuel burnt to drive the high-temperature clinkerization process, while the other half arises from the high-temperature calcination reactions. If we intend to limit our CO₂ production as a species, it is vital that the high-temperature chemistry of cement production is optimized. Unfortunately, due to the enormous scales of production, low profit margins, and the requirement for a product that must last for decades, it is very challenging to experimentally explore even small changes to

the production process. Any changes must have a high confidence of not affecting the final product, meaning precise process models are required. This is challenging as the reaction system is enormously complex due to the diversity in raw material. The stability and cementitious properties of the key phases can be drastically affected by the presence of even a few percent of so-called “minor” elements; thus, the seemingly small details of low concentration components can be extremely important to the quality of the produced clinker.

Interestingly, the metals industry is another high-temperature large-scale production process which is highly influenced by the presence of minor elements. Thermodynamic researchers in this field have made enormous strides by coalescing their efforts around the so-called CALPHAD approach (CALculation of PHAse Diagrams for the modelling of thermodynamic properties in multicomponent systems). Key to this approach is a progressive increase in complexity, first focusing on unary phase models, such as those of a single metal, before attacking binary, ternary, and higher-order systems containing combinations of these elements. This is a critical concept, as the non-ideal interaction parameters are challenging to determine, and the lower-order models can be directly carried over into the interaction models for the higher-order systems. Each stage carries out a thermodynamic assessment, which is a collation and critical review of all available experimental data for a particular thermodynamic system along with a careful estimate for the key thermodynamic properties (i.e., phase diagrams, enthalpic information, etc.). Looking at ordinary Portland cement (OPC) clinker, the major cementitious constituents are alite (Ca_3SiO_5 with dissolved minor elements) and belite (Ca_2SiO_4 with dissolved minor elements). In the cement literature, alite and belite are often designated by C_3S and C_2S which corresponds to the reduced cement notation in which $\text{C}=\text{CaO}$ and $\text{S}=\text{SiO}_2$. This leads to the $\text{CaO}-\text{SiO}_2$ binary system being one of the most critical assessments which is why this is reviewed here as the first system in our study. The solid compounds contained within this system include the four polymorphs of C_2S (β , γ , α' and α), three polymorphs of C_3S (triclinic, monoclinic, and rhombohedral), the two polymorphs of CS (wollastonite and pseudo-wollastonite) and C_3S_2 (rankinite) which is important for Solidia [2] type cements (inorganic binders hardening by reaction with CO_2). Fortunately, cement production is carried out in oxidizing conditions, thus for the $\text{CaO}-\text{SiO}_2$ system there is no need to model the metallic sub-system and oxygen as a separate component.

The first comprehensive assessment and modelling of the thermodynamic properties of the solid compounds in $\text{CaO}-\text{SiO}_2$ was carried out by Haas et al [3]. The results of their study and the experimental data it reviews are often chosen as the basis of all modern assessments for the $\text{CaO}-\text{SiO}_2$ system. While seminal and largely correct, the study by Haas et al has typographical errors in the equations [4] which become obvious when comparing against the tabulated data. This, coupled with the availability of new experimental data justifies a review of the solids again. Commercial databases such as FACTSAGE [5] and SGTE also contain extensive information for the calcium silicates; however, recent advances in modelling, regression, and updates to the CaO [6] and SiO_2 [7] end-members have not yet been incorporated. There is also a shortage of experimental data in the literature for the calcium silicates. For example, it is often the case to only include the hatrurite high-temperature-stable polymorph of C_3S but other meta-stable low-temperature polymorphs do exist and are very important for Portland cements [8]. Additionally, the C_3S_2 solid lacks thermodynamic data at higher temperatures, with data previously only available up to 300 K [9], making fits speculative. Likewise, the high temperature polymorphs of

C_2S : α and α' , lack data at low temperature which we found was essential in fitting the parameters to the new CALPHAD models and to correctly calculate the phase diagram.

Previous assessments in the $\text{CaO}-\text{SiO}_2$ system have all used polynomial models to fit the experimental data, such as the popular Shomate [10] polynomials. This approach, although simple, is unreliable when extrapolating or interpolating far from experimental measurements. This makes connecting low and high temperature data difficult; however, this is vital for cements which are produced at high temperature but utilized/reacted closer to room temperature. In addition, there is a lot of data available at low temperatures for fitting, while high temperature data is more limited, thus extrapolation is vital. The latest development in CALPHAD modelling [11] attempts to overcome these issues through the use of a so-called 3rd generation approach which makes use of Einstein terms for the low temperature data and one or more polynomial corrections to take into account the anharmonic contributions at high temperature (see Eq. 1). This combination yields a single function which can be used to model data over the full temperature range from 0K to the melting point with no junction points, thanks to the Einstein model terms capturing the underlying vibrational nature of the internal energy.

The $\text{CaO}-\text{SiO}_2$ liquid phase has previously been modelled using a variety of models including the two-sublattice ionic model [12,13], the modified quasi-chemical model [14,15], the associates model [16,17], and the cellular model [18]. The main difficulty with this system is the modelling of the miscibility gap in the silica rich region which is important for the extension to higher-order systems. Many previous assessments over-estimate the temperature at the onset of immiscibility due to limitations in the model chosen. Regarding extensions to higher order systems, Pelton and Blander (modified quasi-chemical model) and Hillert et al (two-sublattice) were able to extend their binary models to the $\text{CaO}-\text{FeO}-\text{SiO}_2$ and $\text{CaO}-\text{SiO}_2-\text{Al}_2\text{O}_3$ systems respectively, making their models promising choices for this system; however, in this work the associates model is employed as described in Barry et al [17]. The associates model is also similar for the melt phase when compared to the popular two-sublattice ionic model [19] but it is simpler due to the inclusion of oxide species on the sublattice (i.e., oxygen does not need to be considered as a separate species on a separate sublattice). The model for this binary system will be used to extend to the important cement system, $\text{CaO}-\text{Al}_2\text{O}_3-\text{SiO}_2$ in later work.

The rest of this contribution is organized as follows: First, Sec. 4 and Sec. 5 describes the data in the literature surrounding the calcium silicates used in our assessment. Sec. 2 details the model used to describe all phases in the system. In Sec. 5, the fitting procedure for thermodynamic properties from 0K to the melting point of all solid calcium silicates is described. The proceeding sections then describe the associates' model, and then our approach to fitting the associates model using an information criterion. Experimental and DFT procedures for Ca_2SiO_4 and $\text{Ca}_3\text{Si}_2\text{O}_7$ are explained in Sec. 8 and 9 respectively. Finally, the error estimates from the resultant fit to the data points are assessed. This results in an update to the full $\text{CaO}-\text{SiO}_2$ assessment including a complete phase diagram making use of the recent updates to the endmembers with novel experimental and DFT data.

2. Literature review of the solid phases

In the $\text{CaO}-\text{SiO}_2$ system, all solid compounds are considered stoichiometric; however, many of the stoichiometric phases have multiple polymorphs. For example, C_2S has 5 polymorphs:

β -C₂S (which is a meta-stable, pressure stabilized compound which but appears in higher-order systems and in real cements), γ -C₂S, α' L-C₂S, α' H-C₂S and α -C₂S. This section first considers each compound and its transitions between polymorphs before then considering the existing literature data used to fit the 3rd generation model described in the previous section.

The structural properties of Ca₃SiO₅ are complex [8]. The available literature was reviewed by Regourd [20] and more recently by Dunstetter et al [21]. Ca₃SiO₅ exists in 6 polymorphic modifications but only the high temperature rhombohedral structure is stable [22,23]. The low temperature triclinic modifications (designated T_I, T_{II} and T_{III} in the literature [22,24]) and the intermediate monoclinic ones (designated M_I and M_{II} in the literature [25–27]) are all meta-stable but are important as they are observed in cement clinkers. All observed phase transformations are of the displacive type in which small shift of atoms lead to orientation disorder between SiO₄ tetrahedral units and distorted CaO₆ polyhedra. Therefore, the observed heat of transitions, as measured by quantitative thermal analysis, are small [28]. In this assessment the polymorphs of C₃S have been simplified to monoclinic, triclinic and rhombohedral, as this captures the fundamental structural changes where sufficient data exists to distinguish them in this system.

Calcium orthosilicate Ca₂SiO₄ exists in five modifications. The space groups, lattice parameters, and atomic positions of all modifications are known with precision thanks to a careful study by Mumme et al [29] using high temperature neutron diffraction combined with Rietveld analysis. The stable modification at room temperature, γ -Ca₂SiO₄ sometimes also called calcio-olivine, transforms to α' L-Ca₂SiO₄ at 880°C [30]. This transformation is of the reconstructive type and accompanied by a considerable contraction of the cell volume [30]. Other transition temperatures for this have been reported in the literature. This is due to the fact that the kinetics of this transformation are very sluggish and in addition affected by a small solubility range of +0.4 wt% CaO on the lime rich side and +0.2 wt% SiO₂ on the silica rich side with respect to ideal 2:1 stoichiometry [30]. α' L-Ca₂SiO₄ transforms into α' H-Ca₂SiO₄ with increasing temperature. This transition is second order and of the displacive type [29]. Following this, α' H-Ca₂SiO₄ transforms into the high temperature α -Ca₂SiO₄ modification above 1425°C [30] through a semi-reconstructive transition [29]. The fifth and last modification, β -Ca₂SiO₄ (larnite), is meta-stable at atmospheric pressure, but can be fully stabilized by addition of small amounts of minor elements (e.g. 0.4% of B₂O₃[31]) or by quenching bulk sample from high temperature with a minimum particle size [30]. The α' L– β transformation is of the displacive type which is kinetically favoured over the stable α' L– γ transition. The metastable transition temperature was determined by dilatometry [30] and derived from an experimental p-T phase diagram [32].

The third compound considered here, Ca₃Si₂O₇, exists in two modifications: high temperature rankinite [33] and low temperature kilchoanite [34] (sometimes called Z-Phase in the literature). The transition is irreversible for kinetic reasons and takes place in the temperature interval 954–1090°C [33].

Wollastonite CaSiO₃ exists in two general modifications with a series of derived superstructures due to modified stacking sequences. The low temperature wollastonite compound [35] transforms into the pseudo-wollastonite modification [36–38] (sometimes also called cyclo-wollastonite in the literature).

The structural information of all compounds is summed up in Table 1. The available data on the phase transitions temperatures and enthalpies are presented in Table 2.

Heat capacity data for the Ca_2SiO_4 - β and - γ polymorphs has been measured by Todd [39], King [9], and Grevel et al [40] with these experiments being at low temperature allowing for the entropy at 298K to be derived; however, no low temperature data exists for the high temperature polymorphs; α and α' . The relative enthalpy for the four polymorphs of Ca_2SiO_4 measured by Coughlin [41] is used to aid fitting of the Cp for the high temperature polymorphs. Similarly, heats of formations at 298K only exists for the low temperature polymorphs [42,43]. For the C_3S solid, the heat capacity was also measured by Todd [39] and the relative enthalpy was measured by Gronow and Schweite [44]. The heat of formation is often taken from the heat of decomposition as measured by Brunauer [45]. To overcome the lack of data surrounding the monoclinic and rhombohedral Ca_3SiO_5 polymorphs, each were given identical heat capacities derived from the triclinic form but are then individually corrected using their respective inversion temperatures and enthalpies as measured by Bigare et al [8]. For C_3S_2 only the low temperature heat capacity was measured by King [2]. A heat of formation measurement by Wilford [46] and EMF measurements by Benz and Wagner [47] are also used calculate the heat of formation and fix the absolute enthalpy; however, there is significant disagreement with the fit model around the Benz measurements so not all data was used [13]. The heat capacity of both polymorphs of CaSiO_3 were measured by Wagner [48] and the relative enthalpy for wollastonite was measured by Gronow [44], Courtial [49], and Pascal and Richet [50] for cyclowollastonite. The heat of formation for both polymorphs was also measured by Charlu et al [51].

For the end-members CaO and SiO_2 , the latest assessments by Defferenes et al [6] and Bajenova [7] et al respectively, were used without any need for corrections as they proved to be fully compatible with our present work. All experimental data used in the solid phase fitting is summarised in Table A.2.

Table 1 Structural information, polymorphism & transition data for the solid phases in the $\text{CaO}-\text{SiO}_2$ binary system as found in the literature.

Compound	Designation	Space Group	Reference
Ca_3SiO_5	T1	P-1	[22,24]
	T2	-	[20,21]
	T3	-	[20,21]
	M1	Pc	[27]
	M2	-	[20,21]
	M3	Cm (Am)	[25,26]
	R	R3m	[22,23]
Ca_2SiO_4	γ olivine	Pnma	[29]
	β larnite	P2 ₁ /c	[29]
	α_H'	Pna2 ₁	[29]
	α_L'	Pnma	[29]
	α	P6 ₃ /mmc	[29]
$\text{Ca}_3\text{Si}_2\text{O}_7$	kilchoanite	Ima2	[34]
	rankinite	P2 ₁ /c	[33]
CaSiO_3	wollastonite	P2 ₁ /c	[35]
	pseudo-wollastonite	C2 ₁ /c C-1	[36] [37]

Table 2 Properties of the polymorphic transitions for all solids in the CaO-SiO₂ system found in the literature.

Compound	Transition reaction	Transition temperature [°C]	Transition heat [kJ/mol]	Experimental technique
Ca ₃ SiO ₅	T _I → T _{II}	620	0.57	DTA[28]
	T _{II} → T _{III}	920	0.96	DTA[28]
	T _{III} → M _I	980	0.48	DTA[28]
	M _I → M _{II}	990	0.05	DTA[28]
	M _{II} → R	1050	0.048	DTA[8,28]
Ca ₂ SiO ₄	$\gamma \rightarrow \alpha'_L$	847	7.757-15.460	DTA[30]
			14.393	drop calorimetry [41]
		711	13.020	DTA, at 0.34GPa[32]
	$\beta \rightarrow \alpha'_L$	680	1.439	DTA[29]
			1.841	drop calorimetry [41]
		711	1.780	DTA, at 0.34GPa[32]
	$\gamma \rightarrow \beta$		4.678	DTA[30]
			4.48	sol. calorimetry 20°C[31]
		711	11.250	DTA, at 0.34GPa[32]
	$\alpha'_L \rightarrow \alpha'_H$	1160	0.720	DTA[30]
	$\alpha'_H \rightarrow \alpha$	1425	13.305 14.184	DTA[30] drop calorimetry [41]
Ca ₃ Si ₂ O ₇	kilch → rank	954-1090		[32]
CaSiO ₃	woll → p-woll	1125		[38]

3. Literature review for the liquid phase

The thermodynamic properties of the end-members CaO and SiO₂ were recently assessed by Deffrennes et al [6] and Bajenova et al [7] respectively with a 3rd generation CALPHAD model, thus a reassessment of these is not required and instead their expressions, which incorporate a two-state model for the liquid phase, are adopted here unmodified. The Phase Diagram for Ceramists [52] contains a complete study of the phase diagram of the CaO-SiO₂ system and lists the majority of the experimental liquidus points to be found for this system in the literature. Rankin and Wright [53] are the primary source and determined the melting points of C₂S and CS as well as the CS and C₃S₂ eutectic; However, corrections for the CaO side are required due to the dramatic change in the melting point of CaO in the recent reassessment [12]. Modelling of the immiscible region of the phase diagram was most recently investigated by Tehwey and Hess [54] with similar results from Greig [55]. It should also be noted that the activities of SiO₂ and CaO in the liquid phase of the C-S system has been extensively studied in the range of 1773-1873 K through a variety of different techniques [56-59].

4. Third generation modelling of thermodynamic properties

In assessing the C-S system, the first objective is to establish data for the end members, which is to say the solid and liquid forms of pure CaO and SiO₂. These oxides are stable as stoichiometric solids and have been recently remodelled [6,7] using the 3rd generation CALPHAD approach [11]. This equation was developed using combinations of Einstein terms with a small polynomial correction to allow modelling from absolute zero up to the melting point of the solid with a single function. Including absolute zero in the fit is vital, as it is the primary method of connecting to the third law of thermodynamics and thus establishing the entropy which cannot be directly measured. Using only one expression for all temperatures also ensures thermodynamic consistency, as piece-wise expressions have discontinuities in their derivatives which may lead to unphysical discontinuities in their thermodynamic and derived properties. The 3rd generation CALPHAD function has the following general form [11],

$$G_{\alpha,solid}(T) = H_{0,\alpha} + \sum_j C_{j,\alpha} T^j + 3 R \sum_{i=1}^{N_{E,\alpha}} D_{i,\alpha} \left[\frac{\theta_{E,i,\alpha}}{2} + T \ln(1 - e^{-\theta_{E,i,\alpha}/T}) \right], \quad (1)$$

where $G_{\alpha,solid}(T)$ is the Gibbs free-energy of the solid compound α , $H_{0,\alpha}$ is a constant setting the absolute enthalpy of the compound at 0K, R is the universal gas constant, and T is the temperature. There are $N_{E,\alpha}$ Einstein terms with the i th term having an Einstein temperature $\theta_{E,i,\alpha}$ and prefactor $D_{i,\alpha}$. These terms have some constraints; for example, the sum of the Einstein prefactors, $\sum_i^N D_{i,\alpha}$, should sum to the number of atoms in the chemical formula so that the Dulong-Petit law is approximately true (i.e., $\lim_{T \rightarrow \infty} C_v \approx 3NR$). The Einstein terms model lattice vibrations, thus the number of these terms should be correlated to the modes in the lattice; however, modern assessments such as that of CaO [6] tend to standardise around using three Einstein functions. The more realistic Debye model can be substituted for the Einstein model; however, it results in a non-analytic expression for the Gibbs free energy and therefore it is not a popular choice [60]. To add flexibility in fitting real data, polynomial correction terms are also added with prefactors $C_{j,\alpha}$ to approximate the anharmonic effects at high temperature. Initially, only two non-zero prefactor exponents $j = \{2, 3\}$ were recommended [11]; however, further modelling by Chen and Sundman [60] recommended using exponents $j = \{2, 5\}$ to fit a wider spectrum of phases. When modelling CaO, it was found that pure oxides typically exhibit an increase in heat capacity just before melting [6] therefore, it is better to use a pair of $j = \{2, 13\}$ terms or the triplet $j = \{2, 7, 8\}$. In this assessment, $j = \{2\}$ is found sufficient to describe the data for all compounds due to the limited experimental thermodynamic data close to the melting points. Our modelling of the C-S system is unique as it is the first to use these 3rd generation CALPHAD functions for multicomponent oxides and a reassessment of all data from the experimental results. This is outlined in the following section which discusses the fitting process.

5. Solid phases: Fitting methodology

Faced with a broad spectrum of experimental data with unknown confidence intervals, a holistic approach is taken here to optimize all model parameters simultaneously to all data in two separate rounds. First, the stoichiometric solid models are fit, then their associated coefficients

are fixed while the liquid model is fit. The liquid model fitting is carried out separately due to the relatively slow and complex calculations required, which include solving for multi-phase equilibrium. For the stoichiometric phases, a custom code has been written which takes as its input experimental data in its original reported units to minimize transcription errors. This is then transformed into standardized units and constraints to carry out a non-linear least-squares regression. All experimental conditions and observations/measurements have uncertainties attached to them, and these uncertainties are propagated through to the final uncertainty estimate for that measurement which is then used to scale its contribution to the error term.

To illustrate this, consider a single experimental observation/measurement enumerated by α for a thermodynamic property (e.g., a measured enthalpy of reaction, or heat capacity), $y_{obs,\alpha}$ with estimated measurement uncertainty $\sigma_{y,\alpha}$. This is observed at experimental conditions (i.e., temperature and pressure), $\vec{x}_{obs,\alpha}$, which may also have associated uncertainties $\vec{\sigma}_{x,\alpha}$. The corresponding value predicted by the model is given by $y(\vec{c}, \vec{x}_{obs,\alpha})$ where \vec{c} are the fit coefficients. The reduced error, e_α , is then given by the following expression,

$$e_\alpha(\vec{c}) = \sigma_\alpha^{-2} \left(y_{obs,\alpha} - y(\vec{c}, \vec{x}_{obs,\alpha}) \right)^2, \quad (2)$$

where the total uncertainty, σ_α , assuming no correlations between variables and Gaussian distributed noise, can be estimated using the standard expression for uncertainty propagation,

$$\sigma_\alpha = \sqrt{\sigma_{y,\alpha}^2 + \sum_i \sigma_{x_i,\alpha}^2 \left(\frac{\partial y}{\partial x_i} \right)^2}. \quad (3)$$

The uncertainty estimates on the observed value σ_y typically account for all sources of uncertainty in the experimental conditions, $\vec{\sigma}_x$; however, transition temperatures are entered as reactions with an “observed” Gibbs free energy change of zero as this is true at a transition. To capture the uncertainty of the measurement in terms of free energy, uncertainty is assigned to the transition temperature, which is much more natural and easily propagated to the free energy by this approach.

In general, the values of the uncertainties are the subject of much debate in thermodynamic modelling. Although they are absolute measures, the fitting process only considers their relative magnitude. To reduce human bias, the estimation of the uncertainties of each dataset is optimised deterministically. In the first instance the author’s stated uncertainties for the experimental measurement are entered. After an initial fit, the deviation between the model predictions and the experimental measurements are used to scale the uncertainty estimates. The error limits suggested by Haas et al[3] are employed, where the uncertainties are adjusted with the goal to keep 95% of the data within 2σ (standard deviations) of the final fit and no more than a 1/3 of data outside of 1σ , to prevent over and under weighting of datasets. This method is a deterministic way of estimating uncertainty where there is conflicting data; however, where there is no conflicting data, such as many of the transition temperatures in this assessment, the uncertainty estimates converge to zero. This is not a problem, simply an indication that there is only a single source for this thermodynamic information.

The automatic approach taken here to determine the uncertainties has been discussed in the literature [61]; however, there is no solid consensus on the best approach as of yet. The simple approach used here still requires that data which is clearly unphysical or seriously conflicting is excluded entirely as it can move the initial fit too far from the consensus fit, thus resulting in a lack

of convergence. But even with this limitation, the simple approach applied here is a powerful method that allows corroboration of results from separate authors and techniques. Figure 1 gives an example error plot of the heat capacity data for the C₂S polymorphs used within this assessment, error plots like this are produced for each compound in this system to compare and validate the uncertainties placed on the differing experimental results. A table of all the data alongside their initial and final uncertainties used in our fit to achieve acceptable results (reduced error ~1) can be seen in Table A.2.

To provide an initial estimate of the coefficients for the global optimisation, individual phases are added to the optimisation sequentially as determined by the required data dependencies before a global optimization is carried out. The underlying minimiser used is the COIN-OR IPOpt solver [62] and all derivatives required for the minimisation, uncertainty propagation, and thermodynamic functions are generated using a custom Computer Algebra System (CAS). This allows arbitrary thermodynamic functions to be fit with little work and facilitated early comparisons with Debye functions, as well as transformations into other thermodynamic calculation software.

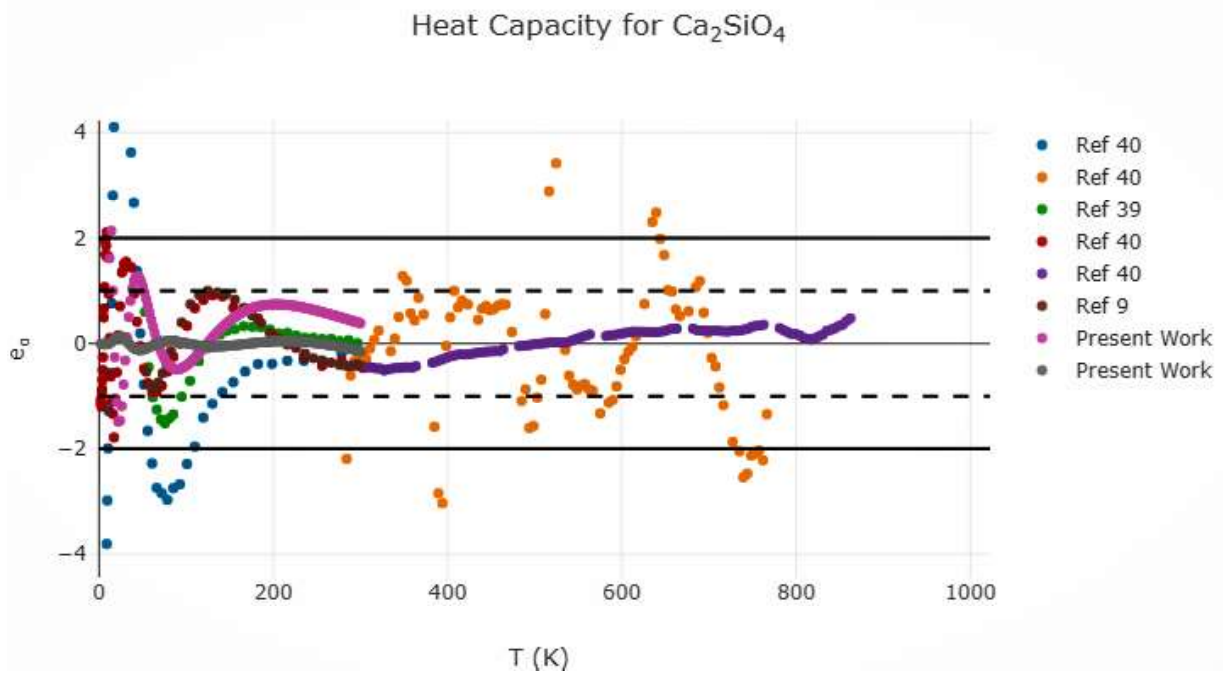


Figure 1: An example diagnostic plot displaying the error (see Eq. (2)) of all experimental heat capacity measurements [9,39,40] considered while fitting C₂S polymorphs. Outer horizontal lines indicate the 2σ deviation limit that should contain 95% of the data set, while the dashed horizontal lines indicate the 1σ deviation which should contain 2/3 of data outside of 1. These guidelines are held true by adjusting the error estimates reported here.

6. The model for the liquid phase

The model used here for the liquid phase approximates the melt as a mixture of neutral species, called the ``associates''. This model is popular in systems where the melt phase exhibits

short range order [63] which is the case in metal-oxygen system such as C-S. In addition to this, the associates model is readily implemented in popular thermodynamic software. The fictitious associates are formed from the liquid end-members but may be normalised in different ways; for example, in previous studies of the C-S system, authors have normalised associates to have 2 non-oxygen atoms per mole of species [16]; However, in this assessment a simple direct linear mixing of the end members with corrections for the enthalpy and entropy are used. This was chosen as it produced satisfactory results and it is similar to the normalisation found in MTDATA thermodynamic software package [64].

$$G_{C_xS_y} = x G_{CaO,liq} + y G_{SiO_2,liq} + \Delta H_{C_xS_y,0} - T \Delta S_{C_xS_y,0}, \quad (4)$$

where $\Delta H_{C_xS_y,0}$ and $T \Delta S_{C_xS_y,0}$ are constant enthalpy and entropy correction terms respectively for the intermediate associates and are zero for the pure end-member associates. The set of possible associates, and thus potential values of x and y in Eq. (4), is determined by considering the four-way bonding of silicon to other atoms via an oxygen species. A so-called bridging oxygen links two Si atoms, while non-bridging oxygens link Si to a metal atom. This leads to the idea of Q^n species, where n is the number of non-bridging oxygens atoms: $Q^4 = SiO_2$, $Q^3 = Si_2O_5^{2-}$, $Q^2 = SiO_3^{2-}$, $Q^1 = Si_2O_7^{6-}$, $Q^0 = SiO_4^{4-}$. The Q^2 and Q^0 species combined with the metal atom (Ca^{2+}) to form neutral species gives the C_2S and CS associates which are used here. These associates appear to be justified by experimental spectroscopic evidence for their stable existence in significant quantities in the melt [65,66]. The $Q^1=C_3S_2$ associate also appears but at less than 5% [65,66], thus it is not included here, and attempts to include it were rejected by the AIC approach discussed later. In addition, the congruent melting points at the C_2S and CS compositions are more easily captured by using associates, unlike the C_3S_2 composition which melts in a peritectic.

The overall expression for the free energy of the associate model for the melt phase is then given by the following expression,

$$g_{melt} = \sum_{\alpha} x_{\alpha} g_{\alpha} + R T \sum_{\alpha} x_{\alpha} \ln(x_{\alpha}) + \sum_{\alpha, \beta \neq \alpha} x_{\alpha} x_{\beta} (x_{\alpha} - x_{\beta})^k L_{\alpha, \beta, k}, \quad (5)$$

where x_{α} is the mole fraction of the associate, α . The final term of Eq. 5 is a Redlich-Kister (RK) correction for non-ideal melt interactions (excess Gibbs energy) between the associates and $L_{\alpha, \beta, k}$ is the coefficient for the k th-order correction term between associate α and β , where $k \geq 0$. The interaction terms may be composed of several corrections,

$$L_{\alpha, \beta, k} = h_{\alpha, \beta, k} + s_{\alpha, \beta, k} T + c_{p, \alpha, \beta, k} T \ln T, \quad (6)$$

where $h_{\alpha, \beta, k}$ is an enthalpy shift term, $s_{\alpha, \beta, k} T$ is an entropy shift term, and $c_{p, \alpha, \beta, k} T \ln T$ is a heat-capacity shift term. Generally, the absolute minimum number of non-zero RK terms are desired, as the melt phase stretches across all systems in higher-order assessments, thus the additional complexity brought on by higher-order RK terms can be disruptive when extending the assessment. Enthalpy terms are also preferable over entropy and heat capacity RK terms as they do not interfere with the zero-kelvin entropy which is included in all 3rd generation models, even in the liquid model here thanks to the two-state model of the liquid end-members and the use of Eq. (4) to define associates; however, this “rule” is often overlooked due to the large uncertainties in the extrapolation of the liquid models to very low temperatures anyway, thus the use of both enthalpy and entropy RK terms is very common. The choice of which RK interaction terms to include is discussed in the following section.

7. CaO-SiO₂ Liquidus Modelling

When faced with the task of modelling the liquid, there are an enormous number of choices that can be made. Even fixing on the associates model, the choice remains on which Q-species associates to include, in addition to the arbitrarily large number of possible RK terms between the associates. Here, the choice of associates is fixed as discussed in the previous chapter; however, our ongoing work in other systems includes automatic selection of associates so this is discussed here for generality. The choice of which RK terms and associates to include follows some basic rules. The minimum number of terms required to gain a good fit is preferable as it simplifies interpretation and extension. In addition, lower-order interaction terms, i.e., small k , are preferred over higher-order terms as they are less likely to induce spurious features. Finally, the values of the coefficients are also bounded by experience. For example, the term $s_{\alpha,\beta,k}$ directly affects the entropy of the phase at absolute zero, thus its use can introduce a thermodynamic inconsistency and odd behaviour at low temperatures. While liquid phases in our application are rarely extrapolated to very low temperatures this may happen numerically during the solution to equilibrium leading to spurious re-entrant liquid phases. In addition, the $s_{\alpha,\beta,k}$ term becomes more important in the free-energy at high temperatures, thus positive values may lead to fictitious miscibility gaps appearing. The C-S system has a real miscibility gap between CS and S (see Figure 8), so positive $L_{\alpha,\beta,k}$ terms are required between pairs of associates spanning this region (i.e., $L_{CS,S,k}$, $L_{C_2S,S,k}$, and/or $L_{C,S,k}$); however, care must be taken that this is the only location where they appear.

Even with this guidance, assessments typically proceed by trial and error, with researchers adding terms to address deficiencies in the calculated diagram after successive calculations. While experts can produce high quality diagrams this way in short order, it is not deterministic, and it is difficult to know if the optimal choice has been made. Furthermore, for higher-order fitting to ternary systems such as CaO-Al₂O₃-SiO₂ or CaO-MgO-SiO₂ the problem of term selection and optimisation becomes factorially harder.

Here a novel automated mathematical optimization approach is used to select the RK and associate terms in the liquid to find the best combination of terms. To prevent overfitting, the objective function that is optimised is the corrected Akaike information criteria [67],

$$AiCc = 2k - 2\ln(\mathcal{L}) + \frac{2k^2 + 2k}{n - k - 1}, \quad (7)$$

where AiCc the corrected Akaike information criteria, k is the number of parameters (in this case the number of $h_{\alpha,\beta,k}$ and $s_{\alpha,\beta,k}$ terms), n is the number of experimental data points, and \mathcal{L} is the maximum of the likelihood function when the $h_{\alpha,\beta,k}$ and $s_{\alpha,\beta,k}$ terms are optimised to fit the experimental data. The log likelihood is the sum of the error terms in Eq. (2). The corrected equation is used to avoid overfitting in cases where the number of samples is sparse. Using the AICc, the model with the lowest score is the model that fits the data the best when traded off against the complexity of the model. This approach is entirely inspired by ESPEI [68] where it is currently used for thermochemical data fitting (i.e. stoichiometric solids).

To find the globally optimal parameterisation according to Eq. (7) would require optimising all possible model variations and their coefficients against the experimental dataset to determine their likelihoods, before ranking them by Eq. (7). This is computationally infeasible at this time as it's a factorially hard problem and the optimisation in this system takes minutes per

parameterisation to complete; however, a model with a low number of terms is the likely solution thus exploring the full range of possible parameterisations is not required. A gradient-descent type of approach from an initial zero-parameter model seems to be a sensible approach. While it might not guarantee a globally optimal solution, it will at least provide a local optimum which may be sufficient for practical purposes. Proving this is beyond the scope of this paper and would require examination of the results across many thermodynamic assessments, so the results presented here will only be evaluated by comparing against previous parameterisations for this system later.

The method proceeds from an initial parameterisation (i.e., an ideal system) in a stage-by-stage manner. At each stage, all as-yet unused/zero interaction terms are individually enabled and optimised with the current set of enabled terms. All RK terms up to an order of $k = 3$ are tested as higher-order terms are avoided where possible. At the end of each stage, the interaction term that is enabled permanently is the term that decreases the AiCc parameter the most. These stages continue until enabling any additional parameter no longer decreases the AiCc. The optimisation of all interaction parameters against the experimental data is carried out using ESPEI. ESPEI uses a Bayesian approach that finds the maximum likelihood at each stage (more details on this technique can be found in [68]). Unfortunately, this approach currently struggles to optimise miscibility gaps when the initial guess does not capture the experimental data points well. Thus, for this assessment the optimisation for the C-S system is begun by including $h_{CS,S,0}$, $h_{CS,S,1}$, $h_{CS,S,2}$, $s_{CS,S,0}$, $s_{CS,S,1}$ and $s_{CS,S,2}$ with an initial hand-fit. Anecdotally, the automatic approach appears to function well in systems where there is no miscibility gap (such as the CaO-MgO system), and the issue appears to only be one of local/global convergence, thus we expect it to work with further improvements to ESPEI. From this initial point, the algorithm outlined here adds a $s_{C,C_2S,2}$ then adds a $s_{C_2S,S,0}$ term. At this point, any additional terms do not lower the AiCc score (the full parameter set can be seen in Table 8).

8. Experimental procedure

The data that is available for this system is discussed in Section 2. There are several key measurements which should be repeated, or missing data that must be ascertained to complete a thermodynamic assessment targeted at modelling cement clinker formulation. This section details the experimental methods and preparation used to obtain these measurements. The starting materials are CaCO_3 (Alpha Aesar, 99.5%) and SiO_2 (Sibelco, 99%) which are dried in a muffle furnace at 500°C in air for 24 hours. Rankinite ($\text{Ca}_3\text{Si}_2\text{O}_7$) is prepared from a dry powder mixture of CaCO_3 ($6.25 \pm 0.01\text{g}$) and SiO_2 ($2.50 \pm 0.01\text{g}$). The mixture is homogenized in a mechanical mixer for 24 hours and pelletized using a hydraulic workshop press (4.5 tons on 3g of powder). The first thermal treatment is carried out at $1000^\circ\text{C}/1\text{h}$ to calcine the limestone (CaCO_3) and is followed by a high temperature isothermal annealing step at 1380°C for 12 hours. The annealing process is repeated four times at $1420^\circ\text{C}/12\text{h}$ with intermediate grinding steps between each thermal treatment. The compositional analysis reveals a loss on ignition of 31.9444 %. For Ca_2SiO_4 , a powder mixture of CaCO_3 ($6.97 \pm 0.01\text{g}$) and SiO_2 ($2.09 \pm 0.01\text{g}$) is calcined at 1000°C for 1h and annealed at 1550°C for 8 hours followed by slow cooling to room temperature. A loss on ignition of 34.0844% is recorded. The mineralogical composition of the samples was carried out using X-ray diffraction (X'Pert Pro MPD, PANalytical), with $\text{CuK}\alpha$ radiation of $\lambda = 1.5419 \text{\AA}$.

A MHTC96 (Setaram) high temperature calorimeter with a drop measuring head (Type S, 1300°C max) was used for the heat content measurements. The measurements are carried out using an alumina crucible with a platinum inlay (diameter 13mm and height 46mm). The measurements were performed under flowing Ar atmosphere. The calorimeter is calibrated using pure alumina (Al_2O_3 , 99.95%) pieces which are dried and calcined at 1400°C for 12h. The pellets have a mass ranging from 15 to 150mg (uncertainty $\pm 0.02\text{mg}$). Three series of 6 or 7 alumina samples are dropped for each temperature at 600°C, 700°C, 800°C, 900°C, 1000°C, 1100°C, and 1200°C and the associated heat effect recorded and integrated using the Calypso software package (Setaram). The resulting calibration constant at a given temperature is calculated using heat content values for Al_2O_3 from the FTOxid database [5]. The measured heat flux area (in $\mu\text{V.s}$) for each sample is plotted as a function of heat content of Al_2O_3 . The calibration constant (in $\mu\text{V.s/J}$) was calculated by performing a linear regression passing through origin for each series at a given temperature. The uncertainty of the calibration constant corresponds to twice the standard variation of the slope. The temperature of introduction was measured with a thermocouple (uncertainty $\pm 0.1\text{K}$). The variation of the high temperature calorimeter is $\pm 0.4\text{K}$ and a return to the baseline is observed within 25min.

For the heat content measurement of $\text{Ca}_3\text{Si}_2\text{O}_7$ and Ca_2SiO_4 , pellets are produced with sample weights ranging from 15 to 80 mg (uncertainty $\pm 0.02\text{mg}$). Again, two series of 6/7 pellet are dropped at each temperature of calibration. The observed integrated heat effects (surface area of peak in $\mu\text{V.s}$) are plotted as a function of the phase amount introduced into the calorimeter. A linear regression forced passing through the origin is performed to determine the slope. The uncertainty of the measurement corresponds to twice the uncertainty on the slope (95% confidence interval). The measured heat content corresponds to the slope divided by the calibration constant. Again, the introduction temperature was measured by thermocouple ($\pm 0.1\text{K}$) and corrected to 298.15K using the low temperature heat capacity data from King [9] for $\text{Ca}_3\text{Si}_2\text{O}_7$ and Ca_2SiO_4 .

Additionally, the melting point of $\text{Ca}_3\text{Si}_2\text{O}_7$ was measured by differential scanning calorimetry in a Labsys™ Evo apparatus designed by SETARAM. Calibration of the DSC equipment was carried out using the melting point of pure NaCl (99.9% Alfa Aesar) as well as the α - β transition and the melting point of K_2SO_4 (99.5% Alfa Aesar) as reference samples with 5K and 10K heating and cooling rates.

9. DFT calculations

To supplement the experimental datasets, DFT calculations were also performed to generate additional theoretical data. This is important especially for high temperature phases like α' - C_2S , for which low temperature data does not exist (these low temperature data is important in the fitting of the 3rd generation function). The ground state properties of all experimentally stable calcium silicates were calculated using density functional theory (DFT) [69,70]. The Vienna ab-initio software package (VASP v. 5.4.4) was used for the theoretical ground state calculations [71,72]. The semi-local SCAN exchange functional [73] was used for the many-body exchange-correlation interaction. The GW PAW potentials (Ca_sv_gw, Si_gw and O_gw_new in VASP notation) were used for the calculations as they give the most accurate description of the lattice volume of SiO_2 in its a-quartz structure at low temperature. For Ca, the 3s, 3p and 4s

orbitals, for Si, the 3s and 3p orbitals and for O the 2s and 2p orbitals were considered as valence states in the calculations. The cut-off energy was set to 800 eV.

A gamma centred grid of k-points in the irreducible part of the Brillouin zone is automatically generated following the Monkhorst–Pack scheme [74]. The k-grids are 2x1x1 for Ca_3SiO_5 , 4x7x9 for $\gamma\text{-Ca}_2\text{SiO}_4$, 5x4x2 for $\beta\text{-Ca}_2\text{SiO}_4$, 1x2x4 for $\alpha'\text{-Ca}_2\text{SiO}_4$, 3x3x2 for $\text{Ca}_3\text{Si}_2\text{O}_7$, 3x3x3 for CaSiO_3 wollastonite and 2x3x2 for CaSiO_3 pseudo-wollastonite. The lattice parameters as well as the internal atomic coordinates of all investigated compounds are fully relaxed. The linear tetrahedron method with Blöchl corrections [75] is used to calculate the electronic density of states (DOS). The relaxations are performed with a convergence criterion of 10^{-8} eV/Å for the total energy.

Finite temperature properties such as the Helmholtz free energy F and heat capacities at constant volume/pressure C_V/C_P are approximated using lattice dynamics theory [76]. The phonon spectrum of selected compounds are determined using the frozen phonon (supercell) method. The vibrational modes are calculated using the phonopy code [77] coupled to VASP. The convergence criteria for the Hellman–Feynman forces is set to 10^{-8} eV/ Å to avoid residual strain in the lattice. To treat the long-range interaction of the macroscopic electrical field induced by polarization of collective motions near the Γ -point, the Born effective charges Z for the independent atoms in the primitive cell are calculated and used to calculate the non-analytical term corrections to the dynamical matrix.

10. Results and Discussion

The following sections discuss the results of the experiments, fitting, and overall phase diagram in comparison to the literature.

10.1. Calorimetric measurements

The results of the heat content measurements for Rankinite are summarised in Table 3. No experimental data exists in the literature on the heat capacity or heat content of Rankinite at these high temperatures, thus this data is compared to the estimated data of Haas et al [3] and the commercial FTPs database [5]. The estimated heat content together with the experimental values from 298.15K to 1471.65K are presented in

Figure 2. There is some agreement with the estimation of Haas but the calculated values using FTPs clearly overestimate the heat content compared with the experimental results.

The DSC results for C_3S_2 were only interpretable on heating due to the peritectic nature of its melting reaction. On cooling, the sample contained $\gamma\text{-Ca}_2\text{SiO}_4$ and CS which did not completely convert to C_3S_2 . However, the melting temperature obtained is 1737 ± 5 K, which is identical to the value reported by Levin [52].

Table 3 Rankinite ($\text{Ca}_3\text{Si}_2\text{O}_7$) heat content measurement. The uncertainty corresponds to a 95% confidence interval.

Heat Contents $\text{Ca}_3\text{Si}_2\text{O}_7$ (mol. wt. 288.42)				
T	T	$H_T - H_{298\text{K}}$	uncertainty	
°C	K	$\text{J mol}^{-1} \text{K}^{-1}$	$\text{J mol}^{-1} \text{K}^{-1}$	%
25	298.15	-	-	-
599.3	872.45	147433.0	3570.3	2.4
699.8	972.95	180036.6	4109.9	2.3
799.2	1072.35	206085.9	5517.3	2.7
899.0	1172.15	233439.6	6032.1	2.6
998.8	1271.95	264146.9	6983.6	2.6
1097.7	1370.85	293304.5	7690.3	2.6
1198.5	1471.65	322841.2	6913.1	2.2

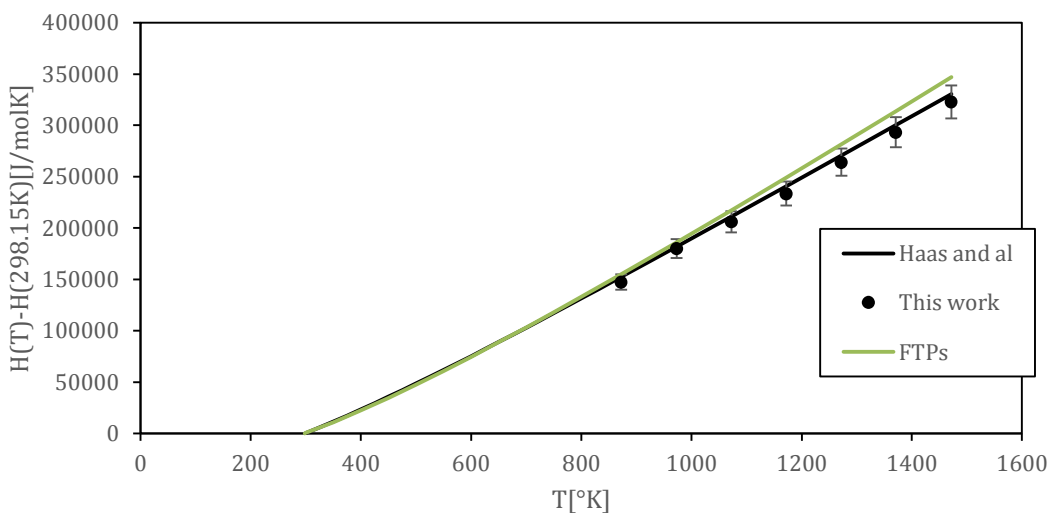


Figure 2 Rankinite ($\text{Ca}_3\text{Si}_2\text{O}_7$) heat content measurements compared to estimated values calculated using FTPs[5] and Haas and al[3]. Haas et al's data[3] arise from the Neumann-Kopp rule using heat capacity data for CaO and SiO_2 .

Table 4 (γ , α') Ca_2SiO_4 heat contents measurements from 972.86 to 1471.05K. Transition from γ to α' occurs at 1170 K.

Heat Contents (γ , α') - Ca_2SiO_4 (mol. wt. 172.24)				
T	T	$H_T - H_{298\text{K}}$	uncertainty	
°C	K	J mol^{-1}	J mol^{-1}	%
25	298.15	-	-	-
699.7	972.86	108430.8	3617.9	3.3
798.9	1072.09	123306.7	3251.5	2.6
898.2	1171.39	148801.8	3879.2	2.6
998.5	1271.67	171305.2	4185.5	2.4
1097.9	1371.05	187889.9	4479.1	2.4
1197.9	1471.05	212360.1	6444.6	3.0

The results of the heat content measurements for belite are summed up in Table 4. The heat content measurements of $\gamma \rightarrow \alpha'$ Ca_2SiO_4 have not been available previously. Coughlin & O'Brien [41] measured the β , α' - Ca_2SiO_4 heat contents by an inverted drop calorimetric technique. The temperature of transition $\gamma \rightarrow \alpha'$ is situated near 1120K. Therefore, in this present work the measured heat contents values include the γ - Ca_2SiO_4 to α' - Ca_2SiO_4 in the temperature range 972.86-1471.65K. The obtained results compared to calculated values using the FTPs database are plotted in Figure 3

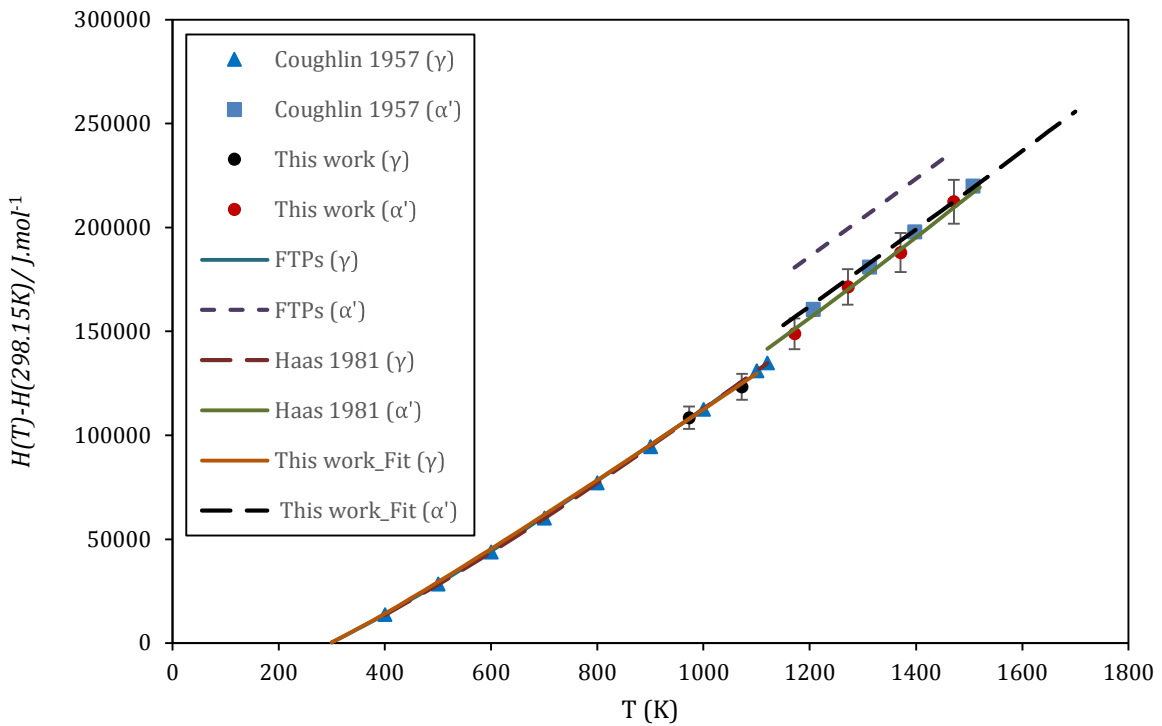


Figure 3 γ , α' - Ca_2SiO_4 Heat contents measurement. Lines were calculated using data from FactSage FTPs data [5] and Haas [3]: γ - Ca_2SiO_4 300K to 1072.0K, α' - Ca_2SiO_4 1171.39K to 1471.05K. Coughlin [44] values for α' - Ca_2SiO_4 have been corrected with enthalpy of transition $\gamma \rightarrow \beta$ from Forest [35] to have the same reference state.

Above 1072 K, γ - and α' - Ca_2SiO_4 measurements do not agree with calculated values using FTPs. For α' - Ca_2SiO_4 , our measured values are 24 to 32 kJ lower. However, there is good agreement with Haas' [3] data and Coughlin's [44] values. The measured values for γ - Ca_2SiO_4 in the temperature range 972-1072 K are in agreement with the calculated ones from FTPs [5] but also those of Haas [3] and Coughlin [44].

10.2. DFT calculations

The ground state energies of all considered compounds are summarised in Table 5 together with the calculated transition energies at 0K for the various Ca_2SiO_4 and CaSiO_3 modifications. All data are given in eV per formula unit. For Ca_3SiO_5 , only the monoclinic modification is calculated as it is the only modification with completely occupied lattice sites. For Ca_2SiO_4 , the γ , β and α' modifications are calculated. The high temperature α -modification has a more complicated crystal structure with partially occupied lattice sites and could therefore not be calculated with sufficient precision.

The calculated heat of formation at 0K are summed up in Table 6. The data for Ca_2SiO_4 have an additional contribution from the Zero Point energy calculations (-0.4 kJ/mol for γ - Ca_2SiO_4 and -2.5 kJ/mol for β - Ca_2SiO_4 and α' - Ca_2SiO_4).

Table 5 Calculated ground state energies at 0 K in eV per formula unit.

Compound	$E^\circ(0K)$ (eV mol ⁻¹)	$dE(0K)$ (eV mol ⁻¹)
CaO	-27.36219	Ground state
Alpha quartz-SiO ₂	-31.66647	Ground state
Monoclinic-Ca ₃ SiO ₅	-114.97448	Ground state
γ -Ca ₂ SiO ₄	-87.74651	Ground state
β -Ca ₂ SiO ₄	-87.65976	0.08675
α' -Ca ₂ SiO ₄	-87.63451	0.11200
Ca ₃ Si ₂ O ₇	-147.61658	Ground state
CaSiO ₃ -wollastonite	-59.91709	Ground state
CaSiO ₃ -cyclowollastonite	-59.83180	0.085

Table 6 Calculated heat of formation at 0 K in kJ/mol relative to the oxides CaO and α -SiO₂ (low quartz) and calculated heat of transitions for the different Ca₂SiO₄ and CaSiO₃ modifications.

Compound	$E_{\text{for}}(0K)$ (kJ mol ⁻¹)	$E_{\text{trans}}(0K)$ (kJ mol ⁻¹)
Monoclinic-Ca ₃ SiO ₅	-117.9	-
γ -Ca ₂ SiO ₄	-131.2	-
β -Ca ₂ SiO ₄	-124.8	6.2
α' -Ca ₂ SiO ₄	-122.4	8.8
Ca ₃ Si ₂ O ₇	-212.0	-
CaSiO ₃ -wollastonite	-85.7	-
CaSiO ₃ -cyclowollastonite	-77.5	8.2

10.3. Thermodynamic Modelling

The resultant coefficients for the solid phases in the C-S system are given in the Table A.1. Additionally, a TDB file for this system has also been provided and has been tested for use in Thermo-calc [78], Pandat [79] and ESPEI [68] (see supplementary material). A table showing the full set of experimental data along with their reported and calculated uncertainties is given in Table A.2. These fits allow for an evaluation of the new data for C₃S₂ and α' - and α -C₂S. A comparison of the H_{298} and S_{298} values between the new fit and the values of Haas et al [3] is given in Table 7. Most of the values are within the expected error of each other; however, disagreement exists for the H_{298} of rankinite-Ca₃Si₂O₇. This is expected and was previously reported by Hillert et al [13]. The H_{298} and S_{298} of α' -Ca₂SiO₄ also disagree with the Haas values, this is explained by the use of new data for both the enthalpy and heat capacity presented in this assessment. Figure 4 shows the calculated enthalpy of formation relative to the oxides for the compounds within this system (for which experimental data exists) and compares them against the experimental data. There is generally a good agreement between these values with the only discrepancy being the C₃S-triclinic phase ($x=0.25$). This is due to the incorporation of the value of Brunauer et al [45] which provides some conflict to the value of King [42]. They measured the enthalpy of formation of C₃S from the C+C₂S reaction.

Table 7 H_{298} and S_{298} of the compounds in the C-S system as calculated by the model presented here and compared to values from Haas et al [3].

Compound	$H_{298} \text{ (kJ mol}^{-1}\text{)}$		$S_{298} \text{ (J mol}^{-1} \text{ K}^{-1}\text{)}$	
	Calc.	Haas.	Calc.	Haas.
monoclinic- Ca_3SiO_5	-2932	-	166.4	-
triclinic- Ca_3SiO_5	-2933	-2933	166.5	168.6
rhombohedral- Ca_3SiO_5	-2932	-	166.4	-
rankinite- $\text{Ca}_3\text{Si}_2\text{O}_7$	-3951	-3973	207.6	210.6
wollastonite- CaSiO_3	-1634	-1634	79.6	81.0
cyclowollastonite- CaSiO_3	-1627	-1627	87.6	87.2
α - Ca_2SiO_4	-2293	-2548*	132.7	84.91*
α' - Ca_2SiO_4	-2304	-2198	130.4	116.0
β - Ca_2SiO_4	-2307	-2306	126.1	126.7
γ - Ca_2SiO_4	-2316	-2316	119.0	120.5

*This value is extrapolated beyond the temperature limits of the curve.

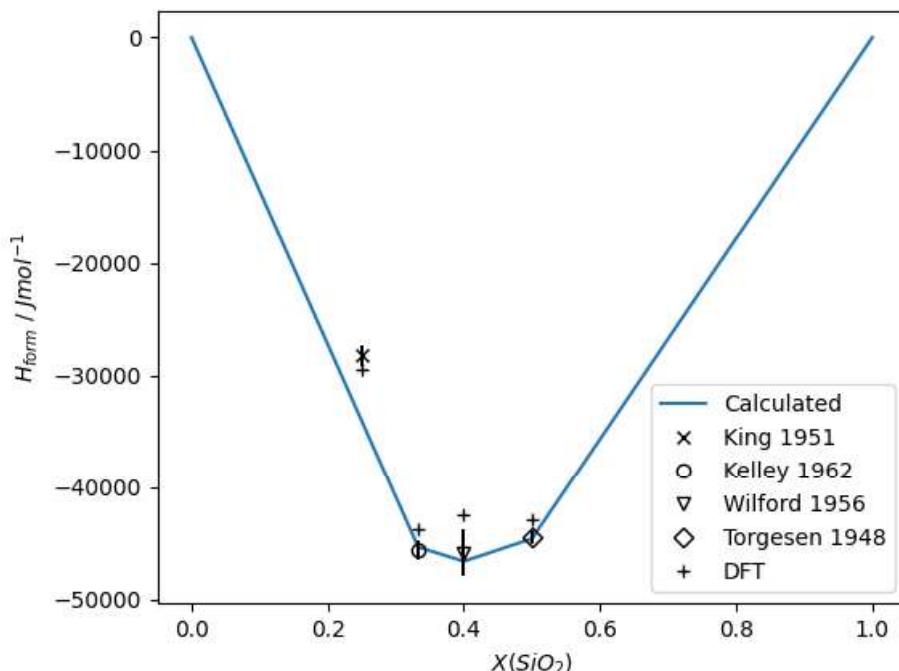


Figure 4 Graph of enthalpy of formations at 298 K of the stable phases at room temperature (C_3S is metastable at room temperature), relative to the single oxides compared against the experimental

data from Ref [42,43,46,80]. DFT data is the calculated enthalpy of formation at 0 K in the present work.

Table 8 Table showing the functions found for the melt phase used for the C-S phase diagram.

Thermodynamic Properties of the C-S melt phase	
G_{Liquid} (C, C₂S, CS, S):	
$G_C = G_{CaO,Liquid}$ [6]	
$G_S = G_{SiO_2,Liquid}$ [7]	
$G_{C_2S} = 2G_{CaO,Liquid} + G_{SiO_2,Liquid} - 183422.297315552 - 2.28483183782731 * T$	
$G_{CS} = G_{CaO,Liquid} + G_{SiO_2,Liquid} - 116624.5108961 + 3.86841542916429 * T$	
$L_{CS,S,0} = 251273.138042155 - 132.4131763105 * T$	
$L_{CS,S,1} = -76026.8593265931 + 22.9753135769968 * T$	
$L_{CS,S,2} = 117268.159674298 - 40.3850726577932 * T$	
$L_{C,C_2S,2} = 8.99637059634927 * T$	
$L_{C_2S,S,0} = 9.04086951648876 * T$	

The resulting optimised liquid phase model including the Gibbs energy terms of the associates is presented in Table 8 and the calculated phase diagram is shown in Figure 8. The calculated liquidus shows good agreement with the available experimental data. To facilitate precise reading of key points of the phase diagram a summary of the invariant points is given in Table 9. Whilst activity data was not fit in this assessment, the calculated model activities of SiO₂ and CaO alongside experimental comparisons can be seen in Figure 5 and 6 respectively. Although the activity data is not fit, the calculated values are within the experimental error for the activity data and in line with the values calculated by previous models of the CaO-SiO₂ system [12,15].

Direct comparisons of the model reported here can be made with the assessment conducted by Besmann and Spear [16] who also made use of an associates model for the C-S system. They used an additional C₃S associate, which is unfavourable as it is not evidenced to exist via spectroscopic measurements [65,66]. Furthermore, adding an associate adds additional complexity from the resulting corrections as well possible complications in the higher order system which is why it was avoided in this assessment. Our agreement with the experimental data demonstrates this associate is not needed from a pure fitting perspective. Not enough information is given to compare the parameterisation further; however, we estimate they use a total of 10 parameters to capture the liquid by assuming they used an enthalpy and entropy correction for each associate and this can be compared to our 12-parameter fit. Our assessment uses two more parameters to capture the miscibility gap, thus our automatic selection process arrived at the same level of parameterisation which is a great success considering the difficulty in selecting and optimising parameters given 60 potential parameters were available for insertion. Hillert et al carried out two assessments for the CaO-SiO₂ system using two variations on an ionic two-

sublattice model [12,13], which due to the species they chose to represent the melt phase is a comparable model to our associates model (i.e. (Ca^{2+}), (SiO_4^{4-} , SiO_3^{2-} , O^{2-} , SiO_2)). In one model they included SiO_3^{2-} while in the other it was removed. Their models use 6 interactions terms between their sublattice species and SiO_2 to capture the liquid; However, they use a clever trick to lower the parameterisation level by repeating coefficients to neutralise a drawback of the immiscibility gap model outside of the region of the gap. Our optimiser does not attempt these variations as they are highly customised for the system, but an equivalent model in our standardised description would have 12 parameters, thus they are comparable in complexity; however, our approach also shows not all the species require interaction parameters between them to fit the phase diagram and avoids the use of higher-order ideal interactions (i.e., $k = 3$ RK terms) used by Hillert et al [12,13]. These are both advantageous when extending to higher order systems or higher temperatures so this might be viewed again as a successful automatic fit.

The liquid model can also be compared against the spectroscopic data of Mysen et al [66]. Point equilibrium calculations to obtain the abundance of the associate species in our melt phase and the results are as follows: At the $x(\text{SiO}_2) = 0.5$ composition, Mysen et al measure ~80% abundance of SiO_3^{2-} species whilst we calculated an abundance of 60%. Furthermore, at $x(\text{SiO}_2) = 0.5$, a 15% abundance of SiO_4^{4-} species is reported, compared to the calculated value of ~19% (see Figure 7). These values are in reasonable agreement given the uncertainties involved and the high experimentally measured abundances of those species in the C-S melt justifies the use of both the CS associate and C_2S associate. Furthermore, the low abundance of CS species calculated at $x(\text{SiO}_2) = 0.5$ compared to the experimental data is most likely due to the interaction terms between CS and S associates required to fit the miscibility gap which was also described by Hillert et al [12].

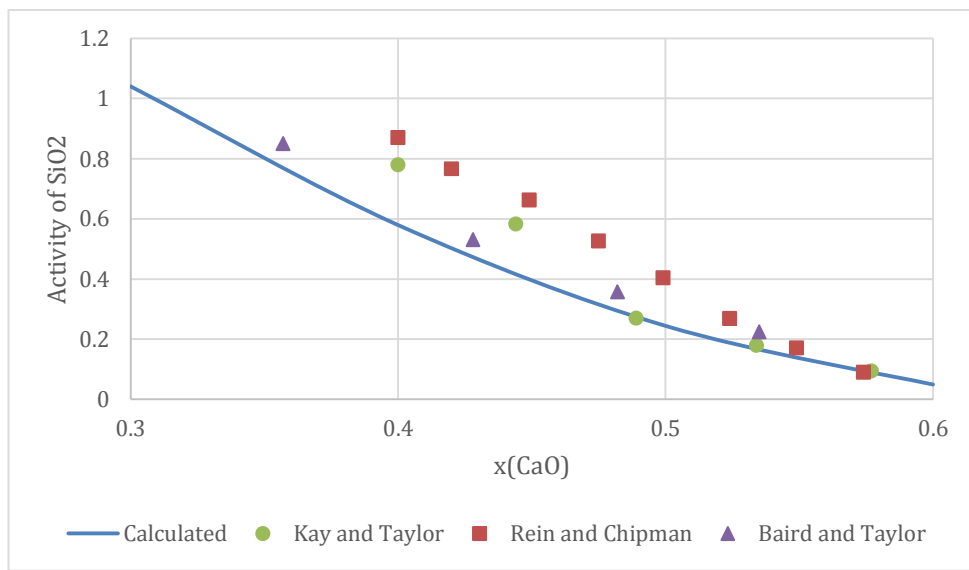


Figure 5 Activity of SiO_2 (at 1823K, reference: cristobalite) calculated from the model compared with experimental data [56,58,59].

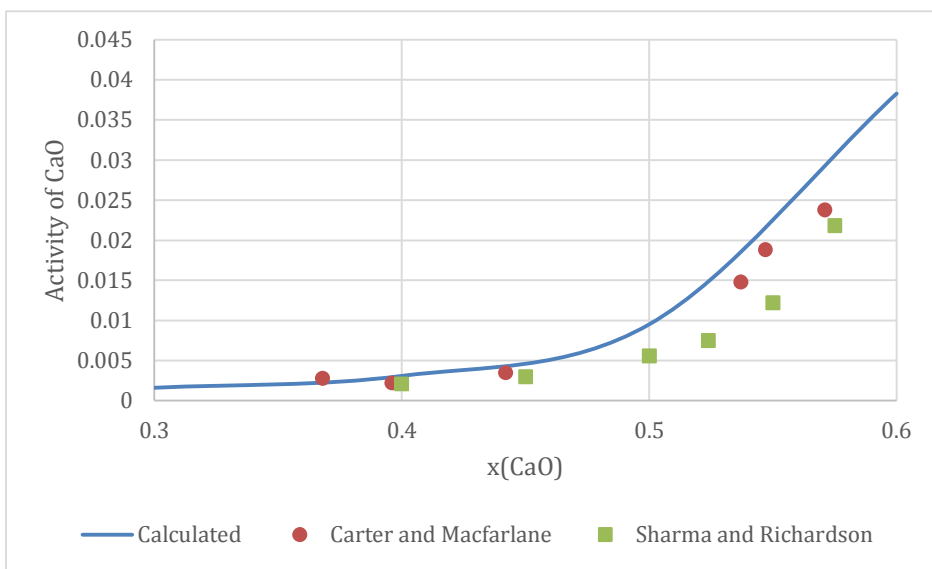


Figure 6 Activity of CaO (1773 K, reference: solid CaO) calculated from the model compared with experimental data [57,81].

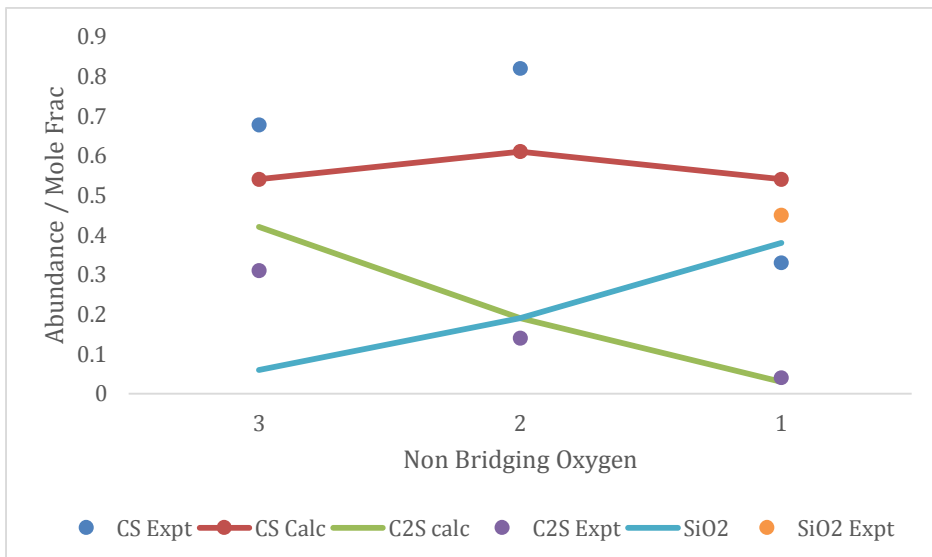


Figure 7 Abundance (Mole Frac) of C₂S and CS species in the melt compared against spectroscopic data from Mysen et al [66].

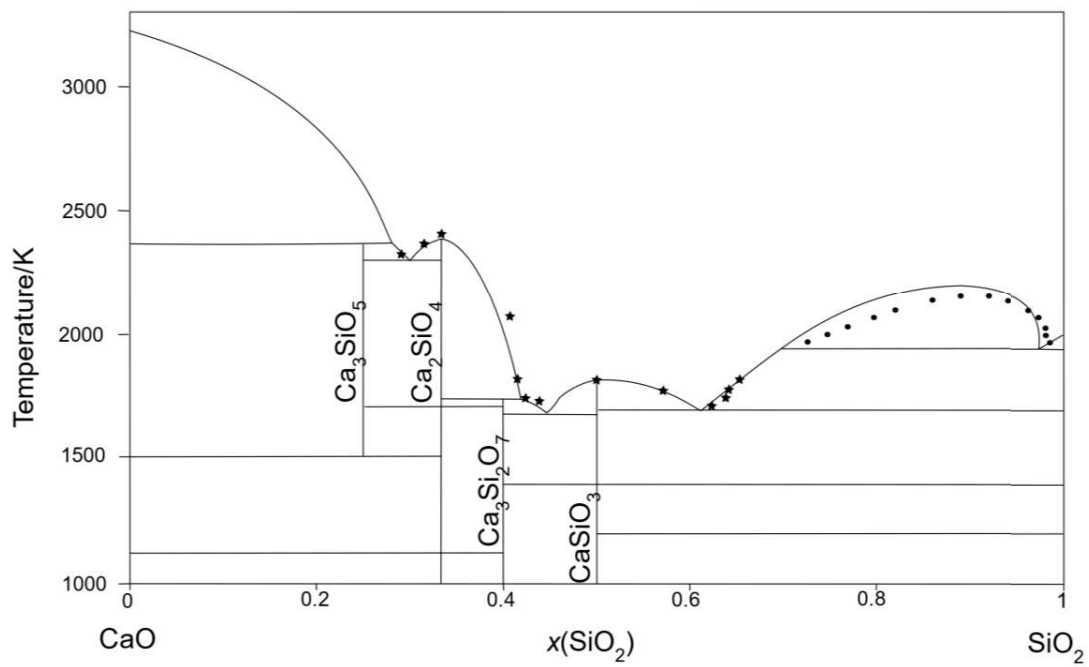


Figure 8 CaO-SiO₂ phase diagram calculated in this assessment plotted with experimental points obtained from Ref. [52,54].

Table 9 Summary of transitions and invariant reactions in the C-S system from the calculated phase diagram compared to experimental data in parentheses. The composition values correspond to the liquid phase.

Transition	T (K)	$H_{\text{transition}}$ (kJ mol ⁻¹)
$\gamma\text{-Ca}_2\text{SiO}_4 \rightarrow \alpha'\text{-Ca}_2\text{SiO}_4$	1120 (1120) [82]	14.3 (14.3) [41]
$\beta\text{-Ca}_2\text{SiO}_4 \rightarrow \alpha'\text{-Ca}_2\text{SiO}_4$	970 (970) [82]	2.17 (1.84) [41]
$\alpha'\text{-Ca}_2\text{SiO}_4 \rightarrow \alpha\text{-Ca}_2\text{SiO}_4$	1710 (1710) [82]	16.2 (14.1) [41]
wollastonite \rightarrow cyclo-CaSiO ₃	1397 (1398) [38]	8.68 (5.85) [51]
triclinic \rightarrow monoclinic-Ca ₃ SiO ₅	1254 (1253) [8]	0.477 (0.477)
monoclinic \rightarrow rhombohedral-Ca ₃ SiO ₅	1317 (1323) [8]	0.047 (0.047)
Invariant	T (K)	X(SiO ₂) in Liquid
Liquid + CaO \rightarrow Ca ₃ SiO ₅	2423 (2423) [52]	0.27 (0.27)
Liquid \rightarrow Ca ₃ SiO ₅ + $\alpha\text{-Ca}_2\text{SiO}_4$	2305 (2323) [52]	0.30 (0.29)
Liquid + $\alpha\text{-Ca}_2\text{SiO}_4 \rightarrow \text{Ca}_3\text{Si}_2\text{O}_7$	1746 (1737) [52]	0.41 (0.43)
Liquid \rightarrow Ca ₃ Si ₂ O ₇ + CaSiO ₃	1739 (1733) [52]	0.43 (0.44)
Liquid \rightarrow SiO ₂ + CaSiO ₃	1709 (1709) [52]	0.62 (0.61)
Compound	T _{melting} (K)	H_{fusion} (kJ mol ⁻¹)
$\alpha\text{-Ca}_2\text{SiO}_4$	2390 (2403) [53]	62.1 (61.0)[83]
cyclo-CaSiO ₃	1822 (1817)	61.3 (57.3) [84]

11. Conclusion

The CaO-SiO₂ is the most important system for Portland cement clinkers but modelling this system is challenging due to the miscibility gap, the large number of phases, and the polymorphs requiring revaluation, as well as the diversity of thermodynamic data. Novel results for the relative enthalpy of rankinite Ca₃Si₂O₇ at high temperatures, the relative enthalpy of $\gamma\text{-Ca}_2\text{SiO}_4$ including the transition to the α' modifications, and phonon calculations to determine the low temperature heat capacity of α' Ca₂SiO₄ are presented here. This has led to a full re-evaluation of the solid compounds in this system, as well as the inclusion of updates to the CaO and SiO₂ end-members [6,7] and the inclusion of the Ca₃SiO₅ polymorphs within the model, an important feature when extending the system. The produced model appears to accurately reproduce all known experimental data, including all solid and liquid phases. Further work will focus on extending this assessment to carry out equilibrium calculations like those done by Hanein et al [4,85] for Portland cement clinkers. The key improvement being the inclusion of precipitation of phases from the melt which is a key dynamic in that application.

A modern fitting approach has been developed and tested in this paper with the use of the 3rd generation CALPHAD functions and the associate's model. The use of information criterion to

select parameters appears to have been successful, although this is only a preliminary result in the development of these techniques. The resulting model has equal complexity in terms of parameter count to existing fits in the literature, while having fewer higher order terms and better agreement. Further assessments to complete the cement clinker system will provide ample opportunity for further testing this approach. These techniques will allow extensions with relative ease and work is already underway to complete the CaO-Al₂O₃-SiO₂-Fe₂O₃ which is a system that contains all of the major clinker phases found in Portland cement, with the iron-oxide being a key component in correctly capturing the bulk melting point. Completion of this modelling will allow us to carry prediction calculations for the composition of the clinker, which is the ultimate goal of our work.

Acknowledgements

The authors would like to acknowledge Dr Frank Bellmann for their correspondence regarding the experimental data.

Funding: This work was supported by Nanocem as part of the CP17 project.

References

- [1] J. Lehne, F. Preston, Chatham House Report Making Concrete Change Innovation in Low-carbon Cement and Concrete, The Royal Institute of International Affairs, 2018. <https://doi.org/10.1088/1742-6596/1015/3/032163>.
- [2] V. Meyer, N. de Cristofaro, J. Bryant, S. Sahu, Solidia cement an example of carbon capture and utilization, in: Key Eng. Mater., Trans Tech Publ, 2018: pp. 197–203.
- [3] J.L. Haas Jr., G.R. Robinson Jr., B.S. Hemingway, Thermodynamic tabulations for selected phases in the system CaO-Al₂O₃- SiO₂-H₂ at 101.325 kPa (1 atm) between 273.15 and 1800 K, J. Phys. Chem. Ref. Data. 10 (1981) 575–670. <https://doi.org/10.1063/1.555645>.
- [4] T. Hanein, F.P. Glasser, M.N. Bannerman, Thermodynamic data for cement clinkering, Cem. Concr. Res. 132 (2020) 106043. <https://doi.org/https://doi.org/10.1016/j.cemconres.2020.106043>.
- [5] C.W. Bale, E. Béolis, P. Chartrand, S.A. Dectorov, G. Eriksson, A.E. Gheribi, K. Hack, I.H. Jung, Y.B. Kang, J. Melançon, A.D. Pelton, S. Petersen, C. Robelin, J. Sangster, P. Spencer, M.A. Van Ende, FactSage thermochemical software and databases, 2010–2016, Calphad Comput. Coupling Phase Diagrams Thermochem. 54 (2016) 35–53. <https://doi.org/10.1016/j.calphad.2016.05.002>.
- [6] G. Deffrennes, N. Jakse, C.M.S.S. Alvares, I. Nuta, A. Pasturel, A. Khvan, A. Pisch, Thermodynamic modelling of the Ca–O system including 3rd generation description of CaO and CaO₂, Calphad Comput. Coupling Phase Diagrams Thermochem. 69 (2020) 101764. <https://doi.org/10.1016/j.calphad.2020.101764>.
- [7] I. Bajenova, A. Khvan, A. Dinsdale, A. Kondratiev, Implementation of the extended Einstein and two-state liquid models for thermodynamic description of pure SiO₂ at 1 atm, Calphad. 68 (2020) 101716. <https://doi.org/https://doi.org/10.1016/j.calphad.2019.101716>.
- [8] M. Bigaré, A. Guinier, C. Mazières, M. Regourd, N. Yannaquis, W. Eysbl, T.. Hahn, E. Woermann, Polymorphism of Tricalcium Silicate and Its Solid Solutions, J. Am. Ceram.

- Soc. 50 (1967) 609–619. [https://doi.org/https://doi.org/10.1111/j.1151-2916.1967.tb15009.x](https://doi.org/10.1111/j.1151-2916.1967.tb15009.x).
- [9] E.G. King, Low Temperature Heat Capacities and Entropies at 298.15°K. of Some Crystalline Silicates Containing Calcium, *J. Am. Chem. Soc.* 79 (1957) 5437–5438. <https://doi.org/10.1021/ja01577a028>.
- [10] M.W. Chase Jr., NIST-JANAF Thermochemical Tables, Fourth Edition, *J. Phys. Chem. Ref. Data. Monograph* (1998) 1–1951. <https://doi.org/10.18434/T42S31>.
- [11] M.W. Chase, I. Ansara, A. Dinsdale, G. Eriksson, G. Grimvall, L. Hoglund, H. Yokokawa, Group 1: Heat capacity models for crystalline phases from 0 K to 6000 K, *Calphad Comput. Coupling Phase Diagrams Thermochem.* 19 (1995) 437–447.
- [12] M. Hillert, B. Sundman, X. Wang, An assessment of the CaO-SiO₂ system, *Metall. Trans. B.* 21 (1990) 303–312. <https://doi.org/10.1007/BF02664198>.
- [13] M. Hillert, B. Sundman, X. Wang, T. Barry, A reevaluation op the rankinite phase in the CaO-SiO₂ system, *Calphad.* 15 (1991) 53–58. [https://doi.org/10.1016/0364-5916\(91\)90025-F](https://doi.org/10.1016/0364-5916(91)90025-F).
- [14] A.D. Pelton, M. Blander, Thermodynamic analysis of ordered liquid solutions by a modified quasichemical approach-Application to silicate slags, *Metall. Trans. B.* 17 (1986) 805–815. <https://doi.org/10.1007/BF02657144>.
- [15] G. Eriksson, P. Wu, M. Blandert, A.D. Pelton, Critical evaluation and optimization of the thermodynamic properties and phase diagrams of the MnO-SiO₂ and CaO-SiO₂ systems, *Can. Metall. Q.* 33 (1994) 13–21. <https://doi.org/10.1179/cmq.1994.33.1.13>.
- [16] T.M. Besmann, K.E. Spear, Thermochemical Modeling of Oxide Glasses, *J. Am. Ceram. Soc.* 85 (2002) 2887–2894. <https://doi.org/10.1111/j.1151-2916.2002.tb00552.x>.
- [17] T.I. Barry, A.T. Dinsdale, J.A. Gisby, Predictive thermochemistry and phase equilibria of slags, *Jom.* 45 (1993) 32–38. <https://doi.org/10.1007/BF03223284>.
- [18] J.R. Taylor, A.T. Dinsdale, Thermodynamic and phase diagram data for the CaO-SiO₂ system, *Calphad.* 14 (1990) 71–88. [https://doi.org/10.1016/0364-5916\(90\)90041-W](https://doi.org/10.1016/0364-5916(90)90041-W).
- [19] M.N. De Noirlfontaine, S. Tusseau-Nenez, C. Girod-Labianca, V. Pontikis, CALPHAD formalism for Portland clinker: Thermodynamic models and databases, *J. Mater. Sci.* 47 (2012) 1471–1479. <https://doi.org/10.1007/s10853-011-5932-7>.
- [20] M. Regourd, Polymorphism Of Tricalcium Silicate - New X-Ray-Diffraction Data, *Comptes Rendus Hebd. Des Seances L Acad. Des Sci. Ser. B.* 289 (1979) 17–20.
- [21] F. Dunstetter, M.N. De Noirlfontaine, M. Courtial, Polymorphism of tricalcium silicate, the major compound of Portland cement clinker: 1. Structural data: Review and unified analysis, *Cem. Concr. Res.* 36 (2006) 39–53. <https://doi.org/10.1016/J.CEMCONRES.2004.12.003>.
- [22] J.W. Jeffery, The Crystal Structure Of Tricalcium Silicate, *Acta Crystallogr.* 5 (1952) 26. <https://doi.org/10.1107/S0365110X52000083>.
- [23] F. Nishi, Y. Takéuchi, The rhombohedral structure of tricalcium silicate at 1200 C, *Zeitschrift Für Krist. Mater.* 168 (1984) 197–212.
- [24] N.I. Golovastikov, R.G. Matveeva, N.V. Belov, Crystal structure of tricalcium silicate, 3CaOSiO₂ = C3S, *Sov. Phys. Crystallogr.* 20 (1975) 441–445.
- [25] W.G. Mumme, Crystal-Structure Of Tricalcium Silicate From A Portland-Cement Clinker And Its Application To Quantitative Xrd Analysis, *Neues Jahrb. Fur Mineral.* (1995) 145–160.
- [26] F. Nishi, Y. Takéuchi, I. Maki, Tricalcium silicate Ca₃O [SiO₄]: the monoclinic superstructure, *Zeitschrift Für Krist. Mater.* 172 (1985) 297–314.
- [27] Á.G. De La Torre, S. Bruque, J. Campo, M.A.G. Aranda, The superstructure of C3S from synchrotron and neutron powder diffraction and its role in quantitative phase analyses, *Cem. Concr. Res.* 32 (2002) 1347–1356.
- [28] A. Guinier, M. Regourd, Structure of Portland Cement Minerals, in: 5th Int. Congr. Chem.

- Cem. Part 1, 1968: pp. 1–43.
- [29] W.G. Mumme, L. Cranswick, B. Chakoumakos, Rietveld crystal structure refinement from high temperature neutron powder diffraction data for the polymorphs of dicalcium silicate, *Neues Jahrb. Fuer Mineral. Abhandlungen*. 170 (1996) 171–188.
- [30] J. Forest, Knowledge Of Dicalcium Silicate, *Bull. La Soc. Fr. Mineral. Cristallogr.* 94 (1971) 118.
- [31] W. Lerch, Approximate glass content of commercial Portland cement clinker, *J. Res. Nat. Bur. Stand.* 20 (1938) 77–81. <https://doi.org/10.6028/jres.020.045>.
- [32] F. Hanic, J. Kamarad, J. Stracelsky, I. Kapralik, The P-T Diagram of Ca₂SiO₄, *Br. Ceram. Trans. J.* 86 (1987) 194–198.
- [33] S. Saburi, I. Kusachi, C. Henmi, A. Kawahara, K. Henmi, I. Kawada, Refinement of the structure of rankinite., *Mineral. J.* 8 (1976) 240–246. <https://doi.org/10.2465/minerj.8.240>.
- [34] S.O. Agrell, P. Gay, Kilchoanite, a polymorph of rankinite, *Nature*. 189 (1961) 743.
- [35] K.F. Hesse, Refinement of the crystal structure of wollastonite-2M (parawollastonite), *Zeitschrift Fur Krist. - New Cryst. Struct.* 168 (1984). <https://doi.org/10.1524/zkri.1984.168.1-4.93>.
- [36] H. Yang, C.T. Prewitt, Crystal structure and compressibility of a two-layer polytype of pseudowollastonite (CaSiO₃), *Am. Mineral.* 84 (1999). <https://doi.org/10.2138/am-1999-11-1217>.
- [37] T. Yamanaka, H. Mori, The structure and polytypes of α-CaSiO₃ (pseudowollastonite) , *Acta Crystallogr. Sect. B Struct. Crystallogr. Cryst. Chem.* 37 (1981). <https://doi.org/10.1107/s0567740881004962>.
- [38] Y.K. Voronko, A.A. Sobol, S.N. Ushakov, J. Guochang, Y. Jinglin, Phase Transformations and Melt Structure of Calcium Metasilicate, *Inorg. Mater.* 38 (2002).
- [39] S.S. Todd, Low-temperature Heat Capacities and Entropies at 298.16°K. of Crystalline Calcium Orthosilicate, Zinc Orthosilicate and Tricalcium Silicate, *J. Am. Chem. Soc.* 73 (1951) 3277–3278. <https://doi.org/10.1021/ja01151a084>.
- [40] K.D. Grevel, F. Bellmann, J. Majzlan, E. Dachs, A. Benisek, H.M. Ludwig, Thermodynamic data of belite polymorphs, *Cem. Concr. Res.* 152 (2022) 106621. <https://doi.org/10.1016/J.CEMCONRES.2021.106621>.
- [41] J.P. Coughlin, C.J. O'Brien, High Temperature Heat Contents of Calcium Orthosilicate, *J. Phys. Chem.* 61 (1957) 767–769. <https://doi.org/10.1021/j150552a016>.
- [42] E.G. King, Heats of Formation of Crystalline Calcium Orthosilicate, Tricalcium Silicate and Zinc Orthosilicate1, *J. Am. Chem. Soc.* 73 (1951) 656–658. <https://doi.org/10.1021/ja01146a046>.
- [43] K.K. Kelley, Heats and free energies of formation of anhydrous silicates, *U.S Dept. Inter. Mines.* (1962).
- [44] H.E. von Gronow, H.E. Schwiete, Die spezifischen Wärmen von CaO, Al₂O₃, CaO.Al₂O₃, 3CaO.Al₂O₃, 2CaO.SiO₂, 3CaO.SiO₂, 2CaO.Al₂O₃.SiO₂ von 20° bis 1500° C, *Zeitschrift Für Anorg. Und Allg. Chemie.* 216 (1933) 185–195. <https://doi.org/https://doi.org/10.1002/zaac.19332160212>.
- [45] S. Brunauer, D.L. Kantro, C.H. Weise, The heat of decomposition of tricalcium silicate into β-dicalcium silicate and calcium oxide, *J. Phys. Chem.* 60 (1956) 771–774. <https://doi.org/10.1021/j150540a015>.
- [46] W.F. Weeks, Heats of Formation of Metamorphic Minerals in the System CaO-MgO-SiO₂-H₂O and Their Petrological Significance, *J. Geol.* 64 (1956) 456–472. <http://www.jstor.org/stable/30057040>.
- [47] R. Benz, C. Wagner, Thermodynamics of the solid system CaO-SiO₂ from electromotive force data, *J. Phys. Chem.* 65 (1961) 1308–1311. <https://doi.org/10.1021/j100826a007>.
- [48] H. Wagner, Zur Thermochemie der Metasilikate des Calciums und Magnesiums und des Diopsids, *Zeitschrift Für Anorg. Und Allg. Chemie.* 208 (1932) 1–22.

- <https://doi.org/https://doi.org/10.1002/zaac.19322080102>.
- [49] P. Courtial, C. Tequi, P. Richet, Thermodynamics of diopside, anorthite, pseudowollastonite, CaMgGeO₄ olivine and akermanite up to near the melting point, *Phys. Chem. Miner.* 27 (2000) 242–250.
<https://doi.org/https://doi.org/10.1007/s002690050253>.
- [50] P. Richet, G. Fiquet, High-temperature heat capacity and premelting of minerals in the system MgO-CaO-Al₂O₃-SiO₂, *J. Geophys. Res. Solid Earth.* 96 (1991) 445–456.
<https://doi.org/https://doi.org/10.1029/90JB02172>.
- [51] T. V Charlu, R.C. Newton, O.J. Kleppa, Enthalpy of formation of some lime silicates by high-temperature solution calorimetry, with discussion of high pressure phase equilibria, *Geochim. Cosmochim. Acta.* 42 (1978) 367–375.
[https://doi.org/https://doi.org/10.1016/0016-7037\(78\)90267-3](https://doi.org/https://doi.org/10.1016/0016-7037(78)90267-3).
- [52] E.M. Levin, C.R. Robbins, H.F. McMurdie, A.C. Society., *Phase diagrams for ceramists*, American Ceramic Society, Columbus, Ohio, 1964.
- [53] G.A. Rankin, The Ternary System CaO-Al₂O₃-SiO₂, *Am. J. Sci.* XXXIX (1915) 1–79.
- [54] T. JD, H. PC, The Two Phase Region in the CaO-SiO₂ System: Experimental data and Thermodynamic analysis, *Phys. Chem. Glas.* 20 (1979) 41–52.
- [55] J.W. Greig, Immiscibility in silicate melts, *Am. J. Sci.* 13 (1927) 1–44.
- [56] R.H. Rein, J. Chipman, Activities in the liquid solution SiO₂-CaO-MgO-Al₂O₃ at 1600 C, *Trans. Met. Soc. AIME.* 233 (1965) 415–425.
- [57] R.A. Sharma, F.D. Richardson, Solubility of Calcium Sulphide and Activities in Lime-Silica Melts, *J. Iron Steel Inst.* 200 (1962) 373-.
- [58] J.D. Baird, J. Taylor, Reaction between silica and carbon and the activity of silica in slag solution, *Trans. Faraday Soc.* 54 (1958) 526–539.
- [59] D.A.R. Kay, J. Taylor, Activities of silica in the lime+ alumina+ silica system, *Trans. Faraday Soc.* 56 (1960) 1372–1386.
- [60] Q. Chen, B. Sundman, Modeling of thermodynamic properties for Bcc, Fcc, liquid, and amorphous iron, *J. Phase Equilibria.* 22 (2001) 631–644.
<https://doi.org/10.1361/105497101770332442>.
- [61] S. Zomorodpoosh, B. Bocklund, A. Obaied, R. Otis, Z.-K. Liu, I. Roslyakova, Statistical approach for automated weighting of datasets: Application to heat capacity data, *Calphad.* 71 (2020) 101994.
<https://doi.org/https://doi.org/10.1016/j.calphad.2020.101994>.
- [62] A. Wächter, L.T. Biegler, On the implementation of an interior-point filter line-search algorithm for large-scale nonlinear programming, *Math. Program.* 106 (2006) 25–57.
<https://doi.org/10.1007/s10107-004-0559-y>.
- [63] R. Schmid, Y.A. Chang, A thermodynamic study on an associated solution model for liquid alloys, *Calphad.* 9 (1985) 363–382. [https://doi.org/https://doi.org/10.1016/0364-5916\(85\)90004-5](https://doi.org/https://doi.org/10.1016/0364-5916(85)90004-5).
- [64] J. Gisby, P. Taskinen, J. Pihlasalo, Z. Li, M. Tyrer, J. Pearce, K. Avarmaa, P. Björklund, H. Davies, M. Korpi, S. Martin, L. Pesonen, J. Robinson, MTDATA and the Prediction of Phase Equilibria in Oxide Systems: 30 Years of Industrial Collaboration, *Metall. Mater. Trans. B Process Metall. Mater. Process. Sci.* 48 (2017) 91–98.
<https://doi.org/10.1007/s11663-016-0811-x>.
- [65] J.D. Frantza, B.O. Mysen, Raman spectra and structure of BaO□SiO₂ SrO□SiO₂ and CaO□SiO₂ melts to 1600°C, *Chem. Geol.* 121 (1995) 155–176.
[https://doi.org/10.1016/0009-2541\(94\)00127-T](https://doi.org/10.1016/0009-2541(94)00127-T).
- [66] B.O. Mysen, D. Virgo, F.A. Seifert, The structure of silicate melts: Implications for chemical and physical properties of natural magma, *Rev. Geophys.* 20 (1982) 353–383.
<https://doi.org/https://doi.org/10.1029/RG020i003p00353>.
- [67] J.E. Cavanaugh, Unifying the derivations for the Akaike and corrected Akaike information

- criteria, Stat. Probab. Lett. 33 (1997) 201–208. [https://doi.org/10.1016/S0167-7152\(96\)00128-9](https://doi.org/10.1016/S0167-7152(96)00128-9).
- [68] B. Bocklund, R. Otis, A. Egorov, A. Obaied, I. Roslyakova, Z.-K. Liu, ESPEI for efficient thermodynamic database development, modification, and uncertainty quantification: application to Cu–Mg, MRS Commun. 9 (2019) 618–627. <https://doi.org/DOI:10.1557/mrc.2019.59>.
- [69] P. Hohenberg, W. Kohn, Inhomogeneous electron gas, Phys. Rev. 136 (1964). <https://doi.org/10.1103/PhysRev.136.B864>.
- [70] W. Kohn, L.J. Sham, Self-consistent equations including exchange and correlation effects, Phys. Rev. 140 (1965). <https://doi.org/10.1103/PhysRev.140.A1133>.
- [71] G. Kresse, J. Furthmüller, Efficient iterative schemes for ab initio total-energy calculations using a plane-wave basis set, Phys. Rev. B - Condens. Matter Mater. Phys. 54 (1996). <https://doi.org/10.1103/PhysRevB.54.11169>.
- [72] G. Kresse, D. Joubert, From ultrasoft pseudopotentials to the projector augmented-wave method, Phys. Rev. B. 59 (1999) 1758–1775. <https://doi.org/10.1103/PhysRevB.59.1758>.
- [73] J. Sun, A. Ruzsinszky, J. Perdew, Strongly Constrained and Appropriately Normed Semilocal Density Functional, Phys. Rev. Lett. 115 (2015). <https://doi.org/10.1103/PhysRevLett.115.036402>.
- [74] H.J. Monkhorst, J.D. Pack, Special points for Brillouin-zone integrations, Phys. Rev. B. 13 (1976). <https://doi.org/10.1103/PhysRevB.13.5188>.
- [75] P.E. Blöchl, O. Jepsen, O.K. Andersen, Improved tetrahedron method for Brillouin-zone integrations, Phys. Rev. B. 49 (1994). <https://doi.org/10.1103/PhysRevB.49.16223>.
- [76] J.M. Ziman, Electrons and phonons: the theory of transport phenomena in solids, Oxford university press, 2001.
- [77] A. Togo, I. Tanaka, First principles phonon calculations in materials science, Scr. Mater. 108 (2015). <https://doi.org/10.1016/j.scriptamat.2015.07.021>.
- [78] J.-O. Andersson, T. Helander, L. Höglund, P. Shi, B. Sundman, Thermo-Calc & DICTRA, computational tools for materials science, Calphad. 26 (2002) 273–312. [https://doi.org/https://doi.org/10.1016/S0364-5916\(02\)00037-8](https://doi.org/https://doi.org/10.1016/S0364-5916(02)00037-8).
- [79] S.L. Chen, S. Daniel, F. Zhang, Y.A. Chang, X.Y. Yan, F.Y. Xie, R. Schmid-Fetzer, W.A. Oates, The PANDAT software package and its applications, Calphad Comput. Coupling Phase Diagrams Thermochem. 26 (2002) 175–188. [https://doi.org/10.1016/S0364-5916\(02\)00034-2](https://doi.org/10.1016/S0364-5916(02)00034-2).
- [80] D.R. Torgeson, T.G. Sahama, A Hydrofluoric Acid Solution Calorimeter and the Determination of the Heats of Formation of Mg₂SiO₄, MgSiO₃, and CaSiO₃, J. Am. Chem. Soc. 70 (1948) 2156–2160. <https://doi.org/10.1021/ja01186a048>.
- [81] P.T. Carter, T.G. Macfarlane, Part II-The thermodynamic properties of CaO-SiO₂ slags, J. Iron. Steel I. 185 (1957) 62–66.
- [82] M.A. Bredig, Polymorphism of Calcium Orthosilicate, J. Am. Ceram. Soc. 33 (1950) 188–192. <https://doi.org/https://doi.org/10.1111/j.1151-2916.1950.tb12789.x>.
- [83] I. Barin, F. Sauert, E. Schultze-Rhonhof, W. Shu Sheng, Thermochemical data of pure substances , VCH, Weinheim, Germany, 1989.
- [84] K. Adamkovicova, The heat of fusion of CaSiO₃, (1980).
- [85] T. Hanein, F.P. Glasser, M. Bannerman, Thermodynamics of Portland Cement Clinkering, 14th Int. Congr. Chem. Cem. (2015). <http://www.iccc2015beijing.org/dct/page/1> (accessed January 21, 2020).
- [86] W. Köther, F. Müller, Thermochemische Untersuchung zur Stabilität von Orthosilikaten und-germanaten, Zeitschrift Für Anorg. Und Allg. Chemie. 444 (1978) 77–90.
- [87] E.T. Carlson, The Decomposition of tricalcium silicate in the temperature range 1000° - 1300° C, Bur. Stand. J. Res. 7 (1931).
- [88] M. Akaogi, M. Yano, Y. Tejima, M. Iijima, H. Kojitani, High-pressure transitions of

diopside and wollastonite: Phase equilibria and thermochemistry of CaMgSi₂O₆, CaSiO₃ and CaSi₂O₅-CaTiSiO₅ system, Phys. Earth Planet. Inter. 143 (2004) 145–156.
<https://doi.org/10.1016/j.pepi.2003.08.008>.

Appendices

Table A.1. Table of the optimised coefficients for the solid phases in the C-S system, for use in the 3rd generation CALPHAD function given in Eq. (1).

α (Compound)	$D_{1,\alpha}$	$\theta_{1,\alpha}$	$D_{2,\alpha}$	$\theta_{2,\alpha}$	$D_{3,\alpha}$	$\theta_{3,\alpha}$	C_2	H_0
cyclowollastonite-CaSiO ₃	3.20933	398.726519	0.448513	113.639538	1.337919	179.149444	-0.004177	-1686958.147895
monoclinic-Ca ₃ SiO ₅	2.721575	216.554568	4.322571	502.02771	1.955837	1253.079747	-0.013441	-3026014.386963
rankinite-Ca ₃ Si ₂ O ₇	3.262669	201.048711	5.228277	471.758995	3.509145	1114.209222	0.001345	-4081064.820333
rhombohedral-Ca ₃ SiO ₅	2.728885	216.897351	4.322171	502.823393	1.948978	1257.541676	-0.013504	-3026101.460607
triclinic-Ca ₃ SiO ₅	2.770329	217.322399	4.397009	511.911036	1.832799	1306.969635	-0.013446	-3026703.415132
wollastonite-CaSiO ₃	0.021926	39.983404	1.364237	180.16112	3.611497	777.592204	-0.00094	-1685783.296919
α -Ca ₂ SiO ₄	3.310467	427.508038	1.659827	174.273816	2.029525	1235.840109	-0.008061	-2368644.112281
α' -Ca ₂ SiO ₄	0.626679	122.320053	3.608269	315.618264	2.756109	1092.028025	-0.005737	-2377633.243328
β -Ca ₂ SiO ₄	0.452659	258.5222081	3.03791	835.357211	3.509071	259.231418	-0.008614	-2385856.23658
γ -Ca ₂ SiO ₄	0.151692	88.647382	2.689799	257.3199	4.158219	759.369678	-0.001096	-2384448.968068

Table A.2. Table of all experimental measurements from literature including the uncertainty used in the fitting. The reported uncertainties are the uncertainties reported by the respective authors for that measurement and the fitted uncertainties are uncertainties used in the simultaneous fit. In the case where the uncertainties were not stated or incorrect by the author, standard error estimates of 5% were used depending on the experiment type. Additionally, where no conflicting data exists, we have not presented a “fitted uncertainty” (see discussion in Section 3). All values are in SI units.

* These measurements were not fit and are only reported for comparison, their fitted uncertainty refers to the uncertainty to ensure the measurement is 1 sigma from the fit

Variable	Chemistry	T(K)	Value(J/mol)	Reported Uncertainty	Fitted Uncertainty	Ref
Cp	0.957 β -Ca ₂ SiO ₄ + 0.043 CaOH ₂	2.2107 → 302.887	0.0010 → 127.07 0.28	8.02% → 0.22%	0.01 → 42.49	1203.1% → 33.44% [40]*
Cp	0.957 β -Ca ₂ SiO ₄ + 0.043 CaOH ₂	282.354 → 463.843	123.47 → 151.70 0.09 → 0.04	0.07% 5.25	0.02 → 0.88%	[40]*

Variable	Chemistry	T(K)	Value(J/mol)	Reported Uncertainty	Fitted Uncertainty	Ref
Cp	0.957 β -Ca ₂ SiO ₄ + 0.043 CaOH ₂	480.85 → 768.943	147.73 → 286.23	1.36 → 3.88 0.24% → 0.46%	2.56 → 5.39 1.67% → 3.19%	[40]*
Cp	β -Ca ₂ SiO ₄	2.19619 → 302.975	0.0012 → 127.85	0.0 → 0.32 11.4% → 0.25%	0.01 → 29.86 1072.06% → 23.35%	[40]*
Cp	β -Ca ₂ SiO ₄	284.136 → 766.466	125.13 → 171.60	0.08 → 1.28 0.06%	0.02 → 1.28 0.06%	[40]
H _r -H _{298.15}	β -Ca ₂ SiO ₄	406.0 → 964.6	14811.36 → 108784.0	740.57 → 5439.2 5.0%	740.57 → 5439.2 5.0%	[41]
Cp	β -Ca ₂ SiO ₄	52.66 → 296.48	17.08 → 128.11	0.85 → 6.41 5.0%	0.85 → 6.41 5.0%	[39]
ΔH	2 CaO + α quartz-SiO ₂ → β -Ca ₂ SiO ₄	298.15	-126314.96	962.32 0.76%	962.32 0.76%	[42]
ΔH	β -Ca ₂ SiO ₄	298.15	-2308400	4600.0 0.2%	4600.0 0.2%	[40]
ΔH	2 CaO + α -quartz-SiO ₂ → β -Ca ₂ SiO ₄	967.0	-149200	1500.0 1.01%	22500.0 15.08%	[86]
H _r -H _{293.15}	triclinic-Ca ₃ SiO ₅	573.15 → 1173.15	55354.32 → 196688.16	1000.0 1.81% → 0.51%	1000.0 1.81% → 0.51%	[44]
Cp	triclinic-Ca ₃ SiO ₅	54.26 → 298.16	23.3 → 171.87	0.19 0.82% → 0.11%	1.5 6.43% → 0.87%	[39]
ΔH	3 CaO + α -quartz-SiO ₂ → triclinic-Ca ₃ SiO ₅	298.15	-112884.32	920.48 0.82%	4602.4 4.08%	[42]

Variable	Chemistry	T(K)	Value(J/mol)	Reported Uncertainty	Fitted Uncertainty	Ref
ΔH	$\text{CaO} + \beta\text{-Ca}_2\text{SiO}_4 \rightarrow \text{triclinic-Ca}_3\text{SiO}_5$	296.15	8786.4	836.8 9.52%	836.8 9.52%	[45]
$T_{\text{transition}}$	$\text{monoclinic-Ca}_3\text{SiO}_5 \rightarrow \text{triclinic-Ca}_3\text{SiO}_5$	1253.0	-	5.0 K -	- -	[8]
ΔH	$\text{triclinic-Ca}_3\text{SiO}_5 \rightarrow \text{monoclinic-Ca}_3\text{SiO}_5$	1253.0	477.6036	23.8 5%	- -	[8]
$T_{\text{transition}}$	$\text{rhombohedral-Ca}_3\text{SiO}_5 \rightarrow \text{monoclinic-Ca}_3\text{SiO}_5$	1323.0	-	5.0 K -	- -	[8]
ΔH	$\text{monoclinic-Ca}_3\text{SiO}_5 \rightarrow \text{rhombohedral-Ca}_3\text{SiO}_5$	1323.0	47.76036	2.38 5%	- -	[8]
C_p	$\gamma\text{-Ca}_2\text{SiO}_4$	2.20845 → 302.96	0.003 → 0.25	0.0 → 0.19% 2.91% → 3.52%	1.93 → 3.52 58.21% → 3.88%	[40]*
C_p	$\gamma\text{-Ca}_2\text{SiO}_4$	282.386 → 862.307	123.11 → 173.696	6.16 → 8.68 5.0%	6.16 → 8.68 5.0%	[40]
$H_T\text{-H}_{298.15}$	$\gamma\text{-Ca}_2\text{SiO}_4$	405.2 → 1112.9	13807.2 → 133134.88	690.36 → 6656.74 5.0%	690.36 → 6656.74 5.0%	[41]
C_p	$\gamma\text{-Ca}_2\text{SiO}_4$	54.15 → 298.15	16.05 → 126.81	0.8 → 6.34 5.0%	0.8 → 6.34 5.0%	[9]
$H_T\text{-H}_{298.15}$	$\gamma\text{-Ca}_2\text{SiO}_4$	972.86 → 1072.09	108430.8 → 123306.7	3617.9 → 3251.5 3.34%	3617.9 → 3251.5 3.34%	Present work
ΔH	$2\text{ CaO} + \alpha\text{-quartz-SiO}_2 \rightarrow \gamma\text{-Ca}_2\text{SiO}_4$	298.15	-136816.8	836.8 0.61%	836.8 0.61%	[43]
ΔH	$\gamma\text{-Ca}_2\text{SiO}_4$	298.15	-2316000	4500.0 0.19%	4500.0 0.19%	[40]

Variable	Chemistry	T(K)	Value(J/mol)	Reported Uncertainty	Fitted Uncertainty	Ref
Cp	α' -Ca ₂ SiO ₄	12.0 → 300.0	0.21 → 128.69	0.01 → 6.43	5.0%	0.01 → 6.43
ΔH	β -Ca ₂ SiO ₄ → α' -Ca ₂ SiO ₄	974.1 → 1690.6	111796.48 → 252755.44	5589 → 12637	5.0%	7825.75 → 17692.88
ΔH	γ -Ca ₂ SiO ₄ → α' -Ca ₂ SiO ₄	1171.39 → 1471.05	148801.8 → 212360.1	3879.2 → 6444.6	2.61%	3879.2 → 6444.6
T _{transition}	α' -Ca ₂ SiO ₄ → γ -Ca ₂ SiO ₄	1120.0	-	10.0 K	-	-
T _{transition}	α' -Ca ₂ SiO ₄ → β -Ca ₂ SiO ₄	970.0	-	10.0 K	-	-
ΔH	γ -Ca ₂ SiO ₄ → α' -Ca ₂ SiO ₄	1120.0	14100.08	705	5%	2092.0
ΔH	β -Ca ₂ SiO ₄ → α' -Ca ₂ SiO ₄	970.0	1422.56	71	5%	418.4
T _{transition}	CaO + α' -Ca ₂ SiO ₄ → triclinic-Ca ₃ SiO ₅	1524.0	-	10.0 K	-	-
ΔH	β -Ca ₂ SiO ₄ → α -Ca ₂ SiO ₄	1730.5 → 1816.0	274763.28 → 291750.32	13735 → 14585	5.0%	2747.63 → 2853.49
T _{transition}	α -Ca ₂ SiO ₄ → α' -Ca ₂ SiO ₄	1710.0	-	10.0 K	-	-
ΔH	α' -Ca ₂ SiO ₄ → α -Ca ₂ SiO ₄	1710.0	16800	815	5.0%	1000.0
ΔH	α' -Ca ₂ SiO ₄ → α -Ca ₂ SiO ₄	1710.0	13472.48	2092.0	15.53%	2092.0
Cp	rankinite-Ca ₃ Si ₂ O ₇	53.45 → 298.15	29.60 → 214.38	0.28	0.95% → 0.13%	0.14
					0.47% → 0.07%	[9]

Variable	Chemistry	T(K)	Value(J/mol)	Reported Uncertainty	Fitted Uncertainty	Ref		
H _r -H _{298.15}	rankinite-Ca ₃ Si ₂ O ₇	872.45 → 1471.65	148228.7 → 411438.02	3574.7 → 7015.8	2.41% → 6.9%	1818.81 → 1344.66	0.72% → 20.69%	Present work
ΔG	β-Ca ₂ SiO ₄ → 0.5 CaO + 0.5 rankinite-Ca ₃ Si ₂ O ₇	943.0 → 963.0	10999.32 → 11578.24	771.88	7.02% → 6.45%	2315.65	21.05% → 19.35%	[47]*
ΔG	α'-Ca ₂ SiO ₄ → 0.5 CaO + 0.5 rankinite-Ca ₃ Si ₂ O ₇	971.0 → 1143.0	11192.29 → 12736.06	771.88	6.9% → 6.45%	2315.65	20.69% → 19.35%	[47]*
ΔH	3 CaO + 2 α-quartz-SiO ₂ → rankinite-Ca ₃ Si ₂ O ₇	298.15	-229136.76	4184.0	1.83%	4184.0	1.83%	[46]
ΔH	3 CaO + 2 α-quartz-SiO ₂ → rankinite-Ca ₃ Si ₂ O ₇	0.0	-212000	10000.0	4.72%	20000.0	9.43%	Present work
Cp	wollastonite-CaSiO ₃	9.81 → 303.8	0.192 → 86.06	0.02 → 8.61	10.0%	0.02 → 8.61	10.0%	[48]
Cp	wollastonite-CaSiO ₃	373.2 → 1173.2	97.4 → 123.3	1.0	1.03% → 0.81%	1.0	1.03% → 0.81%	[48]
H _r -H _{293.15}	wollastonite-CaSiO ₃	573.15 → 1373.15	28503.08 → 124987.79	761.0	2.67% → 0.61%	761.0	2.67% → 0.61%	[44]
ΔH	CaO + α-quartz-SiO ₂ → wollastonite-CaSiO ₃	298.15	-88910	543.92	0.61%	543.92	0.61%	[80]
ΔH	CaO + α-quartz-SiO ₂ → wollastonite-CaSiO ₃	970.0	-89872.32	1506.24	1.68%	1506.24	1.68%	[51]
ΔH	CaO + α-quartz-SiO ₂ → wollastonite-CaSiO ₃	298.15	-86520	4340.0	5.02%	4340.0	5.02%	[88]

Variable	Chemistry	T(K)	Value(J/mol)	Reported Uncertainty	Fitted Uncertainty	Ref
ΔH	wollastonite-CaSiO ₃	298.15	-1634320	2710.0 0.17%	2710.0 0.17%	[40]
ΔG	wollastonite-CaSiO ₃ → CaO + β -quartz-SiO ₂	898.15 → 1148.15	88380.57 → 89731.36	771.88 0.87%	771.88 0.87%	[47]
Cp	cyclowollastonite-CaSiO ₃	10.7 → 1573.2	0.22 → 127.61	0.01 → 6.38 5.0%	0.02 → 12.76 10.0%	[48]
Cp	cyclowollastonite-CaSiO ₃	373.2 → 1573.2	95.81 → 132.42	1.0	1.04% → 0.76% 1.0	[48]
H _r -H _{273.15}	cyclowollastonite-CaSiO ₃	815.9 → 1488.9	57803.0 → 141370.0	2000.0 3.46% → 1.41%	2000.0 1.04% → 0.76% 1.0	[50]
H _r -H _{273.15}	cyclowollastonite-CaSiO ₃	1102.3 → 1806.5	92588.0 → 188830.0	2000.0 1.72% → 1.13%	2000.0 1.72% → 1.13%	[49]
ΔH	CaO + α -quartz-SiO ₂ → cyclowollastonite-CaSiO ₃	970.0	-83345.28	1297.04 1.56%	1297.04 1.56%	[51]
ΔH	lime-CaO+ alpha quartz-SiO ₂ → cyclowollastonite-CaSiO ₃	298.15	-81922.72	1589.92 1.94%	1589.92 1.94%	[43]
ΔG	0.5 rankinite-Ca ₃ Si ₂ O ₇ → 0.5 CaO + cyclowollastonite-CaSiO ₃	943.15 → 1003.15	80082.83 → 81240.65	1157.82 1.43% → 1.44%	57891.2 71.26% → 71.77%	[47]*
T _{transition}	cyclowollastonite-CaSiO ₃ → wollastonite-CaSiO ₃	1398.0	-	10.0 K -	-	[38]